Politecnico di Torino

ScuDo
Scuola di Dottorato ~ Doctoral School
WHAT YOU ARE, TAKES YOU FAR

Doctoral Dissertation
Doctoral Program in Electrical Engineering (36^{th}cycle)

Design and Testing of e-Motors for Transportation

By

Gaetano Dilevrano

******

Supervisor:
Prof. Gianmario Pellegrino, Supervisor
Dr. Simone Ferrari, Co-Supervisor

Doctoral Examination Committee:
Prof. Phil Kollmeyer, Referee, McMaster University
Dr. Mauro Di Nardo, Referee, Politecnico di Bari
Dr. Claudio Bianchini, Università degli Studi di Modena e Reggio Emilia
Dr. Andrea Credo, Università degli Studi dell'Aquila
Dr. Sandro Rubino, Politecnico di Torino

Politecnico di Torino
2024

Declaration

I hereby declare that the contents and organization of this dissertation constitute my own original work and do not compromise in any way the rights of third parties, including those relating to the security of personal data.

Gaetano Dilevrano
2024

Acknowledgements

I would like to express my heartfelt gratitude to my supervisors, Prof. Gianmario Pellegrino and Dr. Simone Ferrari, for their trust in me and their indispensable guidance both personally and professionally. Their mentorship has been invaluable throughout this journey.

A significant portion of my gratitude also goes to the SyR-e Team, with special thanks to Dr. Paolo Ragazzo, my friend and fellow traveler on this PhD journey. I conducted most of my research activities alongside him, and we supported each other in improving the quality of our work and solving problems. I also extend my sincere thanks to Dr. Paolo Pescetto and Andrei Bojoi for their support and collaboration.

I would like to express special thanks to Dr. Sandro Rubino, who was always available to offer his support in any situation. I am deeply grateful to the entire PEIC group and to all the PhD students who shared this adventure with me.

I am particularly thankful to Dr. Ali Emadi and Dr. Phil Kollmeyer for giving me the opportunity to spend six months with their research group at McMaster University in Canada. It was a transformative experience, and I am grateful to the fantastic individuals I met there, including Fabricio Machado, Eduardo Akira Shiguemoto, and Eduardo Louback, for welcoming me into their activities both during and after work.

Finally, I want to express my deepest gratitude to Chiara and my family for their unwavering support and advice throughout this period. Their love and encouragement have been a constant source of strength for me.

Abstract

The global push towards cleaner energy is gaining momentum, driven by stricter climate policies, technological progress, and economic incentives to cut greenhouse gas emissions and achieve Net Zero Emission (NZE) targets. Among regions, the European Union stands out for its active promotion of the NZE agenda, spurred by environmental concerns and the aim to reduce reliance on fossil fuels from external sources. This transition calls for substantial shifts in both energy production and consumption, with renewable and clean energy sources taking the lead. Electric vehicles play a crucial role in emission reduction, experiencing a surge in global sales, particularly in China, the EU, and the US, despite facing infrastructure hurdles. In the realm of electric machines, there is a growing demand for higher torque and power density, particularly in traction applications. Developing cost-effective, lightweight, and compact designs necessitates a multi-physics approach. While various design methodologies exist, such as analytical models and Finite Element Analysis (FEA) combined with algorithmic optimization, they often entail high computational costs and offer limited insight to designers. One notable contribution addresses this challenge by proposing a hybrid approach, integrating FEA with equations to strike a balance between computational efficiency and design accuracy. This method, grounded in the design plane and considering magnetic, mechanical, and inverter specifications, offers promising results. Another proposed approach revolves around design via scaling laws. These laws enable the evaluation of new machines with varying dimensions and ratings with minimal computational burden. By refining these laws, especially for traction motors, and considering specific dimensional and power converter constraints, designers can achieve accurate and optimized solutions. Addressing structural and thermal aspects of scaled designs further enhances the reliability of the design process. The majority of findings from years of research have been experimentally validated, and all procedures are documented in the open-source software SyR-e, to which the author has contributed as one of the developers.

Contents

List of Figures

List of Tables

List of published papers

Conference papers:

- S. Ferrari, P. Ragazzo, **G. Dilevrano** and G. Pellegrino, "Flux-Map Based FEA Evaluation of Synchronous Machine Efficiency Maps," 2021 IEEE Workshop on Electrical Machines Design, Control and Diagnosis (WEMDCD), Modena, Italy, 2021, pp. 76-81, doi: 10.1109/WEMDCD51469.2021.9425678.
- S. Ferrari, P. Ragazzo, **G. Dilevrano** and G. Pellegrino, "Determination of the Symmetric Short-Circuit Currents of Synchronous Permanent Magnet Machines Using Magnetostatic Flux Maps," 2021 IEEE Energy Conversion Congress and Exposition (ECCE), Vancouver, BC, Canada, 2021, pp. 3697-3704, doi: 10.1109/ECCE47101.2021.9595806.
- S. Ferrari, **G. Dilevrano**, P. Ragazzo and G. Pellegrino, "The dq-theta Flux Map Model of Synchronous Machines," 2021 IEEE Energy Conversion Congress and Exposition (ECCE), Vancouver, BC, Canada, 2021, pp. 3716-3723, doi: 10.1109/ECCE47101.2021.9595187.
- P. Ragazzo, **G. Dilevrano**, S. Ferrari and G. Pellegrino, "Design of IPM Synchronous Machines Using Fast-FEA Corrected Design Equations," 2022 International Conference on Electrical Machines (ICEM), Valencia, Spain, 2022, pp. 1-7, doi: 10.1109/ICEM51905.2022.9910753.
- **G. Dilevrano**, P. Ragazzo, S. Ferrari, G. Pellegrino and T. Burress, "Magnetic, Thermal and Structural Scaling of Synchronous Machines," 2022 IEEE Energy Conversion Congress and Exposition (ECCE), Detroit, MI, USA, 2022, pp. 1-8, doi: 10.1109/ECCE50734.2022.9947472

- P. Ragazzo, S. Ferrari, **G. Dilevrano**, L. Beatrici, C. Girardi and G. Pellegrino, "Scaling of Ferrite-assisted Synchronous Reluctance Machines for Lifting Systems," 2023 IEEE Workshop on Electrical Machines Design, Control and Diagnosis (WEMDCD), Newcastle upon Tyne, United Kingdom, 2023, pp. 1-6, doi: 10.1109/WEMDCD55819.2023.10110927.
- P. Ragazzo, S. Ferrari, **G. Dilevrano**, L. Beatrici, C. Girardi and G. Pellegrino, "Synchronous Reluctance Machines with and without Ferrite Assistance for Lifting Systems," 2023 IEEE International Electric Machines & Drives Conference (IEMDC), San Francisco, CA, USA, 2023, pp. 1-7, doi: 10.1109/IEMDC55163.2023.10239091.
- P. Pescetto, **G. Dilevrano**, G. Pellegrino and A. Boglietti, "Improved Short Time Thermal Transient Model and Testing Procedure for High Power Density Motors," 2023 IEEE International Electric Machines & Drives Conference (IEMDC), San Francisco, CA, USA, 2023, pp. 1-6, doi: 10.1109/IEMDC55163 .2023.10239037.
- **G. Dilevrano**, P. Ragazzo, S. Ferrari and G. Pellegrino, "Comparative Design of Ferrite- and NdFeB-PMSMs using the (x,b) Design Plane," 2023 IEEE International Electric Machines & Drives Conference (IEMDC), San Francisco, CA, USA, 2023, pp. 1-7, doi: 10.1109/IEMDC55163.2023.10238969.
- P. Ragazzo, **G. Dilevrano**, S. Ferrari and G. Pellegrino, "Comparative Turn-off Safe Modes of Ferrite- and NdFeB- Interior PMSMs," 2023 IEEE Energy Conversion Congress and Exposition (ECCE), Nashville, TN, USA, 2023, pp. 4133-4139, doi: 10.1109/ECCE53617.2023.10362467.
- P. Pescetto, **G. Dilevrano**, G. Pellegrino and A. Boglietti, "Real Time Estimator of Winding Hotspot Temperature for PMSM Drives," 2023 IEEE Energy Conversion Congress and Exposition (ECCE), Nashville, TN, USA, 2023, pp. 3822-3828, doi: 10.1109/ECCE53617.2023.10362355.

Journal papers:

- S. Ferrari, P. Ragazzo, **G. Dilevrano** and G. Pellegrino, "Flux and Loss Map Based Evaluation of the Efficiency Map of Synchronous Machines," in IEEE Transactions on Industry Applications, vol. 59, no. 2, pp. 1500-1509, March-April 2023, doi: 10.1109/TIA.2022.3221381.

- S. Ferrari, **G. Dilevrano**, P. Ragazzo, P. Pescetto and G. Pellegrino, "Fast Determination of Transient Short-Circuit Current of PM Synchronous Machines via Magnetostatic Flux Maps," in IEEE Transactions on Industry Applications, vol. 59, no. 4, pp. 4000-4009, July-Aug. 2023, doi: 10.1109/TIA.2023.3265952.

Submitted journal papers:

- S. Ferrari, **G. Dilevrano**, P. Ragazzo, G. Pellegrino and T. Burress, "Rapid Magnetic, Thermal and Structural Scaling of Synchronous Machines based on Flux and Loss Maps," in IEEE Transactions on Industry Applications.
- P. Pescetto, **G.Dilevrano**, G. Pellegrino and A. Boglietti, "Improved Thermal Model and Short Time Transient Testing Procedure for High Power Density Motors," in IEEE Transactions on Industry Applications.
- P. Pescetto, **G.Dilevrano**, G. Pellegrino and A. Boglietti, "Real Time Estimator of Winding Hotspot Temperature for PMSM Motor Drives," in IEEE Transactions on Industry Applications.

Chapter 1

Introduction

Nowadays, the transition to clean energy is accelerating due to stringent green climate policy, new available technologies, and economic reasons. In October 2018, the Intergovernmental Panel on Climate Change (IPCC) stated that the World has to reduce the global GreenHouse Gas (GHG), that are pushing countries to reach Net Zero Emission this century (NZE). In November 2022, 87 countries and the European Union (EU) (yet stated with the European Green Deal, 2019) announced pledges in this direction; this means that 85% of the world's emissions will be covered by achieving this result. In this way, the rise in the global temperature should remain stable at around 1.7°C in 2100 [30, 1].
Moreover, the EU is encouraged, beyond the climate crisis, by ending its dependence form Russian fossil fuels, which were used as economic and political weapons after the invasion of Ukraine, and cost European taxpayers about 100 billion euros per year [31].
Achieving the NZE requires important changes in terms of energy: the energy demand should be reduced and a consistent part of it should be produced by renewable and clean sources as shown in Fig. 1.1. In the NZE scenario an estimated fall of 10% in energy supply-demand is required by 2030, and then by 2050, a total reduction up to 15% is predicted. Regarding the renewables resources, they will increase covering about 40% of the global primary energy, followed by that one comes from nuclear power plants which will be around 12%. However, up to date, fossil fuel represents about 80% of the energy supply that is reflected in relevant GHG emissions [1].

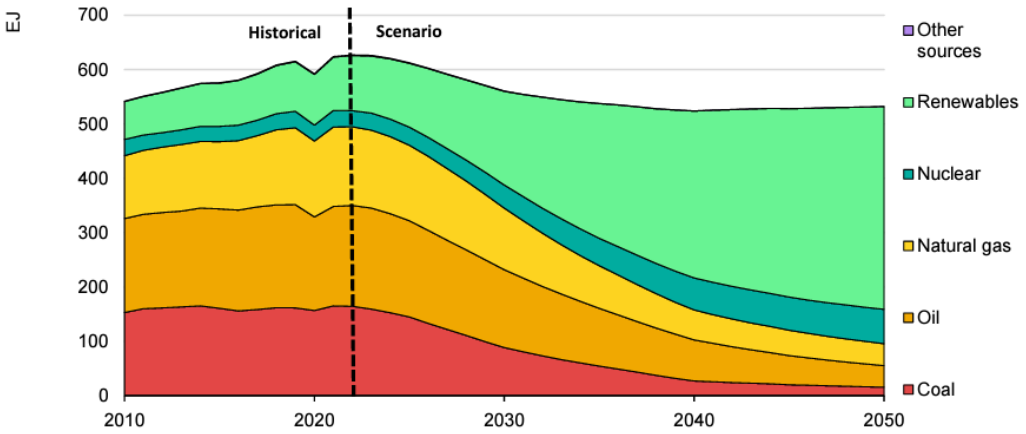

Fig. 1.1 Global energy trend towards the NZE scenario [1].

In Fig. 1.2 and Fig. 1.3, the emission of CO_2 during the year is reported for worldwide and EU areas, respectively. In 2022, the total CO_2 emission reached the maximum value of all-time equals to 36.8 Gt (note that in the charts the data refer to all GHG including CO_2, N_2O, CH_4 and F-gases), after a reverse trend in 2020 due to the COVID-19 that reduced the energy demand by about 5% [1, 30, 32]. The trend is different if only the EU, is considered: it is clear that the CO_2 emission is decreasing during the years, even if seems to be stable in the last after the pandemic.

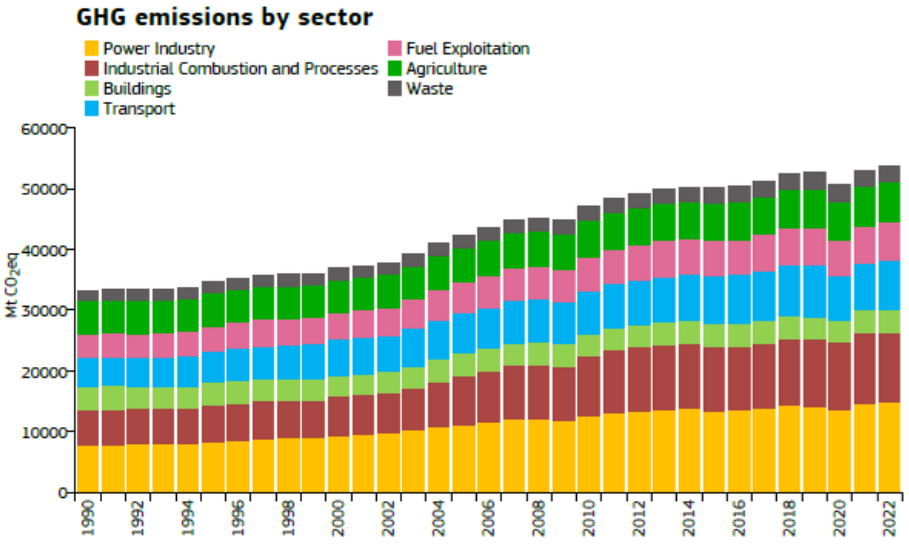

Fig. 1.2 World's GHG emissions [2].

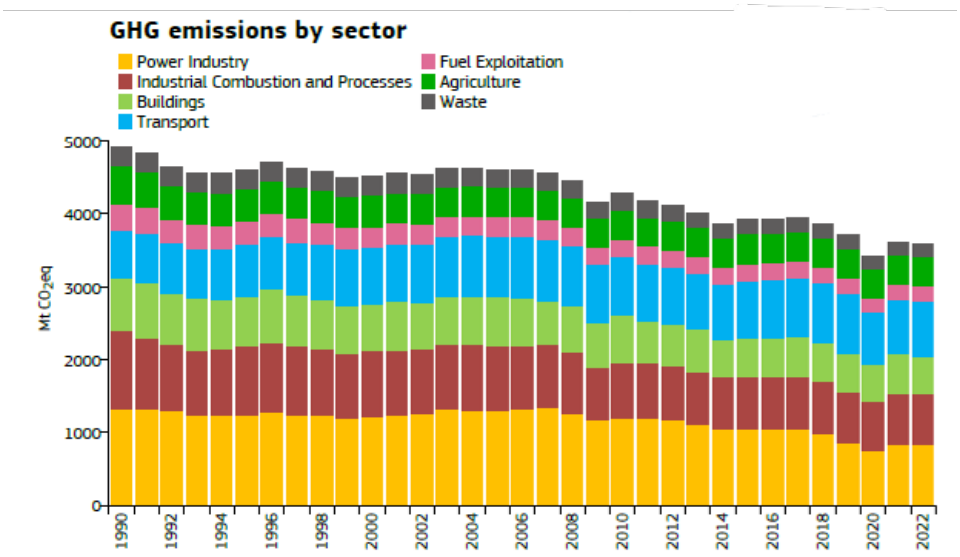

Fig. 1.3 European's GHG emissions [2].

In the same plots, the emissions are grouped by sector and the same trends and considerations can be noted also in Fig. 1.4 and Fig. 1.5. A consistent portion of emissions comes from the transportation sector, about 25%, and is interesting to note that, in Europe, it is the only sector that shows a total rise of 19% since 1990, while all the others fall in a range from 24-44%. Indeed, at the worldwide level, most sectors experienced high emission increases, up to 95% for industrial processes. The last two-year period has not expired a net change in any sector, both considering an EU or global visions.

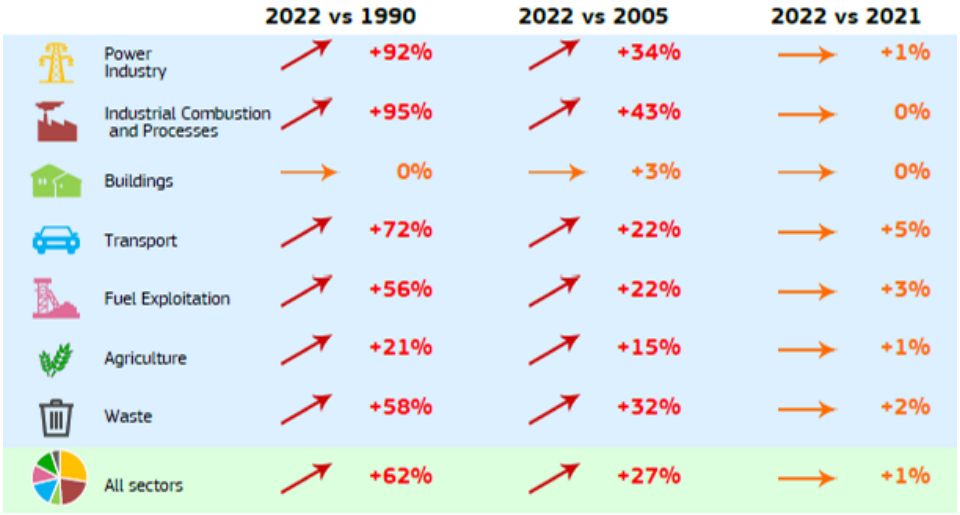

Fig. 1.4 World's GHG emissions trend by sectors [2].

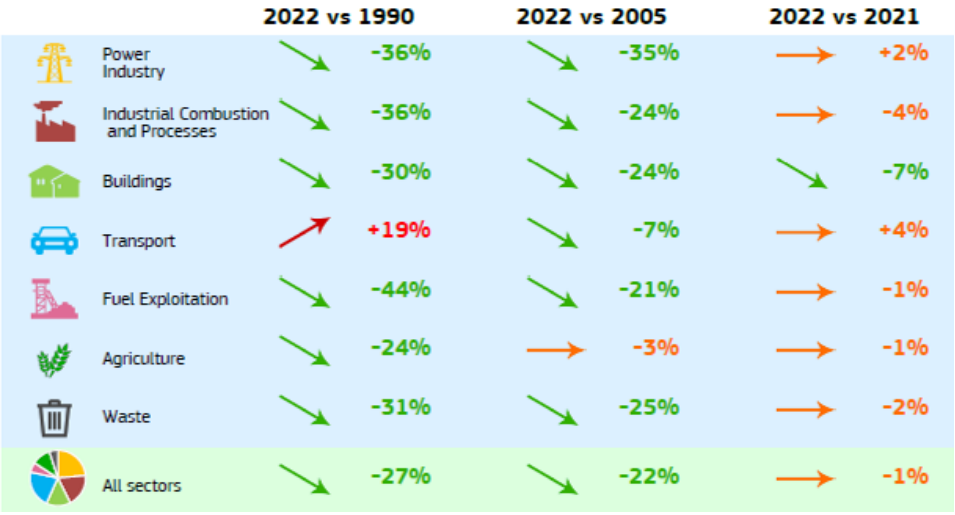

Fig. 1.5 European's GHG emissions trend by sectors [2].

Fig 1.6 depicts the share in the global transport emissions for the year 2022. About 50% of emissions are caused by cars, followed by freight vehicles, aviation, and international shipping (most related to marine). That means that the electrification of cars is crucial for following the NZE path: in fact every electric vehicle, even if powered by fossil fuel electricity, pollutes less than a conventional combustion car, in terms of GHG emissions [2]. The process is already underway, as reported in [33], showing that electric vehicle sales reach 10.2 million units in 2022, representing 14% of the global sales. It has to be considered that before 2010, most of the electric vehicles were just used as prototypes. However, car electrification is focused in China, Europe, and the United States, where electric grid and generation have the capability to satisfy the energy demand. China represents the largest market share of sales (57.8%), helped by the outcome of tax incentives for electric vehicles. Europe has 25.4% of sales, however, Norway has the largest sales in the world, accounting for 72% of sold cars. This data falls around 25% for Germany and 15% for France and the United Kindom. Japan has a very low portion of sales, linked to the electricity shortage caused by the Fukushima incident in 2011. The world's leading manufacturers are Tesla (USA), Volkswagen (Germany), and (China), with 936000, 763000, and 598000 sold vehicles, respectively, in 2021.

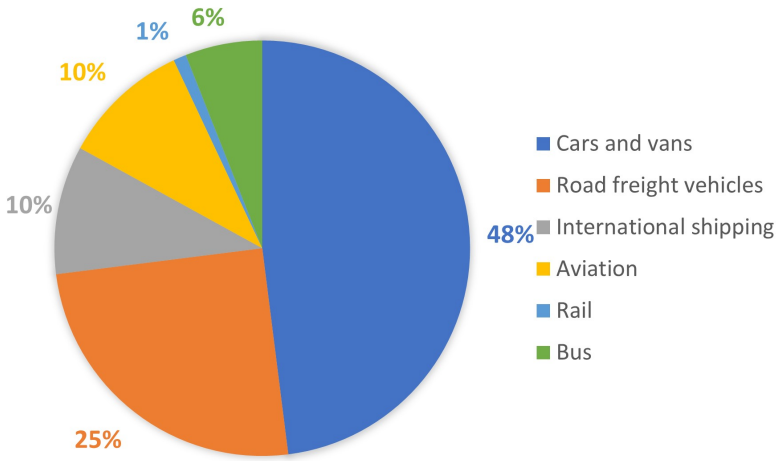

Fig. 1.6 CO_2 emission in transportation sector worldwide [2].

1.1 Powertrain classification and related motors

The aims of this section are to illustrate and classify the different electrified powertrains. They can be categorized in different ways, i.e. according to the electrification level, the propulsion system operational modes, and the architectures. First of all, it is mandatory to define which is the definition of a powertrain and its main components. According to [25, 34, 35] the powertrain is "an assembly of every component that thrusts your car into motion. It includes engine, transmission, driveshaft, axles, and differential." The powertrain is also called the propulsion system and can be divided in 4 subsystems [25]:

1. **Power unit**: provides power to the vehicle. In a hybrid car, it includes the Internal Combustion Enginee (ICE), the Electric Machine (EM) and, the traction inverter. The ICE is a heat engine that supplies power by means of the combustion of fuel. Indeed, the EM provides power by means of electromechanical conversion. The traction inverter converts DC power from the battery into AC power in motor operations and vice-versa, for example during regenerative braking in generator mode.

2. **Driveline**: makes a power link between the power unit and the wheels. The main components are the transmission, which matches the motor and wheels speed; the clutch which disconnects the power unit from the transmission and it allows to operate in idle or to shift gear; the torque converter, which replaces the clutch in the automatic transmission; and the differential which allows the wheels to rotate at different speeds.

3. **Energy**: the core is the battery pack, including cells, modules, sensors, and Battery Management System (BMS). Also, the auxiliary power module converter that provides power to low-voltage auxiliary devices [36] and the onboard battery charger [37] are parts of this subsystem.

4. **Thermal**: is related to all the components such as radiators, pumps, heaters..., and thermal management system that aims to ensure the safety and the reliability of the vehicle and the passenger comfort in the cabin [38, 39]. Due to the electrification, thermal aspects are increasingly relevant for component size reduction, performance, efficiency, and extending the driving range.

1.1.1 Electrification level and hybridization factor

The first way to classify hybrid vehicles is according to their electrification or hybridization degree. It is defined in [40] for non-plug-in vehicles and, the same concept is extended in [41] to the plug-in ones, where the plug-in capability means that the battery can be charged by connecting the vehicle to the electric grid. The definition of the two Hybridization Factors (HF) is reported in (1.1), (1.2).

$$HF = \frac{P_{EM}}{P_{EM} + P_{ICE}} \tag{1.1}$$

$$HF_{plug-in} = \frac{E_{grid}}{E_{grid} + E_{fuel}} \tag{1.2}$$

where P_{EM} and P_{ICE} are the EM and the ICE power, respectively; while E_{grid} and E_{fuel} are the averaged energy from the grid and fuel over the time, respectively. Note that for a traditional combustion vehicle, this ratio is equal to 0, while is 1 for a pure electric one.

The HF is a good qualitative index that links electric power and fuel economy. Generally, vehicles with higher HF tend to be more efficient and greener.

The hybrid vehicles can be divided according to the HF and the different drivetrain functionalities that the vehicle can manage. The main operational modes are [25, 42]:

- **Start-stop**: in idle, when the vehicle is not moving, the ICE is turned off and then restarted when the clutch is pressed or the brake released;
- **Electric torque assist**: the EM provides power for traction, improving the total efficiency and the system response;
- **Regenerative brake**: during the braking time the EM can work in generator mode recovering the kinetic energy from the wheels that is converted and stored in the battery;
- **Electric driving**: the EM provides all the power needed for the motion, it can limit all the vehicle operating points on the torque-speed plane or cover a limited area.

There are also other minor functionality that aims to improve comfort and optimize performance and fuel consumption, for example, start and drive in pure electric below a certain speed (e-launch).

The classification based on the HF is the following [25, 40, 43]:

- **Micro Hybrid Electric Vehicle (mHEV)**: with the lowest HF the vehicle propulsion is only through the ICE while the EM allows start and stop operation and can recovery small quantities of energy in braking. Reference car: Peugeot 208 e-HDi [44].
- **Mild Hybrid Electric Vehicle (MHEV)**: in addition to mHEV, the EM can provides torque joint with the ICE at high load. Reference car: Fiat Panda Hybrid [45].
- **Full Hybrid Electric Vehicle (HEV)**: has a greater HF compared to the previous ones. The EM can provide enough torque and power to move the vehicle without the ICE help. According to its configuration can be divided into series, parallel, and series-parallel hybrid. In series configuration, only the EM propels the vehicle while the engine is used, coupled with a generator, to supply power to the battery and the traction electric machine. In parallel

layout both the ICE and EM supply power for traction. Generally, the electric power flow is used for short drives and into the city, while the thermal power is used at high speeds or on highways. As the name suggests, the series-parallel configuration is a combination of the previous layout and allows the vehicle to operate in both ways. Reference car: Toyota Prius [46].

- **Plug-in Hybrid Electric Vehicle (PHEV)**: it is a HEV that can charge its battery using the electrical grid. Reference car: BMW X5 [47].
- **Extended Range Electric Vehicle (EREV)**: it is an electric vehicle with a small engine that is used joint with a generator to recharge the battery in order to extend the driving range. Reference car: BMW i3 [44].
- **Battery Electric Vehicle (BEV)**: this is a pure Electric Vehicle EV configuration, no engine. The only source of energy is the battery that is plug-in rechargeable. Reference car: Audi e-tron [48].

The Tab.1.1 summarizes the characteristics of the different categories of vehicles.

Table 1.1 Electrification levels and operating modes [25].

Operation mode	**mHEV**	**MHEV**	**HEV**	**PHEV**	**EREV**	**BEV**
Start-stop	+	+	-	-	/	/
Torque assist	+/-	+	++	++	/	/
Regenerative braking	+/-	+	++	++	++	++
Electric driving	-	-	+/-	+	++	+++
Plug-in capability	-	-	-	+	+	++
Fuel economy (%)	2-5	$<$20	20-50	35-80	$>$70	100

In Fig. 1.7 is reported as an example, the hybrid and electric car fleet by Ford. It is interesting to see that the Ford Kuga is sold in 3 different versions: MHEV, HEV and PHEV. In Fig. 1.8 the propulsion system of MHEV and PHEV version is reported.

Fig. 1.7 Ford hybrid and electric car fleet [3].

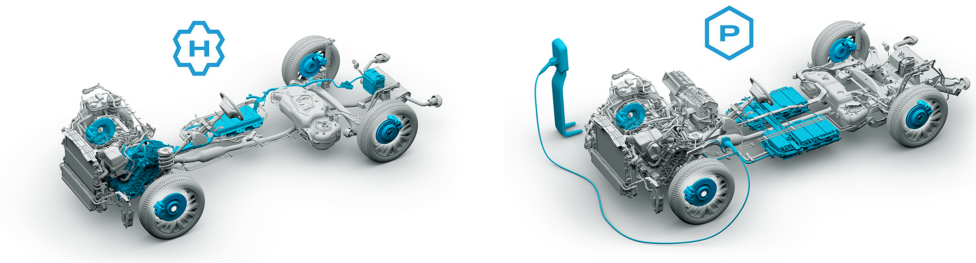

Fig. 1.8 Ford Kuga powertrain: (left) HEV and (right) PHEV version [4].

1.1.2 Powertrain architectures

Another way to group hybrid vehicles is based on the architecture of the powertrain, i.e. according to the components layouts [25, 42, 49, 5] described in the following and shown in Fig. 1.9.

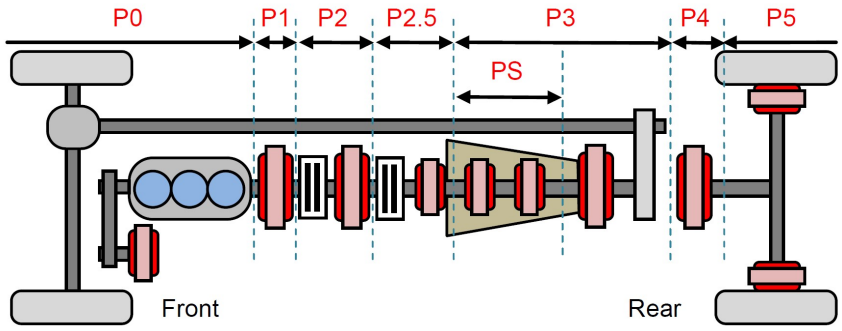

Fig. 1.9 Powertrain architectures [5].

- **P0**: EM is side-attached with the ICE front through a belt and it is used to start the ICE.
- **P1**: EM is connected to the ICE crankshaft and before the clutch. Can be coaxial to the shaft or connected through a gearbox.
- **P2**: EM is side attached through a belt or integrated between ICE and the transmission and can be completely disconnected from the ICE. For a double-clutch transmission, the architecture can be defined as **P2.5**.
- **P3**: EM is connected through a gear with the output of the transmission. Two EMs can be connected by planetary gears and integrated into the gearbox, in the so-called power-split configuration **PS**: the goal is to improve the fuel economy by splitting the power path in mechanical and electrical and change the power ratio according to the load. The **PS** configuration is adopted by Toyota known as the Hybrid Synergy Drive System. Another similar approach is the two-mode hybrid [50, 51] adopted from General Motors. Compared to the Toyota system, it is more complex but has more operating modes.
- **P4**: EM is connected through a dedicated gear on one axle.
- **P5**: EMs are in the wheels. Nowadays there is limited series production of this kind of vehicle.

However, the choice of an architecture is not unique. In fact, in a vehicle with multiple EM a layout can be a component using 2 of the main structures previously illustrated; for example, P1P4 is an architecture in which the rear axle is fully

electric while the front axle is composed by a conventional engine coupled with a small electric motor. It Tab. 1.2 reported the possible architectures according to the electrification degrees, while Fig. 1.10 shows some data concerning the different powertrains.

Table 1.2 Powertrain architectures and electrification levels [25].

	mHEV	MHEV	PHEV	EREV	BEV
P0					
P1					
P2					
P3					
P4					
P0P4					
P1P4					
P0P2					
P1P2					
P0P3					
P1P3					
P2P3					
P4P4					

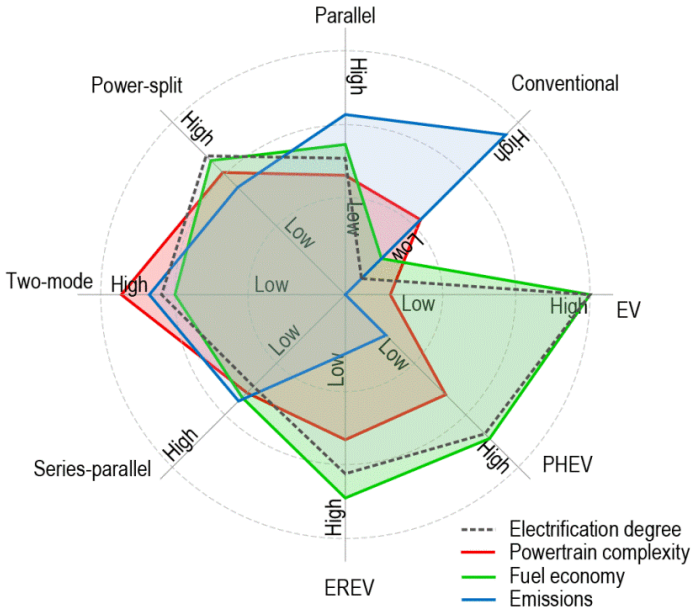

Fig. 1.10 Electrified powertrain architecture comparisons [6].

1.1.3 Powetrain examples

Toyota Prius

The Toyota Prius is one of the most famous HEV since 1997. Its PS architecture is called Toyota Hyrbid Sinergy Drive System (HSD) and is shown in Fig. 1.11. It combines an engine and two electric motors, named MG1 and MG2, through a power split device. The power split device is a planetary gearset that consists of a sun gear, a planet carrier, and a ring gear. It allows the vehicle to seamlessly transition between different power sources based on driving conditions, maximizing fuel efficiency and minimizing emissions. The MG1 motor works mostly as a generator. It is a 23 kW and 40 Nm Surface Permanent Magnet (SPM) motor with Concentrated Windings (CW). Indeed, MG2 is mainly used for traction as a motor. It has a maximum power of 53 KW and a peak torque of 163 Nm. As MG1 uses Permanent Magnet (PM) but with a different rotor topology, is an Internal Permanent Magnet (IPM) motor with hairpin Distributed Windings (DW). Instead, the gasoline engine can reach a power of 72 KW at 3600 rpm. The total HSDsystem output is 90 kW. Regarding the Nickel-metal hydride (NiMH) battery, the nominal voltage is 201.6 V and the capacity is 1.31 kWh [52].

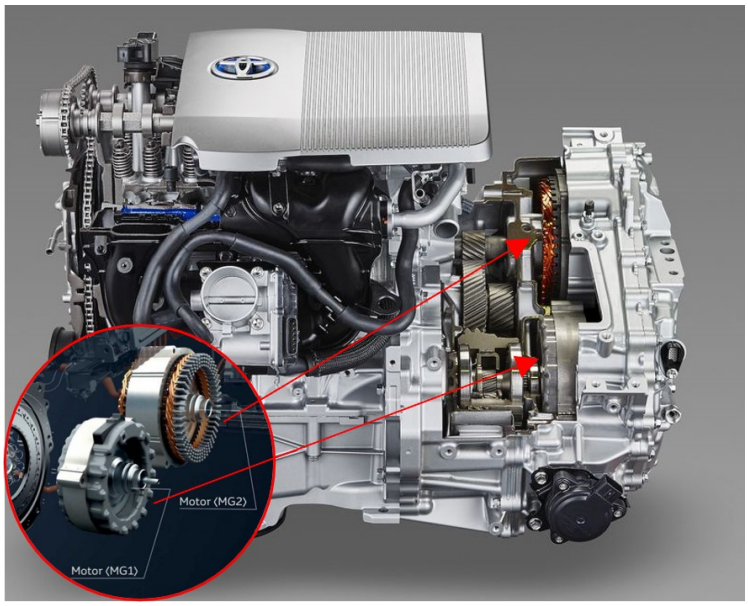

Fig. 1.11 Toyota Prius Gen 4 powertrain [7, 8].

Jeep Renegade 4xe

A PHEV SUV is the solution proposed by Jeep for the Renagade 4xe [53] with a P2P4 architecture. The rear axle is full electric: an Induction Motor (IM) of 44 KW and 250 Nm supplied by an 11.4 KWh and 400 V battery. It allows to drive the vehicle at up to 130 km/h and 46 km range. The front axle is propelled a 177 kW, 270 Nm gasoline engine joint with a 48 V IPMwith 15 kW and 55 Nm peak positioned after the clutch [54]. In combination, the two axle allow All Wheel Drive (AWD) traction and operation like e-lunch and e-boost [55].

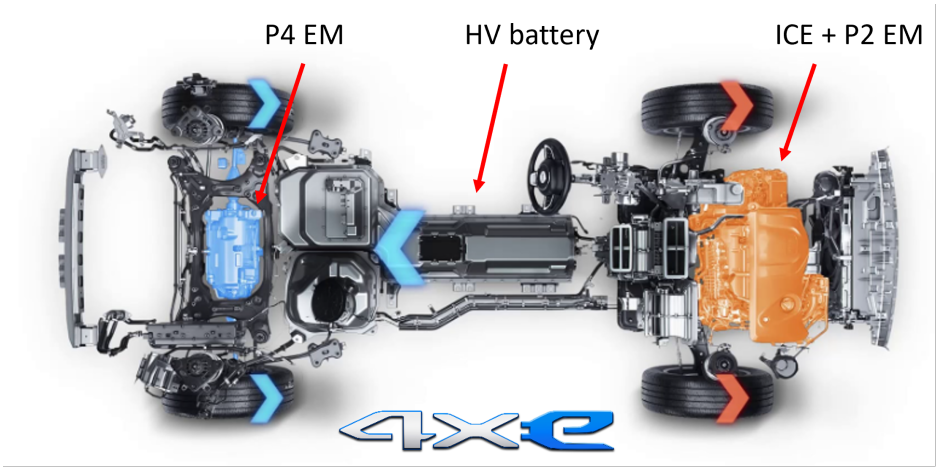

Fig. 1.12 Jeep Renegade 4xe powertrain [9].

1.2 State of art and trends of electric traction motors

In 2018, a comprehensive survey on electric machines and energy storage for electric and hybrid vehicles is presented in [56], focusing exclusively on commercial vehicles, excluding buses, bikes, and trucks. The study compiled data from over 200 vehicles spanning the years 1884 to 2016. Until the early 1900s, there was a modest increase in the production of electric vehicles, with a notable emphasis on taxis used in urban areas. These vehicles were primarily employed in applications where they could be recharged after short trips. Then, for over 50 years, there were no sales of electric vehicles due to the large availability of oil that pushed up the production of combustion engines. This trend changed during the oil crisis in 1970. The interest in electric machines has surged once again, with permanent magnet machines emerging

as dominant players in the transportation application market. The sales of this machine topology experienced a rapid increase, closely followed by the induction machine. Comparing data on the analyzed machines over the last century and the past decade reveals a significant rise in the popularity of PMSMs, which now account for approximately 80% of sales. Conversely, DC machines have seen a decline in usage due to maintenance issues, lower efficiency and power density.

In [57] and [10] electric motors from 2005 to 2019 are compared, in terms of topology, performance and technology. It's apparent that most machines utilize rare earth magnets, with exceptions like the Chevy Volt Motor Generator B (MGB), which employs ferrite magnets, the Renault Zoe featuring a Wound Field Synchronous Motor (WFSM), and the Tesla Model S utilizing an induction motor, as shown in Fig. 1.13. In this application, it is common to encounter V-shape motors, such as the Honda Civic with a single layer of magnets, or more intricate solutions like the Chevy Volt Motor Generator A (MGA), Toyota Prius 2018, and BMW i3, all with 2V-layer configurations, though the latter two utilize U-shape magnets. In ferrite motors, the classical rotor topology typically consists of three or more circular barriers to better exploit the reluctance torque. Recently, Wound Field Synchronous Motors (WFSMs) have gained popularity as a viable alternative to PMSMs [58]. By adjusting the rotor field, WFSMs can achieve a wide constant power speed range, although this comes with the drawback of requiring more complex controls. So probably, commercial solutions will be presented in the next future using this kind of machine.

1.2.1 Hairpin windings

To achieve high-power density a good practice can be to use hairpin windings instead of traditional stranded windings. This represents a relatively recent solution enabling a higher slot filling factor, essentially optimizing the utilization of the slot area, and allowing higher heat extraction. Rectangular conductors with larger cross-sectional areas are utilized compared to circular conductors and are inserted into rectangular slots. However, the hairpin solution is not without its drawbacks. Designing this type of winding necessitates adherence to stringent constraints, and their manufacturability is more intricate compared to traditional options, particularly concerning the welding and soldering aspects. In the following, a summary of the basic rules for designing a motor with hairpin windings is provided [59–61]. The winding layer must be even, usually falling within the range of 4 to 10 layers. In

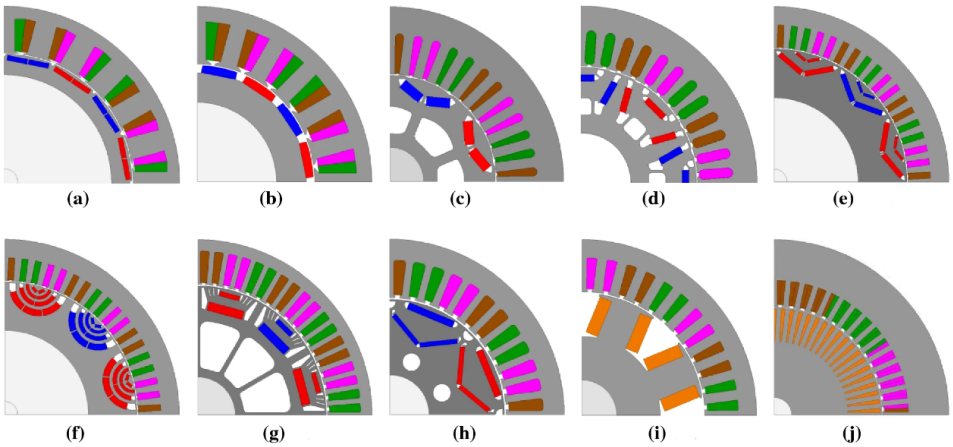

Fig. 1.13 Cross section of benchmark machines in [10]. Honda (a) Accord and (b) Civic 2005; Toyota Prius (c) 2010 and (d) 2018; Chevrolet Volt 2016 (e) MGA and (f) MGB; (g) BMW i3 2014; (h) Nissan Leaf 2012; (i) Renault Zoe 2014; (j) Tesla Model S 2012. Into the rotor, the permanent magnets are colored in blue and red (from (a) to (h)); the rotor windings (i) and the rotor bars (j) are in orange.

instances of parallel paths, the wire must span all the slot layers for each path to ensure the same inductance and same current distribution and, cover all the slots per pole of that phase to guarantee the same electromotive force (EMF). Furthermore, special attention should be given to high-frequency operation, during which the AC copper losses are higher compared to stranded windings.

The Tesla Model 3 has transitioned its winding topology over the years, shifting from traditional windings (Tesla Model 3 3D5) to the hairpin configuration (Tesla Model 3 3D6), with the cross sections shown in Fig. 1.14.

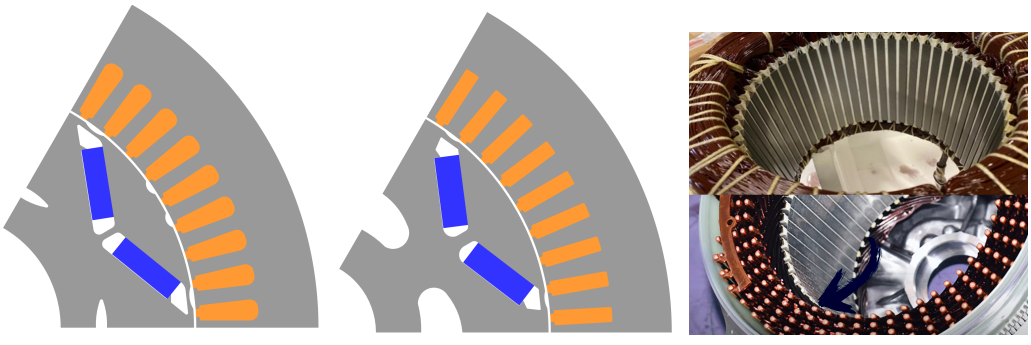

Fig. 1.14 Cross section of the reconstructed (a) Tesla Model 3 3D5 and (b) Tesla Model 3 3D6 and (c) picture of the windings of both versions [11, 12].

1.2.2 Wrapped rotor

Another promising new technology is represented by Wrapped Interior Permanent Magnet (WIPM) motors. The trend towards increasing the maximum speed of electrical drives to enhance power density poses challenges for mechanical rotor design. The structural integrity of the IPM rotor relies on radial and tangential ribs that secure the magnets within the rotor. However, increasing the speed necessitates thicker ribs, which can result in reduced permanent magnet flux linkages, leading to decreased torque and power performance. Therefore, above a certain speed, a viable solution is to entirely remove the ribs and incorporate a prestressed sleeve to retain all rotor components [16]. This solution is adopted by the Tesla Model S Plaid, which utilizes a WIPM motor instead of the induction machine used in the traditional version.

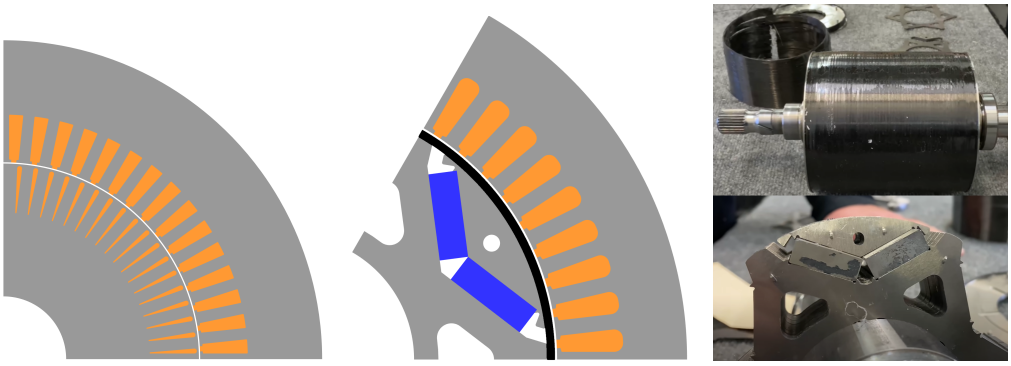

(a) (b) (c)

Fig. 1.15 Cross section of the reconstructed (a) Tesla Model S and (b) Tesla Model S Plaid and (c) picture of the Model S Plaid rotor [13–16].

In Tab. 1.3 are reported the main materials used for the rotor sleeve where the main characteristics are shown.

Table 1.3 Properties of common rotor sleeve materials [26].

		Inconel718	B20AT1200	Glass Fiber	Carbon Fiber
Density	$[g/cm^3]$	8.20	7.60	2.54	1.76
Tensile strength	[MPa]	1030	435	3447	3750
Thermal conductivity	[W/mK]	11.4	30.0	1.0	5.0
Resistivity	[Ω·m]	$1.25 \cdot 10^{-6}$	$5.91 \cdot 10^{-7}$	$4.0 \cdot 10^{12}$	$1.5 \cdot 10^{-5}$

1.3 Permanent Magnets

A good portion of the electric motors for traction relies on PM machines that use Rare-Earth (RE) magnets with high energy. From the U.S. Department of Energy (DOE) data can be noted that about one-third of the total cost of the electric motor is related to the magnets cost especially due to heavy RE i.e. Neodymium (Nd), Samarium (Sm) and Dysprosium (Dy) that can provide higher flux-density and coercive force, that can be translated as their strong against demagnetization [62]. Besides the high cost, the price of these materials is volatile as depicted in Fig. 1.16. For example, the Neodymium cost rose to its maximum level in March 2022 (about 425%), after a stable period since 2018. Then the price fell down and up to date is about double compared to the same period in 2018. Moreover, the main RE materials used to produce permanent magnets are under supply risk as reported in Fig 1.17. The supply risk is strictly to the dependence on China, that dominates the RE market. Different nations have sought to address the challenges linked to their reliance on China by diversifying their supply chains. However, these endeavors have encountered hurdles, including the substantial investment required for mining and production, entailing infrastructure development costs, and the environmental impact associated with mining and processing RE elements. These factors have posed challenges for countries aiming to establish self-reliant supply chains successfully [63].

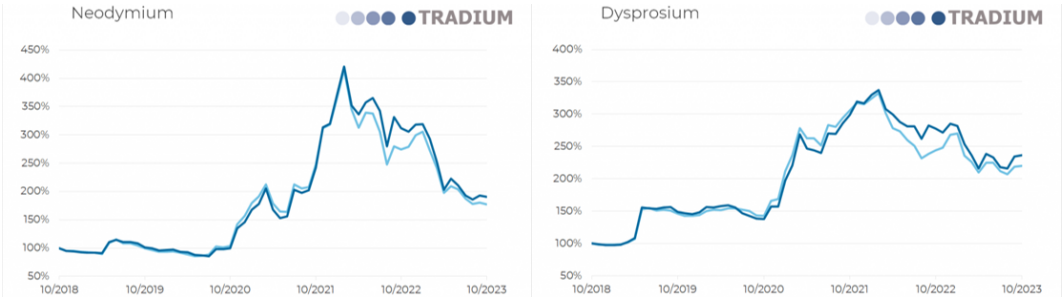

(a) (b)

Fig. 1.16 Market trend of (a) Neodymium and (b) Dysprosium between 2018-2023 [17]. The costs are normalized to the first day of October 2018. The dark blue curve refers to the Euro, while the light blue to the dollar.

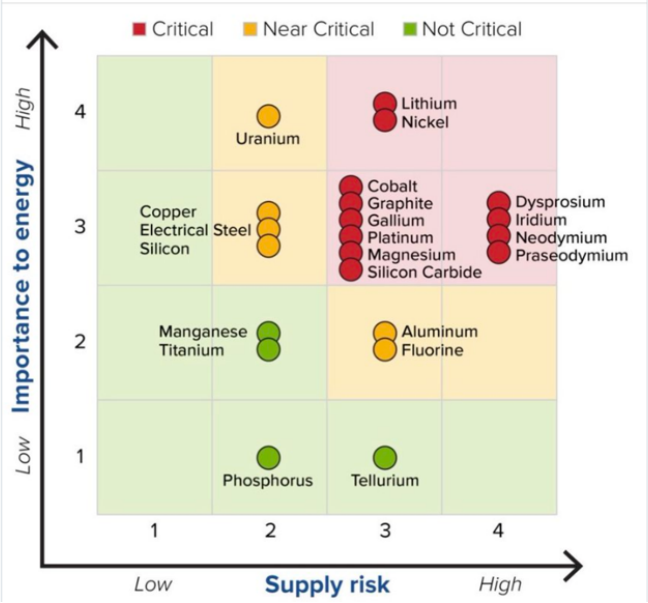

Fig. 1.17 Critical material assessment [18].

Alternative materials can be used to replace RE magnets such as Ferrite or Aluminium-Nickel-Cobalt, but is challenging as will be discussed later in this section. Anyway, the main reason is related to the demagnetization problem and low (BH) energy product, a key figure of merit. This Key Performance Indicator (KPI) is depicted in Fig. 1.18 for different kinds of magnets with respect to the technological progress during the years.

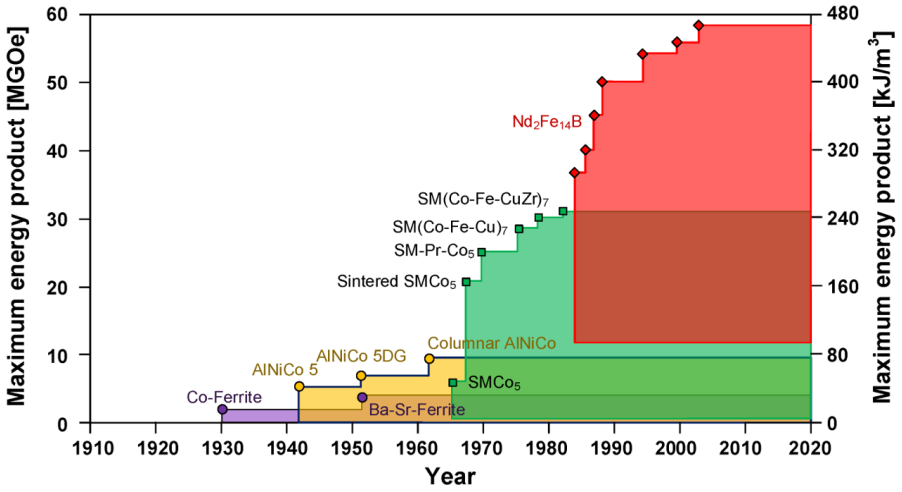

Fig. 1.18 Permanent magnets maximum energy product trend during the years [19].

1.3.1 B-H Characteristic

All ferromagnetic materials are marked by their $B-H$ characteristic curve. A virgin magnet, so not magnetized, is composed of magnetic dipoles that are randomly oriented with respect to each other and the total magnetic moment M is null. By applying an external magnetic field H, the dipoles tend to be aligned with it. If the field is gradually increased, the number of aligned dipoles increases until the saturation is reached. From this instant, all the dipoles are aligned and provide the maximum magnetic moment, and other significant increase of H produces very little increments of M. In the $B-H$ plane the so-called initial magnetization (or virgin) curve is followed. When the field is gradually removed, the magnetic moment plots a different curve that has an offset for $H=0$. A portion of the energy supplied to magnetize the material is stored in the material itself: the dipoles are still strongly oriented in equilibrium and the associated flux-density is called remanence or residual induction B_r. By applying progressively more external negative fields, the second quadrant is explored. When the field is equal to zero, it is called the coercive force H_c. It represents coercivity which is a measure of the resistance to demagnetization by an external magnetic field: the more to the left this point is positioned on the graph, the higher the strength of the magnetic field required to demagnetize the magnet. The remaining portion of the graph exhibits a symmetric pattern. The overall shape of this graph constitutes the hysteresis curve, which characterizes the behavior of a specific magnet material. Actually, there are two characteristic curves:

the intrinsic and the normal ones. The intrinsic curve refers to the characteristic of the only magnet (like there is no airgap between the poles) $J = f(H)$, where J is the magnetic polarization. Indeed, the normal curve describes the proprieties taking into account both the external and induced magnetic field $B = f(H)$. Both are displayed in Fig. 1.19b. The two characteristics are linked by the constitutive relation (1.3) in which $\mu_0 = 4\pi \cdot 10^-7$ H/m is the vacuum permeability.

$$B = \mu_0(H + M) = \mu_0 H + J \tag{1.3}$$

Note that the intrinsic and normal curves always have one point of intersection at $(0, B_r)$.

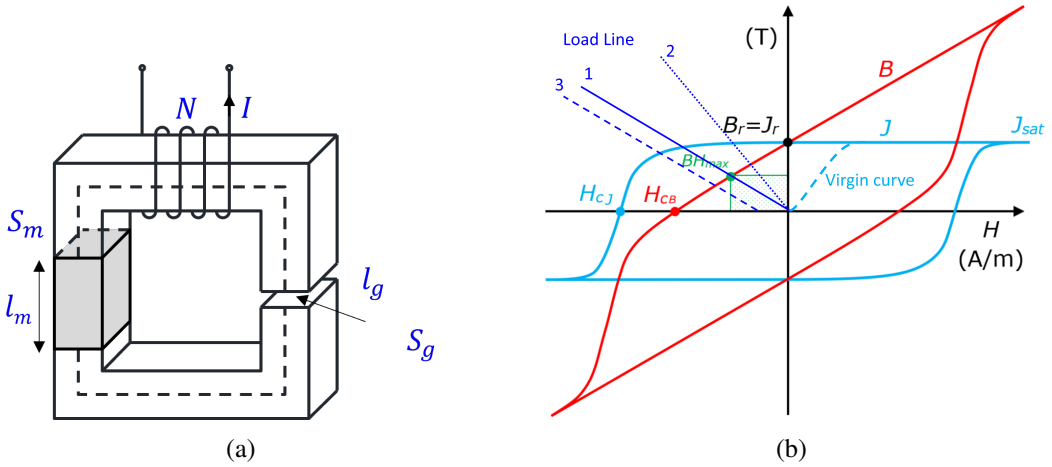

Fig. 1.19 (a) Elementary magnetic circuit. (b) Virgin curve (light blue dashed line), complete intrinsic (light blue) and normal (red) hysteresis loop and load lines (blue) of a permanent magnet. The maximum energy product is marked with a green circle. Figure based on [20].

The first quadrant of the characteristic curve illustrates how easy or difficult it is to magnetize the material until it reaches saturation, which is closely related to the manufacturing process. However, the primary interest lies in the second quadrant, which represents the operating region of the magnet, delimited by the normal curve and the axes. The energy product is defined based on the operating point, determined by the intersection of the normal curve and the load line. The maximum energy product $(BH)_{max}$, highlighted in green in Fig. 1.19, is a key performance index of the magnet. The load line is primarily influenced by the dimensions of the magnet, the air gap, and the applied external field (assuming the magnetic circuit can be considered ideal). By applying Ampere's law (with reference to the magnetic circuit

in Fig. 1.19a), the following condition must be satisfied (1.4):

$$H_m l_m + H_g l_g = NI \tag{1.4}$$

where the subscript m refers to the magnet, g to the airgap, l are the lengths, and NI are the amper-turns of the external circuit. By rearranging the equation and introducing the magnet and airgap sections, indicated with S_m and S_g, respectively, the flux density of the magnet can be retrieved as a function of its magnetic field (1.5).

$$B_m = \mu_0 \frac{l_m \cdot S_g}{l_g \cdot S_m}(-H_m + \frac{NI}{l_m}) = PC \cdot (-H_m + \frac{NI}{l_m}) \tag{1.5}$$

where PC is defined as permanence coefficient.

Some observations can be made by examining Fig. 1.19. Starting with load line 1, according to (1.5), the offset from the origin is attributed to the amper-turns. Load line 1 lacks external excitation unlike load line 3. Furthermore, the slope of the curves is determined by the geometric dimensions. If the ratio between the magnet length and section increases, the load line rotates in a clockwise direction from load line 1 to load line 2. Conversely, if the length of the air gap increases, the load line rotates in the opposite direction. It's crucial to note that irreversible demagnetization can occur due to both overcurrent and an increase in the air gap. This occurs when the operating point moves towards the knee point of the BH curve.

The main typology of permanent magnets will be briefly illustrated starting with RE PMs.

1.3.2 Sintered Neodymium

The Neodymium-Iron-Boron alloy, developed since the '80s, is currently the best available in the market in terms of the performance-to-volume ratio. Magnets of this type are indeed the most widely used in the industrial sector due to their lower cost compared to SmCo and reaching energy products of the order of 400 kJ/m3. It's a combination of high remanence and coercivity that offers a wide range of grades, sizes, and shapes [64]. The sintered NdFeB, magnet stands out as the most extensively produced and widely employed member within the NdFeB, family. Employing the powder metallurgy technique, it is categorized into seven series, namely M, H, SH, UH, BH, and AH, based on the distinct coercivity levels and

temperatures and Dy amount [65] as shown in Fig. 1.20. Powder metallurgy is a

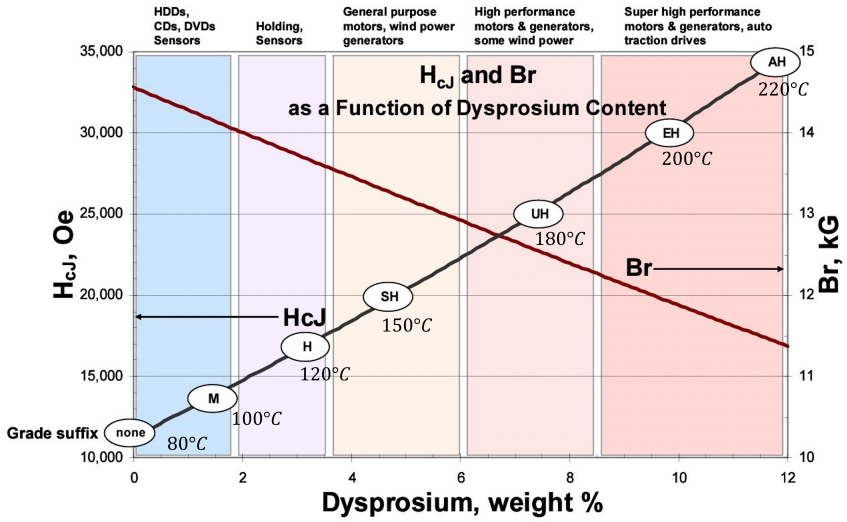

Fig. 1.20 Syntered neodymium magnets thermal and magnetics properties according to the dysprosium content in the alloy [21].

method for preparing metal powder or utilizing metal powder as raw material [66]. This involves shaping, sintering, and special treatments to manufacture a variety of products. The process can be summarized in the following 5 steps [67].

- **Raw material powder preparation**: The existing techniques for producing powder are broadly categorized into mechanical (such as crushing and atomization) and physical-chemical (like electrochemical corrosion, reduction, chemical processes, and electrolysis methods. Reduction, atomization, and electrolysis are the most commonly employed methods among these.

- **Mixing**: is the procedure of blending different powders in specific proportions and homogenizing them to form a compact mixture. Three mixing methods are commonly employed: dry, semi-dry, and wet.

- **Forming billets**: the goal is to create a billet of a specific shape and size with defined density and hardness. The methods for forming billets can be broadly categorized into pressure forming and pressureless forming.

- **Sintering**: is a crucial step in the process. Once the billet is formed, it undergoes sintering to achieve the required final physical and mechanical properties. Sintering can be classified into unit sintering and multi-component

sintering. For solid-phase sintering, the temperature is below the melting point of the metal and alloy used. In multi-component liquid-phase sintering, the temperature is generally below the melting point of the refractory component but higher than the melting point of the fusible component.

- **Products post-processing treatments**: various methods can be employed based on distinct product requirements such as finishing, oil immersion, machining, heat treatment, and electroplating.

Commercially available sintered NdFeB magnets boast a remanence of up to 1.45 T and an intrinsic coercive force reaching 2786 kA/m. The operational temperature range varies between 80° and 230° depending on the coercivity. From a mechanical standpoint, despite lower density, the material is less fragile and more resistant to compression, traction, and bending compared to SmCo magnets. However, on the downside, NdFeB magnets are prone to rapid oxidation that tends to pulverize the material; therefore, the use of surface coating systems is mandatory for the application of this alloy. These magnets are primarily used in electric motors, actuators, linear motors, magnetic couplings, and sensors [64]. As a benchmark, the datasheet of BMN-52UH is reported in Fig. 1.21.

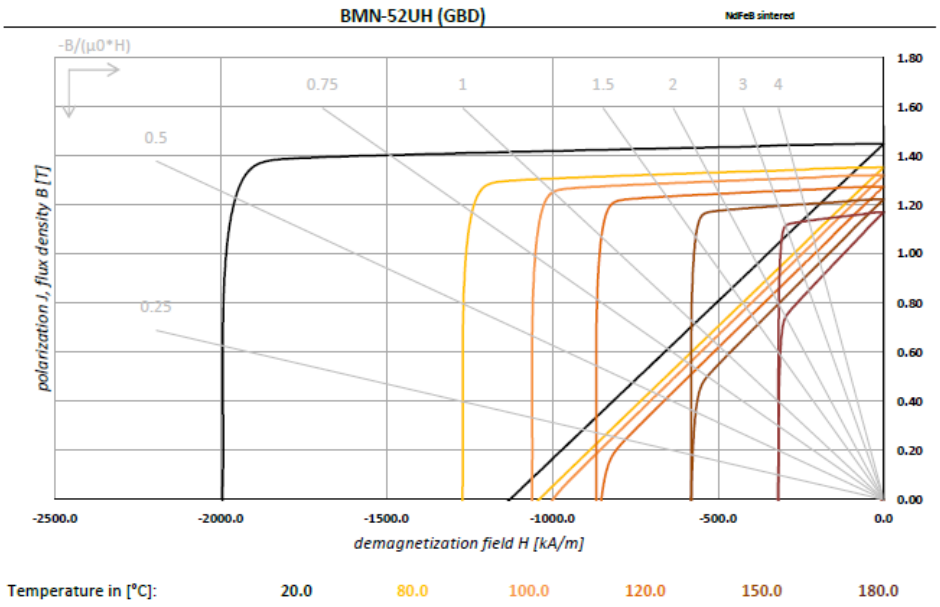

Fig. 1.21 BMN-52UH sintered Nd magnet characteristics from BOMATEC [22].

1.3.3 Bonded Neodymium

Sintered NdFeB magnets pose challenges in shaping special forms, being prone to cracking, breaking, and complicating the assembly process. To address these issues, attempts were made to crush permanent magnets, mix them with plastic binding matrices, and press them into shape within a magnetic field, leading to the development of bonded (or plastic) NdFeB magnets. These magnets offer advantages such as cost-effectiveness, high dimensional accuracy, flexibility in shaping, robust mechanical strength, and a lightweight nature. They have found widespread applications in the market [64]. The formation of bonded neodymium magnets involves four main processes: calendering, injection molding, extrusion, and compression molding, with compression and injection being more commonly used:

- **Injection molding**: the process allows for the creation of intricate shapes with high precision and the incorporation of additional components like shafts or metal inserts through overmolding. Due to a higher proportion of plastic binder compared to compressed magnets, injected plastic magnets exhibit lower magnetic force values. Typically, these magnets consist of a magnetic raw material blended with a plastic matrix such as PA6, PA12, or PPS, with the magnetic content ranging from 83 to 93 percent. The injection molding technique also facilitates overmolding with other components in a single process. In injection molded magnets, the plastic matrix can be composed of Polyamide 6 (PA 6), Polyamide 12 (PA 12), or Polyphenylene Sulfide (PPS). Maximum operating temperatures vary based on the magnetic raw material and the matrix type: 160°C for PA 6, 140°C for PA 12, and 220°C for PPS, typically [68].

- **Compression molding**: when high flux density and uncomplicated magnet shapes, such as rings, disks, or cylinders, are needed, compression molding is the preferred method. In NdFeB compressed magnets, the magnetic raw material is encapsulated in a thermoset plastic matrix, often using epoxy resin as a primary plastic binder. These magnets are axially pressed into molds. With the NdFeB powder constituting approximately 97 percent, significantly higher magnetic values can be achieved compared to injection-molded magnets. The equipment required for compression molding is less intricate and more cost-

effective. In most instances, compressed plastic magnets do not necessitate anti-corrosion surface coatings. Neodymium plastic magnets exhibit magnetic values ranging from 2 to 12 MGOe [68].

Due to the addition of a significant amount of adhesive, bonded NdFeB magnets typically achieve only 80% of theoretical density, resulting in magnetic properties weaker than those of sintered NdFeB magnets. Bonded NdFeB magnets exhibit isotropic magnetism, meaning they have the same magnetic properties in all directions, allowing for the convenient production of multi-pole monolithic magnets. It's worth noting that bonded NdFeB magnets can also be manufactured as anisotropic magnets [66]. The plastic matrix also generates a more balanced and corrosion-resistant end product. The maximum temperature to which this type of magnet can be subjected is around 150 °C, meeting the majority of market demands. The primary applications for these magnets include electric motors, systems with Hall sensors, and magnetic couplings [64]. As a benchmark, the datasheet of BMNpi-55/104 is reported in Fig. 1.22.

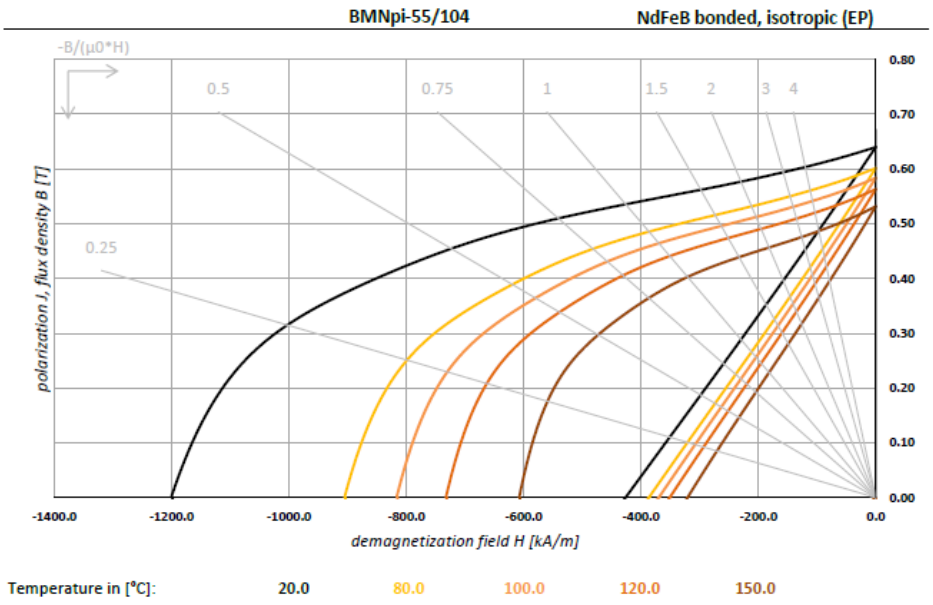

Fig. 1.22 BMNpi-55/104 bonded Nd magnet characteristics from BOMATEC [22].

1.3.4 Samarium-Cobalt

The SmCo magnet was the first commercial rare-earth-based magnet, composed of the rare earth Samarium and the transition metal Cobalt. It is still considered the most suitable material for high-temperature applications, especially for its ability to operate in environments up to 350°C. There are two variants of Samarium-Cobalt: SmCo5 and Sm2Co17. Sm2Co17 has higher performance but requires a higher magnetization intensity [64]. SmCo has two significant advantages compared to NdFeB: corrosion resistance and excellent thermal behavior. While their strength is comparable to neodymium magnets, SmCo magnets exhibit superior performance in retaining their magnetic strength. Consequently, they prove effective in applications that operate under extremely high or low temperatures [69]. Generally, Samarium-Cobalt magnets do not require coating or plating after processing; in some cases, it is still preferable to increase the level of protection and scratch resistance of the finished product by using coatings. These types of magnets are also used in military, aerospace, and medical applications, including sensors, speakers, electric motors, measuring instruments, and switches. As a benchmark, the datasheets of BMNpi-55/104 and BMSCPa-8210 are reported in Fig. 1.23 and Fig. 1.24, respectively.

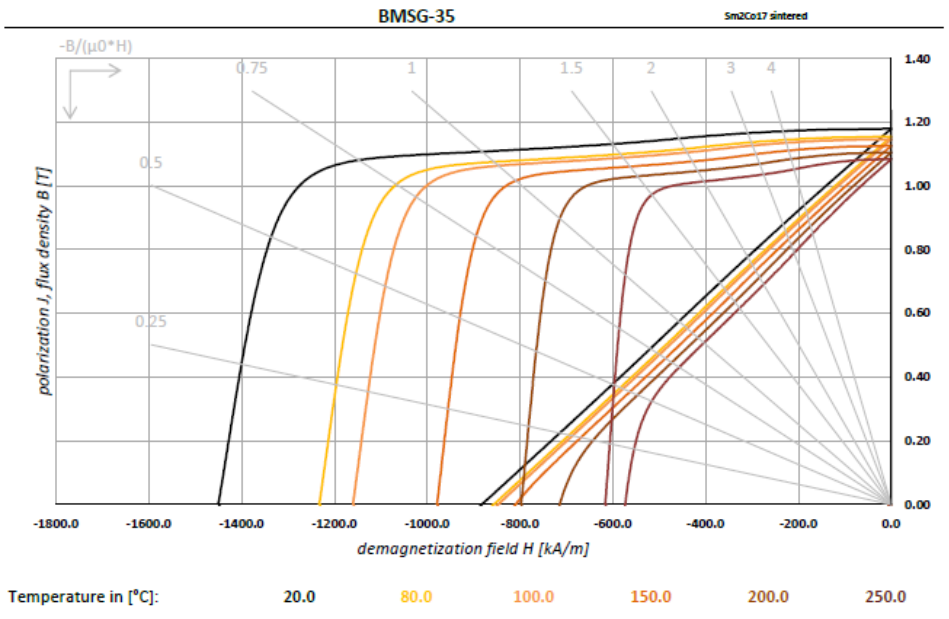

Fig. 1.23 BMSG-34 sintered SmCo magnet characteristics from BOMATEC [22].

Now, it is time to talk about RE-free magnets. The most common are ferrite and AlNiCo magnets.

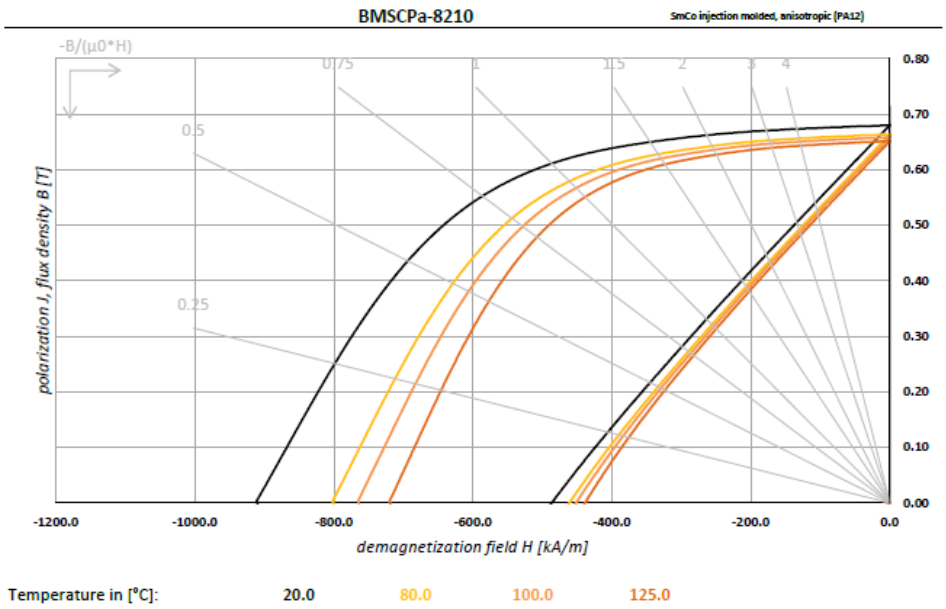

Fig. 1.24 BMSCPa-8210 bonded SmCo magnet characteristics from BOMATEC [22].

1.3.5 Sintered Ferrite

Ferrite magnets, used since the 1950s, are produced using iron oxides, strontium carbonate, and barium carbonate. The low cost of raw materials, combined with a relatively simple manufacturing process, makes ferrite an economical material, albeit with reduced performance compared to rare earth magnets. Despite its limitations, ferrite, being an oxide, exhibits high corrosion resistance and can be used at relatively high temperatures, up to about 250°C. Moreover, it is the only material among permanent magnets that has a positive temperature coefficient relative to H_c. This means that the demagnetization curves in the second quadrant shift to the left as the temperature increases. This shift will continue until the Curie temperature is reached. The primary components of ferrite magnets are strontium oxide or barium oxide and iron trioxide. In some high-grade varieties, additional chemical components such as cobalt (Co) and lanthanum (La) may be added to enhance their magnetic properties. Subsequently, the compound is reduced to fine powder through grinding machinery. In the second phase, the powder is mixed with a ceramic binder to obtain the final mixture used in the molding phase of the finished product. During this process, heat will be provided up to 1300°C to achieve the sintering of the material in a few hours. Basically the process is the same used for Nd magnets. Ceramic magnets are quite fragile, so they should be handled with care and are

not recommended for structural applications [70], [64]. Ferrite magnets can be categorized into isotropic permanent magnets and anisotropic permanent magnets based on whether an external magnetic field is applied during molding. The isotropic sintered ferrite permanent magnet exhibits weaker magnetic properties but offers the advantage of being magnetized in different directions of the magnet. On the other hand, the anisotropic ferrite permanent magnet possesses stronger magnetic properties but can only be magnetized along the predetermined magnetizing direction of the magnet [70]. Ferrite magnets are commonly employed in low-cost motors and generators, electric pumps, lifting systems, measurement instruments, sensors, and speakers.

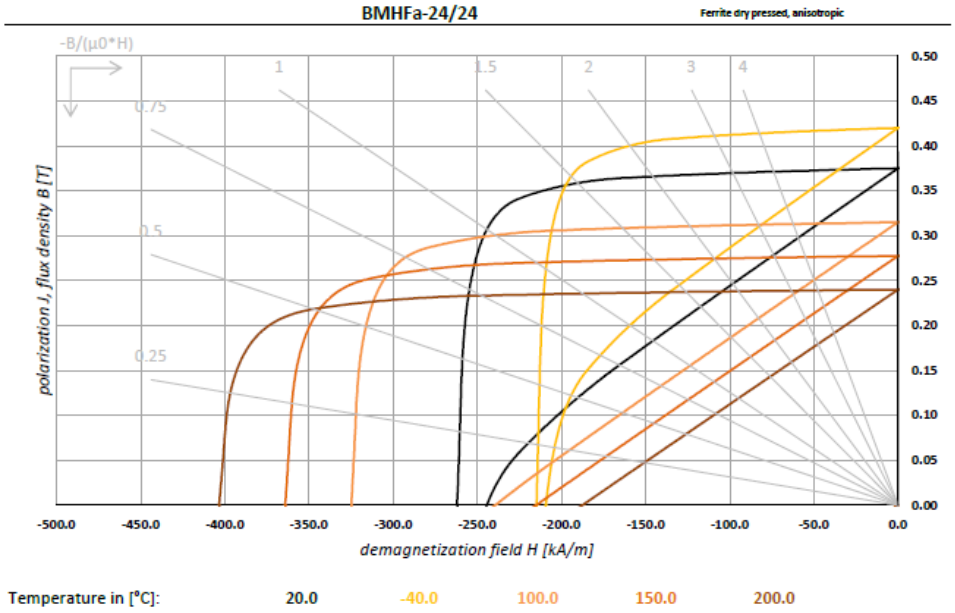

Fig. 1.25 BMHFa sintered Ferrite magnet characteristics from BOMATEC [22].

1.3.6 Bonded Ferrite

Plastic ferrites (Bonded) are obtained by mixing plastic matrices with ferrite oxides, and the production process allows for a wide variety of geometries through injection or compression molding processes. The overmolding capability of this type of magnet avoids additional production processes, improving the accuracy of the final assembly by eliminating the need for magnet gluing. Finally, the high resistance to oxidation and chemical attack makes these magnets particularly suitable for

applications with frequent or continuous contact with water or aggressive liquids, even at temperatures exceeding 120°C [64]. The soft and elastic magnet, crafted from bonded ferrite powder and synthetic rubber, is commonly referred to as a rubber magnet [70]. As a benchmark, the datasheet of BMFPa-1220A is reported in Fig. 1.26.

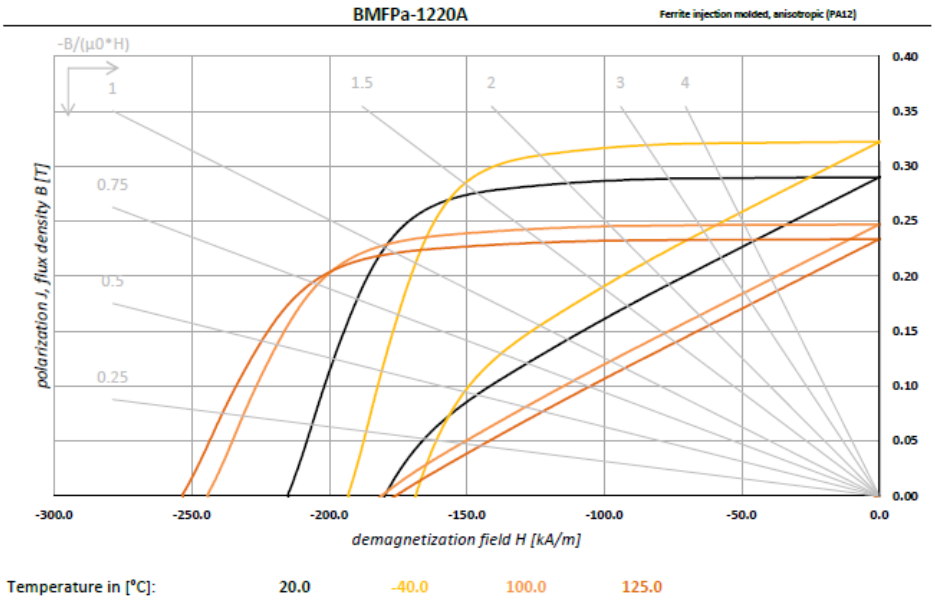

Fig. 1.26 BMFPa-1220A bonded Ferrite magnet characteristics from BOMATEC [22].

1.3.7 Aluminium-Nickel-Cobalt

They consist of an alloy of Aluminum, Nickel, and Cobalt, thus the term Alnico, invented in 1920s [71]. Occasionally, titanium may also be included. Alnico magnets are either Cast or Sintered. These magnets belong to the earliest produced functional nanostructured materials and offer a potential alternative to Nd-based PMs in the near term. This is due to their lower cost and the low temperature dependence of magnetic properties, up to 400°C [21]. Alnico magnets exhibit the most favorable temperature coefficients among various magnet materials. They should be considered the optimal choice for applications involving extremely high temperatures. The prevalent form of Alnico magnet is Cast Alnico. Casting is frequently employed to achieve a near-net shape, which is an industrial technique for manufacturing. As the name suggests that means that the initial object shape is very close to the final one. This casting

process is cost-effective for both low and high volume production, suitable for small as well as very large magnets. Sintered Alnico magnets, on the other hand, are less commonly utilized due to their lower magnetic performance and constraints on more complex shapes [20].

- **Cast Alinco**: in the manufacturing process, the material is melted and then poured into a mold. Once solidified, the material undergoes rough grinding, followed by heat treatment and cooling. Sometimes, a magnetic field is applied during the process. The magnetic field results in an anisotropic structure of the magnets. This orientation enables the material to achieve maximum magnetization and permits a higher magnetic performance. On the other hand, a cast magnet that is not heat-treated in a magnetic field is referred to as an isotropic magnet. After this process, the Alnico material can be ground and then magnetized [72].
- **Sintered Alnico**: its manufacturing process involves creating the magnet from a powdered mixture of ingredients. This mixture is then pressed into a high pressure die. The next steps include sintering the material in a hydrogen atmosphere. Following the sintering process, the magnet is cooled, and this cooling can occur in presence of a magnetic field or not leading to oriented or not material [72].

The drawbacks of Alnico materials are that they exhibit low coercivities, making them susceptible to demagnetization. Their relatively high cost is attributed to the inclusion of both nickel and cobalt. Cast magnets may present casting pores and voids, posing challenges in terms of aesthetics, and the presence of large voids may reduce the predicted magnetic flux [71]. Caution is advised when dealing with alnico material due to its brittleness, which makes it prone to chipping or breaking upon impact with a hard surface [72]. As a benchmark, the datasheet of BMAca-60/6 is reported in Fig. 1.27.

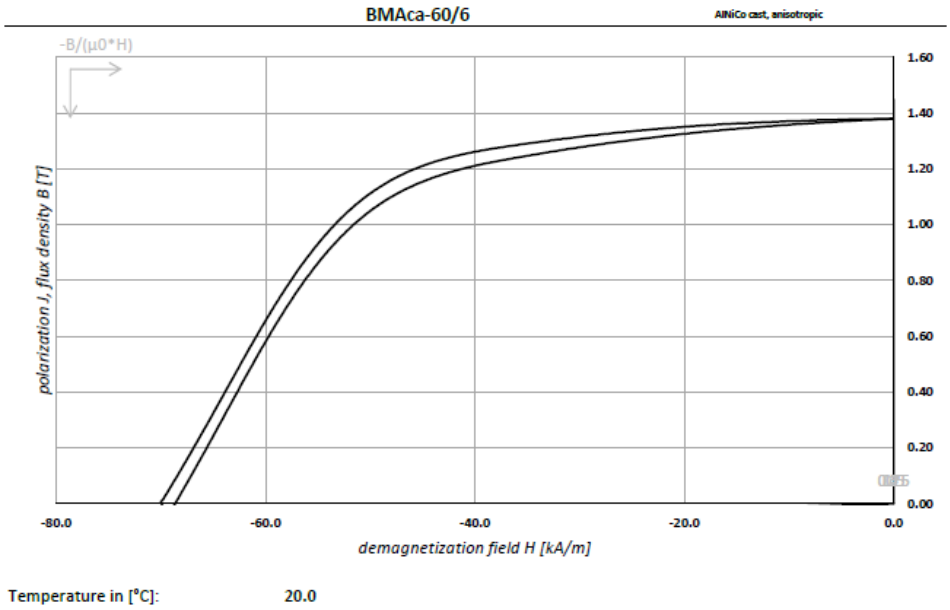

Fig. 1.27 BMAca-60/6 cast Alnico magnet characteristics from BOMATEC [22].

1.3.8 Iron Nitride

A compelling solution for Rare Earth free magnets lies in Iron Nitride (FeN) materials. According to a study documented in [73], significant advancements have been made in the synthesis process of α"-Fe16N2. The outstanding performance of this material is attributed to its ability to achieve high flux density, reaching up to 2.9 T. Theoretical calculations suggest that the maximum energy product of these magnets could be double that of the strongest neodymium magnets. However, it's more accurate to characterize this as a rediscovery of the material. Initially identified as a metastable phase in 1951 [74], the magnetic properties of this phase were not extensively explored until 1972, when Kim and Takahashi reported significant saturation magnetization in FeN thin films containing partial α"-Fe16N2 phase [75]. Subsequent demonstrations of high saturation magnetization in single crystals occurred in the 1990s [76]. Today, Niron Magnetic is heavily investing in this technology, with their Clean Earth Magnets being recognized as one of TIME's Best Inventions of 2023, highlighting their potential to revolutionize modern life. "Niron's Clean Earth Magnet technology will enable mass production of high-performance permanent magnets based entirely on low-cost, sustainable input materials." is reported on the website. Moreover, high-temperature stability is guaranteed. They are developing

the second generation of magnets that aims more to the automotive market compared to the previous generation more suitable for industrial and audio applications. The main drawback of these magnets are related to their lower coercitivity compared to RE ones.

Permanent magnets summary

To enhance the visualization of the pros and cons of different magnet types, Fig. 1.28a displays the B-H curves of 7 materials. It's important to note that these characteristics are referenced at 20°C. For a comprehensive understanding of how temperature affects magnetic properties, Figure 1.28b shows the remanence function with respect to temperature, plotted until the material's maximum operating thermal limit. Additionally, for insights into the weight percentage of RE and elements posing supply risks, Tab. 1.4 presents key data on magnet composition and performance indices. It's worth noting that these values are reference points and may vary depending on manufacturing technology, supplier, and specific applications.

Table 1.4 Rare Earth and high supply risk elements in permanent magnets and performance index. Data reported as reference. [27, 28]

		NdFeB sintered	NdFeB bonded	SmCo	AlNiCo
Nd	%	20-33	24-26	/	/
Ni	%	0.01-0.4	/	/	12-29
Dy	%	0-12	/	/	/
Sm	%	/	/	20-27	/
Co	%	0-5	2-4.5	45-65	1-40
Pr	%	0-5	/	0-17	/
Hc	*kA/m*	730-1100	300-500	350-900	30-140
Br	*T*	1-1.45	0.3-0.8	0.8-1.2	0.6-1.1
BHmax	*kJ/m3*	205-450	35-100	110-240	9-100

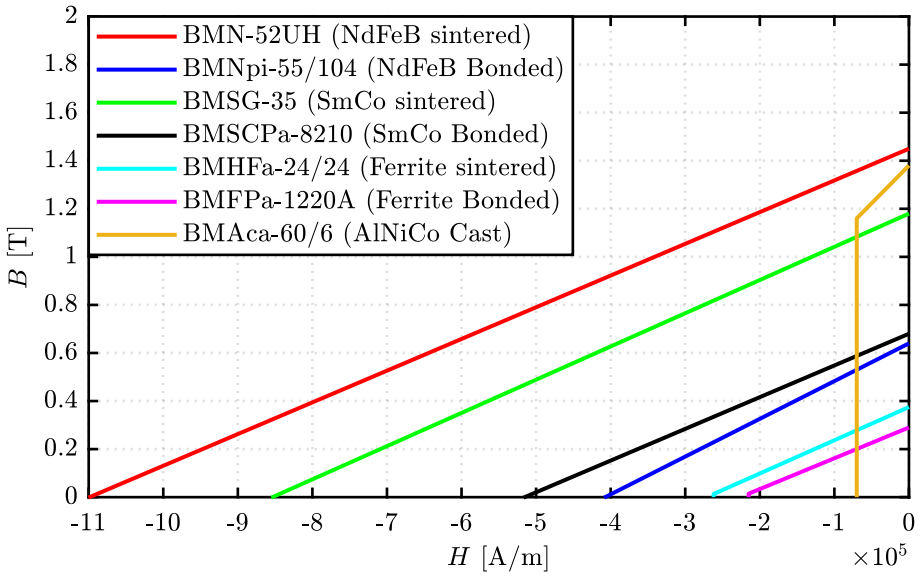

(a)

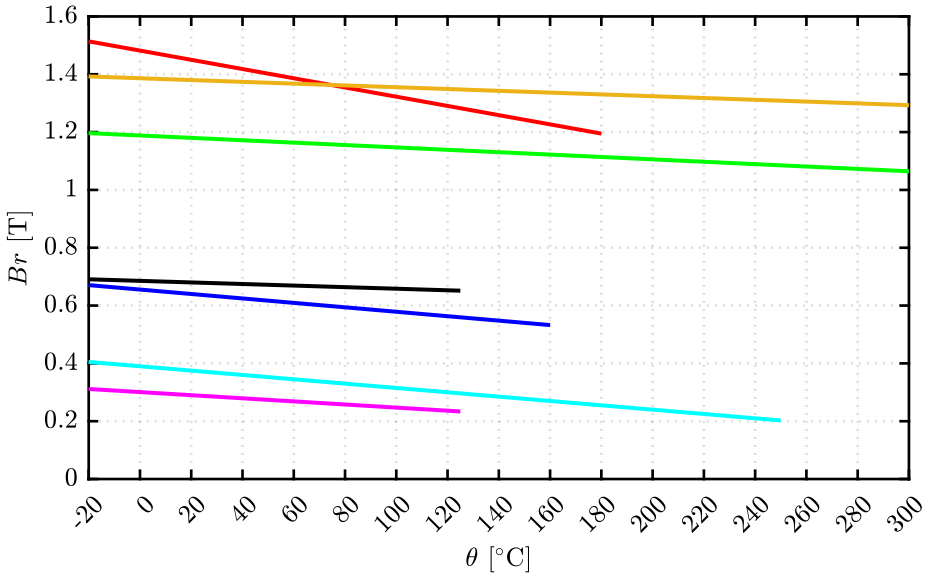

(b)

Fig. 1.28 Permanent magnets comparison: (a) B-H characteristic at 20 °C (b) remanence function of temperature, with respect of the maximum operating temperature.

1.3.9 Reference machines materials

In Tab 1.5 the main characteristics of the permanent magnets and the steel grade of the electrical machines in this thesis are reported.

Table 1.5 Reference machines: permanent magnets main characteristics and electrical steel grade.

	Magnets				**Steel**
		Hc	Br	BHmax	
Tesla Model 3	BMN-52UH	1109	1.45	410	M270-35A
BMW I3	N35EH	887	1.2	279	NO27-15
THOR	BMN-38EHS	969	1.26	303	M330-50
PRIUS	BMN-38EHS	969	1.26	303	M250-35A
SPM	BMN-38EHS	969	1.26	303	M600-50A
IPM	BMN-52UH	1109	1.45	410	M270-35A
PM-SyR	Y38	305	0.46	41	M270-35A
RAWP	/	/	/	/	M600-50A

1.4 Thesis motivation and goals

The increasing drive towards transportation electrification underscores the necessity for a deeper comprehension of electric powertrains. Although electric machines have a long-standing history, recent years have witnessed a significant increase in research efforts. This thesis aims to advance the modeling and design of PMSMs, which are extensively utilized in traction applications. The goal is to tackle the challenges encountered by OEMs and Tier-1 suppliers by offering flexible and accurate design methodologies. The main needs for a machine designer can be summarized as follows. A rapid design procedure that considers various aspects from the preliminary stage is essential. Design optimization algorithms are often employed to identify optimal solutions with minimal human intervention, enabling multi-objective and multi-physics optimization. However, these algorithms might overlook critical factors like the converter's impact, which is fundamental for co-design and integrated solutions today. Another approach is the Design of Experiments (DoE), a structured methodology used to analyze systems with multiple inputs and outputs, exploring complex variable interactions. DoE is more efficient than standard sensitivity analysis, requiring fewer simulations to map the variable space. However, DoE is

more effective with fewer design variables and is not ideal for initial motor design from scratch. In the automotive field, safety is a critical consideration, particularly regarding safe turn-off procedures in case of loss of machine control. Additionally, companies might have existing designs that can be adapted to new applications. In this context, a procedure based on scaling laws can be beneficial. Alongside electromagnetic performance and inverter specifications, especially for high-power density motors, the thermal aspect has become crucial. Accurate estimation of the machine's thermal parameters is fundamental to exploiting its full capabilities without causing damage. The next section provides an overview of the thesis and its organization, illustrating how all these aspects are investigated.

1.5 Manuscript overview

Following the introductory remarks provided in this chapter, it becomes evident that the historical momentum for electrification is currently at its peak. Consequently, the primary aim of this thesis, as well as the entire research conducted over the past three years, is to develop a comprehensive procedure and testing methodologies for designing and evaluating electric traction motors, particularly focusing on traction applications.

Specifically, this work presents two design methodologies. The first, outlined in Chapter 4, utilizes the (x,b) design plane, enabling rapid parametric design from scratch through a combination of analytical models and FEA simulations, ensuring both speed and accuracy. The second approach, discussed in Chapter 5, revolves around design via scaling laws and the starting point is an existing design. Both methodologies incorporate multiphysics analysis and account for inverter constraints aiming for an optimal solution without the need for time-consuming massive optimization.

Chapter 6 addresses the importance of ensuring safe operation modes in the event of faults. Relative indices pertaining to safety are incorporated into both design procedures.

Additionally, Chapter 7 introduces a thermal machine model. Thermal considerations are crucial for high-power density motors, where precise measurement

or estimation of machine temperature is essential to fully utilize the machine's capabilities without risking faults.

To enhance the credibility of the study, experimental tests were conducted, and their outcomes are presented in Chapter 8.

Chapter 2

Simulation tools and procedures

2.1 SyR-e environment

SyR-e stands for Synchronous Reluctance - evolution and is an open-source Matlab-based framework for synchronous motor design and evaluation. Most of the procedures and processes illustrated in this thesis are included and are part of the SyR-e project. It is available on GitHub, so can be freely downloaded. It supports several kinds of synchronous machines such as SyR, PM-SyR, IPM and SPM, but it has also some features related to drawing and simulation of IM. SyR-e allows the parametric design of synchronous motors both with a dedicated design procedure or by means of multi-objective optimization. The motor analysis is conducted by performing FEA, simulations by means of the freeware software FEMM. The data flow between Matlab and FEMM is fully automated by means of scripting and schematized in Fig. 2.1. Moreover, SyR-e is also linked with commercial software like Simcenter Magnet, Ansys Motor-CAD and Maxwell by means of automatic machine export and dedicated simulations procedures. SyR-e has two main Graphical User Inter-

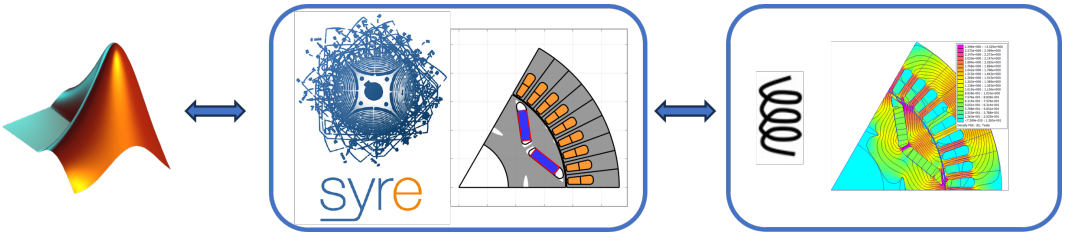

Fig. 2.1 Matlab, SyR-e and FEMM data flow.

faces (GUI) called *GUI_SyRe* and *GUI_SyRe_MMM*. The *GUI_SyRe* is used for motor design and FEA simulations. It is possible the parametric drawing the motor geometry, after selecting the main parameters, such as dimension, number of poles and, type of motor, manually or via the preliminary design tool, which will be addressed in Chapter 5, but also run multi-objective algorithms selecting the desired objective functions (torque, power factor, torque ripple...). Different simulations can be run from this interface ranging from a single working point evaluation to the evaluation of the flux and loss maps. Note that also mechanical analyses can be performed directly in the Matlab environment. The main GUI is displayed in

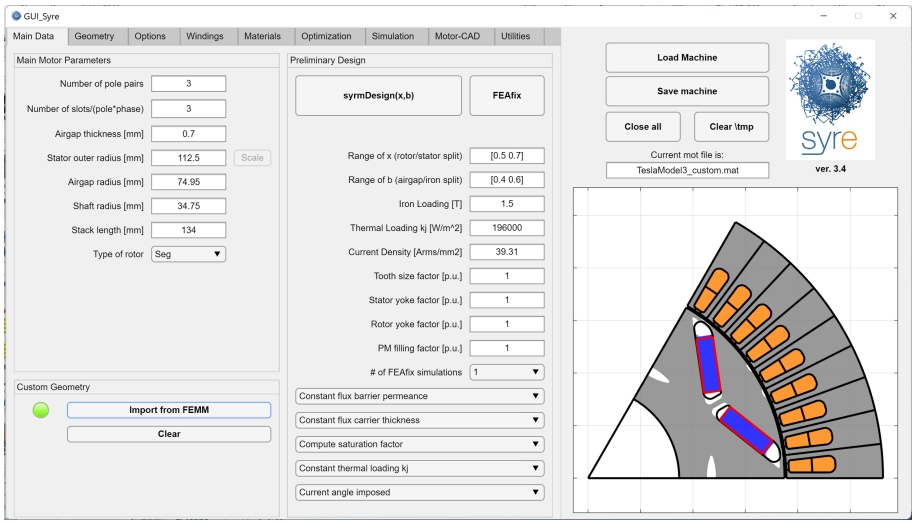

Fig. 2.2 Main GUI of SyR-e for motor design and simulations.

Fig. 2.2. The key result of the first GUI are the flux maps that are the main input for the Magnetic Model Manipulation (MMM) GUI shown in Fig. 2.3. It allows the manipulation of the flux maps in order to retrieve the control trajectories, the inductance maps, the operating limits of the motor, and finally, the efficiency map. Other features are available, for example, motor scaling and skewing, thermal limits evaluation, short circuit current computation... Moreover, from the SyreDrive tab, the tuned Simulink or Plecs model for torque, speed or current control simulation can be created. Moreover, a sensorless control option is available. It is a circuital motor model flux maps based, with time-average or instantaneous PWM inverter. The source code is written in *C*, for a direct implementation in the micro-controller. SyR-e has another GUI called *xbDesignPlaneExplorer* that allows the manipulation of the data coming from the design plane, which main outcome of the preliminary design procedure described in Chapter 5.

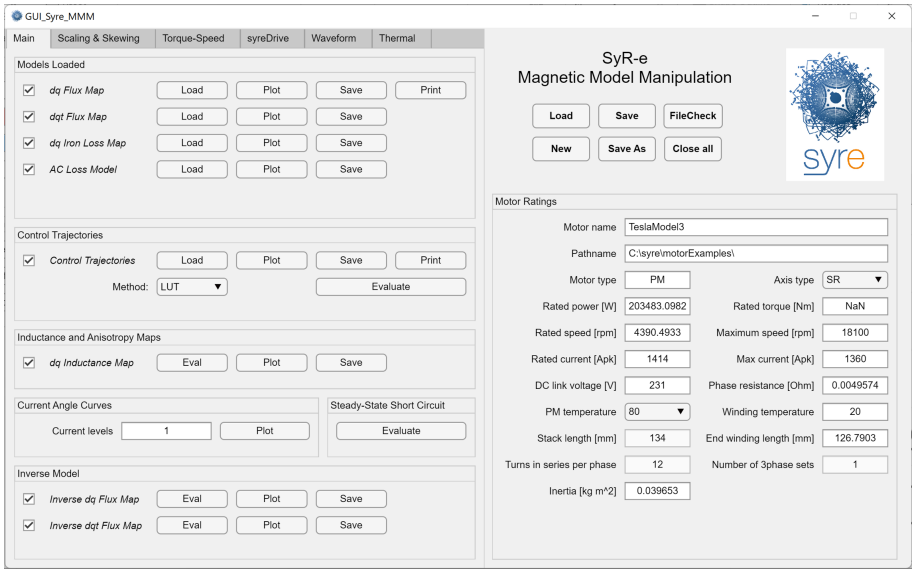

Fig. 2.3 MMM GUI of SyR-e for magnetic model manipulation.

2.2 AC synchronous machines model

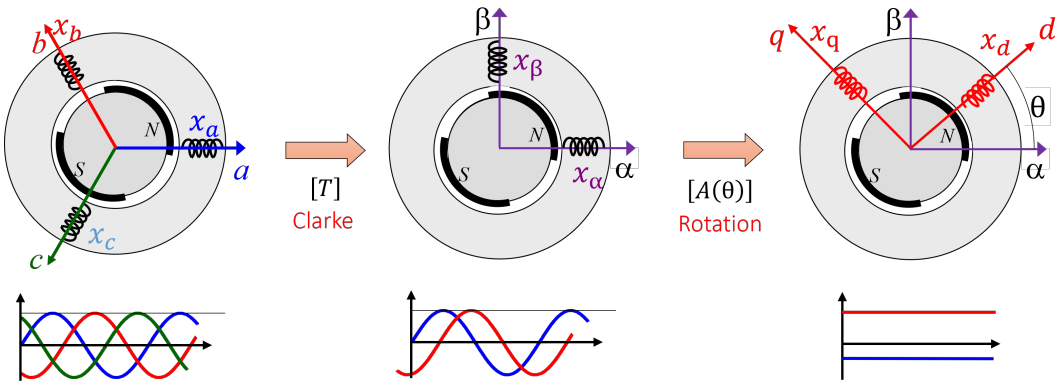

Fig. 2.4 Reference frame for synchronous machines.

This section briefly summarizes how a synchronous motor is modeled. The behavior of the motor is fully described via the electric, magnetic, and torque equations. Starting with the 3-phase reference frame, the voltage equations in matrix form are reported in (2.1)

$$\begin{bmatrix} v_a \\ v_b \\ v_c \end{bmatrix} = R_s \begin{bmatrix} i_a \\ i_b \\ i_c \end{bmatrix} + \frac{d}{dt} \begin{bmatrix} \lambda_a \\ \lambda_b \\ \lambda_c \end{bmatrix} \tag{2.1}$$

Where v, i and λ are the phase voltage, current and flux linkage, respectively and the subscripts refer to the corresponding phase; while R_s is the stator phase resistance. The magnetic equations are reported in (2.2) where L_σ is the leakage phase inductance, L_m and M are the magnetizing self and mutual inductance of the corresponding phase, and λ_m is the magnet flux linkage. Note that the matrix inductance is symmetric.

$$\begin{bmatrix}\lambda_a\\ \lambda_b\\ \lambda_c\end{bmatrix} = L_\sigma \begin{bmatrix}i_a\\ i_b\\ i_c\end{bmatrix} + \begin{bmatrix}L_{m,a} & M_{ab} & M_{ac}\\ M_{ab} & L_{m,b} & M_{bc}\\ M_{ac} & M_{bc} & L_{m,c}\end{bmatrix} \begin{bmatrix}i_a\\ i_b\\ i_c\end{bmatrix} + \begin{bmatrix}\lambda_{m,a}\\ \lambda_{m,b}\\ \lambda_{m,c}\end{bmatrix} \tag{2.2}$$

$$\begin{bmatrix}\lambda_a\\ \lambda_b\\ \lambda_c\end{bmatrix} = L_\sigma \begin{bmatrix}i_a\\ i_b\\ i_c\end{bmatrix} + [L_m(2\theta)] \begin{bmatrix}i_a\\ i_b\\ i_c\end{bmatrix} + [\lambda_m(\theta)] \tag{2.3}$$

Assuming a sinusoidal distribution, the self and magnetizing inductance are functions of 2θ, where θ is the rotor angular coordinate, as reported in (2.3). Each term of the inductance matrix can be expressed as the sum of the average inductance L_{m0} and the differential inductance due to the anisotropy $L_{m\Delta}$. So, considering the 3-phase connection and a zero homopolar current, the inductance matrix can be written as reported in (2.4). While the magnet flux linkage is explicated in (2.5).

$$[L_m(2\theta)] = \frac{3}{2}L_{m0} + \begin{bmatrix} cos(2\theta) & cos\left(2\theta - \frac{2\pi}{3}\right) & cos\left(2\theta + \frac{2\pi}{3}\right)\\ cos\left(2\theta - \frac{2\pi}{3}\right) & cos\left(2\theta + \frac{2\pi}{3}\right) & cos(2\theta)\\ cos\left(2\theta + \frac{2\pi}{3}\right) & cos(2\theta) & cos\left(2\theta - \frac{2\pi}{3}\right)\end{bmatrix} L_{m\Delta} \tag{2.4}$$

$$[\lambda_m(\theta)] = \lambda_m \begin{bmatrix} cos(\theta)\\ cos\left(\theta - \frac{2\pi}{3}\right)\\ cos\left(\theta + \frac{2\pi}{3}\right)\end{bmatrix} \tag{2.5}$$

To report the equations in the $\alpha\beta$ frame the Clark transformation has to be applied, according to Fig 2.4. The Clark matrix is reported in (2.6). Note that the used transformation is amplitude invariant but not power invariant, which means that the current, voltage, and flux keep the same amplitude of the corresponding 3-phase quantities, but for torque and power computation a correction factor is needed.

$$[T] = \frac{2}{3}\begin{bmatrix} 1 & -\frac{1}{2} & -\frac{1}{2} \\ 0 & \frac{\sqrt{3}}{2} & -\frac{\sqrt{3}}{2} \\ \frac{1}{2} & \frac{1}{2} & \frac{1}{2} \end{bmatrix} \tag{2.6}$$

After applying the Clark transformation to the electric and magnetic equations, the equivalent model of the machine in stator stationary reference frame, neglecting the homopolar components, is reported in (2.7) and (2.8).

$$\begin{bmatrix} v_\alpha \\ v_\beta \end{bmatrix} = R_s \begin{bmatrix} i_\alpha \\ i_\beta \end{bmatrix} + \frac{d}{dt}\begin{bmatrix} \lambda_\alpha \\ \lambda_\beta \end{bmatrix} \tag{2.7}$$

$$\begin{bmatrix} \lambda_\alpha \\ \lambda_\beta \end{bmatrix} = L_\sigma \begin{bmatrix} i_\alpha \\ i_\beta \end{bmatrix} + \begin{bmatrix} L_{m,\alpha} & M_{\alpha\beta} \\ M_{\alpha\beta} & L_{m,\beta} \end{bmatrix} \begin{bmatrix} i_\alpha \\ i_\beta \end{bmatrix} + \begin{bmatrix} \lambda_{m,\alpha} \\ \lambda_{m,\beta} \end{bmatrix} \tag{2.8}$$

where the inductance matrix is equal to (2.9) and the flux contribution can be written as in (2.10).

$$\left[L_{m,\alpha\beta}(2\theta)\right] = \frac{3}{2}L_{m0} + \frac{3}{2}\begin{bmatrix} cos(2\theta) & sin(2\theta) \\ sin(2\theta) & -cos(2\theta) \end{bmatrix} L_{m\Delta} \tag{2.9}$$

$$\left[\lambda_{m,\alpha\beta}(\theta)\right] = \lambda_m \begin{bmatrix} cos(\theta) \\ sin(\theta) \end{bmatrix} \tag{2.10}$$

Finally, by applying the rotation matrix (2.11), all the equations can be written in the dq frame.

$$[A(\theta)] = \begin{bmatrix} cos(\theta) & sin(\theta) \\ -sin(\theta) & cos(\theta) \end{bmatrix} \tag{2.11}$$

In voltage equation (2.12) a new motional term appears because a rotating frame in rotor coordinates is used. ω is the rotor angular pulsation.

$$\begin{bmatrix} v_d \\ v_q \end{bmatrix} = R_s \begin{bmatrix} i_d \\ i_q \end{bmatrix} + \frac{d}{dt} \begin{bmatrix} \lambda_d \\ \lambda_q \end{bmatrix} + \omega \begin{bmatrix} 0 & -1 \\ 1 & 0 \end{bmatrix} \begin{bmatrix} \lambda_d \\ \lambda_q \end{bmatrix} \tag{2.12}$$

The real advantage of the dq reference frame can be noted in the magnetic equations (2.13) and (2.14). The two axes are completely decoupled and independent of the rotor position.

$$\begin{bmatrix} \lambda_d \\ \lambda_q \end{bmatrix} = L_\sigma \begin{bmatrix} i_d \\ i_q \end{bmatrix} + \begin{bmatrix} L_{m,d} & 0 \\ 0 & L_{m,q} \end{bmatrix} \begin{bmatrix} i_d \\ i_q \end{bmatrix} + \lambda_m \begin{bmatrix} 1 \\ 0 \end{bmatrix} \tag{2.13}$$

$$\begin{bmatrix} L_{m,dq} \end{bmatrix} = \frac{3}{2} \begin{bmatrix} L_{m0} + L_{m\Delta} & 0 \\ 0 & L_{m0} + L_{m\Delta} \end{bmatrix} \tag{2.14}$$

Grouping the leakage and magnetizing inductances the d and q synchronous inductances are defined, and the magnetic equation becomes (2.15). Moreover, to include cross-saturation effects the L_d and L_q are modeled as functions of the i_d and i_q currents.

$$\begin{bmatrix} \lambda_d \\ \lambda_q \end{bmatrix} = \begin{bmatrix} L_d(i_d, i_q) & 0 \\ 0 & L_q(i_d, i_q) \end{bmatrix} \begin{bmatrix} i_d \\ i_q \end{bmatrix} + \lambda_m \begin{bmatrix} 1 \\ 0 \end{bmatrix} \tag{2.15}$$

The machine's equation can be also expressed in a compact way using the complex notation (2.16), (2.17):

$$\boldsymbol{v}_{dq} = R_s \boldsymbol{i}_{dq} + \frac{d\boldsymbol{\lambda}_{dq}}{dt} + j\omega \boldsymbol{\lambda}_{dq} \tag{2.16}$$

$$\boldsymbol{\lambda}_{dq} = \boldsymbol{L}_{dq} \boldsymbol{i}_{dq} + \boldsymbol{\lambda}_m \tag{2.17}$$

The presented equations refer to a generic IPM machine, but the formulation for the other type of synchronous motors can be easily retrieved:

- **SyR motor**: the permanent magnet flux linkages is equal to zero;
- **SPM motor**: the machine is isotropic so L_d is equal to L_q and is called synchronous inductance L_s;

- **PM-SyR motor**: the same notation used for an IPM machine can be used. However, the d axis should be the one with higher flux linkages, and it is not obvious that coincided with the PM axis. So, a different convention could be used, in which the PMs are aligned along the $-q$ direction.

Dealing with the torque, regardless of the rotor type, the unified expression of the electromagnetic torque is:

$$T_e = \frac{3}{2} \cdot p \cdot \boldsymbol{\lambda} \wedge \boldsymbol{i} \tag{2.18}$$

where p is the number of pole pairs and 3/2 linked with the not power invariant Clarke transformation and $\wedge$ indicates the vectors cross-product. In stationary (2.19) and rotating frames (2.20), the expression is written as follows.

$$T_e = \frac{3}{2} \cdot p \cdot (\lambda_\alpha \cdot i_\beta - \lambda_\beta \cdot i_\alpha) \tag{2.19}$$

$$T_e = \frac{3}{2} \cdot p \cdot (\lambda_d \cdot i_q - \lambda_q \cdot i_d) \tag{2.20}$$

Substituting the (2.17), the reluctance and PM components of torque are retrieved in (2.21).

$$T_e = \frac{3}{2} \cdot p \cdot (L_d - L_q) i_d i_q + \frac{3}{2} \cdot p \cdot \lambda_m i_q \tag{2.21}$$

2.3 dq Flux maps

Flux maps serve as a versatile method for representing the magnetic characteristics of synchronous motors. Typically, these maps express the fundamental dq flux linkages as a function of the dq currents applied to the motor. By evaluating the cross-product of these flux linkages and the current components, or by referencing a dedicated map linked to the same current coordinates, the average electromagnetic torque of the motor can be derived. These flux maps can be acquired through either FEA simulations or by employing specific experimental procedures. In the following, the efficient computation of flux maps using FEA, considering the crucial balance between precision and computational time, will be illustrated.
A SyR machine for industry applications will be used as a reference. Fig. 2.5 reports the cross-section of the considered motor, whose ratings are reported in Table 2.1.

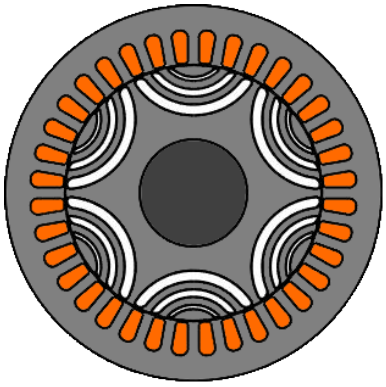

Fig. 2.5 Cross-section of the SyR machine selected as a reference.

Table 2.1 SyR motor ratings

Nominal current	I_{nom}	15	[Apk]
Max current	I_{max}	30	[Apk]
Nominal torque	T_{nom}	17	[Nm]
Max torque	T_{max}	43	[Nm]
DC link voltage	V_{dc}	565	[V]
Nominal speed	n_{nom}	2500	[rpm]
Max speed	n_{max}	6000	[rpm]
Nominal power	P_{nom}	4.4	[kW]
Max power	P_{max}	11.2	[kW]
Number of pole pairs	p	3	

2.3.1 Computation

Flux maps are retrieved using a 2D magnetostatic FEA simulations applied to radial-flux synchronous machines. It's worth noting that this approach extends seamlessly to 3D simulations, transient FEA, and various types of synchronous machines, ensuring its versatility and applicability. To expedite the simulation process, leveraging geometric and electrical symmetries is imperative. The anti-periodic symmetry permits the simulation of just one pole, which equates to 1/6 of the entire motor, along with a rotational angle of 60 electrical degrees, amounting to 1/6 of the electrical period. Operating under these defined conditions, simulating a single operating point supplying i_d and i_q currents, with a mesh composed of 5095 elements, and assessing 30 positions spanning 60 electrical degrees requires only 75 seconds to complete. In Fig. 2.6 presents the outcomes in terms of flux linkage and torque waveforms, prominently displaying the 30 simulated points marked in

red. It's important to emphasize that the full-cycle waveforms, depicted by the continuous blue lines, are derived through the exploitation of symmetry, ensuring a comprehensive representation of the motor. Note that for particular geometry, such as machines with asymmetric poles, at least one pole pair has to be simulated.

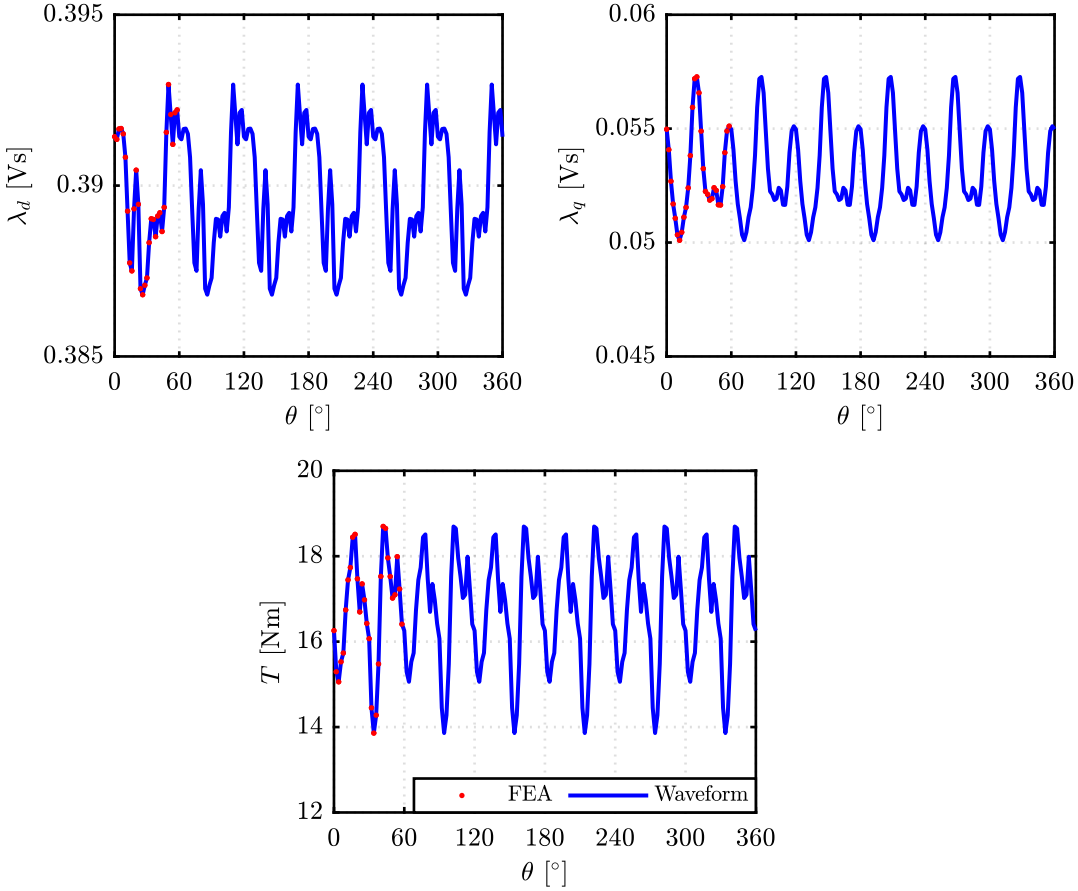

Fig. 2.6 Waveforms for d and q axis flux linkages and torque: FEA point simulated in red and complete waveform in blue.

2.3.2 Organization

The fundamental flux maps are computed by repeating simulations described above on a regular grid in the (i_d, i_q) domain. The numbers of considered i_d and i_q values are called n_d and n_q, respectively. The resulting flux linkages λ_d, λ_q and torque T are averaged with respect to θ and saved in corresponding matrices. The flux map functions are denoted with capital bold symbols, so $\mathbf{\Lambda}_d(i_d, i_q)$ and $\mathbf{\Lambda}_q(i_d, i_q)$

are the average dq flux linkages maps, while $\boldsymbol{T}(i_d, i_q)$ is the average torque map. Further matrices can be computed, for example, the peak-to-peak torque ripple map $\boldsymbol{\Delta T}(i_d, i_q)$. The grid of current values is organized as (2.22), while the λ_d matrix is defined accordingly (2.23). The same structure is adopted for the others quantities, such as torque and torque ripple maps.

$$\boldsymbol{I}_d = \begin{bmatrix} i_{d,1} & \dots & i_{d,n_d} \\ \dots & \dots & \dots \\ i_{d,1} & \dots & i_{d,n_d} \end{bmatrix}, \boldsymbol{I}_q = \begin{bmatrix} i_{q,1} & \dots & i_{q,1} \\ \dots & \dots & \dots \\ i_{q,n_q} & \dots & i_{q,n_q} \end{bmatrix} \tag{2.22}$$

$$\boldsymbol{\Lambda}_d = \begin{bmatrix} \lambda_d(i_{d,1}, i_{q,1}) & \dots & \lambda_d(i_{d,n_d}, i_{q,1}) \\ \dots & \dots & \dots \\ \lambda_d(i_{d,1}, i_{q,n_q}) & \dots & \lambda_d(i_{d,n_d}, i_{q,n_q}) \end{bmatrix} \tag{2.23}$$

The dq current grid must cover the overload condition. it's advisable to employ a dq current grid with a reasonable number of points. Regarding the number of simulated rotor positions, it's noteworthy that a minimum of 6 positions can be suitable for fundamental model flux maps, where the emphasis lies on capturing the average quantities. However, when precision is paramount, particularly in evaluating the peak-to-peak torque ripple map, it is recommended to consider a higher value for n_θ, reaching, for example, 30 points over 60 electrical degrees. The total computational time in this process is determined by the combined number FEAinstances, which is given by $n_d \cdot n_q \cdot n_\theta$. In the example provided, the current grid dimension is 15x15, resulting in 255 working points, and n_θ is 30. Consequently, the total number of FEA simulations is equal to 6750. To expedite this extensive computational task, parallel computing can be used. Different dq operating points can be assessed concurrently by separate processor cores, thereby significantly accelerating the simulation process. The flux maps are resampled, involving a finer mesh with $n_d = n_q = 256$ and they are shown in Fig.2.7, where the simulated points are marked with red dots.

2.3.3 Manipulation

The most common manipulation of flux maps are reported in the following.

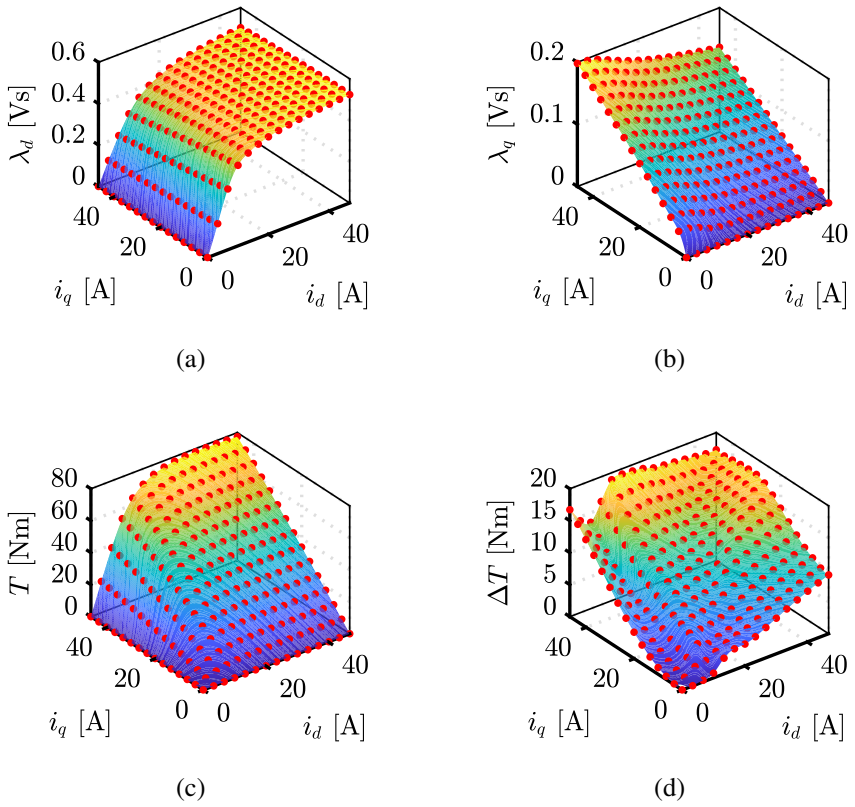

Fig. 2.7 FEA flux maps of the SyR motor. (a) d-axis flux linkage, (b) q-axis flux linkage, (c) average torque, (d) peak-to-peak torque ripple.

Computation of the inverse flux maps

The inversion of flux maps, denoting the generation of current maps as functions of flux linkages $\boldsymbol{I_d}(\lambda_d,\lambda_q),\boldsymbol{I_q}(\lambda_d,\lambda_q)$, is carried out by manipulating the dq maps. These inverse maps find application in solving the dynamic model of the machine when the flux linkages are treated as state variables and they are also used for control simulation purposes. The inverse flux maps are easily retrieved using the *scatteredInterpolant* function in Matlab. Note that particular care is to be taken to not lose some regions in the current domain. The inverse flux maps are displayed in Fig. 2.8.

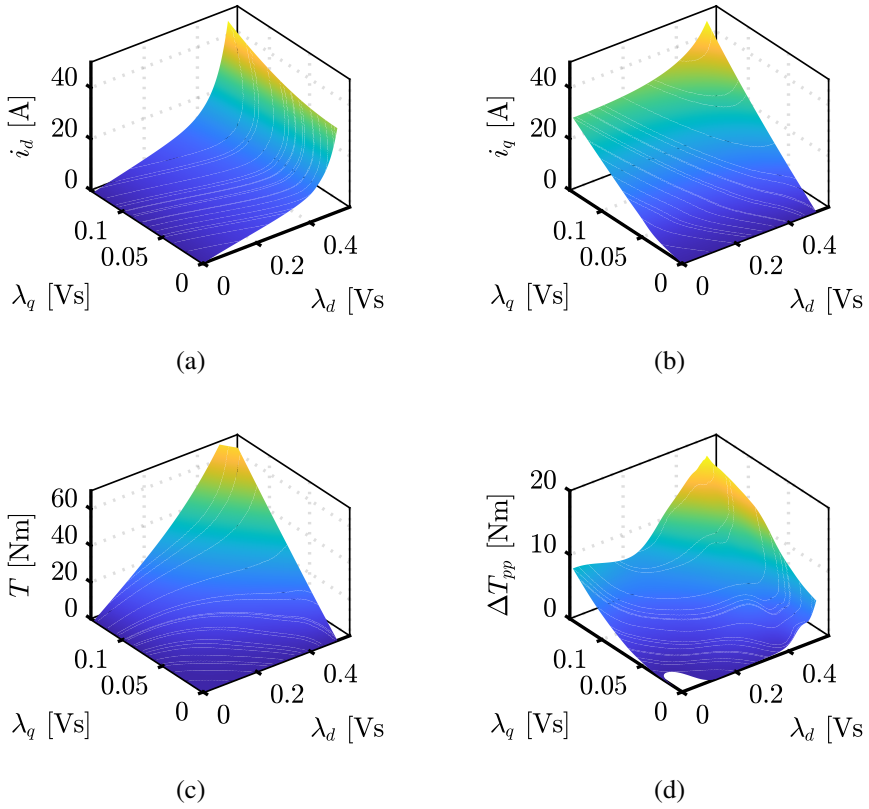

Fig. 2.8 Inverse flux maps: (a) d-axis (b) and q-axis currents, (c) torque and (d) torque ripple.

Identification of the control trajectories

An essential aspect of motor control involves the identification of control trajectories, a crucial process that leverages the dq flux maps while referencing average values. The Maximum Torque per Ampere (MTPA) and Maximum Torque per Voltage (MTPV) loci are frequently considered, although various other trajectories can be defined based on specific needs, such as the Maximum Power Factor per Ampere or Minimum Torque Ripple laws. These loci are typically identified by maximizing or minimizing the ratio of two key figures within the (i_d, i_q) domain. For instance, the MTPA focuses on maximizing the average torque for a given current amplitude. The procedure involves isolating the points of the map that belong to the selected current contour and then evaluating the torque from the torque maps. By determining the combination of (i_d, i_q) values that yields the maximum torque, this pair is recorded as an element of the MTPAtrajectory. This process is subsequently repeated for

various current amplitudes, ranging from zero to the maximum allowed by the current domain depicted in the maps. The MTPV, on the other hand, is computed using a similar algorithm, but it operates along constant flux linkage curves rather than current contours. The MTPA and MTPV trajectories for the SyR machine are presented in Fig. 2.9. These trajectories are expressed as i_d and i_q vectors as functions of torque T. By analyzing these trajectories, it becomes possible to extract a wealth of information from the flux and torque maps, including flux linkages (dq components, amplitude, angle), torque ripple, and more.

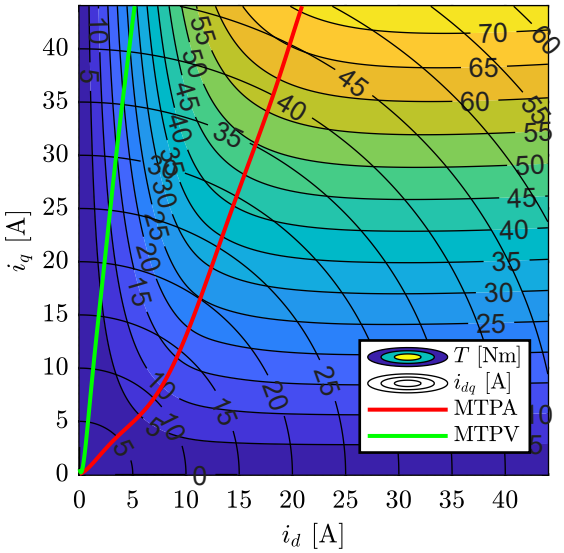

Fig. 2.9 MTPA (red) and MTPV (blue) locus on the torque map.

Flux maps scaling

Electric motor scaling is a valuable procedure in the design phase that can eliminate the need FEA simulations of a scaled machine. Scaling includes axial and radial scaling and rewinding. Moreover, extra inductance can be added on both axes to consider 3D effects. These scaling options allow designers to modify critical parameters of the motor, which is particularly useful for prototype development and optimizing motor designs without the need for resource-intensive FEA simulations, especially when dealing with 2D models. Full exploitation of the scaling procedure will be addressed in Chapter 5.

2.4 dq-theta Flux maps

The fundamental dq flux maps have a limitation to be a lossy way of storing simulation results. This is because they average the flux linkages and torque waveform, leading to a loss of rotor position information. In contrast, the $dq\theta$ approach represents a more efficient organization of the same simulated data. In the $dq\theta$ approach, the data is stored in 3-dimensional matrices, preserving the dependency on the d and q axis currents and, the rotor phase angle. Note that for the dq and $dq\theta$, the required simulations are exactly the same, that means that no extra-time is needed. The $dq\theta$ domain is defined with reference to the current steps in dq frame (Δi_d and Δi_q) and the rotor angle step $\Delta\theta$. The indexes i, j, and k are utilized along the respective dimensions, as described in (2.24) and, Fig. 2.10 graphically visualize the stored a generic $dq\theta$ quantity. This enhanced structure provides a more complete representation of the motor's behavior, including spatial harmonics.

$$\begin{cases} i_d(i,j,k) = (i-1)\cdot\Delta i_d \\ i_q(i,j,k) = (j-1)\cdot\Delta i_q \\ \theta(i,j,k) = (k-1)\cdot\Delta\theta \end{cases} \tag{2.24}$$

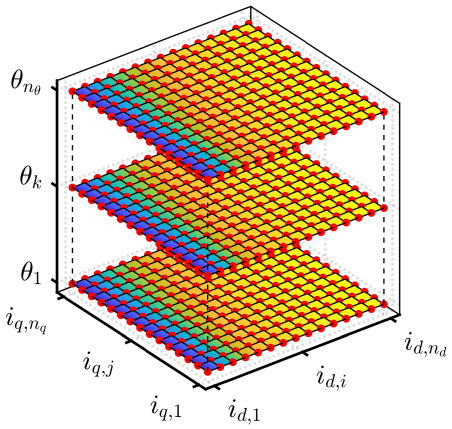

Fig. 2.10 Composition of the 3D matrices of the d-axis flux linkages, by stacking 2D matrices. Three values of rotor position are shown for clarity.

All the considerations for dq model are valid or are easily extended to the $dq\theta$ maps. Moreover, the rotor position dependency allows the possibility of further

manipulations that are described in the following paragraphs. However, to ease the manipulations, the rotor position domain is extended to one electrical period (from 60 to 360 electrical degrees), always exploiting the symmetry described in the previous section. So, the final matrix has a dimension equal to $n_d \cdot n_q \cdot 6n_\theta$. Another difference is the method used to interpolate the data: this time is *griddedInterpolant*, instead of *interp2*.

2.4.1 Torque and flux waveform

One of the advantages of the $dq\theta$ model is its capacity to retrieve flux linkage and torque waveforms without conducting additional FEA simulations. These waveforms are derived through interpolation from the corresponding 3D matrix using the $dq\theta$ model. The interpolation process requires constant i_d, i_q vectors as inputs, and θ vector spanning the entire electrical period. Fig. 2.11 shows a comparison between the dq flux linkages and torque waveforms obtained via FEA simulations and those interpolated from the $dq\theta$ model. The waveforms computed by both methods exhibit a perfect overlap, demonstrating the robustness of the interpolation process even when the selected operating point falls outside the nodes of the identification grid. However, it's important to acknowledge that the match between the two methods can be less accurate if the number of FEA simulations, in terms of rotor positions used to create the $dq\theta$ model is limited.

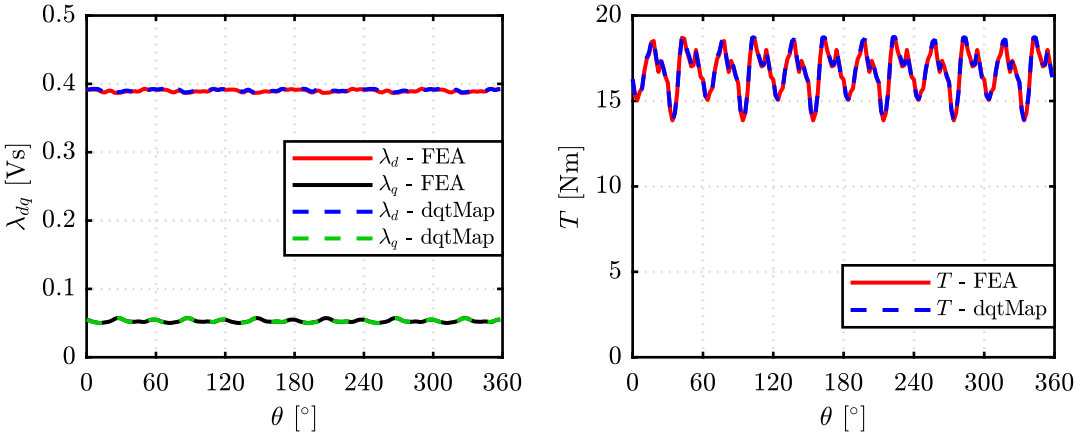

Fig. 2.11 Validation of the $dq\theta$ waveform interpolation: (a) flux linkages (b) and torque waveform FEA evaluated (dashed lines) and interpolated from $dq\theta$ flux maps (solid lines).

2.4.2 Motor skewing

Skewing is a widely employed method to reduce torque ripple in electric machines. It involves rotating the rotor laminations axially by a defined angle known as the skew angle θ_{skew}. When aiming to mitigate a specific harmonic order h in torque ripple, the mechanical skew angle in mechanical degrees can be calculated using the formula:

$$\theta_{skew} = \frac{360}{p \cdot h} \tag{2.25}$$

In the context of PM motors, step-skewing is the most common. This approach involves segmenting the rotor into a number of axial slices n_{slice} and rotating each slice from the adjacent one. The goal is to mimic continuous skewing, which can be seen as an extreme case where the number of slices equals the number of laminations. To evaluate the performance of a skewed motor, 3D FEAsimulations are typically necessary due to the inherent three-dimensional nature of the problem. However, a simpler approach known as multi-slice simulation can be implemented. In this method, assuming n_{slice} axial slices, n_{slice} 2D FEA simulations are conducted, with each simulation corresponding to one axial section. The results of these simulations are then combined to assess the impact of skewing on torque ripple reduction and motor performance. Each slice's initial position is shifted relative to the others, and the current remains the same for all simulations. This means that the dq currents set for each slice are slightly different due to the angular shift. For instance, consider the scenario of a $n_{slice} = 3$ step-skewed motor, as depicted in Fig. 1.12. The figure illustrates a simplified top view of the motor, highlighting the three slices with different colors and a black reference line to emphasize the skewing. Since n_{slice} is an odd number, the dq reference of the central slice remains the same as that of the full machine, while the dq axes of the other slices are slightly rotated because of the skewing. The rotation of each slice concerning the previous one is calculated as θ_{skew}/n_{slice}. Fig. 1.12, it can be observed that the same dq current on the local dq axis of each slice, with colors corresponding to those in Fig. 1.12. The effect of the angular skewing is apparent in the rotation of the dq currents as well. The blue section aligns with the whole machine's dq axis and, therefore, has no shift in position.

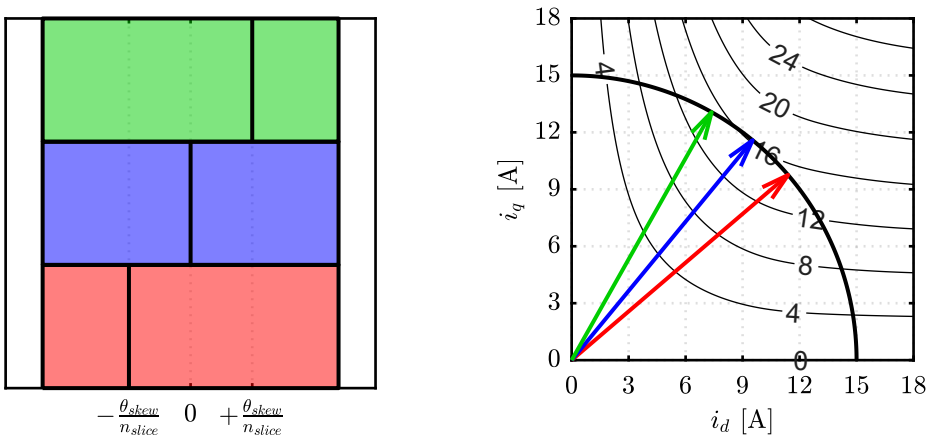

(a) (b)

Fig. 2.12 Three slices step-skewing: (a) axial sketch of the motor and (b) currents on the dq plane for each slice.

In Fig 2.13, the torque contribution of the three slices and the resulting torque waveform of the step-skewed motor are shown. The waveform of the skewed motor is determined by summing the contributions from the three slices waveform and is depicted by the solid black line. For the sake of comparison, the waveform of an unskewed motor is also displayed with a black dotted line. This comparison highlights both the reduction in torque ripple and the slight decrease in average torque caused by skewing. Evaluating flux maps in a skewed motor through FEA simulations typically takes n_{slice} times longer than evaluating flux maps in an unskewed motor, due to the considerations mentioned earlier. However, the capability to obtain torque and flux linkage waveforms from the proposed $dq\theta$ flux maps significantly expedite the evaluation process. In fact, the flux maps for skewed motors can be derived through post-processing from the flux maps of the unskewed motors. The computational time for this post-processing step is roughly one minute All the necessary information is extracted from $dq\theta$ flux maps by selecting appropriate dq currents and rotor angles. For each slice, the corresponding flux maps are computed while accounting for the shorter axial length. During the interpolation process, special attention is paid to the dq reference system when combining the contributions from different slices.

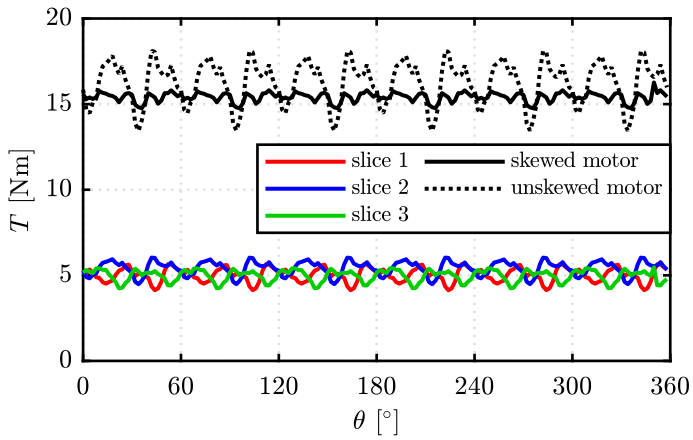

Fig. 2.13 Torque waveform of the step-skewed motor: single slice waveform (colored), skewed motor waveform (solid black), and unskewed motor waveform (dotted black).

2.4.3 dq-theta model for control simulation

The dq and $dq\theta$ flux maps can be effectively utilized to construct the dynamic model of the machine, particularly for control simulations. The dynamic model used in this paragraph is built into the Simulink environment and uses the inverse flux maps, that are implemented as lookup tables. The reference control diagram scheme is displayed in Fig. 2.14. The difference of using the $dq\theta$ approach is takes into account the dependency on rotor position, with a minimal impact on the computational time. To illustrate the practical benefits of this approach, some results are shown in Fig. 2.15 which refer to dq (above) and $dq\theta$ models (below). Note that in both cases, sinusoidal three-phase currents are injected with an amplitude of 15 A. However, it's crucial to note that the dq model provides only the fundamental values of flux linkage, resulting in a continuous torque waveform. In contrast, the $dq\theta$ model returns more waveforms that include spatial harmonics.

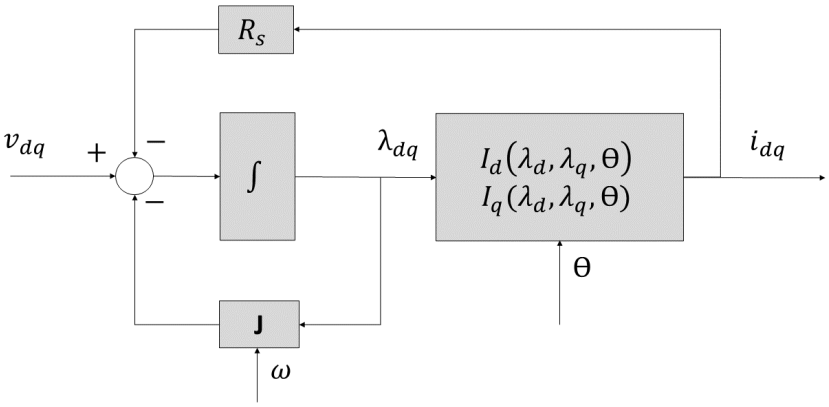

Fig. 2.14 Block diagram of the motor dynamic model with the $dq\theta$ approach.

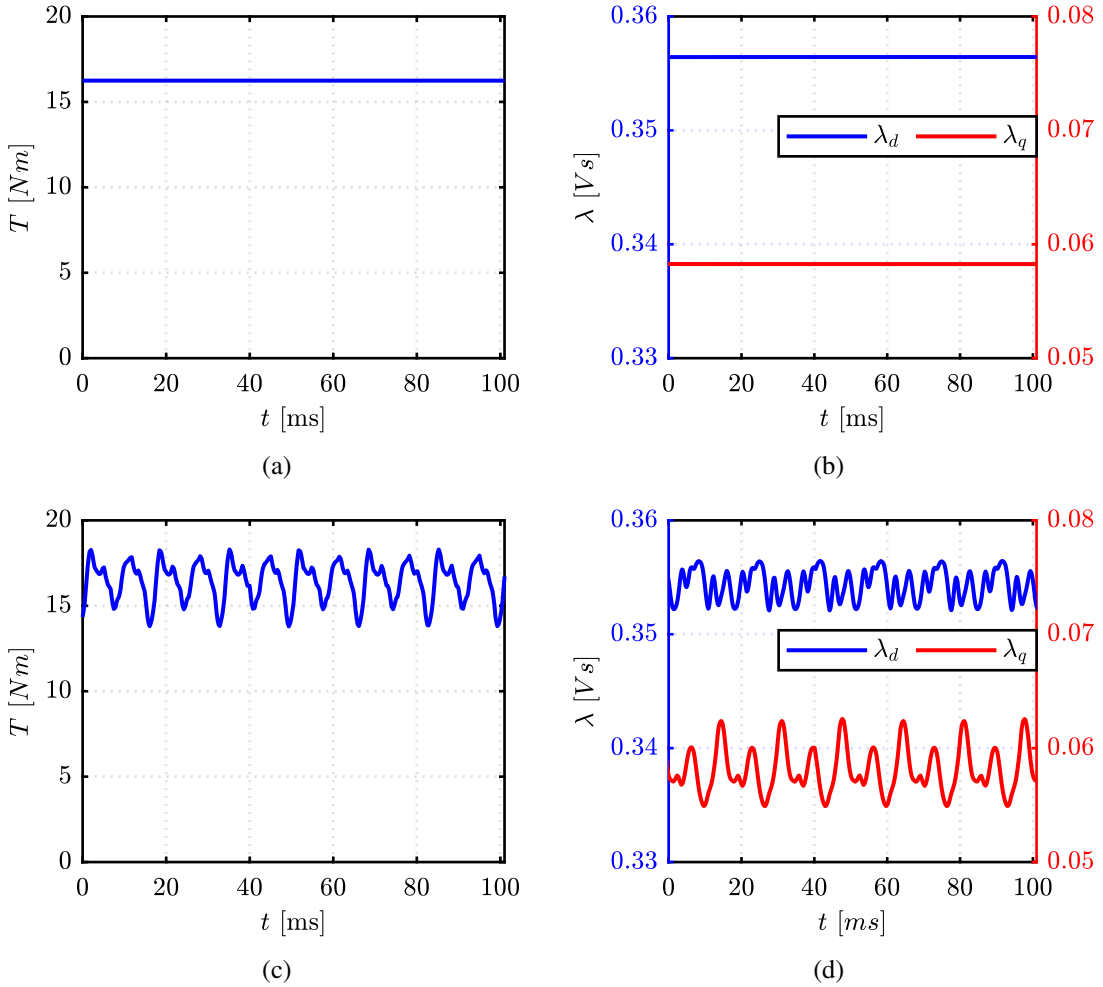

Fig. 2.15 Result of dynamic model simulation using the dq (above) and $dq\theta$ (below) models showing (a),(c) torque waveforms and (b),(d) flux linkages waveforms.

2.5 Efficiency maps

The efficiency map is one key performance metric for those applications where a variety of working points is explored on the torque-speed plane, such as traction [77]. This section proposes a comprehensive method to compute the efficiency map of a PMSM based on FEA-evaluated flux and loss maps. The flux-map based steady-state model of the machine will be introduced and it is discusses how the different loss terms are evaluated using magneto-static FEA. Following, the evaluation of the efficiency maps procedure is described. Finally, experimental results and the evaluation and validation of PWM generated loss terms. The case of study is the PM-SyR machine described in Fig. 2.16 and Table 2.2, identified as THOR.

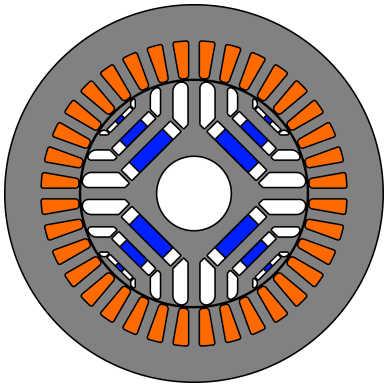

Fig. 2.16 Cross-section of the THOR machine selected as a reference.

Table 2.2 THOR motor ratings

Nominal current	i_{nom}	22	[Apk]
Max current	i_{max}	44	[Apk]
Nominal torque	T_{nom}	19	[Nm]
Max torque	T_{max}	43	[Nm]
DC link voltage	V_{DC}	310	[V]
Nominal speed	n_{nom}	2500	[rpm]
Max speed	n_{max}	9000	[rpm]
Nominal power	P_{nom}	5	[kW]
Max power	P_{max}	11.5	[kW]

2.5.1 AC synchronous machines steady-state model

The steady-state solution of an AC synchronous machine can be easily retrieved by imposing the derivative term in (2.16) equal to zero. The resulting equivalent circuit is shown in Fig. 2.17 in which the R_{Fe} resistance models the iron e PM loss of the machine. According to (2.27), the total current is equal to the sum of the magnetizing current $\boldsymbol{i}_{dq}^{m}$ and the $\boldsymbol{i}_{dq}^{Fe}$ drained in the iron resistance branch. Remember that R_{Fe} is not a constant: as described in the previous section, it depends on the working point.

$$\boldsymbol{v}_{dq} = R_s \cdot \boldsymbol{i}_{dq} + j \cdot \omega \cdot \boldsymbol{\lambda}_{dq} \tag{2.26}$$

$$\boldsymbol{i}_{dq} = \boldsymbol{i}_{dq}^{m} + \boldsymbol{i}_{dq}^{Fe} \tag{2.27}$$

Note that the flux maps are functions only of the magnetizing current.
The electrical power can be expressed as the product between current and voltage in dq frame (2.28), where $(^*)$ denotes the conjugated complex vector and $\mathbb{R}$ indicates the real part of the quantity. The same power can be computed as the sum of copper loss P_{Cu}, iron loss P_{Fe} and PM loss P_{PM} and electromagnetic power P_{em}, which can be retrieved by (2.29), (2.30), (2.31), respectively.

$$P_{elt} = \mathbb{R}\left(\frac{3}{2} \cdot \boldsymbol{v}_{dq} \cdot \boldsymbol{i}_{dq}^{*}\right) = P_{Cu} + P_{Fe} + P_{PM} + P_{em} \tag{2.28}$$

$$P_{Cu} = \frac{3}{2} \cdot R_s \cdot \left(i_d^2 + i_q^2\right) = \frac{3}{2} \cdot R_s \cdot |\boldsymbol{i}_{dq}|^2 \tag{2.29}$$

$$P_{Fe} + P_{PM} = \frac{3}{2}\omega\left(\lambda_d i_q^{Fe} + \lambda_q i_d^{Fe}\right) = \mathbb{R}\left[\frac{3}{2} \cdot \left(j\omega\boldsymbol{\lambda}_{dq}\right) \cdot \left(\boldsymbol{i}_{dq}^{Fe}\right)^*\right] \tag{2.30}$$

$$P_{em} = T_{em} \cdot \omega_m \tag{2.31}$$

where ω_m is the mechanical angular speed.
The T_{em} is computed as a cross-product between flux and current and only the magnetizing current is responsible for the torque production.

$$T_{em} = \frac{3}{2} p \cdot \left(\lambda_d i_q^m - \lambda_q i_d^m\right) \tag{2.32}$$

$$T = T_{em} - T_{mech} \tag{2.33}$$

By multiplying T and T_{mech} by ω_m the shaft power P and the the mechanical power P_{mech} are respectively retrieved. The latter is hard to compute, but a polynomial

expression that includes winding, friction bearing and gear losses can be adopted (2.34).

$$P_{mech} = a \cdot n^3 + b^2 \tag{2.34}$$

All the lossy terms can be grouped into the power loss as reported in (2.35).

$$P_{loss} = P_{Cu} + P_{Fe} + P_{pm} + P_{mech} \tag{2.35}$$

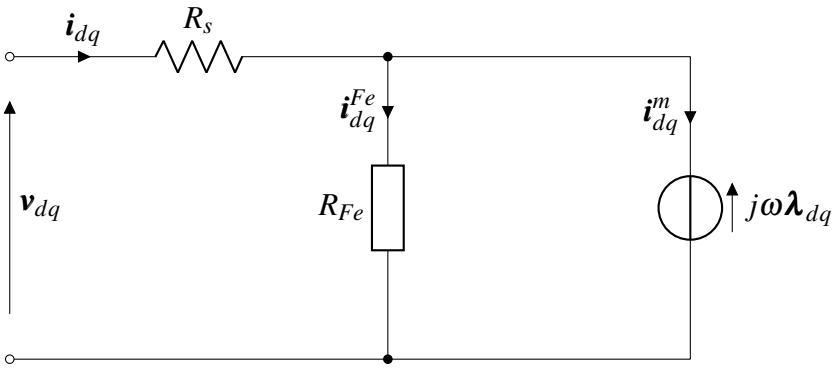

Fig. 2.17 Steady-state equivalent circuit model of the machine.

2.5.2 Iron loss model

The iron loss model incorporates the improved Generalized Steinmetz Equation (iGSE) [78], augmented to address the DC bias effect [79], and accounting for stator mechanical stress due to shrink-fitting [80]. Below is a concise overview; for comprehensive insights, please refer to the provided literature. To illustrate iron loss phenomena in PMSM, Fig. 2.18 displays hysteresis loops generated by sinusoidal flux density waveforms with varying frequencies, amplitudes, and DC bias B_{DC}. Regarding the loss model, the original iGSE [78] is initially employed through MATLAB scripting on the FEMM field solution to calculate the iron loss of each mesh element (2.36).

$$p_{Fe,iGSE} = \frac{1}{T}\int_0^T k_{iGSE}\left|\frac{dB}{dt}\right|^{\alpha}(\Delta B)^{\beta-\alpha}dt \tag{2.36}$$

In the equation, ΔB represents the peak-to-peak flux density of the analyzed loop, and k_{iGSE} is determined using the Steinmetz coefficient as shown in (2.37), which is obtained through fitting the manufacturer's loss curves.

$$k_{iGSE} = \frac{k_{SE}}{(2\pi)^{\alpha-1} \int_0^{2\pi} |\cos\theta|^{\alpha} 2^{\beta-\alpha} d\theta} \tag{2.37}$$

where θ is the angular position in electrical degrees.

Once the iron losses for each mesh element and hysteresis loop are calculated based on the original iGSE ($p_{Fe,iGSE}$), modifications are made to account for the minor loop enlargement resulting from the flux density DC bias and the compressive stress induced by the shrink fitting, as described in (2.38).

$$p_{Fe} = k_{Fe,DC} \cdot k_{Fe,mech} \cdot p_{Fe,iGSE} \tag{2.38}$$

where the DC bias factor [79] is computed as:

$$k_{Fe,DC} = 0.65 B_{DC}^{2.1} + 1 \tag{2.39}$$

and the compressive stress factor [80] is computed as:

$$k_{Fe,mech} = 1 + (C_{h,max} - 1) e^{-\frac{B}{B_h}} \cdot (1 - e^{-\frac{|\sigma|}{\sigma_h}}) \tag{2.40}$$

here the coefficients $C_{h,max}$, B_h and σ_h describe the loss variation with flux density and stress.

2.5.3 Magnet loss model

The static PM losses $P_{PM,stat}$, disregarding reaction field and 3D effects, are derived from the FEMM field solution using the formulation (2.41).

$$P_{PM,stat} = 2\sigma_m \pi^2 \sum_h \int_V \left(f_h \cdot J_{m,h} \right)^2 dV \tag{2.41}$$

In the equation, σ_m represents the magnet conductivity, V stands for the magnet volume, while $J_{m,h}$ and f_h denote the current density and frequency at the h-th harmonic, respectively. Following this, coefficients $k_{PM,RF}$ and $k_{PM,3D}$ are introduced to adjust every loss harmonic, transforming the original formulation of the PM losses (2.41) into (2.42).

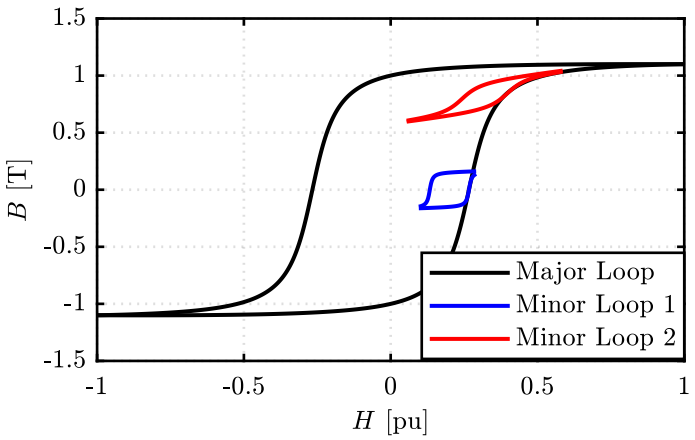

(a)

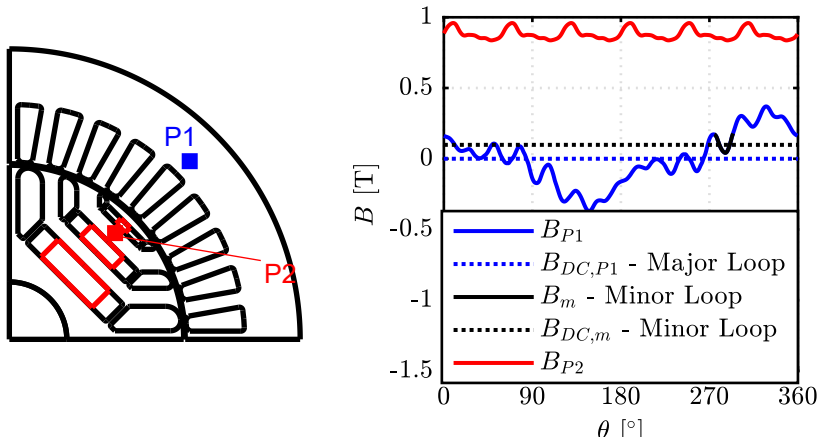

(b)

Fig. 2.18 Flux density waveforms trace the major hysteresis loop in blue, while the minor loops are represented in red and black.

$$P_{PM} = 2\sigma_m \pi^2 \sum_h \left(k_{PM,RF,h} \cdot k_{PM,3D,h} \int_V \left(f_h \cdot J_{m,h} \right)^2 dV \right) \tag{2.42}$$

Further information on the coefficients $k_{PM,RF}$ and $k_{PM,3D}$ can be found in [81]. Consequently, once the current density results from a static FEA are obtained, each PM loss harmonic is multiplied by its corresponding coefficients $k_{PM,RF,h}$ and $k_{PM,3D,h}$ to account for the reaction field and 3D effects.

2.5.4 Iron and PM loss map and speed adjustment

The iron losses under sinusoidal (fundamental) excitation are plotted across the (i_d^m, i_q^m) domain, similar to flux maps, at a single speed value n_0. The two maps $\mathbf{P}h,0$ and $\mathbf{P}e,0$ represent the hysteresis and eddy-current loss, respectively, as functions of i_{dq}^m, for the frequency $f_0 = n_0 \cdot \frac{60}{p}$. To calculate iron loss at a different speed (i.e., different fundamental frequency), the values are adjusted based on the frequency coefficients of the Steinmetz equation:

$$\mathbf{P}_{Fe} = \mathbf{P}_{h,0} \cdot \left(\frac{f}{f_0}\right)^{\alpha} + \mathbf{P}_{e,0} \cdot \left(\frac{f}{f_0}\right)^{2} \tag{2.43}$$

Another simplifying yet conservative assumption is to assume that PM loss is proportional to f^2, significantly simplifying data handling. Based on these assumptions, the PM loss map with sinusoidal excitation $\mathbf{P}_{PM,0}$ at a single speed n_0 is calculated across the (i_d^m, i_q^m) grid and subsequently scaled according to speed by the square of the respective fundamental frequency values:

$$\mathbf{P}_{PM} = \mathbf{P}_{PM,0} \cdot \left(\frac{f}{f_0}\right)^{2} \tag{2.44}$$

2.5.5 AC copper loss

AC winding loss is primarily caused by skin and proximity effects, which is particularly relevant for traction motors utilizing hairpin windings with large cross-sectional copper bars rather than wire bundles. Although the machine under examination features stranded conductors, the method employed holds general applicability. Regarding copper loss, the pre-calculated AC factor map ($k_{AC} = \frac{R_{AC}}{R_{DC}}$) is utilized. This map, illustrated in Fig. 2.19 in relation to the case study, is a function of frequency and copper temperature, constructed through linear time harmonics simulation. Specific simulations are conducted on two slot models at various frequencies and copper temperatures to ascertain the AC loss effect along the active length ($k_{AC,act}$) and in the end-winding ($k_{AC,ew}$).

$$k_{AC,act} = \frac{R_{AC,act}}{R_{DC,act}} \tag{2.45}$$

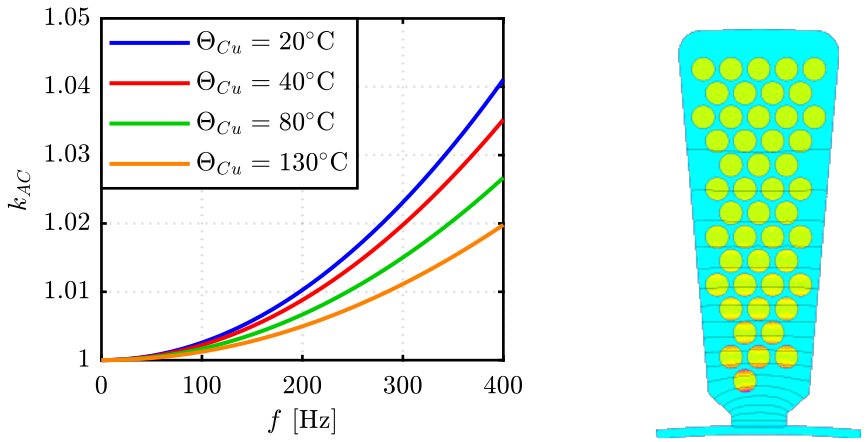

(a) (b)

Fig. 2.19 AC factor function of the frequency, for different winding temperature (a) and slot model solved at 300 Hz and 20°C.

$$k_{AC,ew} = \frac{R_{AC,ew}}{R_{DC,ew}} \tag{2.46}$$

In the equations, the subscripts '*act*' and '*ew*' attached to the resistances correspond to the active length and end-winding values, respectively. Thus, the AC loss factor k_{AC} is determined by combining both contributions:

$$k_{AC} = k_{AC,act} \cdot \frac{l}{l + l_{ew}} + k_{AC,ew} \cdot \frac{l_{ew}}{l + l_{ew}} \tag{2.47}$$

where l and l_{ew} represent the active and end-winding lengths, respectively.

The results from the benchmark motor are depicted in Fig.,2.19a. As anticipated, the AC factor is minimal: staying below 5% for the examined PM-SyR motor when considering the fundamental frequency (with a maximum speed of 9000 rpm corresponding to 300 Hz). This observation aligns with the utilization of stranded conductors with a small cross-section (1.2 mm diameter).

2.5.6 Efficiency maps evaluation procedure

The efficiency map test points are selected on the (T, n) plane and the data are stored in a matrix in which the torque index moves on the rows while the speed index moves along the columns. To be independent of the inverter type and modulation techniques, the efficiency map is first evaluated in sinusoidal supply. Consideration

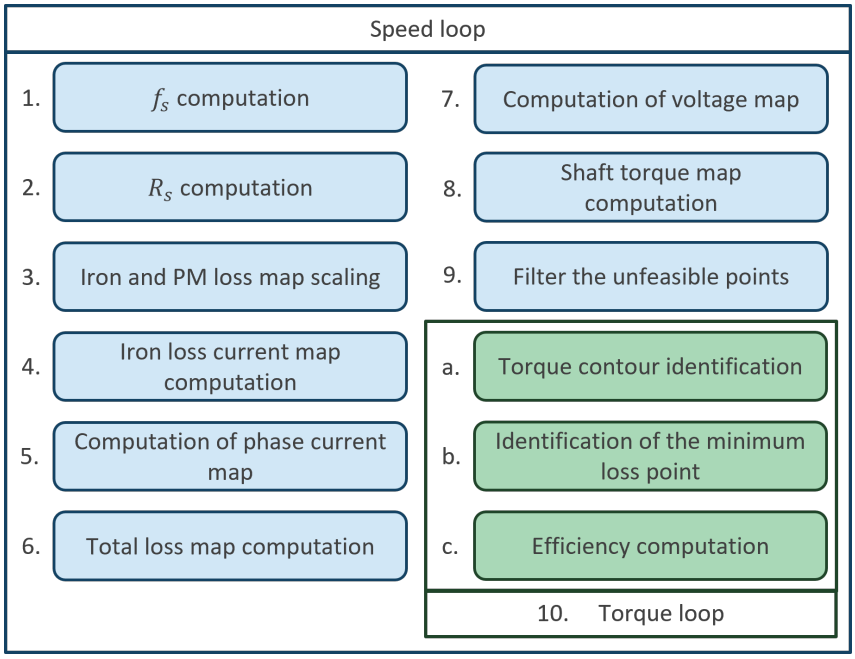

Fig. 2.20 Efficiency maps evaluation flowchart.

on the PWM effects will be discussed later. According to the flowchart in Fig. (2.20), the algorithm is based on two nested loops. The first loop regards the speed and is indexed with j, while the deeper loop regards the torque and uses i as the index.

The procedure is flux and loss maps based, but other inputs are required:

- the inverter limits in terms of maximum current I_{max} and DC link voltage V_{dc};
- the phase resistance $R_{s,0}$ defined at a reference copper temperature $\theta_{Cu,0}$;
- the permanent magnet temperature θ_{pm};
- the temperature θ_{Cu} at which the efficiency map is evaluated.

The control trajectories followed during the procedure aim to maximize the efficiency contemplating, as said, the inverter limits. There is a negligible difference compared to the common experimental control strategy that refers to MTPA and MTPVcontrol locus at low and high speed, respectively. For clarity, the element-wise matrix product and division operators "$\odot$"and "$\oslash$"are defined.

All the steps illustrated in Fig. (2.20) are detailed in the following:

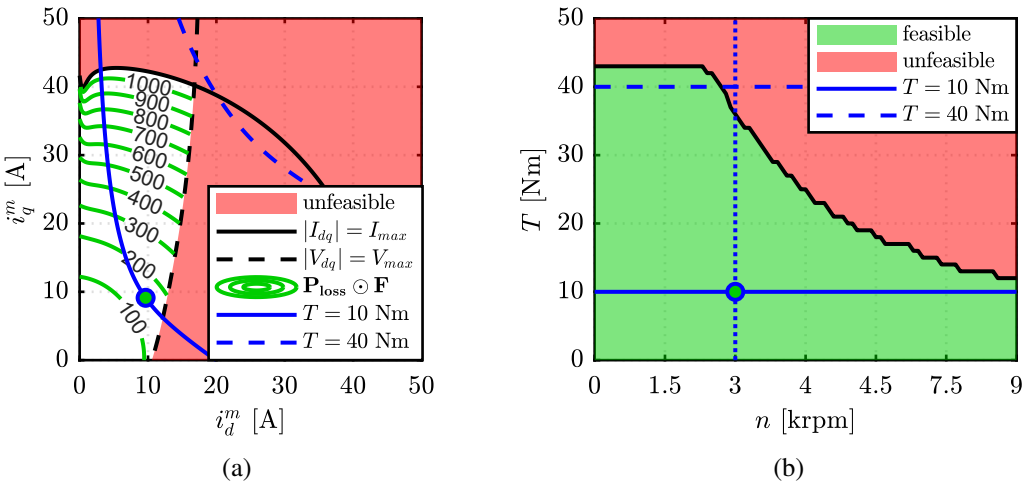

Fig. 2.21 Efficiency evaluation of the $T_i = 40$ Nm (unfeasible point) and $T_i = 10$ Nm (feasible point) at 3000 rpm working points: (a) dq plane and (b) $T - n$ plane.

1. the electrical frequency f_j and the electrical pulsation ω_j are computed according to the rotor speed n_j;

2. the stator resistance is computed accounting for the f_j, adding the AC resistance and it is reported at the evaluation temperature (2.48);

$$R_{s,\theta} = R_s \cdot \left[1 + \alpha_{Cu}\left(\theta_{Cu} - \theta_{Cu,0}\right)\right] \tag{2.48}$$

   where α_{Cu} is the copper temperature coefficient;

3. the iron and PM loss maps $\boldsymbol{P}_{Fe}, \boldsymbol{P}_{pm}$ are computed at f_j;

4. the loss current vector map $\boldsymbol{I}_{dq}^{Fe}$ is computed as the inverse of (2.30):

$$\boldsymbol{I}_{dq}^{Fe} = \left[\frac{2}{3} \cdot (\boldsymbol{P}_{Fe} + \boldsymbol{P}_{pm}) \oslash \left(j \cdot \omega_j \cdot \boldsymbol{\Lambda}_{dq}\right)\right]^* \tag{2.49}$$

5. the total current map $\boldsymbol{I}_{dq}$ is computed (2.50). The copper loss map $\mathbf{P}_{Cu}$ is also computed (2.29);

$$\boldsymbol{I}_{dq} = \boldsymbol{I}_d + j\boldsymbol{I}_q + \boldsymbol{I}_{Fe} \tag{2.50}$$

6. the total loss map $\boldsymbol{P}_{loss}$ is now evaluated as:

$$\boldsymbol{P}_{loss} = \boldsymbol{P}_{Cu} + \boldsymbol{P}_{Fe} + \boldsymbol{P}_{pm} + P_{mech} \tag{2.51}$$

7. the voltage map $\boldsymbol{V}_{dq}$ is computed from (2.26);

8. the torque matrix $\boldsymbol{T}$ is retrieved from the electromagnetic torque $\boldsymbol{T}_{em}$ and the mechanical loss, by means of (2.33);

9. the feasibility matrix $\boldsymbol{F}$ is defined:

$$\begin{cases} \boldsymbol{F} = NaN & \text{where } |\boldsymbol{I}_{dq}| > I_{max} \\ \boldsymbol{F} = NaN & \text{where } |\boldsymbol{V}_{dq}| > V_{DC} \\ \mathbf{F} = 1 & \text{elsewhere} \end{cases} \tag{2.52}$$

   where *NaN* stands for not a number. All the previous computed matrices are multiplied by the feasibility matrix, so all the working points over the current and voltage limits are removed;

10. torque nested loop:

    (a) for the selected torque level T_i, the torque contour is retrieved from the $\boldsymbol{T} \odot \boldsymbol{F}$ map. All the (i_d^m, i_q^m) coordinates that provide T_i are saved;

    (b) the (i_d^m, i_q^m) point that minimized the losses is selected;

    (c) the total efficiency is evaluated as:

$$\eta_{ij} = \frac{T_{ij} \cdot \omega_{m,ij}}{T_{ij} \cdot \omega_{m,ij} + P_{loss,ij}} \tag{2.53}$$

The evaluation of the (i_d^m, i_q^m) coordinates of minimum loss for two torque-speed combinations is graphically described in Fig. 2.21. Two levels of torque (10 and 40 Nm) are considered at $n_j = 3000$ rpm. The point $T_i = 40$ Nm, $n_j = 3000$ rpm is not feasible, abd thus the family $(i_d^m, i_q^m)_{T_i}$ is empty, so the algorithm sets the corresponding efficiency point as *NaN*. Conversely, if $(i_d^m, i_q^m)_{T_i}$ is not empty like for $T_i = 10$ Nm, the minimum loss i_{dq}^m point (green dot) is determined and used to calculate all the quantities related to the (T_i, n_j) point (voltages, flux linkages, currents, loss terms) from the respective maps.

The determination of the (i_d^m, i_q^m) coordinates corresponding to the minimum loss for two $(T-n)$ combinations is illustrated in Fig. 2.21. At a speed of $n_j = 3000$ rpm, two torque levels are considered. The point $T_i = 40$ Nm is found to be unfeasible because violates the inverter limits. Consequently, the algorithm designates the

efficiency point for this configuration as NaN. On the contrary, for $T_i = 10$ Nm, the minimum loss point (depicted as a green dot) is identified. Starting with this combination of current, all the other electrical quantities are retrieved according to the described procedure.

2.5.7 Results and validation

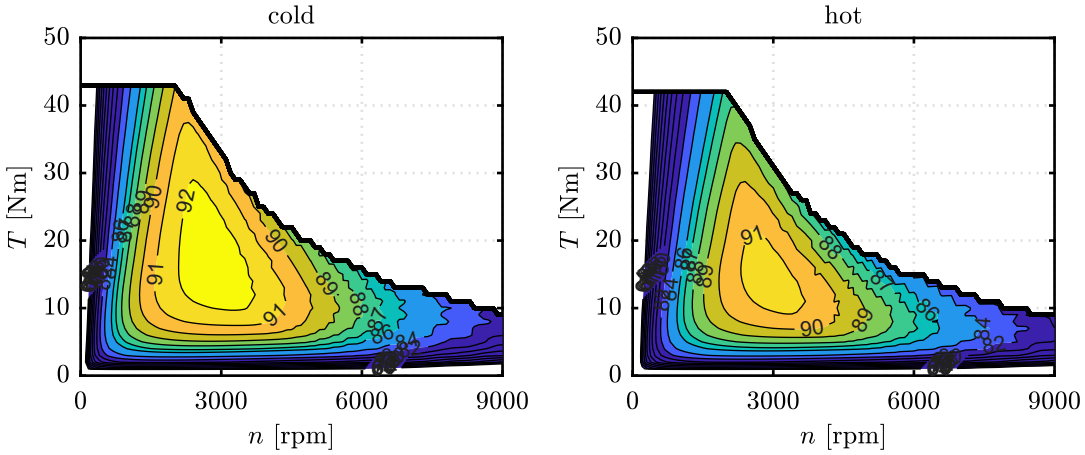

Fig. 2.22 Efficiency maps of the benchmark motor with maximum efficiency control in cold (a) and hot (b) conditions.

The iron loss map is created by conducting individual simulations on a 15x15 grid, encompassing 90 rotor positions across a 180° electrical degree range. This procedure typically requires around 60 minutes on the designated workstation. Two different temperature conditions are taken into account:

- cold condition: winding temperature $\Theta_{Cu} = 40°$C and PM temperature $\Theta_{PM} = 20°$C;
- hot condition: winding temperature $\Theta_{Cu} = 130°$C and PM temperature $\Theta_{PM} = 120°$C.

Increasing winding temperature naturally leads to higher copper loss, particularly impacting the high torque region. Additionally, PM temperature affects PM remanence, consequently influencing the output torque for a given current. Figure 2.22

illustrates the comparison of efficiency maps under cold and hot conditions. As anticipated, efficiency is higher in the cold scenario due to lower phase resistance and higher PM remanence. Moreover, PM temperature slightly affects maximum torque in the low-speed region, with torque production being slightly lower in hot conditions compared to cold ones (a difference of 1 Nm).

The impact of PM loss on total loss is minimal, with PM loss accounting for less than 1% of iron loss across all operating points, specific to the tested machine rather than a general observation for interior PM machines.

Moreover in Fig. 2.23 are reported the losses breakdown for two different operating points in hot condition, 43 Nm at 2000 rpm and 14 Nm at 6000 rpm, respectively. So the points refer to high torque and low speed and vice versa.

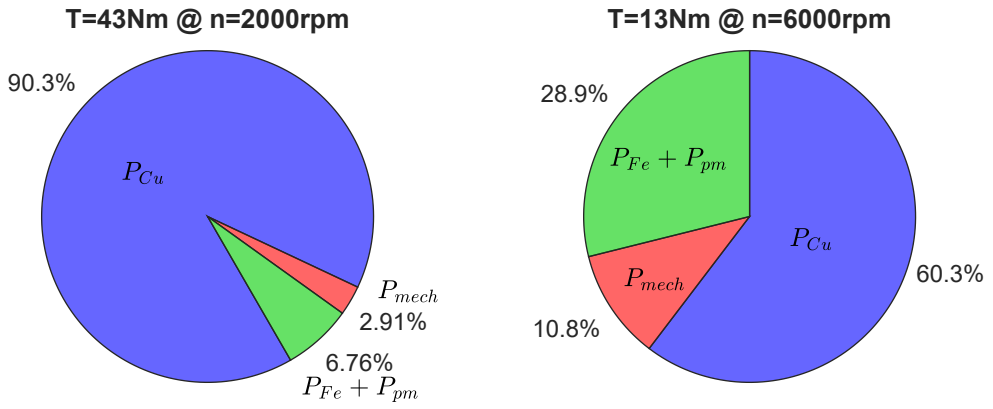

(a) (b)

Fig. 2.23 Losses breakdown at two operating points.

Experimental validation involves two steps: identifying flux maps at constant speed and measuring efficiency maps. Experimental data are compared to FEA-calculated efficiency maps. Direct flux vector control (DFVC) with maximum torque per ampere (MTPA) and flux weakening is employed for the tests [82]. Flux maps are measured at 300 rpm using the method outlined in [24], with a PM temperature of 20°C. Minor adjustments are made to the FEA model to account for mechanical tolerances in the air gap, PM dimensions, and rib dimensions. These quantities are modified in the FEA model to match the worst-case scenario of mechanical tolerances. Figure 2.24 compares the results of the FEA model with experimental findings, demonstrating good agreement in current and flux linkage amplitude versus

torque under MTPA conditions, with a relative error below 5% for the current range during operation.

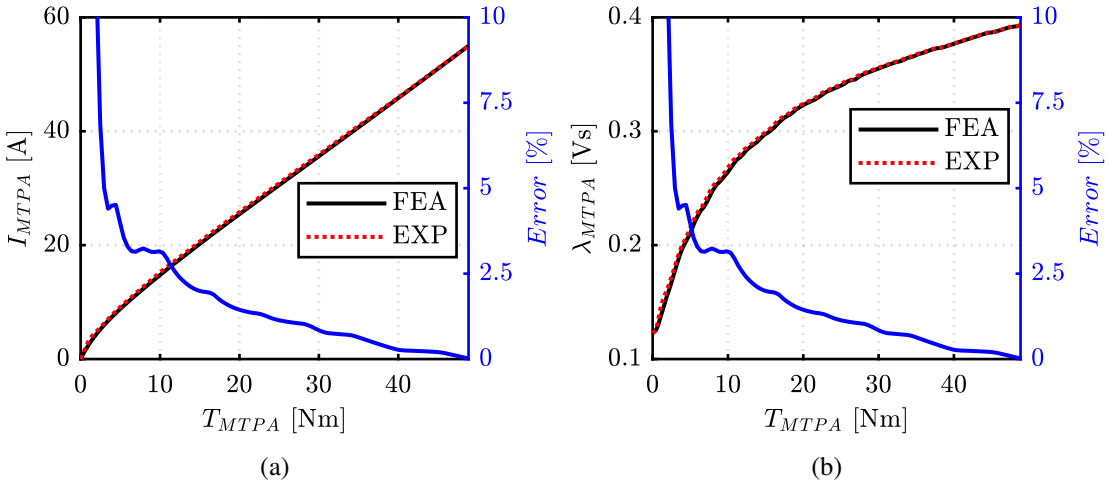

Fig. 2.24 FEA and experimental models: (a) MTPA current versus torque and (b) MTPA flux linkage versus torque.

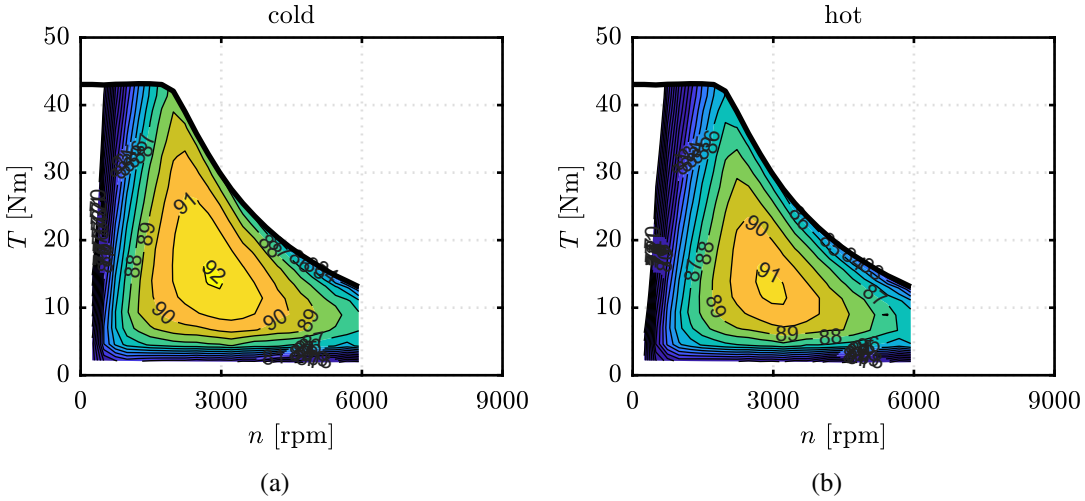

Fig. 2.25 Experimental efficiency maps in (a) cold and (b) hot conditions. MUT tested up to 6000 rpm.

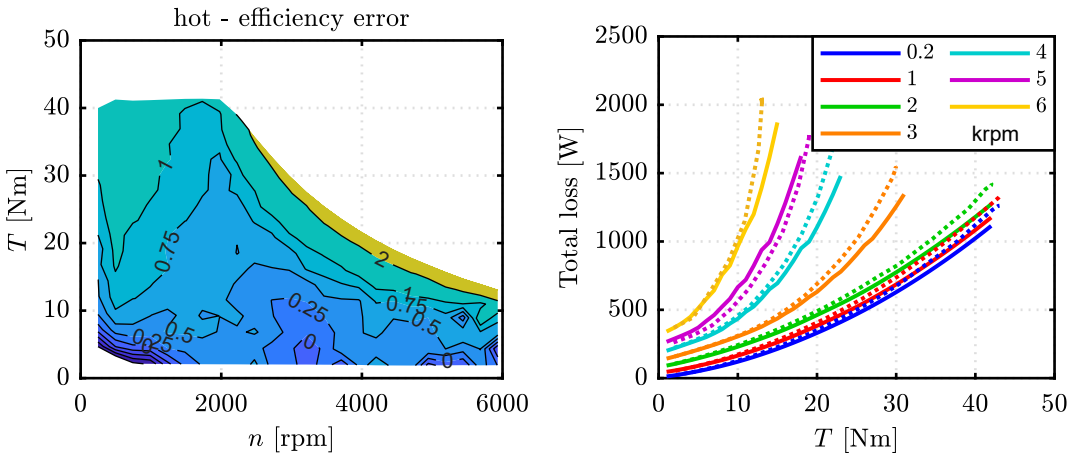

(a) (b)

Fig. 2.26 (a) Experimental versus simulated efficiency map error in hot condition. (b) Experimental (dotted lines) versus simulated (solid lines) total loss.

Efficiency maps are obtained by controlling the machine under test (MUT) torque using direct flux vector control (DFVC). Experimental flux maps are utilized in the DFVC flux observer and for offline evaluation of the reference maximum torque per ampere (MTPA) trajectory of the control. The speed is capped at 6000 rpm due to limitations imposed by the dynamometer drive.

For each reference speed, a reference torque staircase is applied, and data are recorded for each torque value for a multiple of one mechanical cycle after an appropriate settling time. Before proceeding to the next torque staircase at the next speed level, a resistance test is conducted by setting the speed to zero and controlling the rated torque. The phase resistance measured in DC conditions serves to track the average winding temperature during the test. A similar procedure is employed to monitor PM temperature, based on the measurement of open-circuit voltage before and after each torque sequence.

The efficiency maps are initially measured from room temperature conditions (cold map) and then again after preliminary heating to 120°C PM temperature (hot map). Due to the relatively quick mapping sequence, the rise in PM temperature from the beginning to the end of the mapping process is negligible overall (less than 5°C). The results are depicted in Fig. 2.25. A comparison with Fig. 2.22 reveals a significant agreement with the model. The error map in Fig. 2.26 illustrates

the difference between the measured efficiency and that obtained with sinusoidal simulations; this difference can be reduced through an analysis of the PWM effect.

2.5.8 Accounting for PWM

A circuit-based model of the electric drive is employed to assess motor currents when subjected to PWM supply and field-oriented control (FOC). This model, implemented in PLECS [83], follows the Voltage Behind Reactance (VBR) approach [84] and utilizes flux maps. In the model, depicted in Fig. 2.27, the motor is represented as an RLE load with a three-phase coupled inductor. Controlled voltage generators enforce the back electromotive force (EMF) voltage. The coupled inductor term L_s incorporates the incremental inductances in dq coordinates, calculated from predetermined dq flux maps. Meanwhile, the back-EMF voltages are determined by the dq flux linkage at the respective operating point multiplied by the angular frequency in abc coordinates, using the flux linkage maps. This model is integrated into the SyR-e platform's tool syreDrive [85].

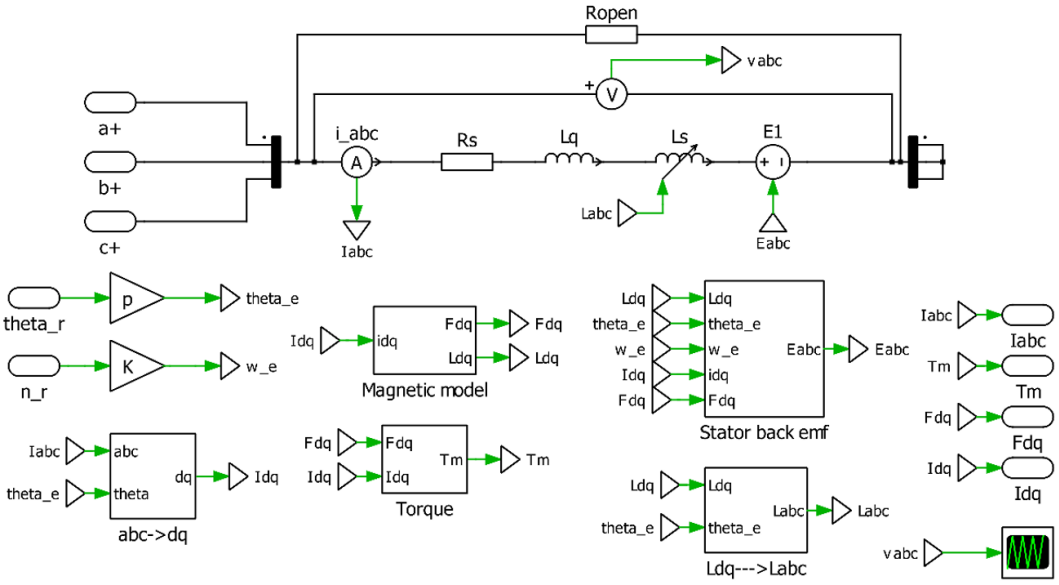

Fig. 2.27 Circuital model of the PMSM.

The circuital model's accuracy is verified through experimental validation, which involves comparing simulated and measured waveforms under steady-state conditions. These tests were conducted using the Brusa HSM1-6.17.12 commercial

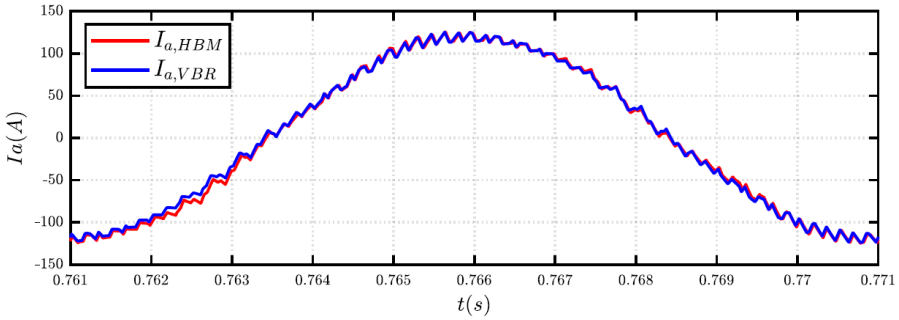

Fig. 2.28 Brusa motor: (red) measured and (blue) simulated current waveform.

automotive motor [86], which is rated for 130 Nm and 70 kW peak power, with a maximum speed of 12000 rpm.

Fig. 2.28 presents the measured and simulated current of phase a for the Brusa motor under steady-state conditions at 2000 rpm, allowing for an assessment of the accuracy of current waveform evaluation from the circuital model. The same methodology is applied to the motor under test under specified test conditions. This data is utilized to feed the loss model accordingly.

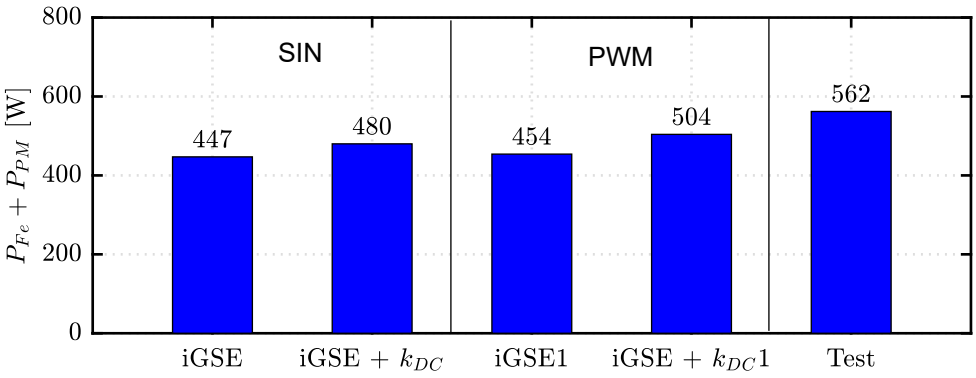

Fig. 2.29 Comparison of iron loss at 13 Nm and 6000rpm

To address the PWM effect on iron losses, the simulation time step is chosen based on the switching frequency. In this case study, with a switching time of 100 μs, a time step of 7 μs proves adequate. This time step corresponds to 0.5° electrical degrees, enabling the simulation to encompass 360 rotor positions across a 180° electrical degree excursion. As shown in Fig. 2.29, the iGSE method, without considering the DC bias effect, estimates a loss of 447 W under sinusoidal

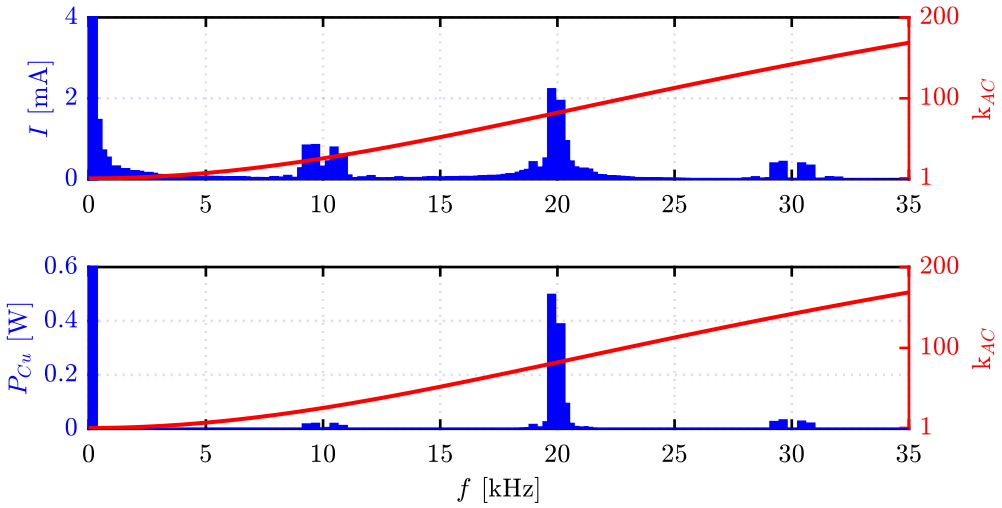

Fig. 2.30 Copper loss and current harmonics at 13 Nm and 6000rpm.

excitation and 454 W under PWM supply. As anticipated, the increase attributed to the additional minor loops (hysteresis) and flux density harmonics (eddy current) remains limited. However, when accounting for the DC bias effect (using the iGSE + k_{DC} method), the estimated losses under sinusoidal and PWM supply rise to 480 W and 504 W, respectively. During experimental testing, the estimated iron loss is measured at 562 W. The difference compared to the iGSE + k_{DC} method's estimate of 504 W under PWM supply serves as a metric for loss estimate error. More broadly, comparing FEA and experimental efficiency maps reveals a 20% increase between the sinusoidal and experimental iron loss. This suggests a correction factor of approximately 1.2 could be applied to the FEA-computed iron loss map to align with the measurements. Notably, electric motor manufacturers commonly employ correction factors ranging between 1.4 and 1.8. For clarity, no correction coefficient was applied to the results presented here.

Regardig copper loss, the non-sinusoidal current waveforms undergo decomposition using a Fast Fourier Transform (FFT), where each harmonic (I_h) is linked to a corresponding AC factor ($k_{AC,h}$), as illustrated in (2.54) and demonstrated in Fig. 2.30 for a specific operating point.

$$P_{Cu} = 3\,R_{DC} \cdot \sum_{h=0}^{\infty} k_{AC,h} \cdot I_h^2 \tag{2.54}$$

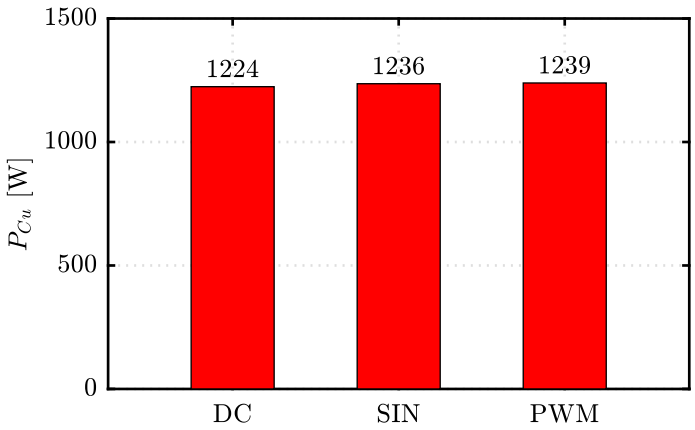

Fig. 2.31 Comparison of copper losses at 13 Nm and 6000rpm.

This stage does not necessitate additional FEAs, as it relies solely on the pre-calculated AC loss map by leveraging the superposition principle. The k_{AC} factor is computed up to 35 kHz and at a temperature of $\Theta_{Cu} = 40°C$. It's worth noting that even when the k_{AC} values reach high levels, exceeding 200, the corresponding P_{Cu} remains insignificant due to low current amplitudes. Additionally, the highest harmonic loss occurs at twice the switching frequency, i.e., 20 kHz. Furthermore, Fig. 2.31 presents a comparison of copper loss under DC, sinusoidal (SIN), and PWM supplies. As expected, the skin effect on this type of windings does not significantly impact the loss: the increase is merely 15 W.

Chapter 3

Short circuit current determination via flux-map manipulation

The symmetric three-phase short-circuit is a critical fault condition for Permanent Magnet (PM) synchronous machines, requiring careful consideration to prevent the risk of irreversible demagnetization [87–89]. While the steady-state fault current is easily calculated as the machine characteristic current i_{ch}, estimating the peak transient short-circuit current necessitates transient simulation [90]. Saturation of the q axis is considered in [91], but cross-saturation is neglected. A comprehensive analytical model was proposed in [92], which still overlooks cross-saturation. In [93], saturation of both axes is contemplated using FEA results at various operating points, aligning with the proposed approach. Currently, transient FEA coupled with circuital simulation is deemed the reference solution, despite being time-consuming [94] and limited to commercial software tools. Lastly, other types of short-circuits have been analyzed in the literature: [95] and [96] studied the prediction of partial-turn short-circuit, single-phase open circuit fault, and phase-to-phase terminal short-circuit. Here, a method for the fast and accurate determination of the peak short-circuit current under symmetric fault conditions using pre-evaluated flux linkage maps. Two methods are developed: one utilizing extended flux maps manipulation to calculate transient fault currents, and a second where the newly introduced hyper-worst-case (HWC) short-circuit current value is directly evaluated using dedicated FEA simulation. The latter allows a quick evaluation of peak short-circuit conditions with limited knowledge of the motor, suitable for use at the preliminary design stage. The analysis of pre-fault conditions and the response of different types of PM and

reluctance synchronous machines are also developed and discussed. The results are validated against transient FEA computations using Simcenter MAGNET. Four motors are used as examples encompassing two interior-PM machines (THOR and PRIUS), one surface-mounted PM machine (SPM), and one synchronous reluctance machine (RAWP), each with their specifications detailed in Tab. 3.1. In particular, the HWC short-circuit current procedure will be used in the next three chapters as a design parameter to assess the risk of demagnetization in the event of a short circuit fault and to evaluate the feasibility of the Active Short Circuit as an emergency measure for shutting down the machine.

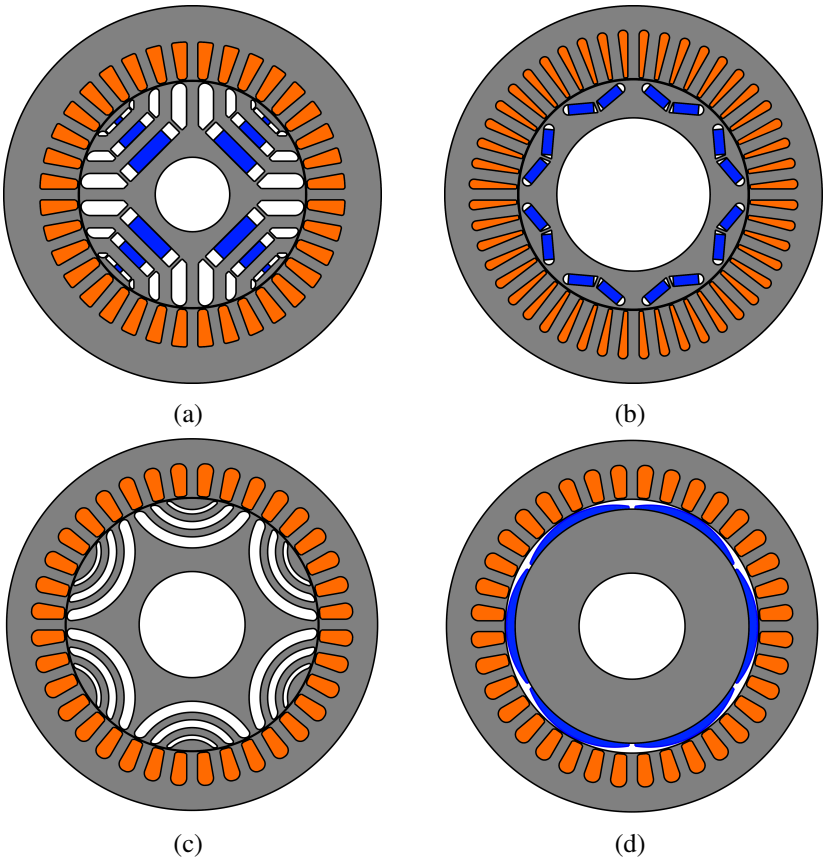

Fig. 3.1 Cross section of the THOR, PRIUS, RAWP and SPM reference machines. Magnets are colored in blue.

Table 3.1 Ratings of the FEA evaluated machines

		THOR	PRIUS	RAWP	SPM
Number of pole pairs	p	2	4	3	3
Max current [Apk]	i_{max}	44	250	30	30
DC link voltage [V]	V_{dc}	310	650	566	566
Max torque [Nm]	T_{max}	43	200	41	62
Nominal speed [rpm]	n_{nom}	2500	4000	2500	2200
Max speed [rpm]	n_{max}	9000	12000	6000	6000
Max power [kW]	P_{max}	11.5	60	10	14

3.1 Steady-state solution

The steady-state voltage maps $\mathbf{V}_d(i_d, i_q)$, $\mathbf{V}_q(i_d, i_q)$ (3.1) are computed by substituting the flux and current maps in the steady-state form of (2.12).

$$\begin{cases} \boldsymbol{V}_d = R_s \cdot \boldsymbol{I}_d - \omega \cdot \boldsymbol{\Lambda}_q \\ \boldsymbol{V}_q = R_s \cdot \mathbf{I}_q + \omega \cdot \boldsymbol{\Lambda}_q \end{cases} \tag{3.1}$$

For each considered angular frequency ω, the steady-state short-circuit current is determined by setting both voltage components to zero. Utilizing the voltage maps, the $v_d = 0, v_q = 0$ contours are identified, and their intersection point i_{ss} represents the steady-state short-circuit current. This process is visually depicted in Fig. 3.2 for the IPM THOR machine from [97], at 250 rpm and 2500 rpm. The short-circuit current aligns with the PM direction, and as the speed increases, it coincides with the characteristic current $i_{ch} = 43$ A at the specified temperature of 20°C. It is noteworthy to observe how the iso-voltage contours evolve at different speeds due to the varying contributions of the resistance voltage component.

The steady-state flux, current, and torque values as functions of speed under short-circuit conditions are illustrated in Fig. 3.3. The torque is negative (indicating braking) across all speeds, reaching a peak of 16 Nm (37% p.u.) at 125 rpm, and asymptotically tends to zero for higher speed values. As expected, the short-circuit current tends to align with the negative PM axis at higher speeds, and both torque and flux linkage amplitude tend to zero. The asymptote corresponds to zero flux linkage, as indicated by the flux characteristic.

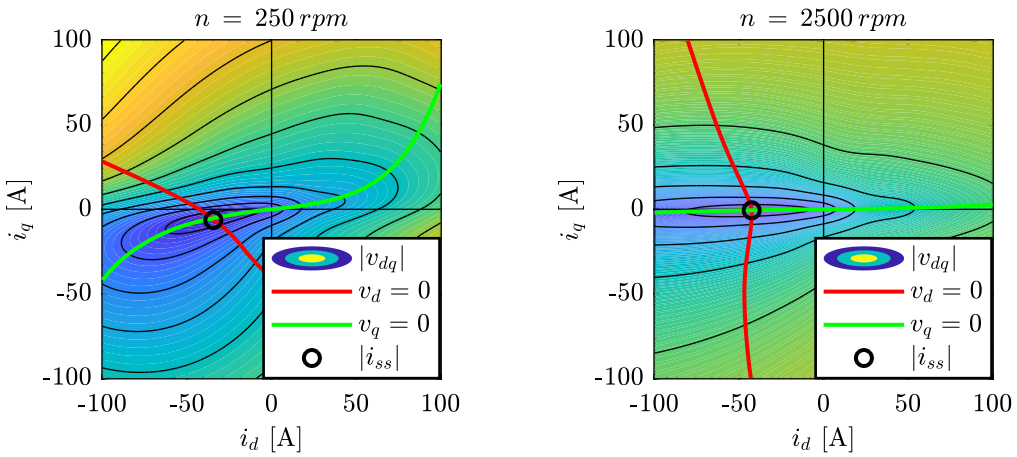

Fig. 3.2 i_{ss} (black circle) computation at speed: (a) 250 rpm and (b) 2500 rpm.

3.2 Transient short circuit computation

The transient short-circuit current waveforms are calculated by solving the voltage equation in discrete-time form. For simplification, iron losses are neglected, and the rotor speed is assumed to be constant. Both assumptions are considered conservative, as demonstrated in the following.

The voltage equation (2.12) is discretized using the Euler method (3.2). Here, Δt represents the time step, and the superscripts k and $k+1$ denote the present and next time samples, respectively, at $t = t_k$ and $t = t_k + \Delta t$.

$$\begin{cases} \lambda_d^{k+1} = \lambda_d^k + \left(-R_s \cdot i_d^k + \omega \cdot \lambda_q^k\right) \cdot \Delta t \\ \lambda_q^{k+1} = \lambda_q^k + \left(-R_s \cdot i_q^k - \omega \cdot \lambda_d^k\right) \cdot \Delta t \end{cases} \tag{3.2}$$

The currents at $k+1$ are determined using the inverse flux maps:

$$\begin{cases} i_d^{k+1} = \boldsymbol{I}_d(\lambda_d^{k+1}, \lambda_q^{k+1}) \\ i_q^{k+1} = \boldsymbol{I}_q(\lambda_d^{k+1}, \lambda_q^{k+1}) \end{cases} \tag{3.3}$$

The inverse flux maps are derived through manipulation of the direct flux maps $\boldsymbol{\Lambda}_{dq}$, as outlined in [98]. Subsequently, the electromagnetic torque is obtained from

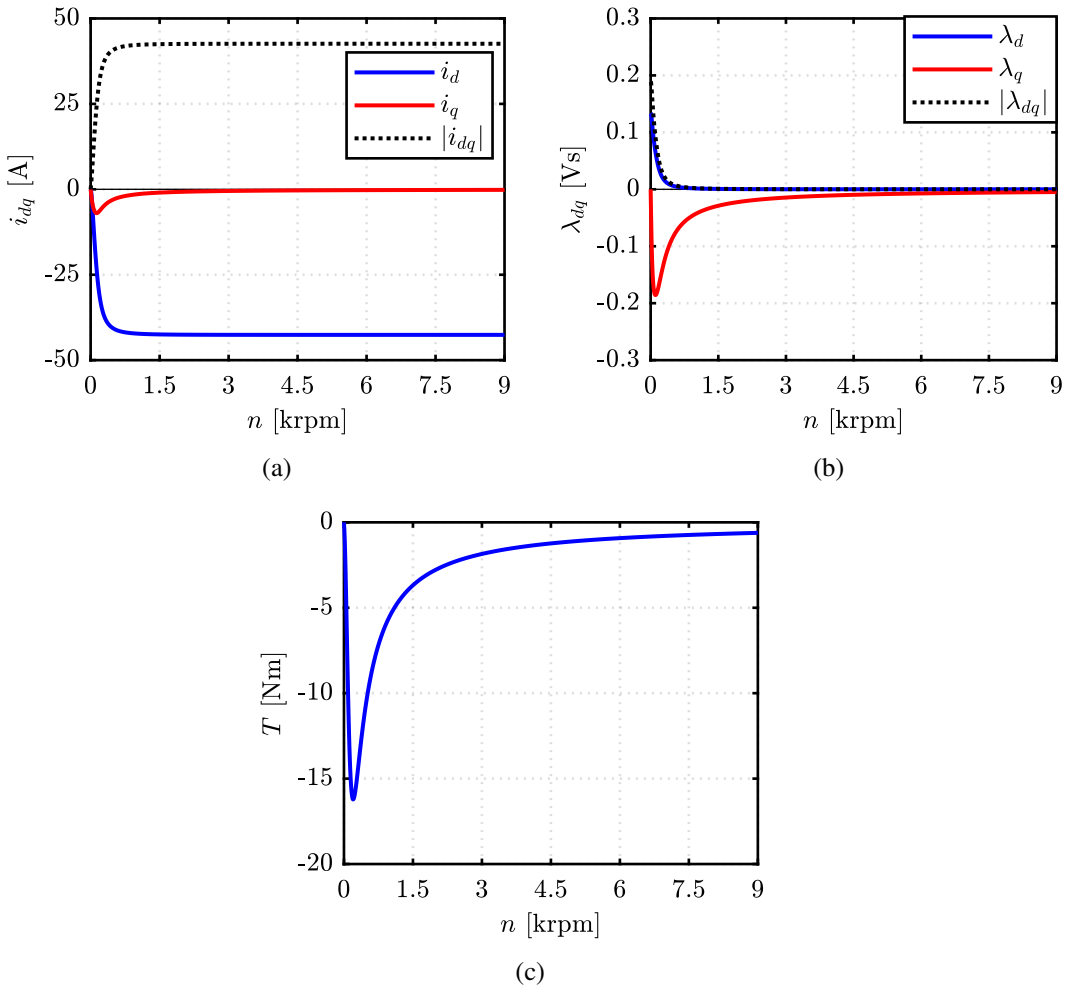

Fig. 3.3 Steady-state short-circuit (a) currents, (b) flux linkages and (c) torque function of rotor speed of the THOR motor.

the torque map:

$$T^{k+1} = \boldsymbol{T}(i_d^{k+1}, i_q^{k+1}) \tag{3.4}$$

The process is iterated for all the specified time instants covering a defined number of electrical cycles of the motor. It's crucial to highlight that the presented model does not directly rely on FEA simulation but is grounded on flux maps, which can be computed using FEA or obtained through measurements on a prototype.

The peak short-circuit current occurs after approximately half a cycle and reaches a value of 183 A (4.25 times the steady-state fault current). The peak torque of 105 Nm is 2.44 times the peak torque in operation and occurs in the vicinity of the

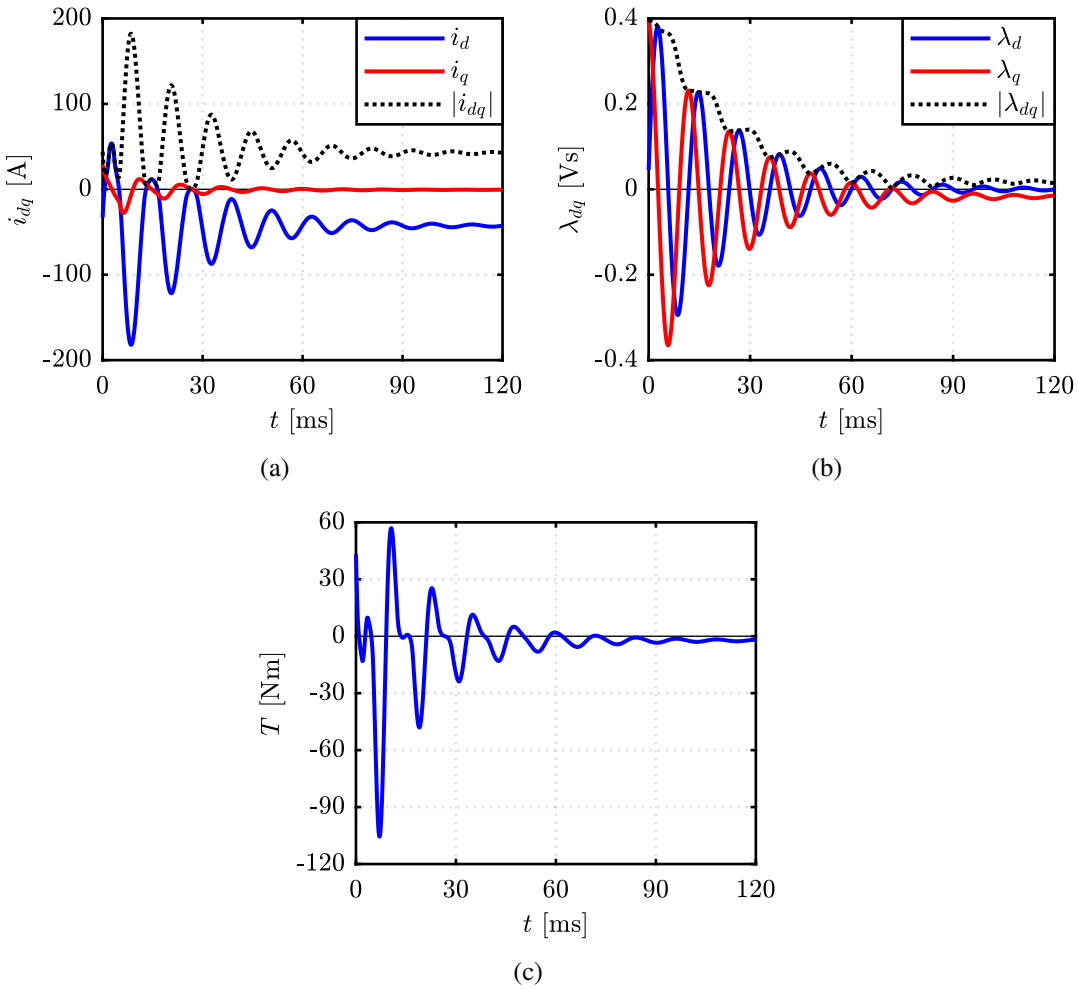

Fig. 3.4 Short-circuit results of the THOR machine. Working point in MTPA conditions at nominal speed. (a) *dq* currents, (b) *dq* flux linkages, (c) torque as a function of time.

current peak. The steady-state values align with what is predicted by the steady-state analysis. The decay of the flux linkage amplitude exhibits oscillations superimposed on exponential decay due to the complex-conjugate poles of the second-order motor transfer function at the considered speed. The computational time required to calculate ten electrical cycles is about 16 seconds, while covering one period to identify the peak transient current takes about 1.5 seconds, assuming FEA flux maps are available. The computer used is a laptop equipped with an Intel i7-8750H CPU and 16 GB of RAM.

3.3 Transient trajectories

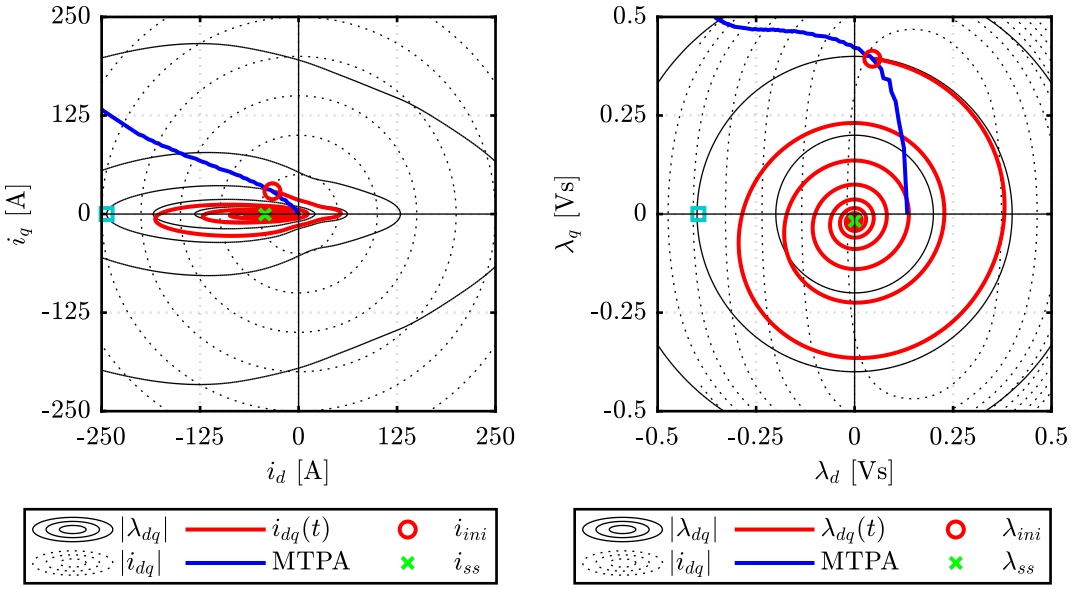

(a) (b)

Fig. 3.5 Short-circuit transient trajectories on the dq planes: (a) Current and (b) flux linkage

The current and flux linkage transient trajectories computed with the presented model and displayed in Fig. 3.4 are plotted in the x-y form in the respective i_d, i_q and λ_d, λ_q planes in Fig. 3.5. The pre-fault condition is indicated with a red circle, and the steady-state solution is marked with a green cross. The flux linkage follows a spiral trajectory starting from the pre-fault MTPA condition, which is also the maximum flux condition for this machine. The rate of decay of the flux amplitude is related to the combination of stator resistance loss and rotor speed, considering that no other type of loss is accounted for in this model. With no loss, the flux linkage vector would move clockwise on the black circle, while if other loss terms were considered (e.g., iron loss), the decay rate would be faster, leading to a smaller peak fault current. Given the clockwise rotation, a first current peak is found along the positive d axis, and the maximum current condition is then found along the negative d axis, half a cycle later. The distance between the maximum current value (183 A) and the maximum current of the constant-flux trajectory (240 A) passing through the initial point relates to the decay of the flux spiral, i.e., to the damping effect of

stator Joule loss. The higher the loss, the faster the decay, and the lower the peak current. This confirms the assumption that neglecting iron loss or other loss terms in the model is on the safe side. The maximum current amplitude corresponding to λ_{max} (flux linkage at the maximum torque condition under MTPA) is defined as hyper-worst-case (HWC) short-circuit current $i_{pk,hwc}$, reported with a light blue square marker in Fig. 3.5. This HWC current corresponds to the peak short-circuit current in lossless conditions.

For a machine with high saliency, such as the one used here, the short-circuit peak current typically falls outside the dq current range used for flux mapping. Therefore, a dedicated, range-extended set of FEA maps is required for transient short-circuit evaluation. In the example, the flux maps of standard size are 80x80A, whereas the ones for short-circuit evaluation have a 240x240A domain.

3.4 Fast Hyper-Worst-Case current computation

The trajectories of flux and current in Fig. 3.5 propose a method for estimating the short-circuit current in the HWC without relying on pre-calculated flux maps. The value of $i_{pk,hwc}$ is determined directly through an iterative search for the current value that, when aligned against the PMs, yields the pre-fault flux linkage amplitude λ_{max}. This process is clarified by equation (3.5), where the non-linear flux linkage curve $\lambda_d(i_d,0)$ remains unknown in the absence of pre-calculated, extended flux maps.

$$\lambda_d(i_d,0) = -\lambda_{max} \tag{3.5}$$

The equation is solved through an iterative process involving successive FEA simulations. The pre-fault flux amplitude λ_{max}, determined, for instance, at maximum current amplitude and MTPA conditions, utilizes non-extended flux maps or specialized FEA simulations. Subsequently, FEA simulations are conducted with negative i_d and $i_q = 0$, incrementing current levels to pinpoint the HWC point using the iterative secant method. The graphical representation in Fig. 3.6 illustrates the process, where $\lambda_d(i_d,0)$ and $-\lambda_{max}$ are continuous lines, and their intersection defines the targeted HWC current value. Numbered circles denote successive FEA results, with Simulations #1 and #2 corresponding to rated and overload current amplitudes. The first secant line (dotted) is computed from these two points to determine

the coordinates of the next FEA simulation #3. Another secant line is then computed from points #2 and #3, and so forth, until the error between the FEA-calculated λ_d reaches the target with an error less than 1% of λ_{max}. In this example, the direct evaluation of $i_{pk,hwc}$ involves 5 FEA iterations, requiring 2 minutes of computation.

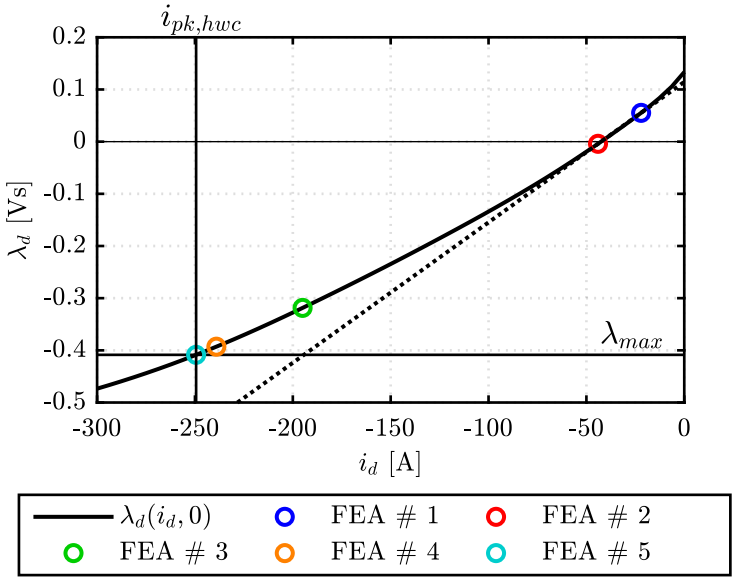

Fig. 3.6 HWC peak current estimation. Magnets axis in solid black line. Simulated points via FEAs during the iterations are marked with colored circles.

3.5 Validation against transient FEA

The proposed method is validated against transient FEA coupled with a circuital model performed in Simcenter MAGNET [99]. The circuit is reported in Fig. 3.7: the three-phase windings are star connected and each phase is supplied by a current source, according to the willed pre-fault conditions. The symmetric short-circuit is modelled with two automatic switches ($S10 - S11$ in Fig. 3.7) that deviate the output of the current source and short-circuit the machine terminals.

The validation is performed in the worst-case pre-fault condition, of maximum torque and rated speed. The simulation results are reported in Fig. 3.8 with blue lines and compared with the proposed method (reported in red dotted lines and labelled as SyR-e). The current waveforms are superimposed, validating the proposed model. Dealing with torque waveform, the differences are more evident, because the

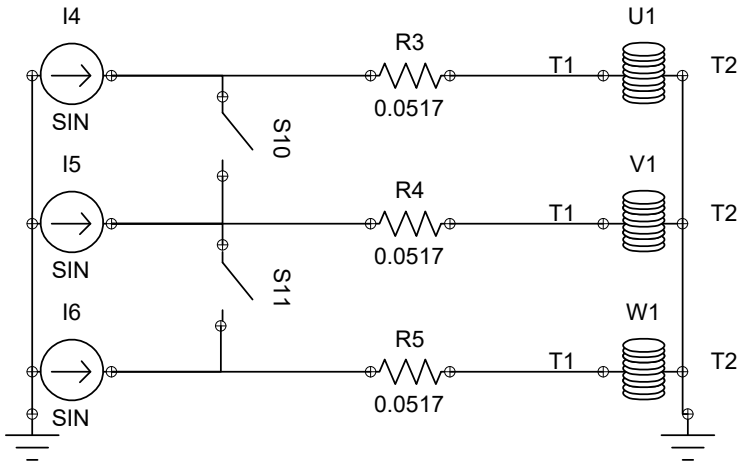

Fig. 3.7 Circuit built in MAGNET to simulate the short-circuit.

proposed model is based on fundamental-model flux maps, thus neglecting space harmonic effects and thus torque ripple. This is highlighted in the zoom window of Fig. 3.8c.

In Tab. 3.2 the computational time of the various approach is reported. A laptop with i7 8750H CPU and 32 GB RAM is used. Note that generally, the HWC algorithm tends to converge in a maximum of 10 iterations.

Table 3.2 Computational effort of different short circuit current evaluation.

	Transient FEA	**Transient Flux-Map**	**HWC**
Time	20 min	16 sec	2 mins
Cycles/iterations	10	10	5
Note	step 0.1sec	flux map required	max 10 iterations

3.6 Pre-fault conditions effect

As indicated by the analysis of the dq current and flux trajectories, the pre-fault condition significantly influences the peak short circuit current. Subsequently, the upcoming section will compare three distinct pre-fault conditions.

1. open circuit at 2500 rpm;
2. T_{max} at 2500 rpm, motor;

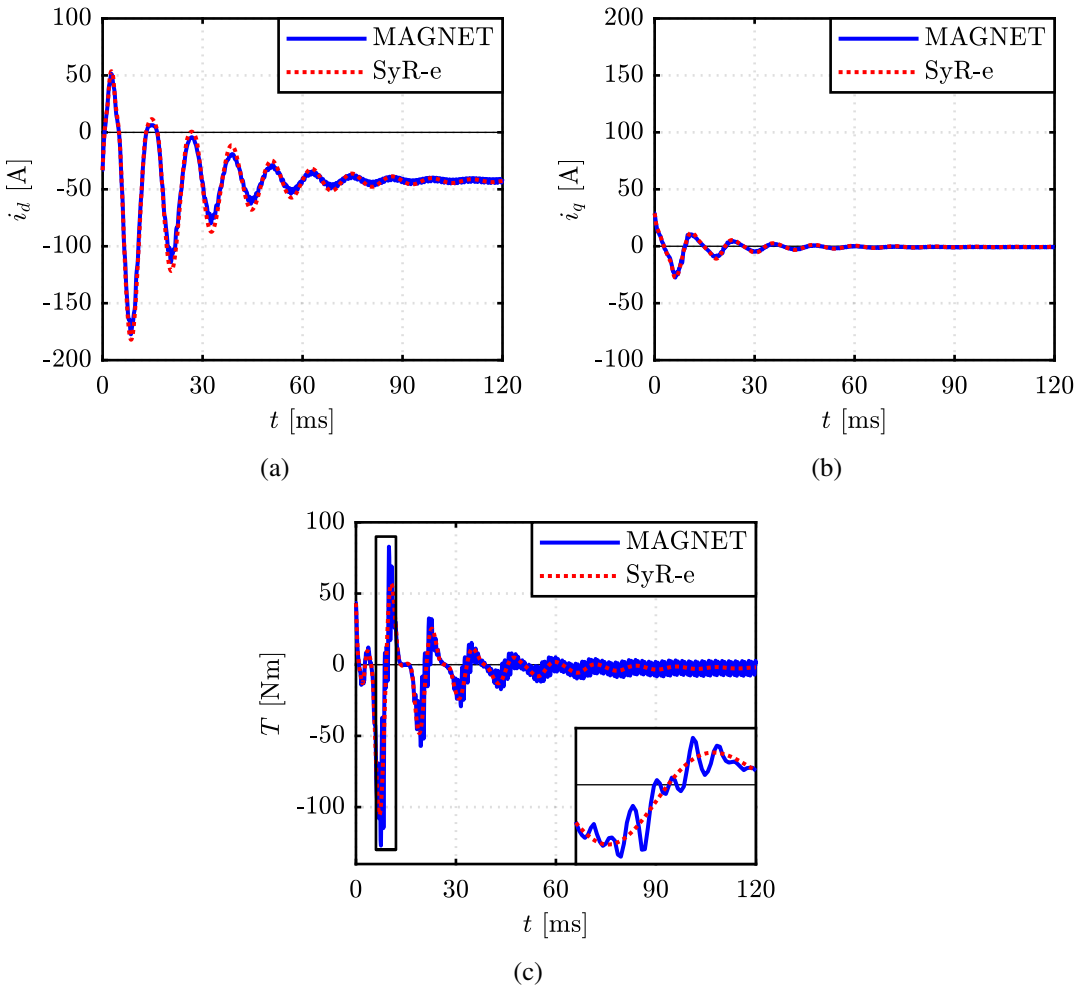

Fig. 3.8 Results of the short circuit computation with the proposed method and transient simulation: (a) d-axis current, (b) q-axis current and (c) torque function of time with pre-fault condition equal to 43 Nm along the MTPA.

3. $-T_{max}$ at 2500 rpm, brake.

A consistent motor speed is employed across all examples to facilitate comparison. Fig. 3.9 presents the current waveform as a function of time for the specified pre-fault conditions. In the plot, circles and asterisks represent the initial and peak current points, respectively. These points are also tabulated in Table 3.3 for a fast comparative analysis.

The findings indicate that the open circuit state is the least severe due to the minimal pre-fault flux linkage amplitude. This observation is elucidated by the fault trajectories of (i_d, i_q) and (λ_d, λ_q) as depicted in Fig. 3.10. In scenarios involving

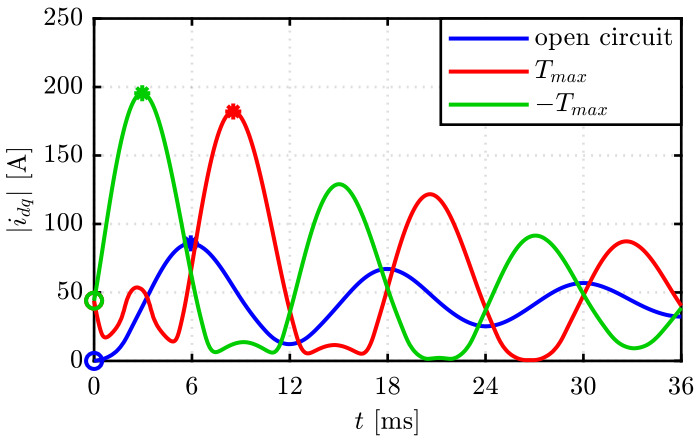

Fig. 3.9 Comparison of the current waveform during the initial cycles of the fault for the considered pre-fault conditions. Maximum current conditions are marked with asterisks.

Table 3.3 different pre-fault conditions comparison.

Scenario	$\|i_{ini}\|$ [A]	$\|i_{pk}\|$ [A]	$\|\lambda_{ini}\|$ [mVs]	$\|\lambda\|@i_{pk}$ [mVs]
open circuit	0	85.8	134	109
T_{max}, motor	44 (i_{max})	182.1	397	306
$-T_{max}$, brake	44 (i_{max})	195.5	397	331

maximum torque, the motoring situation is marginally less critical compared to braking, even when deliberately setting the initial flux amplitude to be the same. As the flux spiral progresses clockwise, placing the initial point in the second quadrant (motor) or third quadrant (brake) results in a longer or shorter path to reach the maximum current condition, consequently leading to a longer or shorter decay time. During braking, the peak short-circuit current occurs within half a cycle, whereas in motoring, it occurs in the second half cycle, resulting in a more pronounced damping effect. Nonetheless, the disparity in peak current is limited, with the motor case being approximately 7% lower.

3.7 Different motors comparison

The impacts of rotor geometry and the quantity of permanent magnets are examined by comparing the outcomes of four distinct machines showcased in Fig. 3.1, with their specifications detailed in Table 5.1. Thus, variations in PM and magnetic

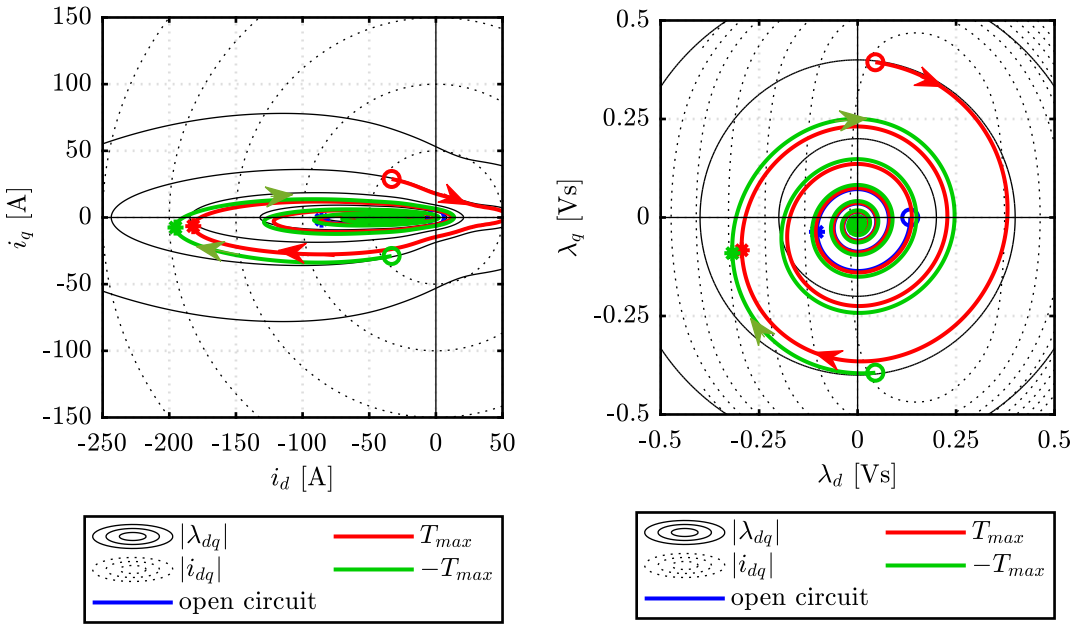

(a) (b)

Fig. 3.10 Comparison of different pre-fault scenarios of short-circuit trajectories: (a) currents (i_d, i_q) plane and (b) flux (λ_d, λ_q) plane.

anisotropy characteristics are explored. The PRIUS machine is a V-type IPM motor based on the 2010 Toyota Prius Hybrid Synergy Drive [100], representing a PM motor with a higher PM contribution compared to the THOR machine. RAWP is SyR motor, as introduced in [101], characterized by high anisotropy and the absence of PMs, an extreme case with less relevance due to the absence of a demagnetization issue. Lastly, SPM is a surface-mounted PM motor, outlined in [102], featuring no magnetic anisotropy and PM flux linkage close to the rated one, essentially the opposite case of SyR motors.

The short-circuit analysis is conducted for all the motors at their base speed and at their maximum torque as the pre-fault condition. The outcomes are presented in Fig. 3.11 and Table 3.4, expressed in per-unit of the pre-fault current amplitude of each motor, facilitating a straightforward comparison. The four motors employ different dq axis conventions: RAWP adopts the axis conventions typical of SyR

motors, whereas THOR, PRIUS, and SPM follow the axis convention of PM motors, aligning the magnet flux linkage along the d axis.

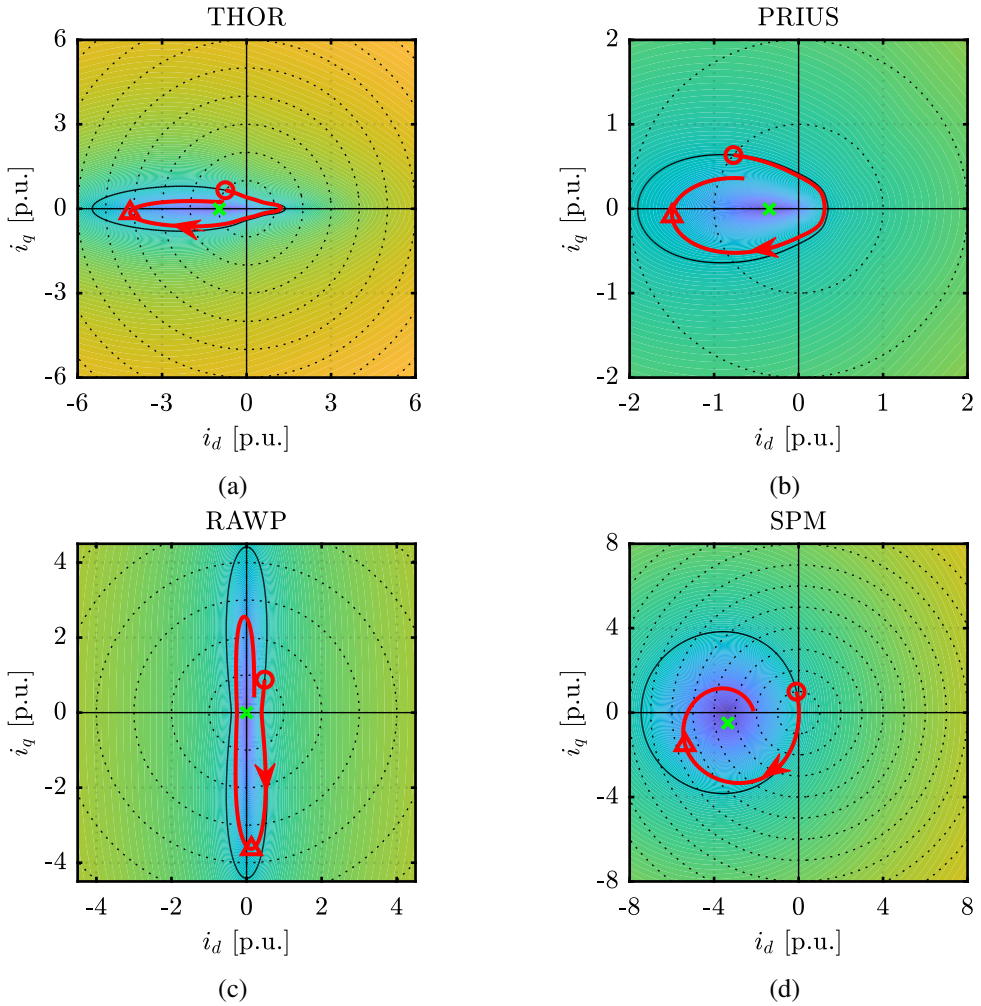

Fig. 3.11 Short-circuit transient first cycle:(a) THOR, (b) PRIUS motors, (c) RAWP motor and (d) SPM motor. The contour representing constant-flux linkage is indicated by the black line, while the trajectory of (i_d, i_q) is depicted by the red line. The steady-state condition is represented by the green cross.

- The constant flux linkage contours of the four machines, represented by solid black lines in Fig. 3.11, exhibit significant differences in shape. Notably, an increased rotor anisotropy results in sharper contours, as observed in the THOR and RAWP motors, leading to heightened overcurrents.
- The peak current during a short circuit is reported normalized by the pre-fault current at maximum torque in Table 3.4, expressed as $\frac{i_{pk}}{i_{max}}$. Based on this

Table 3.4 short-Circuit comparison for different motors

	THOR	PRIUS	RAWP	SPM
i_{ss}/i_{max}	1.00	0.35	0	3.39
$i_{pk,hwc}/i_{max}$	5.48	1.91	4.42	7.45
i_{pk}/i_{max}	4.14	1.50	3.63	5.59
λ_m/λ_{max}	0.34	0.45	0	1.00
i_{pk}/i_{ss}	4.28	4.34	∞	1.65
$i_{pk,hwc}/i_{ss}$	5.67	5.51	∞	2.20
T_{pk}/T_{max}	2.44	1.00	2.17	3.22

parameter, the motor experiencing the most severe short-circuit conditions is the SPM motor, followed by the THOR motor, while the motor with the lowest overcurrent is PRIUS. In the case of the RAWP motor, although it exhibits high overcurrent, the absence of demagnetization risk in SyR machines makes the overcurrent less critical.

- The high peak current during a short circuit can be attributed to multiple causes, categorized into two main factors: high permanent magnet strength and high anisotropy. The former effect is straightforward and is evident in SPM motors, where PMs contribute around 80% of the motor flux linkage, resulting in a steady-state short-circuit current i_{ss} that is more than three times the maximum current of the motor.

- The overshoot of the transient current compared to the steady-state current ($\frac{i_{pk}}{i_{ss}}$) may be limited, the peak current remains high and has the potential to demagnetize PMs and damage the inverter.

- The SyRmotor RAWP exhibits a null steady-state short-circuit current, with the overcurrent solely attributed to motor anisotropy. The stretched flux linkage contours due to saliency justify the overcurrent, as the fault trajectory closely follows this curve.

- THOR and PRIUS motors fall in between, having both PMs and magnetic anisotropy. THOR motor, with limited PM strength but higher anisotropy, experiences a high peak current during the fault, even if the overshoot ($\frac{i_{pk}}{i_{ss}}$) is similar for both motors.

- Table 3.4 also includes the ratio between the HWC current and the steady-state current ($\frac{i_{pk,hwc}}{i_{ss}}$), assessed without flux maps. Additionally, torque is considered since the mechanical system could be damaged by this fault. The numbers are comparable for THOR and RAWP, emphasizing the role of magnetic anisotropy in this phenomenon. Peak torque is highest for the SPM motor, attributed to its high PM strength, and limited for PRIUS due to the limited overcurrent compared to pre-fault conditions.

Chapter 4

Design of PM synchronous motors via the (x,b) design plane

This chapter presents a rapid preliminary design process for PMSMs used in traction applications. Starting with stack diameter and electric loading, the method quickly determines key dimensions such as rotor diameter, stator slot and rotor barriers dimensions, and stack length using FEA-corrected design equations, bypassing extensive optimization. Central to this process is the torque and power factor design plane [101, 103], enhanced by further research. The design plane uses the rotor-to-stator diameter ratio and per unit iron size to derive torque and power factor equations from the machine's magnetic equivalent circuit, refined through targeted FEA simulations. New figures of merit are incorporated for visual matching of output and design constraints. The method emphasizes critical design inputs like current and voltage limits and feasible numbers of turns, tailoring the design to specific needs. Two traction motors are designed and compared based on the Tesla Model 3 3D6 motor specifications. The first design is an IPM motor with NdFeB PMs in a double-V configuration, and the second is a PM-SyR motor with ferrite magnets, featuring a three-layer rotor with circular barriers. A section on ferrite-magnet motors discusses their demagnetization limits, necessitating a longer stack length and higher inverter current due to their lower energy density and coercivity. The chapter concludes with a comparison of the two motors and an overview of the swift preliminary design process from specifications to target figures.

4.1 Design equations

The design plane represented by the coordinates (x,b) facilitates the efficient parametric design and assessment of SyR and PMSM machines [101, 103]. By specifying the outer dimensions of the motor active parts, including the outer diameter D and the stack length L, the maximum current density $J(\mathrm{A/mm^2})$ and the peak flux density $B_{Fe}(\mathrm{T})$, this design plane systematically arranges the machine cross-section based on the rotor split ratio x and the iron/air split ratio b coordinates:

$$x = \frac{D_r}{D} \qquad b = \frac{B_g}{B_{Fe,s}} \tag{4.1}$$

where D_r represents the rotor diameter, B_g denotes the airgap peak flux density, and $B_{Fe,s}$ stands for the stator back iron peak flux density. It's important to note that these definitions assume a sinusoidal flux density distribution at the airgap, as explained later. Note that instead of using J as the electrical loading input, thermal loading can be utilized. Thermal loading is defined as the ratio between the rated copper loss and the stator's outer surface area, expressed in (kW/m^2). From this value, the rated current can be calculated. Choosing between these methods depends on the design specifications. Furthermore, current density is more commonly referenced in literature, while defining copper losses in advance can be more complex. Moreover, keeping J constant generally results in more stable copper losses across the machines on the plane.

The analytical procedure used to obtain these specific quantities is reported. In the initial phase, approximated design equations are employed to estimate the key performance metrics of the motor. The flux equations of a PMSM are presented in (4.2), wherein they are normalized by the number of turns in series per phase N_s.

$$\begin{cases} \dfrac{\lambda_d}{N_s} = \dfrac{L_{md} + L_\sigma}{N_s^2} \cdot (N_s i_d) + \dfrac{\lambda_m}{N_s} \\ \dfrac{\lambda_q}{N_s} = \dfrac{L_{mq} + L_\sigma}{N_s^2} \cdot (N_s i_q) \end{cases} \tag{4.2}$$

The parameters L_{md}, L_{mq}, L_σ, and λ_m represent the magnetizing inductance along the d and q axes, the leakage inductance, and the PM flux linkage, respectively. Their analytical evaluation is elaborated in detail in [101] and [103]. The normalization

by N_s indicates that the design plane illustrates the Ampere-turn function of (x,b) concerning the peak current density J and the Volt-second per turn function of (x,b) concerning the peak flux density B_{Fe}. It's worth noting that these quantities are not yet considered at the machine terminals. The terms L_d and L_q are defined as the sum of the respective magnetizing and leakage inductance.

Key performance metrics are the torque T and power factor $cos(\varphi)$, which are defined as follows:

$$T = \frac{3}{2} p \cdot \left(\lambda_d \cdot i_q - \lambda_q \cdot i_d\right) \tag{4.3}$$

$$cos\varphi = sin(\gamma - \delta) \tag{4.4}$$

Here, p represents the number of pole pairs, while γ and δ denote the current and flux linkage phase angles relative to the d-axis. These angles are related to the corresponding parameters of the torque model. It's important to note that the resistance voltage is neglected in (4.4). On the design plane, torque and power factor are evaluated under MTPA conditions, and they depend on the cross-section geometry represented by D and the coordinates x and b, the stack length L, as well as the peak current density and flux density. Referring to (4.2) and (4.3), it can be observed that, at a given geometry and peak J and B_{Fe}, the torque T remains independent of the number of turns N_s. This characteristic is integral to the proposed design procedure, allowing for the selection and optimization of N_s in the second phase of the design process.

4.1.1 q-axis Design: stator and rotor iron size

The design rules along the q-axis establish the dimensions of the stator back iron and teeth, as well as the size of the rotor flux carriers based on the input (x,b). The geometric parameters are illustrated in Fig. 4.1. Considering a sinusoidal airgap distribution, the one-pole flux can be defined as follows:

$$\Phi_q = \frac{\pi \cdot d \cdot L \cdot B_g}{p} \tag{4.5}$$

where L is the motor stack length.

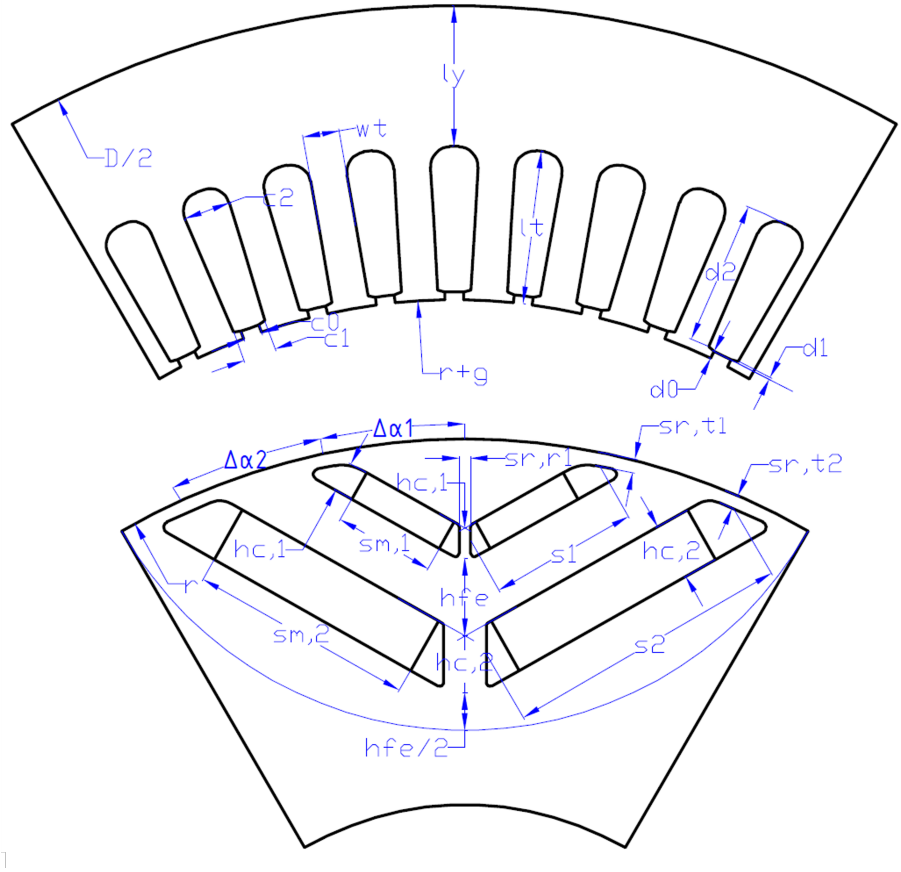

Fig. 4.1 V-shaped rotor and stator parameters.

The $(x \cdot b)$ product can appear substituting (4.1) in the previous equation.

$$\Phi_q = \frac{\pi \cdot D \cdot L \cdot B_{Fe,s}}{p} \cdot xb \tag{4.6}$$

The yoke flux is $\Phi_y = \frac{B_{Fe,s} \cdot ly \cdot L}{k_t}$, neglecting the slot leakage flux, but can also be defined as half of the one-pole flux. So, the determination of the stator yoke size l_y is expressed by (4.7).

$$l_y = \frac{D}{2p} \cdot k_y \cdot x \cdot b \tag{4.7}$$

The reference condition $k_y = 1$ for the non-dimensional yoke-length factor pertains to the scenario where a sinusoidal airgap flux density with amplitude B_g transforms into a back-iron flux density of $B_{Fe,s} = \frac{B_g}{g}$.

Concerning the tooth, its size is determined by the equation (4.8). Here the assumption is to impose the tooth flux $\Phi_t = \frac{B_{Fe}}{k_t} \cdot L \cdot w_t$ equal to the flux in one slot pitch τ_s, where q is the number of slot per pole per phase.

$$w_t = \frac{\pi D}{6pq} \cdot x \cdot b \cdot k_t \tag{4.8}$$

Here, the tooth width factor k_t (4.9) defines the tooth size relative to the yoke size. Typically, a value of $k_t < 1$ is chosen, indicating that the tooth is more saturated than the back-iron [104].

$$k_t = \frac{B_{Fe,s}}{B_{tooth}} \tag{4.9}$$

Regarding the size of the rotor iron paths, the default design condition stipulates that the sum of the flux carriers' size ($l_r = h_{Fe} + \frac{h_{Fe}}{2}$ as defined in Fig. 4.1) is equal to the stator back iron size l_y. In (4.10), the rotor carrier thickness factor $k_{Fe,r}$ is introduced to allow variation in the size of the rotor carriers compared to the default condition. As advice $k_{Fe,r} \geq 1$ can be imposed during the motor design with PM, to better sustain the flux, avoiding iron saturation.

$$k_{Fe,r} = \frac{l_r}{l_y} \tag{4.10}$$

Under this geometric consideration, the width of the permanent magnets is consequently defined, given the hypothesis of assuming a regular pitch to the equivalent rotor slots, as illustrated in the next section.

The Ampere-turns i_q are determined to achieve the desired airgap flux density by neglecting the PM contribution. Equation (4.11) is derived from Ampere's law with ideal iron.

$$N_s i_q = \frac{\pi}{3} \cdot \frac{k_c g}{\mu_0} \cdot \frac{p}{k_w} \cdot B_{Fe,s} \cdot b \tag{4.11}$$

Where N_s represents the number of turns in series per phase, and k_w is the winding factor. Saturation of the q-axis magnetic path is considered by introducing a saturation coefficient $k_{sat} \geq 1$, as defined in [101].

4.1.2 d-axis design: rotor barriers and PMs

The magnetic circuit model, which considers the d-axis magnetomotive force (MMF) and its associated flux components, is depicted in Fig. 4.2. This circuit illustrates half a pole of the machine in the general scenario of n flux barriers.

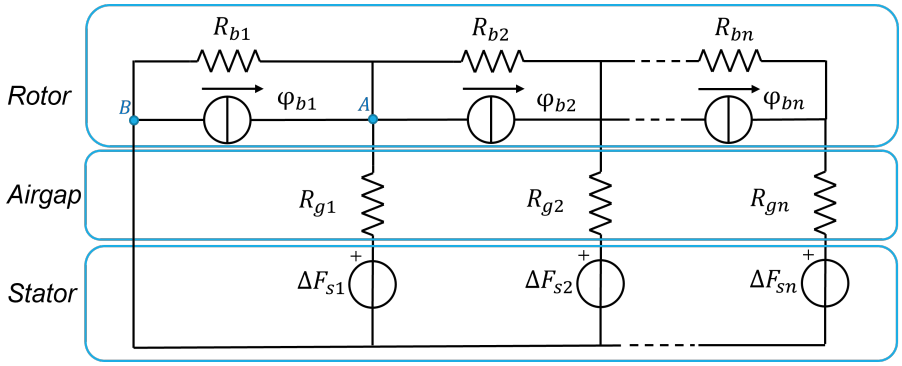

Fig. 4.2 PM Synchronous machine magnetic circuit with multiple rotor barriers.

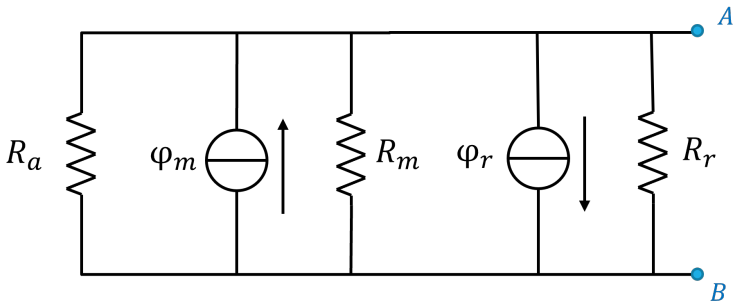

Fig. 4.3 Rotor barrier equivalent circuit.

The stator magnetomotive force (MMF) generated by i_d Ampere-turns is symbolized by the ΔF_s generators within the circuit, following the staircase model outlined in [101]. The j-th MMF step is derived from $N_s i_d$ as per (4.12).

$$\Delta F_{sj} = \frac{3}{\pi} \frac{N_s i_d}{p} k_w \cdot k_{stair,j} \tag{4.12}$$

Here, $k_{stair,j}$ characterizes the step amplitude, with respect to the per-unit MMF staircase, as defined in [101]. The d current component is determined through the vector difference between I_{max} and i_q.

Assuming a regular pitch of the rotor, the airgap reluctance $\mathfrak{R}_g$ is:

$$\mathfrak{R}_g = \frac{2g \cdot k_c}{\mu_0 \cdot \alpha \cdot x \cdot D \cdot L} \tag{4.13}$$

In this expression, g represents the airgap length, k_c is the Carter coefficient, α denotes the airgap angular pitch between two adjacent barriers, and L stands for the stack length.

Analyzing the magnetic circuit of a single barrier (refer to Fig. 4.3), this comprises a PM branch ($\mathfrak{R}_m$ and ϕ_m), an air branch ($\mathfrak{R}_a$) representing the portion of the barrier not occupied by the magnet, and a ribs branch ($\mathfrak{R}_r$ and ϕ_r). The reluctances of these branches are determined as:

$$\mathfrak{R}_a = \frac{h_a}{\mu_0 \cdot s_a \cdot L} \tag{4.14}$$

$$\mathfrak{R}_m = \frac{h_m}{\mu_0 \cdot \mu_m \cdot s_m \cdot L} \tag{4.15}$$

$$\mathfrak{R}_r = \frac{h_r}{\mu_0 \cdot \mu_r \cdot \left(s_{r,t} + \frac{s_{r,r}}{2}\right) \cdot L} = \frac{h_r}{\mu_0 \cdot \mu_r \cdot s_r \cdot L} \tag{4.16}$$

The Norton equivalent at the AB nodes is obtained with (4.17) and (4.18).

$$\mathfrak{R}_b = \left(\frac{1}{\mathfrak{R}_a} + \frac{1}{\mathfrak{R}_m} + \frac{1}{\mathfrak{R}_r}\right)^{-1} \tag{4.17}$$

$$\varphi_b = \varphi_m - \varphi_r \tag{4.18}$$

The magnet flux φ_m and the absorbed total ribs flux φ_r are computed as:

$$\varphi_m = B_r \cdot s_m \cdot L \tag{4.19}$$

$$\varphi_r = B_{sat} \cdot s_r \cdot L \tag{4.20}$$

In these equations, B_r represents the PM remanence at the specified magnet temperature, and $B_{sat} = 2.0$ T denotes the flux density of the saturated ribs.

The circuit is solved by employing the superposition principle. Initially, the rotor flux generators are deactivated, and the flow-through L_{fd} component of L_{md} is determined. Subsequently, the remaining "circulating" component L_{cd}, defined by $L_{md} = L_{fd} + L_{cd}$, is computed following the approach outlined in [101].

In the second step, the stator MMF generators are considered to evaluate the PM flux linkage. The node-voltage analysis leads to the linear system:

$$\underbrace{\begin{bmatrix} \varphi_{b,k} - \varphi_{b,k+1} \\ \varphi_{b,k} - \varphi_{b,k+1} \\ \vdots \\ \varphi_{b,n} \end{bmatrix}}_{\boldsymbol{\Phi}_b} = \underbrace{\begin{bmatrix} \mathfrak{R}_{k,k}^{-1} & \mathfrak{R}_{k,k+1}^{-1} & \dots & 0 \\ \mathfrak{R}_{k,k-1}^{-1} & \mathfrak{R}_{k,k}^{-1} & \dots & 0 \\ \vdots & \vdots & \vdots & \vdots \\ 0 & 0 & \dots & \mathfrak{R}_{n,n}^{-1} \end{bmatrix}}_{\boldsymbol{\mathfrak{R}}^{-1}} \underbrace{\begin{bmatrix} r_1 \\ r_2 \\ \vdots \\ r_n \end{bmatrix}}_{\mathbf{r}} \tag{4.21}$$

$$\mathfrak{R}_{k,k}^{-1} = \mathfrak{R}_{b,k}^{-1} + \mathfrak{R}_{g,k}^{-1} + \mathfrak{R}_{b,k+1}^{-1} \tag{4.22}$$

$$\mathfrak{R}_{k,k+1}^{-1} = -\mathfrak{R}_{b,k+1}^{-1} \tag{4.23}$$

$$\mathfrak{R}_{k,k-1}^{-1} = -\mathfrak{R}_{b,k}^{-1} \tag{4.24}$$

$\boldsymbol{r}$ represents the magnetic potential at the airgap (denoted as the A point), and $\boldsymbol{\mathfrak{R}}$ is the reluctance matrix. It's important to note that k serves as the row index, and the elements that are not defined are considered null. Ultimately, the fundamental PM flux linkage is computed using the relationship (4.25).

$$\lambda_m = 2 \cdot N_s \cdot k_w \cdot k_f \cdot \sum_{k=1}^{n} \frac{r_k}{\mathfrak{R}_{g,k}} \tag{4.25}$$

k_f is used to denote the consideration of the fundamental harmonic only.

4.1.3 Characteristic current computation

A novel contribution is the early computation of the motor characteristic current I_{ch} on the design plane. I_{ch} is defined as in (4.26) and serves as an indicator of the flux weakening capability of the machine. The ratio between the peak and the characteristic current is equal to the ratio of the peak power (at the base speed) and the power at infinite speed (that is the asymptote of the flux weakening region). Note that the machines on the plane are not designed according to constant power range requirements, which are often specified for traction applications, so the selected machine has to be verified afterward.

$$I_{ch} = \frac{\lambda_m}{L_d} \tag{4.26}$$

$$P_{ch} = \frac{3}{2} \cdot V_{dc} \cdot I_{ch} \tag{4.27}$$

The design plane will present the $N_s \cdot I_{ch}$ curves in accordance with the definition in (4.26), along with the method outlined later for correcting the approximate parameters λ_m and L_d.

4.1.4 Peak short circuit current computation

Another innovative feature of the design plane is the estimation of the peak transient short-circuit current (in Ampere-turns) curves. The HWC short-circuit current I_{HWC}, as defined in Chapter 3, corresponds to the peak short-circuit current in a lossless machine and will be utilized here. For a given machine, the HWC current depends on the pre-fault operating point; specifically, the worst pre-fault operating point corresponds to maximum torque and maximum flux linkage λ_{max}. The equation defining I_{HWC} is derived from the magnetic parameters of the motor, is reported here for clarity.

$$\lambda_d(i_d = I_{HWC}, i_q = 0) = -\lambda_{max} \tag{4.28}$$

The analytical expression for the HWC short-circuit current is the following:

$$I_{HWC} = \frac{\lambda_{max}}{L_d} \tag{4.29}$$

Similar to the characteristic current, this equation will be FEA-corrected, as explained later.

4.1.5 Radial ribs size

The size of the k-th radial rib is determined as a function of (x,b) based on the material yield strength σ_y and the according to the analytical approach suggested in [105].The centrifugal force F_j created by the hanging mass m_j rotating at maximum speed n_{max} is determined as in (4.30).

$$F_j = m_j \cdot r_j \cdot n_{max}^2 \cdot \left(\frac{\pi}{30}\right)^2 \tag{4.30}$$

Here r_j defines the radial coordinate related to the j^{th} considered rib of its center of gravity. The required width of the rib can be evaluated as reported in (4.31)

$$s_{r,rk} = \frac{m_j \cdot r_j \cdot n_{max}^2 \cdot \left(\frac{\pi}{30}\right)^2}{L \cdot \sigma_y} \tag{4.31}$$

The goal of this procedure is to design a plane in with each machine have the same mechanical stress at the maximum speed.

4.1.6 FEAfix correction

The inaccuracy in the analytical model is attributed to iron saturation and dq cross-saturation. The FEAfix calibration approach involves applying corrective factors across the (x,b) plane, which are computed through a small number of selected FEA simulations. In the following process, 16 points (representing 16 design cross-sections) arranged in a 4x4 regular grid are chosen as FEA-computed designs with precisely known parameters. The correction factors are determined at these grid points and then extended over the design plane using bi-linear interpolation. To expedite the process, the FEAfix cases are computed in parallel to reduce computational time. For each considered FEAfix cross-section, the MTPA current γ angle is found iteratively. The correction factors are defined as:

$$\begin{cases} k_d = \dfrac{\lambda_d^{FEA}(i_d, i_q) - \lambda_d^{FEA}(0,0)}{\lambda_d^{model} - \lambda_m^{model}} \\ k_q = \dfrac{\lambda_q^{FEA}(i_d, i_q)}{\lambda_q^{model}} \\ k_m = \dfrac{\lambda_d^{FEA}(0,0)}{\lambda_m^{model}} \\ k_{ch} = \dfrac{i_{ch}^{FEA}}{i_{ch}^{model}} \\ k_{HWC} = \dfrac{i_{HWC}^{FEA}}{i_{HWC}^{model}} \end{cases} \tag{4.32}$$

In the notation used, the superscript FEA identifies the results of the FEA simulations, while the superscript $model$ represents the results of the analytical model underlying the design plane. The correction factors are denoted as k_d for d-axis flux linkage (armature contribution), k_q for the q-axis flux linkage, k_m for the PM flux linkage, k_{ch} for the characteristic current, and k_{HWC} for the HWC short-circuit current. The first three factors are computed through an iterative search for the MTPA point (i_d, i_q) plus one open-circuit simulation. The FEA investigation of I_{ch} also requires iterations: the zero current simulation used for the PM flux linkage and k_m serves as the starting point, while subsequent simulations impose increasing currents to obtain null flux linkage along the PM axis. A similar method is adopted to FEA-compute the correct HWC current. As explained in [106], an iterative secant method is employed to solve (4.28). Subsequently, the factor k_{HWC} is computed using this FEA-evaluated HWC current.

In Tab 4.1 the default number of FEA simulations required for each FEAfix point on the (x,b) design plane is reported. Generally, with these parameters, the iterative algorithms used converge. Note that each function can be deactivated, but the MTPA search is strongly recommended.

The baseline version on the design plane is illustrated in Fig. 4.4. In this representation, the two primary performance metrics (torque and power factor) are depicted as contours over the (x,b) domain. The green points correspond to the 16 motors simulated according to the FEAfix procedure. In this context, the correction factors

Table 4.1 FEA simulations required for each FEAfix point on the design plane.

Evaluation type	# FEAs	Correction factor
MTPA search	up to 20	k_d, k_q
PM flux linkage	1	k_m
Characteristic current	up to 10	k_{ch}
HWC short circuit current	up to 10	k_{HWC}

are computed using FEA and then extrapolated to the entire design plane through bilinear interpolation.

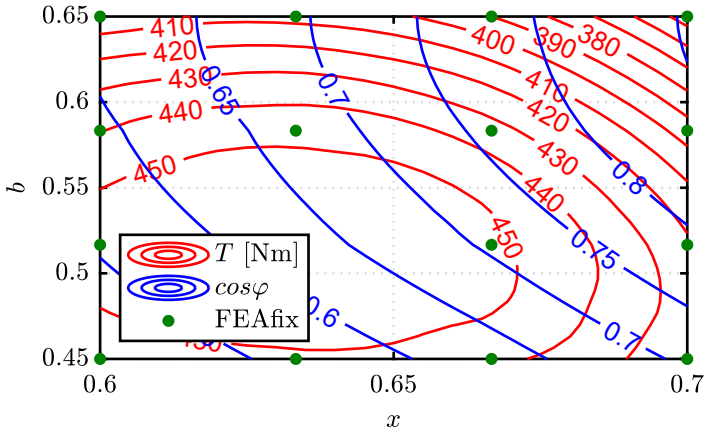

Fig. 4.4 (x,b) design plane: torque T (red conturs) and power factor $cos\varphi$ (blue conturs) function of (x,b). FEAfix points are indicated by the green dots.

The plot in Fig. 4.4 represents the standard format of the design plane generated by default from SyR-e. Beyond showcasing torque and power factor contours, the figure contains additional information stored for various current components, flux linkages, and FEAfix factors. This comprehensive dataset allows for several considerations and post-processing elaborations that form the basis of the design procedure. Moreover, it is possible to instantaneously:

- perform axial scaling as reported in Chapter 5;
- compute the motors performance considering the numbers of turns in series per phase N_s.

To visualize how the machine geometry varies along the design plane, the cross-sections of the machines at each corner are illustrated in Fig.4.5.

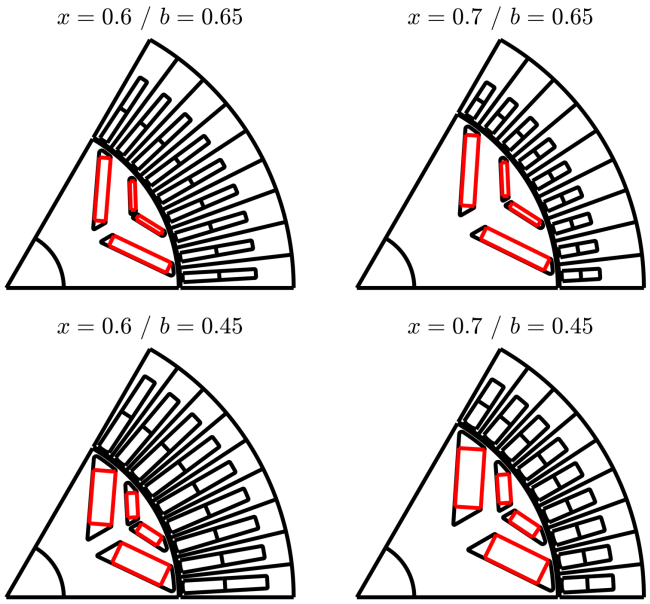

Fig. 4.5 Example of machines at the design plane corners.

4.1.7 Demagnetization analysis

In the design plane, demagnetization is preliminarily assessed at two reference current levels:

- I_{max} at MTPA, ensuring the motor can operate under peak torque conditions;
- I_{HWC}, representing short-circuit conditions.

For each FEAfix design, one dedicated FEA simulation is conducted per current value, and the flux density at each mesh element of the PMs is recorded. If the flux density falls below the knee point of the BH curve of the material, the node is flagged as demagnetized. The outcome of the simulation is the percentage of demagnetized PM volume. Once again, the demagnetization index computed for the 16 FEAfix designs is then extended over the (x,b) plane via interpolation.

4.1.8 Design plane results manipulation

Once the design plane is assessed, its data can be analyzed to facilitate the selection of the most suitable machine for the intended application. The power factor specification

is derived from the specified peak power request and maximum current. Initially, the (minimum) base speed required to meet both T and P targets is determined as:

$$n_{base} = \frac{30}{\pi} \cdot \frac{P_{max}}{T_{max}} \tag{4.33}$$

corresponding to $n_{base} \geq 4775$ rpm for the chosen design. Then, the maximum power associated with this speed value is calculated as:

$$P_{max} = \frac{\sqrt{3}}{2} \cdot V_{dc} \cdot I_{max} \cdot cos\varphi_{base} \cdot \eta \tag{4.34}$$

where η represents the efficiency (which is unknown at this stage). The target power factor is calculated as:

$$cos\varphi_{base} \geq \frac{2}{\sqrt{3}} \frac{P_{max}}{V_{dc} \cdot I_{max} \cdot \eta} \tag{4.35}$$

Assuming a unitary efficiency, the target power factor associated with the data presented in Table 5.1 is approximately 0.7. If the efficiency is lower, a slightly higher target power factor is necessary.

The peak torque and power requirements are consolidated into the torque and power factor constraints specified in (4.36):

$$\begin{cases} T(x,b) \geq T_{max} \\ cos\varphi(x,b) \geq cos\varphi_{base} \end{cases} \tag{4.36}$$

These constraints will delineate two corresponding regions of feasibility within the (x,b) domain.

4.1.9 Selection of the number of turns

A crucial step in selecting a candidate design from the (x,b) plane is determining feasible numbers of turns. This decision must consider the limits of the inverter, the performance metrics (as indicated on the design plane), and the geometric constraints of the motor. If hairpin windings are utilized, as in the benchmark, the feasible number of turns is further constrained, making fine-tuning of this parameter challenging. The number of conductors per slot is limited to an even number, typically below 10, with strict limitations on the number of parallels [60, 61].

For the N_s selection, two quantities are crucial: the ampere-turns contours $N_s \cdot I$ and the flux contours $\frac{\lambda}{N_s}$. These are directly derived from the input current density of the design plane J and the motor geometry. Both quantities are fundamental for considering current and voltage constraints.

To satisfy the current constraint, the design current (computed from the J input) must be less than or equal to the inverter limit. Taking into account the number of turns, this constraint can be expressed as:

$$N_s \cdot I(x,b) \leq N_s^* \cdot I_{max} \tag{4.37}$$

where N_s^* represents an imposed and feasible number of turns.

Regarding voltage, the process is slightly more intricate. Compliance with the voltage limit is expressed as:

$$V_{dc} = n_{base} \cdot p \cdot \frac{\pi}{30} \cdot \lambda_{max} \tag{4.38}$$

where p represents the number of pole pairs, and λ_{max} is the peak flux linkage, typically attained under peak torque conditions at base speed (the operating point evaluated on the design plane). This equation translates the inverter voltage constraint into a flux linkage limit, provided that the base speed requirement (4.33) is met. With an imposed feasible number of turns N_s^*, the voltage constraint is then expressed as:

$$\frac{\lambda}{N_s}(x,b) \leq \frac{\lambda_{max}}{N_s^*} = \frac{V_{dc}}{p \cdot n_{base} \cdot \frac{\pi}{30} \cdot N_s^*} \tag{4.39}$$

Ultimately, for each feasible number of turns N_s^*, a feasibility region can be delineated on the (x,b) plane, in accordance with (4.37) and (4.39), as will be illustrated later through case studies.

4.2 Case studies

The design plane is employed to compare an NdFeB IPM motor and a ferrite PM-SyR motor during the design phase. They are derived from the specifications of the Tesla Model 3 3D6 motor [107], detailed in Table,4.2, with its cross-section depicted

in Fig. 4.6. Both motors are configured identically to the baseline design: 3 pole pairs and 54 slots, utilizing hairpin winding. To enhance anisotropy, the IPM rotor features two layers and a V-type geometry, while the PM-SyR rotor incorporates three circular barriers with arc PMs. Both designs adhere to the same current density requirements of 23 A/mm^2, ensuring comparable thermal behavior.

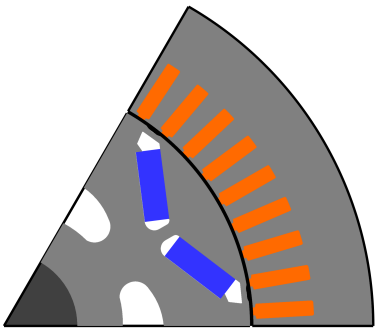

Fig. 4.6 Cross-section of the benchmark, inspired by the Tesla Model 3 3D6.

Table 4.2 Tesla Model 3 3D6 ratings

Peak torque	T_{max}	440	[Nm]
Peak power	P_{max}	220	[kW]
Maximum speed	n_{max}	18100	[rpm]
DC link voltage	V_{dc}	320	[V]
Peak phase current	I_{max}	1131	[A]
Stator outer diameter	D	225	[mm]
Stack length	L	114	[mm]
Airgap length	g	0.7	[mm]
Number of pole pairs	p	3	
Number of slot/pole/phase	q	3	

Regarding feasible numbers of turns, only three combinations are considered:

- $N_s = 9$: 4 conductors per slot with 4 parallel paths;
- $N_s = 12$: 4 conductors per slot with 3 parallel paths;
- $N_s = 18$: 4 conductors per slot with 2 parallel paths.

4.2.1 NdFeB motor

The design plane of the IPM motor with NdFeB PMs is depicted in Fig. 4.7c, where FEA-evaluated machines are denoted by green circles. The plane is computed under hot conditions (80°C), which are the most critical for these PMs in terms of demagnetization strength. For readers' clarity, this figure is split in two:

- in Fig. 4.7a torque and power factor contours are shown in red and blue, respectively, with the target specification highlighted by bold lines. The feasibility area in terms of T and $\cos\varphi$, defined in (4.36), is marked in green. Motors outside this green area cannot meet torque and power specifications given the dimensions and current density.

- Fig. 4.7b regards the selection of the number of turns. It's observed that $N_s = 12$ and $N_s = 18$ are present on the plane (light blue and purple areas), while the $N_s = 9$ solution is not feasible. To clarify, the feasibility region is determined by the relations in (4.37) and (4.39). The $N_s I_{max}$ plot represents the loci where the two terms in (4.37) are equal. Therefore, for a given feasible N_s, the inequality is satisfied in the entire region above the corresponding contour. Accordingly, λ_{max}/Ns plot represents the loci where the two terms in (4.39) are equal, but the region that satisfies the relation lies below the corresponding number of turns contour. The intersection where the two constraints meet represents the feasibility area for the considered feasible number of turns according to inverter current and voltage limits.

However, only the purple area intersects the green feasibility area, so 18 turns are chosen for the IPM motor. As discussed earlier, further performance figures can be considered before selecting a motor. For example, Fig. 4.7d illustrates the characteristic current and HWC short-circuit current contours, represented in per-unit of the design current (i.e., the one computed from the J input), while the color map indicates the percentage of PM volume demagnetized at this operating current. Notably, no demagnetization occurs for the IPM motor, so the demagnetization limit does not constrain the plane. The characteristic current increases from the bottom left to the top right of the plane, suggesting that high-speed power will be higher in this region. Similarly, the peak short-circuit current exhibits a similar trend, with values at least double the pre-fault current.

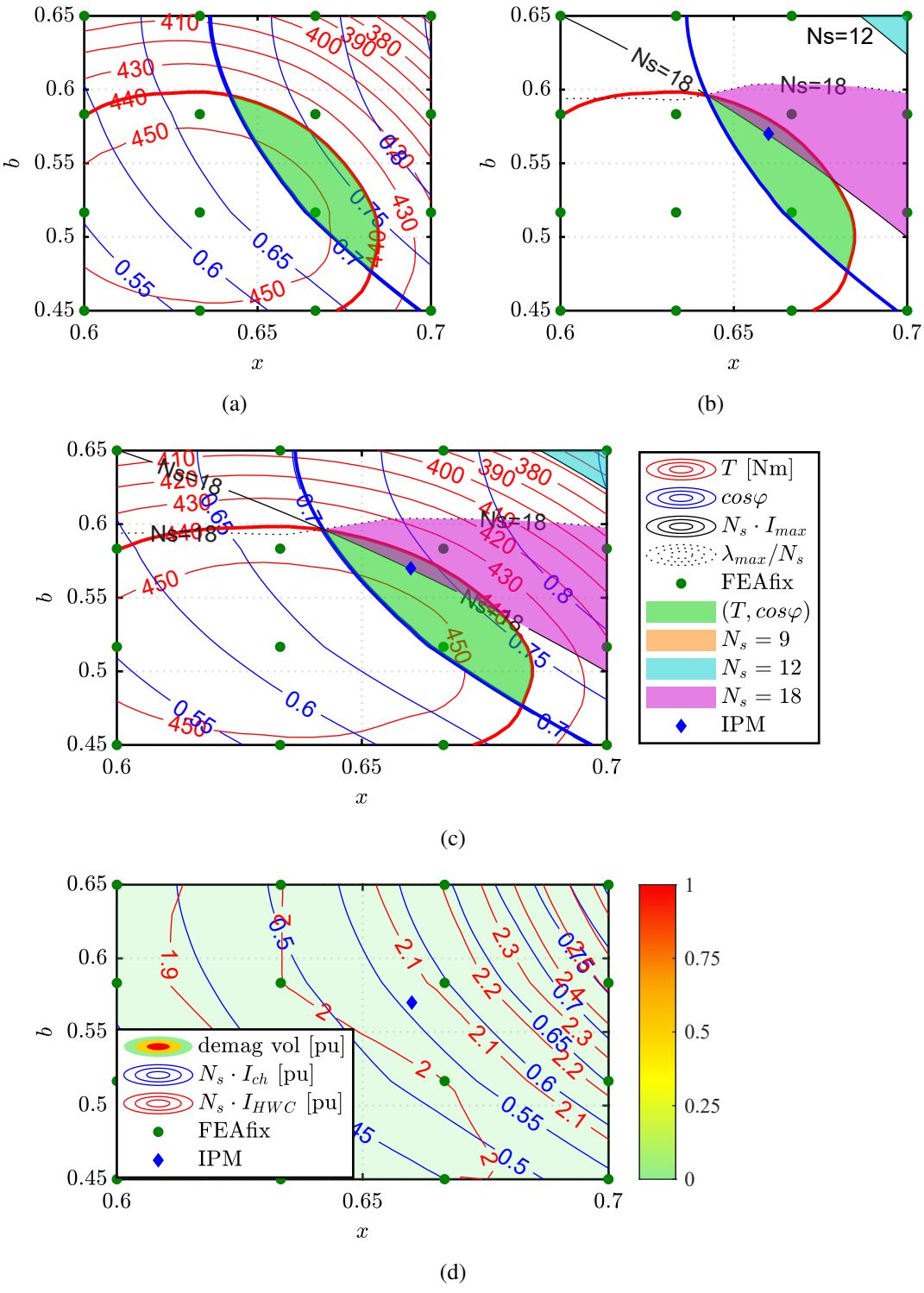

Fig. 4.7 Design planes of the IPM motor: (a) T, $cos\varphi$ and (b) number of turns feasibility areas according (4.36), (4.37) and (4.39); (c) merge of (a) and (b) ;(d) characteristic current, HWC current and demagnetization at rated current. Refers to (c) for the legend of (a) and (b) figures.

Ultimately, the IPM motor is selected at the point marked with a blue diamond, where the feasibility areas overlap. This point lies along the current limit contour, ensuring that the inverter's maximum current I_{max} matches the current imposed by the current density J. Additionally, at this point, torque and power factor margins are achieved, with a torque of 444 Nm and a power factor of 0.74. The motor will not demagnetize either during operating conditions or in HWC conditions, as indicated in Table 4.3. The characteristic current at this point is slightly higher than 55% of the rated current, implying that in deep flux weakening conditions, the output torque will be nearly halved. As for the short-circuit current, its value is slightly higher than twice the pre-fault current, which is the best achievable value within the $(T, \cos\varphi, N_s)$ feasibility area.

4.2.2 Ferrite motor

The design plane of the PM-SyR motor with ferrite PMs is evaluated using the same input as the IPM motor, and it is shown in Fig. 4.8.

The only distinction lies in the PM temperature, which is set at 20°C for the PM-SyR motor to account for the worst demagnetization scenario. Two critical aspects emerge here. Firstly, there is no combination of T and $cos\varphi$ that satisfies (4.36). Secondly, all the motors exhibit PMs completely demagnetized at the operating current. To address this issue, considering the weaker PMs utilized, several strategies need implementation. Initially, the input current density J is reduced to 20 Arms/mm^2, and the ratio between rotor barrier thickness and rotor carrier thickness is adjusted to increase the PM thickness and alleviate the demagnetization concern. The value of the new J and the decision to increase the PM thickness by about 50% are arbitrary choices. Subsequently, the design plane is recomputed with these updated inputs, as depicted in Fig. 4.9.

At this point, resolving the demagnetization issue at the operating current is achieved, at least in certain regions of the design plane, enabling consideration of the other design targets. As depicted in Fig. 4.9, the torque and power factor still fall below the required levels, indicating the necessity to overcome some design constraints.

The torque requirement is addressed through the rapid axial scaling procedure applied to the plane. The overlength ratio is roughly computed as the ratio between

the target torque and the torque contours in the non-demagnetized area, resulting in a stack length of 211 mm. This satisfies the torque specification, but adjustments are necessary for the target power factor as well. Consequently, the inverter size is augmented, thereby reducing the target power factor imposed by the power specification. The new maximum current I_{max} is raised to 1100 Arms. The extra-current ratio is approximately computed as the ratio between the target power factor (for the initial inverter limit) and the power factor in the non-demagnetization area of Fig. 4.9b.

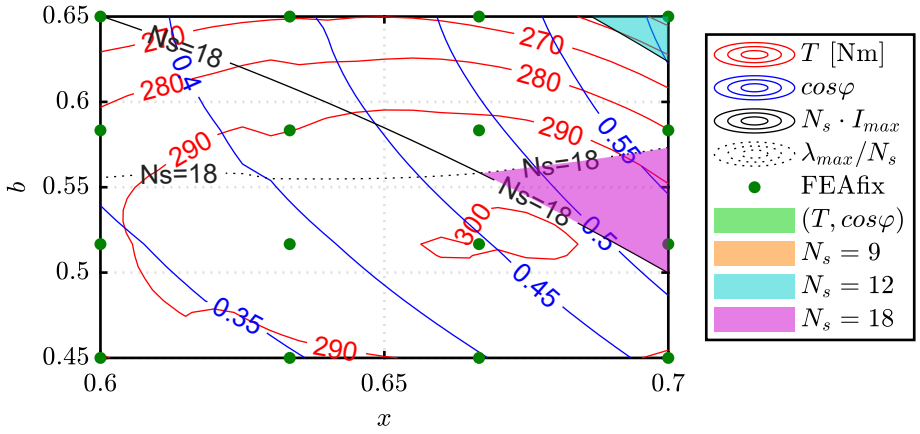

(a)

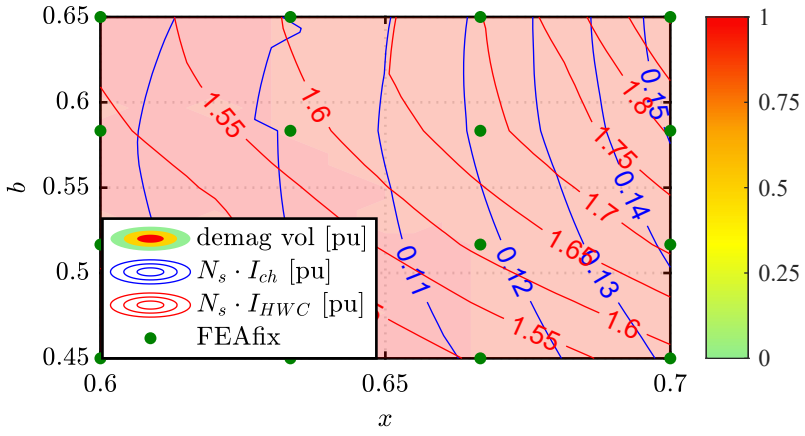

(b)

Fig. 4.8 Design planes of the PM-SyR motor with the same design inputs of IPM motor: (a) T, $cos\varphi$ and feasibility areas according (4.36), (4.37) and (4.39); (b) characteristic current, HWC current and demagnetization at rated current.

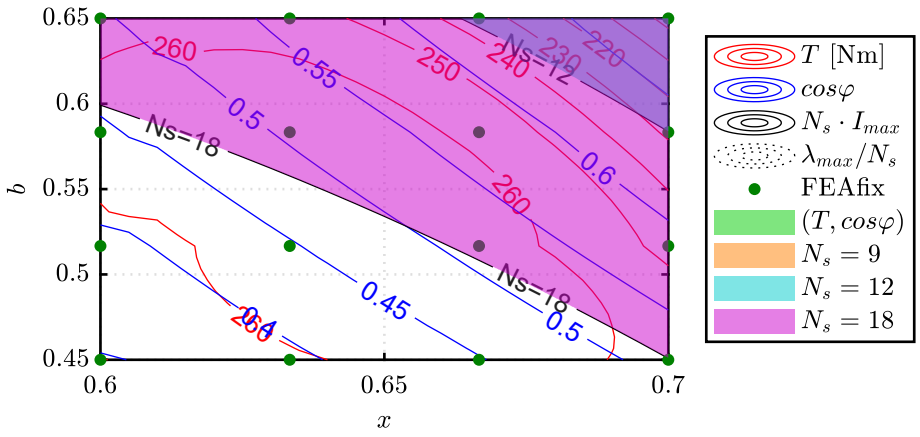

(a)

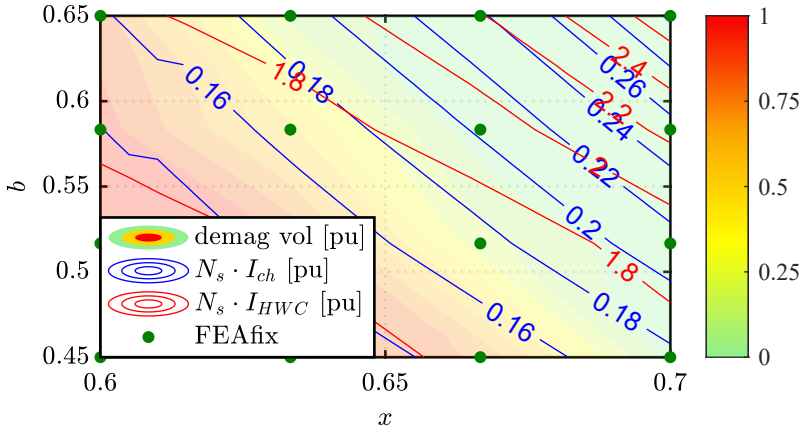

(b)

Fig. 4.9 Design planes of the PM-SyR motor with reduced current density and thicker PMs: (a) T, $cos\varphi$ and feasibility areas according to (4.36), (4.37) and (4.39); (b) characteristic current, HWC current and demagnetization at rated current.

The final PM-SyR design plane is presented in Fig. 4.10. It's notable that the green area in Fig. 4.10 is visible, indicating feasibility, while the demagnetization behavior and the characteristic and HWC current remain unchanged from the axial scaling. At this stage, the PM-SyR motor (denoted by a red diamond) is selected close to the torque limit, within the feasibility area of $N_s = 9$. This selection provides a small margin in current (not precisely coinciding with the limit) and a substantial margin in terms of power factor and voltage limits. These characteristics will enable meeting torque specifications with either no margin or very limited margin and power specifications with a wider margin. Regarding the demagnetization issue,

the motor is secure at the operating current but vulnerable in a short circuit. The characteristic current is approximately 1/4 of the operating current, implying that in flux weakening, the PM-SyR motor will perform worse than the IPM motor (which has a characteristic current of almost half the design current). The short-circuit overcurrent is similar to the IPM motor, even though the PM contribution is lower, owing to the higher anisotropy of the PM-SyR machine.

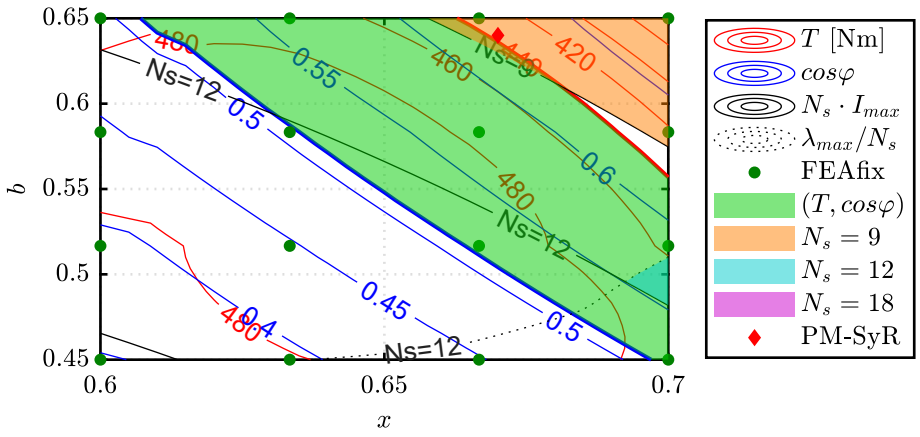

(a)

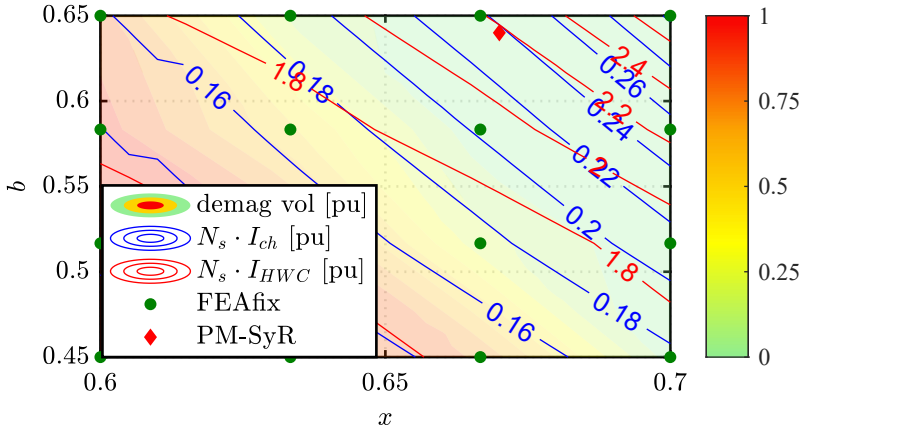

(b)

Fig. 4.10 Design planes of the PM-SyR motor with final stack length and peak current: (a) T, $cos\varphi$ and feasibility areas according (4.36), (4.37) and (4.39); (b) characteristic current, HWC current and demagnetization at rated current.

4.3 Selected design comparison

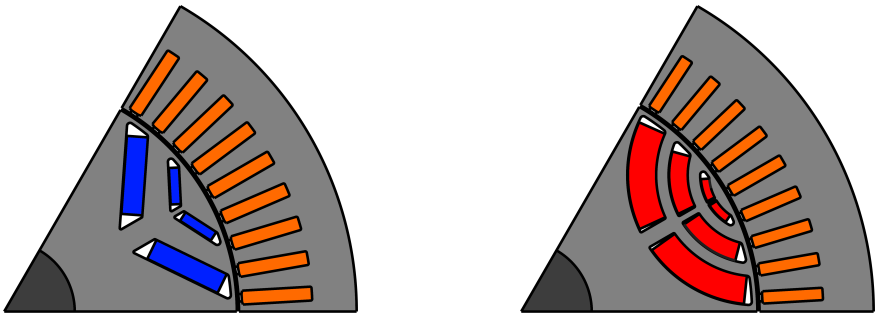

(a) (b)

Fig. 4.11 Cross sections of the designed machines : (a) PMSM and (b) PM-SyR motor

The selected machine cross-sections are depicted in Fig. 4.11, and their specifications are detailed in Tab. 4.3. Both motors meet the torque and power specifications, with the distinction that the PM-SyR motor is 47% longer than the IPM motor and requires an inverter with a peak current 37.5% higher. The torque versus speed and power versus speed curves are illustrated in Fig. 4.12. The blue and red curves represent the IPM and PM-SyR limits, respectively, while the design targets are denoted with dashed black lines. The design margin evident on the plane is apparent in these plots. For the IPM motor, there was a torque margin, as visible in Fig. 4.12a, and a slightly wider power factor margin, which boosts the output power of this motor beyond the design goal. Conversely, the PM-SyR motor exhibited slightly lower torque on the design plane but had wide current and power factor margins. The current margin compensates for the torque output, while the power factor margin enhances the base speed and maximum power. In terms of power during flux weakening, the IPM motor outperforms the PM-SyR motor, as anticipated from the different characteristic currents.

It's important to note that the PM-SyR motor was selected with these margins to address the demagnetization limit, which is another significant issue with ferrite PMs. In fact, the IPM motor with NdFeB PMs is resistant to demagnetization even in a short circuit, whereas the ferrite PM-SyR motor demagnetizes if a short circuit occurs.

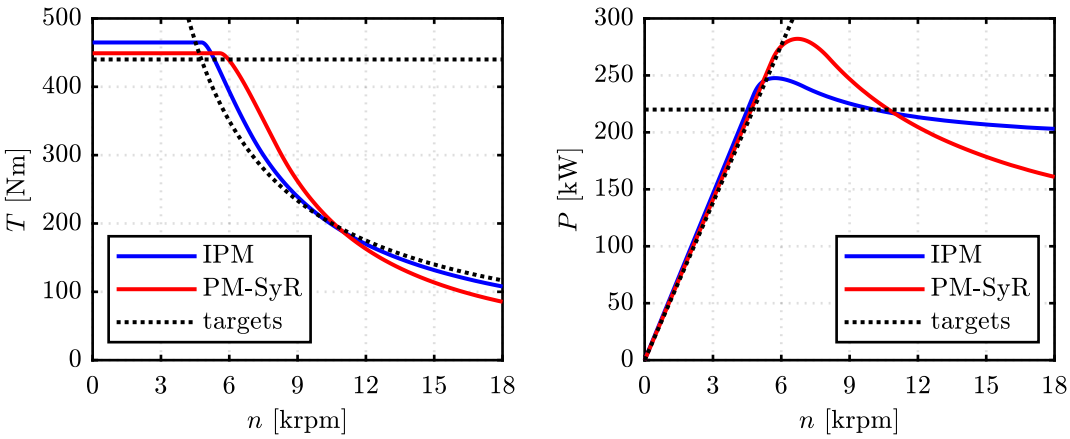

Fig. 4.12 Operating curves of the two motors at maximum inverter limits: (a) torque and (b) power.

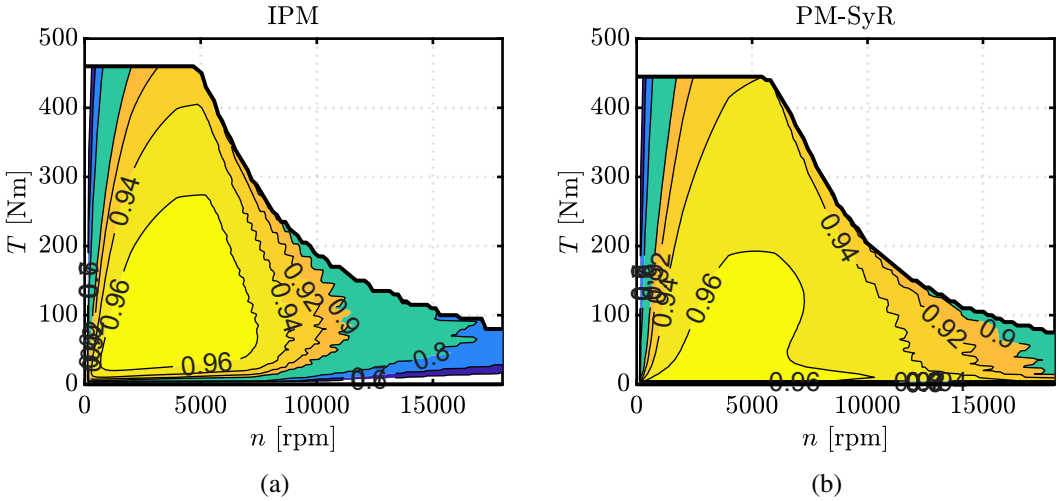

Fig. 4.13 Efficiency map: (a) IPM and (b) PM-SyR motors.

Table 4.3 Designed motor specifications comparison.

		IPM	PM-SyR	
	x	0.66	0.67	
	b	0.57	0.64	
Stator outer diameter	D	225	225	[mm]
Stack length	L	114	211	[mm]
Peak torque	T	444	437	[Nm]
Power factor	$cos\varphi$	0.74	0.62	
Peak power	P	225	256	[kW]
Base speed	n_{base}	4845	5593	[rpm]
DC link voltage	V_{dc}	320	320	[V]
Peak phase current	I_{max}	1131	1556	[Apk]
Number of turns	N_s	18	9	
Characteristic current	I_{ch}	632	357	[Apk]
HWC current	I_{HWC}	2329	3273	[Apk]
Demag vol @ I	dPM_0	0%	0%	[pu]
Demag vol @ I_{HWC}	dPM_{HWC}	0%	100%	[pu]

Chapter 5

Flux-map-based scaling of PM synchronous motors

Irrespective of the chosen design methodology, the inception of a new synchronous motor design often involves starting from an existing design with different dimensions and ratings. Employing scaling laws is a well-established engineering practice, where similitude laws enable the assessment of a new machine with larger or smaller dimensions without incurring an increase in computational time. In [108], the authors specifically focus on the magnetic scaling of PMSMs, including variations in stack outer diameter, active length, and the number of turns. This analysis was subsequently expanded upon in [109] to include the fast scaling of the efficiency maps of the machine. In this Chapter, the application of existing magnetic scaling laws is improved to achieve accurate and optimized designs for new PMSMs, considering specified dimensional constraints (stack diameter and length) and power converter constraints (phase current and DC voltage limits). In addition to evaluating the performance and efficiency maps of scaled designs efficiently, the method enables the minimization of the new machine's volume. The work also delves into the structural and thermal aspects of the scaled design. In contrast to the oversimplified assumption of a constant heat exchange coefficient between the stack and the coolant as presented in [110], improvements are introduced by providing guidelines for scaling the cooling jacket and analytically evaluating the thermal limit of the resulting machine. The electric motor from the BMW i3, as illustrated in the cross-section in Fig. 5.1, serves as the baseline design for this study. It is scaled to align with the specifications of the moto-generator 2 (MG2) of the Toyota Prius Gen IV in two

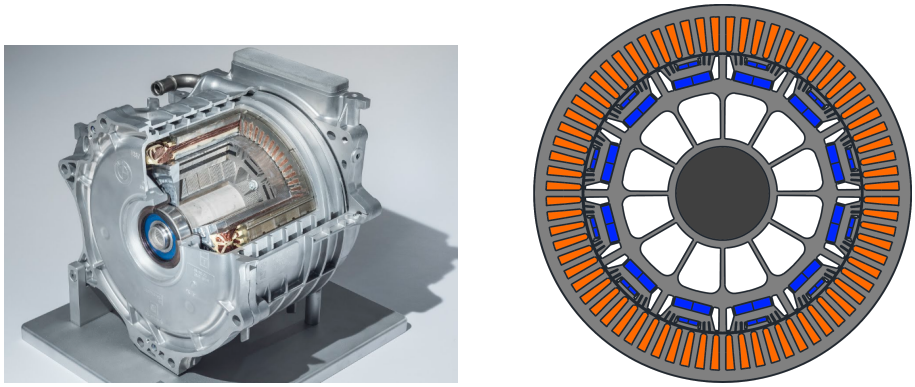

(a) (b)

Fig. 5.1 BMW i3 Traction Electric Motor Type EMP242 of 2016: (a) Machine cut-off; (b) Cross section of the active parts.

Table 5.1 BMW i3 and Prius Gen IV MG2 motor ratings [29]

		i3	Prius MG2	
Max current	I_{max}	530	226	[Apk]
Max torque	T_{max}	250	163	[Nm]
DC link voltage	V_{dc}	355	600	[V]
Nominal speed	n_{nom}	4500	3500	[rpm]
Max speed	n_{max}	11400	17000	[rpm]
Max power	P_{max}	125	53	[kW]
Number of pole pairs	p	6	4	
Outer diameter	D	242	215	[mm]
Stack length	L	132	60	[mm]
Volume	V	6.1	2.2	[L]
Number of turns	N_s	18		

case studies: one maintaining the outer diameter and aspect ratio of the target Prius machine (Mot2), and another with a smaller diameter, as suggested by the stress limit at maximum operating speed (Mot1), as depicted in Fig. 5.2. The specifications of the considered machines are detailed in Tab. 5.1 [29]. The proposed method defines the three scaling factors:

$$k_D = \frac{D}{D_0} \qquad k_L = \frac{L}{L_0} \qquad k_N = \frac{N_s}{N_{s0}} \tag{5.1}$$

These parameters represent the ratio of the outer stator diameter D, stack length L, and the number of turns in series N_s to the corresponding quantities of the reference

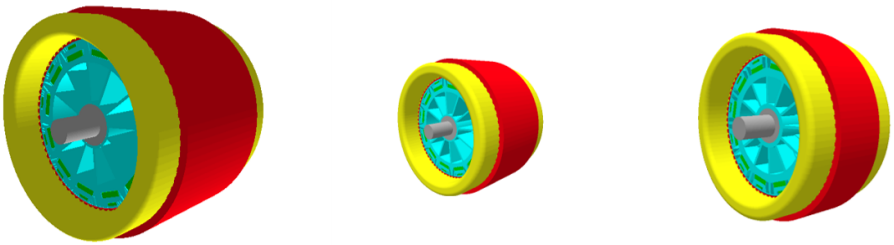

(a) (b) (c)

Fig. 5.2 (a) BMW i3 reference; (b) Scaled Mot1; (c) Scaled Mot2.

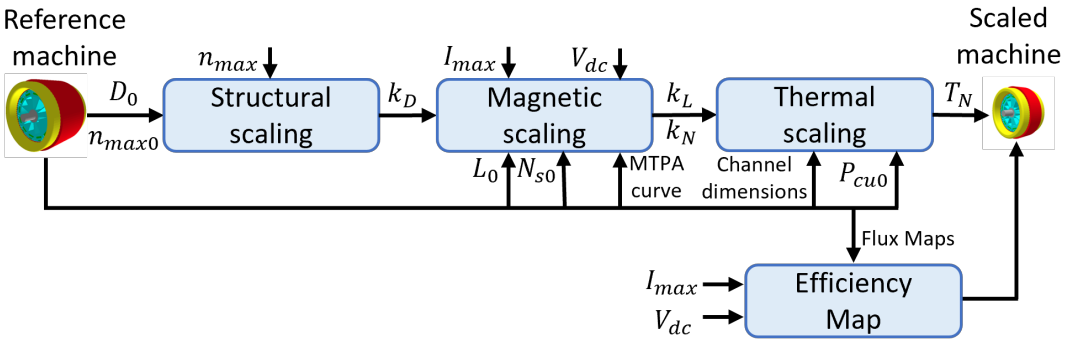

Fig. 5.3 Scaling procedure flowchart.

machine denoted with the subscript 0. Length scaling and rewinding are established procedures governed by intuitive linear relationships. Radial scaling involves the assumption that all cross-sectional dimensions are scaled based on the stator outer diameter ratio k_D, and the distribution of the flux density field remains consistent when the current density is scaled with the diameter [108]. The flowchart outlining the proposed method is depicted in Fig. 5.3.

5.1 Structural scaling

The initial consideration is given to structural scaling due to its direct influence on the diameter ratio, taking into account the maximum operating speed. Examining the rotor illustrated in Fig.5.4 rotating at its maximum speed n_{max}, the force generated by the suspended mass m positioned radially at R_m is supported by the highlighted ribs with a combined cross-sectional area equal to $(A_1 + A_2)$. The resulting mechanical

stress is equal to:

$$\sigma_{max} = \frac{F}{A_1 + A_2} = \frac{(\frac{\pi}{30})^2 \cdot m \cdot R_m \cdot n_{max}^2}{A_1 + A_2} \propto D^2 n_{max}^2 \tag{5.2}$$

The stress scaling rule at maximum speed can be expressed as follows:

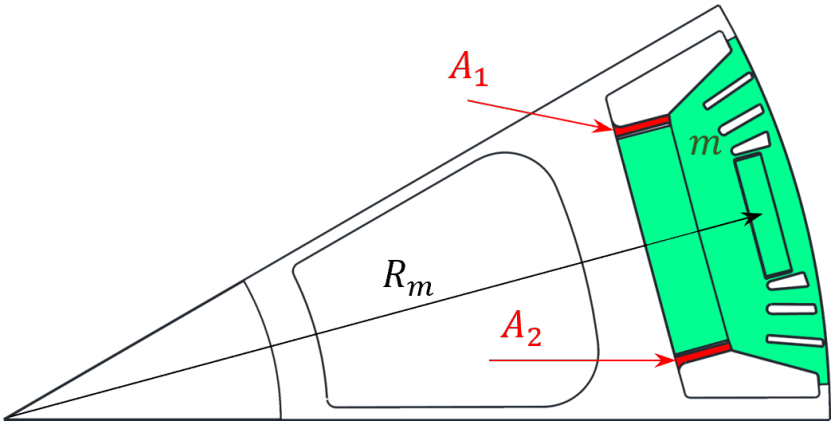

Fig. 5.4 Structural PMSM rotor behavior: the ribs highlighted in red must sustain the hanging mass (green).

$$\frac{\sigma_{max}}{\sigma_{max0}} = \frac{D^2 \cdot n_{max}^2}{D_0^2 \cdot n_{max0}^2} \tag{5.3}$$

This implies that, under constant stress conditions, the diameter ratio behaves inversely to the speed ratio. Assuming the stress limit remains unchanged after scaling, the required diameter ratio is determined by the ratio of maximum operational speeds:

$$k_D = \frac{n_{max0}}{n_{max}} \tag{5.4}$$

The mechanical assessment of the reconstructed benchmark model involves conducting structural analyses using the built-in SyR-e tool. This tool is based on the Matlab Partial Differential Equation (PDE) Toolbox, enabling the solution of differential equations through Finite Element Analysis. The custom geometry is imported from the FEMM file, and mechanical properties in each region are defined based on the material, such as iron, air, or magnet. Boundary conditions are then fixed, and a centrifugal load is applied at the specified input speed. Additionally, the mesh size can be manually adjusted, with the default setting being one order of magnitude lower than the drawing tolerance. The simulation output provides stress results, as

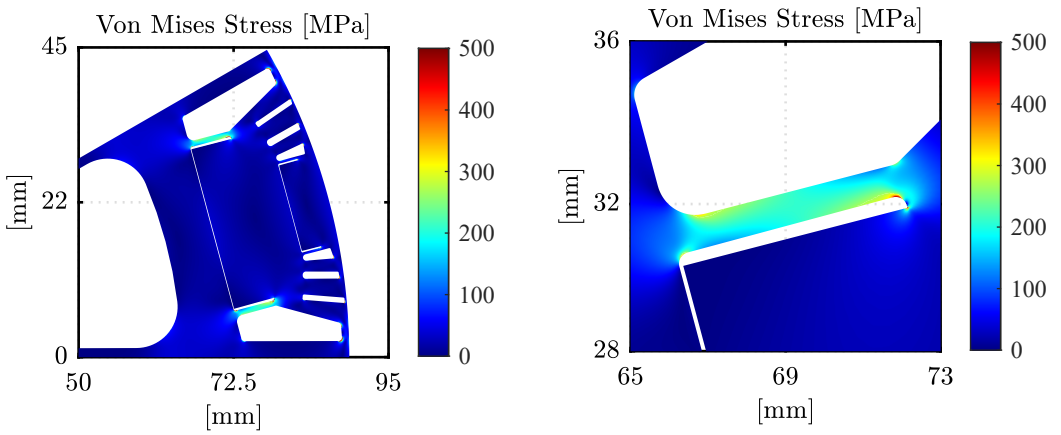

(a) (b)

Fig. 5.5 Mechanical FEA results on BMW i3 at 11400 rpm.

illustrated in Fig. 5.5. The structural analysis, conducted at the maximum speed of 11400 rpm, ensures the integrity of the rotor.

5.2 Flux maps scaling

The magnetic scaling laws from [108] are now referenced, applied to the flux and loss maps of the entire reference machine, rather than just a single operating point (e.g., nominal). In Fig. 5.6, flux maps of the reference machine are depicted, obtained through multi-step Finite Element Analysis simulations on a regular current grid in the dq plane. To expedite the evaluation process, transient FEA is replaced by magneto-static 2D FEA with sequenced rotor positions. Additionally, geometric and electric symmetry is leveraged, and parallel computing is employed to further accelerate the assessment. The average dq flux linkage, torque average, and peak-to-peak torque values from the corresponding simulated points are stored in matrices. For the evaluation of the reference machine, a current grid of 15x15 points was utilized, with each point evaluated at 15 rotor positions spanning 60 electrical degrees. This entire process was completed in less than 15 minutes using a workstation equipped with an Intel Xeon E5-2690 v4 CPU, 14 cores, and 32GB RAM. The variations in the d and q flux maps are described as follows:

$$\frac{\lambda_d(i_d,i_q)}{\lambda_{d0}(i_{d0},i_{q0})} = k_N k_L k_D \qquad \frac{\lambda_q(i_d,i_q)}{\lambda_{q0}(i_{d0},i_{q0})} = k_N k_L k_D \tag{5.5}$$

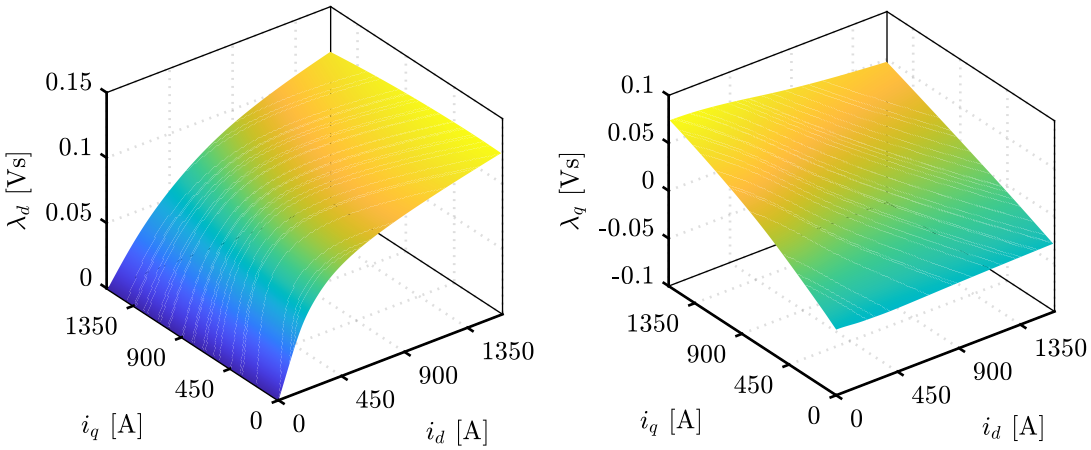

(a) (b)

Fig. 5.6 Reference machine flux maps: (a) d flux linkage and (b) q flux linkage.

assuming that the current components are remapped to maintain the distribution of magnetic flux density, wherein the current density is adjusted in accordance with the diameter, as outlined in [108]:

$$\frac{i_d}{i_{d0}} = k_D k_N^{-1} \qquad \frac{i_q}{i_{q0}} = k_D k_N^{-1} \tag{5.6}$$

In (5.5), the terms related to end-winding flux linkage are omitted for simplicity. However, they can be considered by applying the scaling law applicable to inductances, as reported in [108]. Consequently, the electromagnetic torque map, which is the product of flux linkage and current, undergoes scaling and remapping as follows:

$$\frac{T(i_d, i_q)}{T_0(i_{d0}, i_{q0})} = k_D^2 k_L \tag{5.7}$$

It's important to note that the domain of the flux maps for the reference machine should be sufficiently large to cover the maximum Ampere-turns condition of the target machine.

5.3 Losses scaling

The iron loss map of the reference motor is presented in Fig. 5.7. Each (i_d, i_q) point in the FEA simulation covers a rotor excursion of 180°, leveraging the symmetry properties of alternated waveform to extract information over the entire electrical period. The iron loss computation takes into account both major and minor hysteresis loops, as well as the DC bias effect in the case of the rotor. The loss maps are obtained with a current grid of 15x15 points, each assessed at 180 rotor positions spanning 180 electrical degrees, with the evaluation taking approximately 90 minutes on the reference workstation. Considering that the (i_d, i_q) domain is scaled for flux density conservation, the iron loss maps are scaled with the volume of the stack, i.e., according to D^2L. The same scaling law applies to PM loss.

$$\frac{P_{Fe}(i_d, i_q)}{P_{Fe0}(i_{d0}, i_{q0})} = k_D^2 k_L \tag{5.8}$$

The copper losses are scaled as:

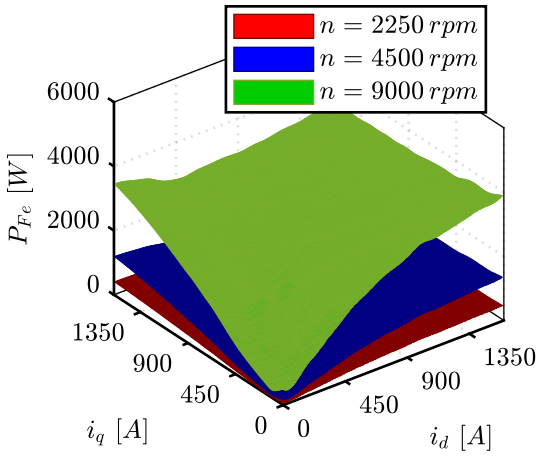

Fig. 5.7 Reference machine Iron loss map function of the rotor speed.

$$\frac{P_{Cu}}{P_{Cu0}} = \frac{k_L P_{Cu,act} + k_D P_{Cu,ew}}{P_{Cu,act0} + P_{Cu,ew0}} \tag{5.9}$$

where the subscript '*act*' refers to the machine's active part, while '*ew*' is related to the end-winding. AC copper loss is neglected in this study.

5.4 (L, Ns) design plane

After establishing the diameter scaling ratio k_D, for example, based on the maximum speed constraint (5.4), the selection of k_L and k_N is not unique. This is addressed through the utilization of the novel length-turns plane depicted in Fig.5.8. The plane pertains to MTPA conditions and illustrates the peak torque at the maximum inverter current and the base speed at the maximum inverter voltage of the scaled design. These are functions of the scaled length and number of turns. The construction

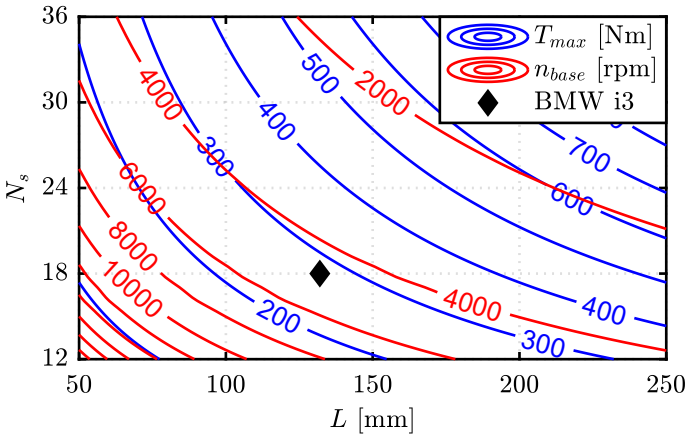

Fig. 5.8 (L, N_s) design plane obtained with $k_D = k_{D0}$ for the BMW i3 motor.

of the length-turns plane initiates from the normalized MTPA law of the reference machine, which shows the *dq* current and flux linkage components as functions of torque. These functions are obtained numerically by manipulating the flux linkage maps. The MTPA curves of the reference machine are then normalized based on the respective scaling quantities, as illustrated in Fig. 5.9. The figure demonstrates how the maximum current condition of the reference machine defines the peak torque value, and this peak torque further establishes the base flux linkage value. Ultimately, the base flux linkage determines the base speed in accordance with the inverter voltage limit equation (5.10).

$$\left\| R_s \cdot (i_{dq})_{max} + j \cdot n_{base} \cdot \frac{\pi p}{30} \cdot (\lambda_{dq})_{max} \right\| = \frac{V_{dc}^2}{3} \tag{5.10}$$

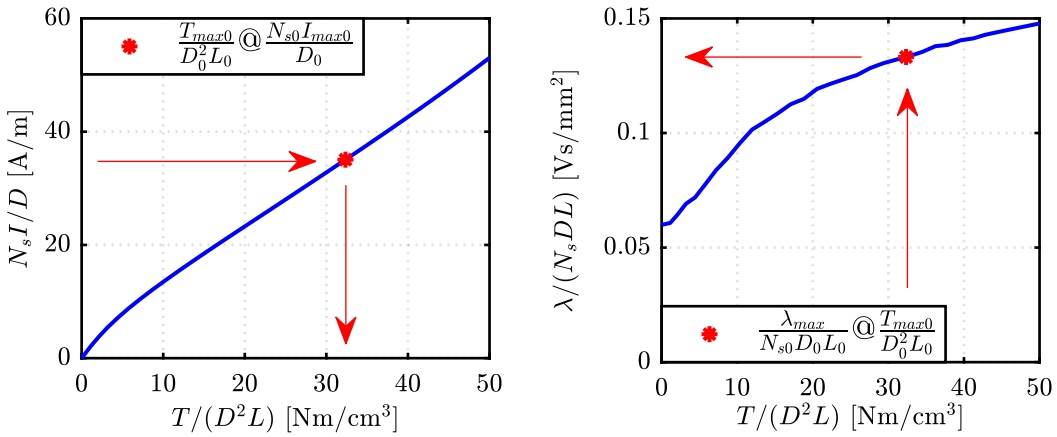

Fig. 5.9 Normalized MTPA curves of the reference machine function of normalized torque.

In the given equation, j represents the complex operator used for space vector representation, and p denotes the number of pole pairs. The voltage limit condition (5.10) establishes the base speed for both the reference and scaled designs, taking into account their respective DC-link voltage values. Given the reference MTPA law, the design plane is constructed as follows (Fig. 5.10). The maximum current and

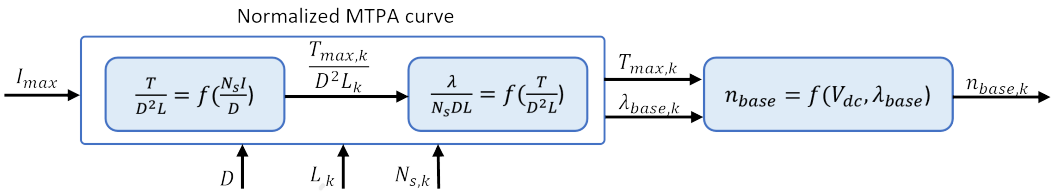

Fig. 5.10 k-th scaled machine performance evaluation flowchart.

DC-link voltage of the target machine are taken into account. The diameter of the scaled machine is preliminarily determined, as mentioned earlier. Considering a pair of arbitrary values for length and number of turns, the normalized peak torque is evaluated after the normalized maximum current. Subsequently, the normalized base flux linkage is determined after the peak torque, and the base speed is calculated according to (5.10). This process is repeated for the range of considered values of length and turns to construct the plane. It is essential to emphasize that the current and voltage limits of the target machine are specific to the target application and are not rigidly constrained by the reference design's scaling of dimensions, torque, and speed.

5.5 Cooling jacket scaling

The heat transfer equations are derived from [111], and the cross-sectional dimensions of the channel are defined in Fig.5.11-a. The scaling of the spiral water jacket is achieved by imposing a **constant flow rate** Q **and constant Reynolds number** Re, while adjusting the dimensions of the channel cross section accordingly. Maintaining a constant Re ensures the preservation of turbulent flow conditions after scaling, and the flow rate values commonly used in automotive applications are relatively independent of the size of the electric motor. The hydraulic diameter D_h is defined in Equation (5.11) for a tube of rectangular cross-section.

$$D_h = \frac{2 \cdot w_c h_c}{w_c + h_c} \tag{5.11}$$

The Reynolds number (5.12) is defined accordingly. It's important to note that ρ represents the mass density, and μ is the dynamic viscosity of the fluid, which in this case is a 50%-50% mixture of water and glycol.

$$Re = \rho \frac{Q}{w_c \cdot h_c} \frac{D_h}{\mu} \propto \frac{Q}{w_c + h_c} \tag{5.12}$$

The flow type, whether laminar or turbulent, is dependent on Re. The threshold values for the considered fluid are provided in Tab. 5.2. Equation (5.12) implies that for a fixed Re and Q, the sum of the channel height and width must remain constant when altering the motor's dimensions. This **constant perimeter** channel scaling law is expressed through the proposed rule (5.13).

$$w_c + h_c = const \rightarrow \begin{cases} \dfrac{h_c}{h_{c0}} = k_D \\ \dfrac{w_c}{w_{c0}} = 1 + \dfrac{h_{c0}}{w_{c0}} \cdot (1 - k_D) \end{cases} \tag{5.13}$$

This decision entails that the channel height varies with the diameter ratio k_D, and the channel width is adjusted accordingly (refer to Fig. 5.12). It's worth noting that alternative choices are also feasible.

Table 5.2 Fluid flow type and reynolds number correlation.

Reynolds Number	Fluid flow type
Re>4000	Turbulent
2300<Re<4000	Transition
Re<2300	Laminar

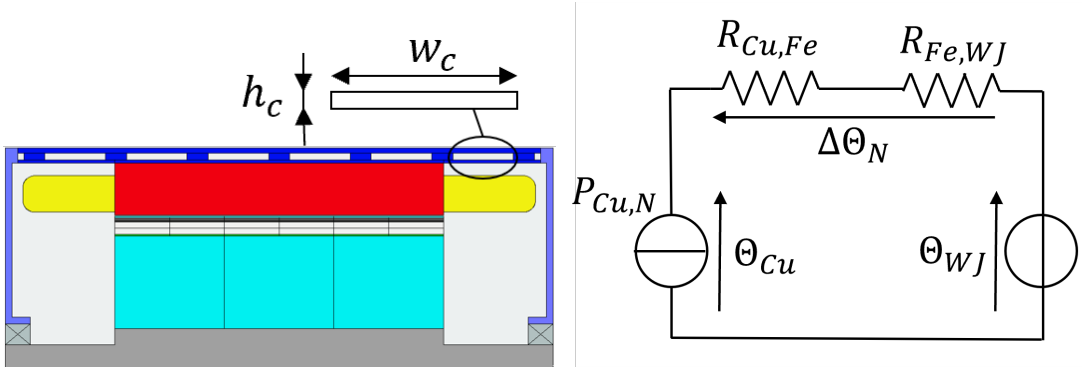

(a) (b)

Fig. 5.11 (a) nomenclature of channel dimensions; (b) stall condition simplified thermal network.

5.6 Heat exchange coefficient scaling

The thermal conductivity of the coolant is a function of the Prandtl and Nusselt numbers. The Prandtl number is defined as:

$$P_r = \frac{\mu \cdot c_p}{k} \tag{5.14}$$

where c_p [J/kg/°C] is the specific heat of the fluid and k [W/m/°C] is the thermal conductivity. The Nusselt number for turbulent flow is defined as (5.15). It's important to highlight that a constant Re corresponds to a constant Nu for a specified fluid.

$$Nu = \frac{f/8(R_e - 1000)P_r}{(1 + 12.7(f/8)^{0.5}(P_r^{2/3} - 1))} \tag{5.15}$$

With the fixed geometric law (5.13), the thermal conductivity of the coolant h [W/°C/m^2] varies according to (5.16). Specifically, it varies independently of axial length and is inversely proportional to the channel cross-sectional area:

$$h = \frac{Nu \cdot k}{D_h} \propto \frac{1}{D_h} \propto \frac{1}{w_c \cdot h_c} \tag{5.16}$$

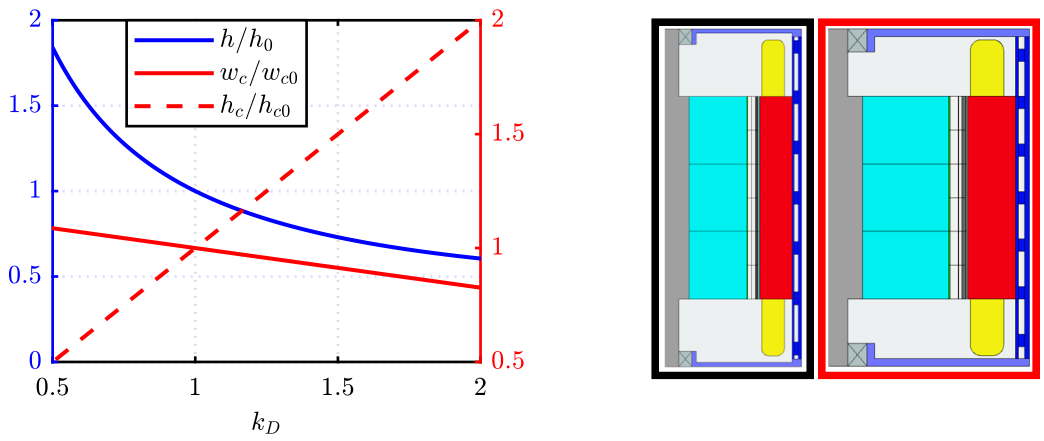

(a) (b)

Fig. 5.12 Thermal conductivity vs k_D following the law (5.13) and effect of radial scaling on the cooling jacket: $k_D = 1$ is red boxed and $k_D = 0.67$ is black boxed.

The scaling law is derived:

$$\frac{h}{h_0} = \frac{w_{c0}}{k_D \cdot (w_{c0} + h_{c0} \cdot (1 - k_D))} \tag{5.17}$$

indicating that a machine with a smaller diameter will experience improved heat extraction, and conversely, a larger diameter will result in reduced heat extraction, as evident in Fig. 5.12. This implies that when scaling up the diameters, it may be necessary to relax some of the proposed assumptions, such as potentially increasing the fluid flow rate.

5.6.1 Stall torque of the scaled machine

The steady-state torque at stall conditions T_N is predicted utilizing the simplified thermal network depicted in Fig.5.11-b, assuming a constant temperature rise at steady state after scaling. The thermal resistance between the iron and water jacket $R_{Fe,WJ}$ is analytically expressed in (5.18).

$$R_{Fe,WJ} = \frac{1}{h \cdot A} \tag{5.18}$$

And it can be scaled according to:

$$\frac{R_{Fe,WJ}}{R_{Fe,WJ0}} = \frac{w_{c0} + h_{c0} \cdot (1 - k_D)}{k_L \cdot k_D \cdot w_{c0}} \tag{5.19}$$

Assuming that the steady-state temperature rise of the reference machine $\Delta\Theta_{N0}$ and the associated DC copper loss $P_{Cu,N}$ are known from simulation or experimental data, the thermal resistance between copper and iron of the initial machine is computed using the network in Fig.5.11-b

$$R_{Cu,Fe0} = \frac{\Delta\Theta_{N0}}{P_{Cu,N0}} - R_{Fe,WJ0} \tag{5.20}$$

where, $\Delta\Theta_{N0}$ represents the difference between the average copper temperature and the average coolant temperature. The scaling rule for the copper-to-iron thermal resistance (5.21) is derived under the assumption that the heat flow cross-section scales with D and L, and the heat flow length scales with D:

$$\frac{R_{Cu,Fe}}{R_{Cu,Fe0}} = \frac{1}{k_L} \tag{5.21}$$

By imposing that the average temperature rise from copper to coolant remains constant, the sustainable copper loss at stall is computed for the scaled machine.

$$\frac{P_{Cu,N}}{P_{Cu,N0}} = \frac{R_{Cu,Fe0} + R_{Fe,WJ0}}{R_{Cu,Fe} + R_{Fe,WJ}} \tag{5.22}$$

With the electrical resistance of the scaled machine given by (5.9), the continuous current at stall can be retrieved, and the corresponding torque is extrapolated from the scaled MTPA curves.

5.7 Efficiency map evaluation and thermal analysis

The efficiency map of the reference machine is assessed by utilizing flux and loss maps, following the methodology outlined in Section 2.5.6. This same approach is employed for the scaled machines, using their respective scaled flux and loss maps without additional FEA simulations. After scaling the flux and loss maps, the optimal operating point for each combination of speed and torque is determined, considering

the MTPA and MTPV laws, along with current and voltage constraints. Fig.5.13 illustrates the efficiency map of the reference machine, emphasizing that the map is based on fixed permanent magnet and copper temperature values.

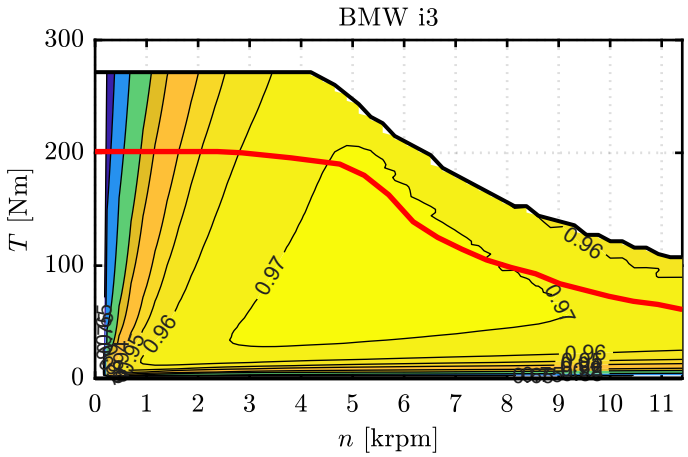

Fig. 5.13 BMW i3 efficiency map and continuous performance curve (red). Winding temperature 180°C and PM temperature 150°C.

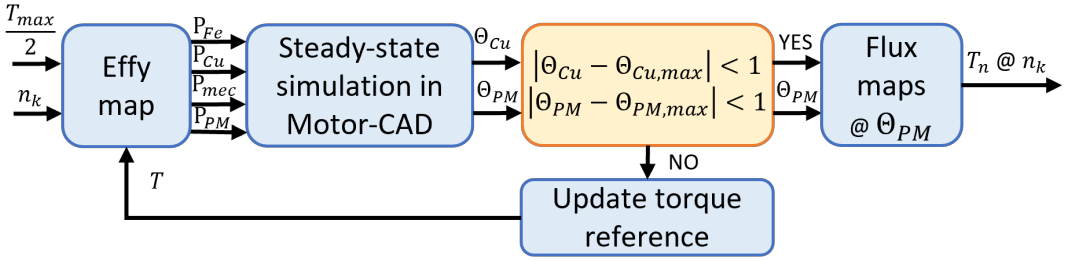

Fig. 5.14 Continuous performance evaluation flowchart at the speed value n_k [rpm].

The calculation of the steady-state torque limit involves iterative static simulations in Ansys Motor-CAD. Initially, the model is generated in Motor-CAD using the automated process outlined in [112], initially designed for SyR machines and extended to PMSMs. Subsequently, Motor-CAD is utilized to compute the continuous torque across the speed range using the custom process illustrated in Fig. 5.14. This process is repeated for each speed value, and with 20 speed steps, it takes approximately 10 minutes in total on the reference workstation.
Considering all the loss contributions at each point of the efficiency map, a SyR-e script iterates the losses from these maps in the Motor-CAD Thermal module until one of the two target temperatures (copper 180°C and magnet 150°C) is achieved.

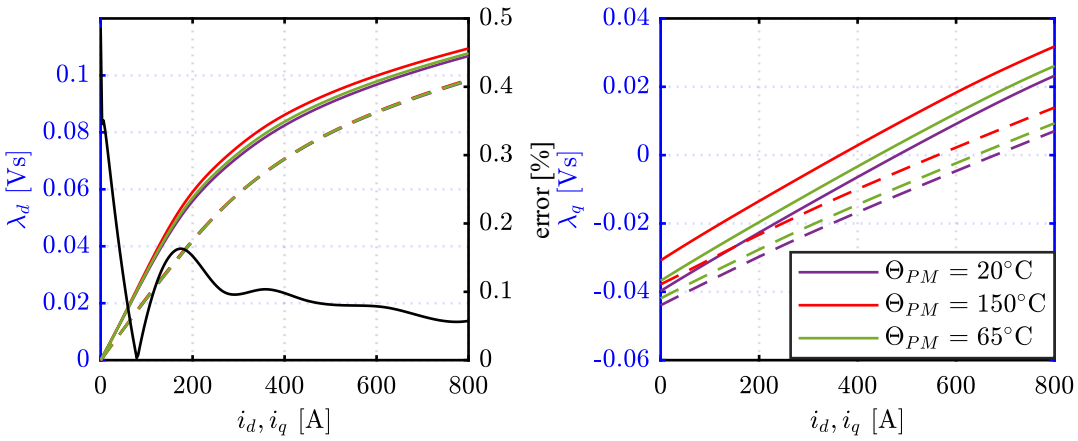

Fig. 5.15 Interpolation of flux curves at a random temperature of 65°C along with the corresponding relative error. The curves at PM temperatures of $\Theta_{PM} = 20°C$ and $\Theta_{PM} = 150°C$ are computed through FEAs. Dashed lines indicate the cross-saturation effect.

Once one of the target temperatures is reached, the script verifies if the other temperature is below the limit. If not, the iterations continue until this condition is met. For each continuous operating point, the obtained magnet temperature is utilized to update the flux maps and retrieve the continuous torque. The flux map at a given magnet temperature is obtained through linear interpolation between two flux maps computed via FEAs at the upper and lower temperature limits of the permanent magnet, namely 20°C and 150°C. An example is presented in Fig. 5.15, where the interpolated flux curves at 65°C exhibit negligible error compared to the results from dedicated FEA simulations. Thus, the new operating point corresponding to the feasible loss is recalculated, and the continuous torque value is saved. It's important to note that the effect of permanent magnet temperature on the loss is neglected.
By applying this method, the continuous performance for the reference machine is obtained and displayed in Fig. 5.20.

5.8 Case studies

In this section, the BMW i3 motor is scaled to match the specifications of the Toyota Prius (Tab. 5.1) IV MG2 regarding maximum torque and power. Additionally, the constraints of the Toyota inverter, such as maximum current and DC-link voltage,

are maintained. There are various methods to scale the motor, and two case studies are described in the following:

A) **fixed maximum speed**: the goal is to have the same top speed as the Prius motor. So, the scaled motor must structurally withstand the target maximum speed, with flexibility regarding the stack diameter;

B) **PRIUS dimensions**: the goal is to have the same volume as the Prius motor. So, the scaled motor must align with the target dimensions, including stack diameter and length, while allowing flexibility in achieving the sustainable maximum speed.

5.8.1 Design case 1: diameter determined by the maximum speed

The diameter ratio is fixed based on the maximum speed values given by (5.4):

$$k_D = \frac{n_{max0}}{n_{max}} = \frac{11400}{17000} = 0.67 \tag{5.23}$$

The resulting stack diameter of 162 mm, determined by the maximum speed constraint, is notably smaller than that of the Toyota MG2.

With the diameter fixed, the other scaling factors k_L and k_N must be determined to meet the peak torque and base speed specifications (163 Nm and 3500 rpm), taking into account the inverter constraints of the Prius IV MG2 ($I_{max} = 226$ Apk and $V_{dc} = 600$ V). The length-turns scaling plane in Fig. 5.16 is employed to emphasize feasible and optimal solutions.

The estimated stall torque contours are also depicted. The region where both specifications are met is highlighted in green. A reasonable criterion for selecting the optimal design is to minimize its volume, specifically its stack length. This leads to identifying Mot1 at the left corner of the green area, with a feasible number of turns set at 72. The design Mot1 with the minimum length has the coordinates $k_L = 0.536$ ($L = 71$mm) and $k_N = 4$ ($N_s = 72$).

The continuous stall torque of Mot1 is predicted to be 50 Nm by the analytical thermal model in the previous section. The efficiency map of the first scaled design, Mot1, is illustrated in Fig. 5.20, showcasing the fulfillment of torque versus speed requirements. Furthermore, a steady-state thermal analysis is conducted in Motor-

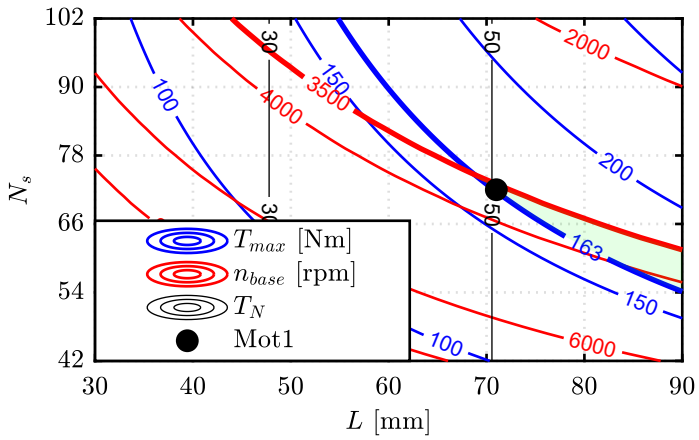

Fig. 5.16 Scaling plane for design case 1. The target torque and speed contours are represented by thicker lines. The domain of feasible machines is shaded in green, with the selected motor marked with a black dot.

CAD to validate the stall torque estimate and complete the continuous torque profile versus operating speed. The process outlined in Fig. 5.14 is utilized to obtain the results displayed with a red line in Fig. 5.20. The results demonstrate a significant correspondence with the analytical estimation.

A dedicated stress analysis, presented in Fig. 5.17a, is conducted for Mot1, confirming the hypothesis of constant stress at maximum speed.

Moreover, an FEA simulation is performed to validate the discussed scaling laws, and the results are shown in Fig 5.18. The BMW i3 motor is supplied with 300 A at a current angle of 135 electrical degrees. To determine the current needed to supply Mot1, the BMW current is multiplied by $k_D k_N^{-1}$, resulting in 50.25 A. It can be easily noted that the magnetic load is perfectly conserved, as shown in Fig 5.18a. Additionally, the current and torque waveforms of the two machines are reported in Fig 5.18b-c. The torque of Mot1 equals the torque of the BMW i3 multiplied by $k_D^2 k_L$ ($137 \cdot 0.67^2 \cdot 0.536 = 33$ Nm).

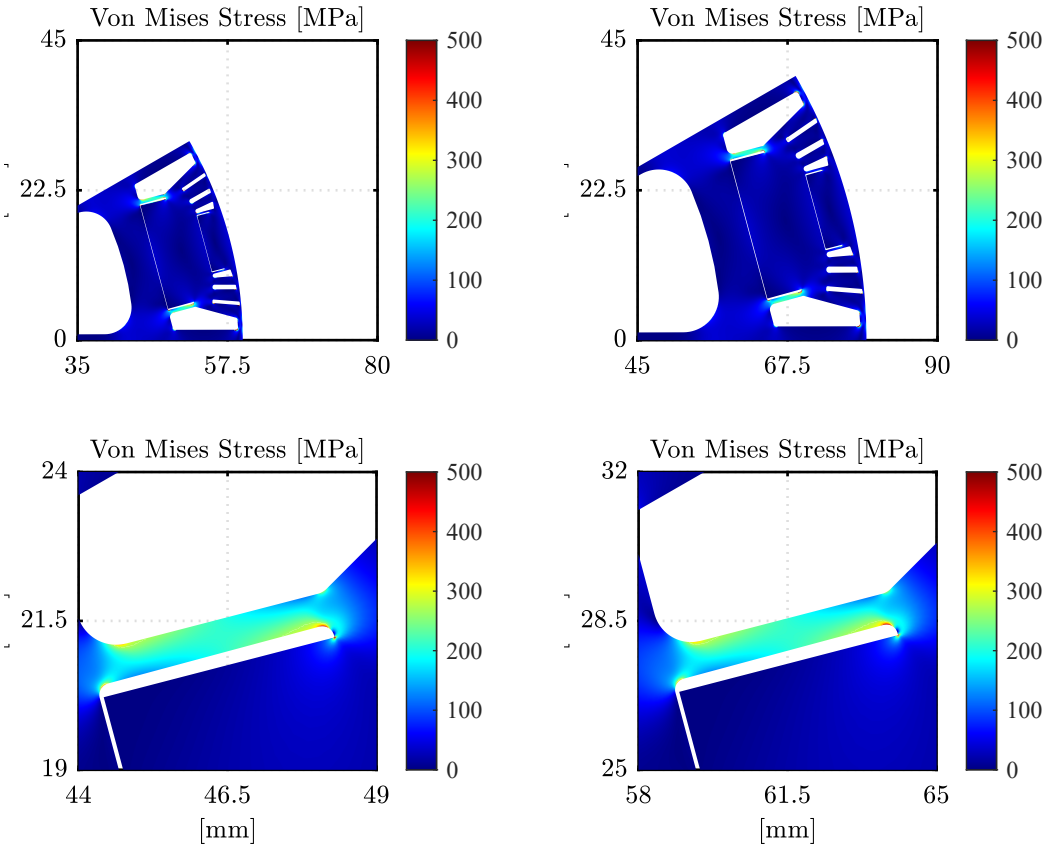

(a) (b)

Fig. 5.17 Results of the mechanical FEA (a) for Mot1 at 17000 rpm and (b) for Mot2 at 12800 rpm.

5.8.2 Design case 2: same diameter and length of PRIUS IV

In this second example, the diameter is set to the value of Prius IV MG2. The scaling ratio is imposed as follows:

$$k_D = \frac{D}{D_0} = \frac{215}{242} = 0.89 \tag{5.24}$$

and the expected maximum speed of the scaled machine is lower than the specified one (5.25).

$$n_{max} = \frac{n_{max0}}{k_D} = \frac{11400}{0.89} = 12800\,rpm \tag{5.25}$$

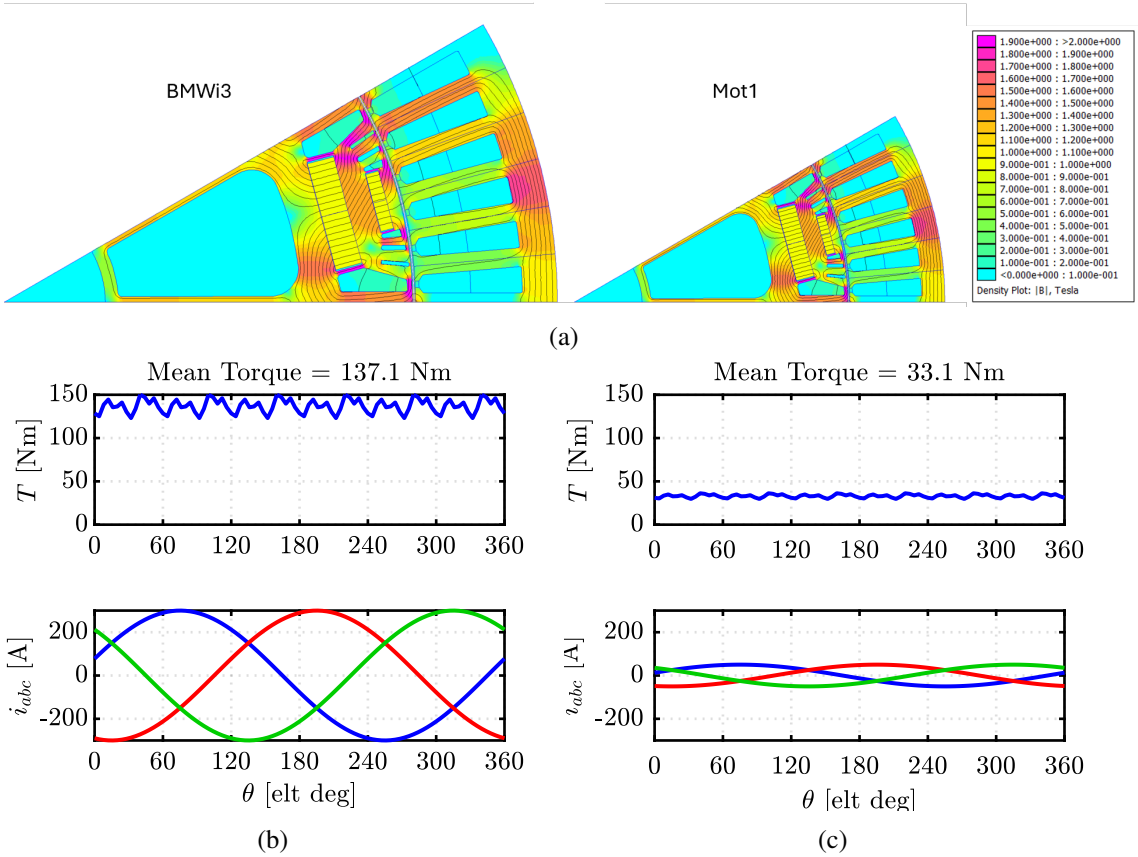

Fig. 5.18 Results of the electromagnetic FEA for BMW i3 and for Mot1 imposing a current equal to 300A ($\gamma = 135^o$C) and 50.25A (according to the selected $k_D = 0.67$ and $k_N = 4$), respectively. (a) Flux density maps. Torque and current waveforms of (b) BMW i3 and (c) Mot1.

To simultaneously match the stack dimensions and the feasible maximum speed, a structural design adjustment would be needed. However, this goes beyond the scope of this chapter, which focuses on linearly scaling all the dimensions of the stack cross-section. The length-turns design plane for this second case is depicted in Fig. 5.19 for $D = 176$mm, with the same current and voltage limits as in case 1. Taking the stack length of the Prius MG2 as a reference and considering a feasible number of turns, Mot2 is selected at $k_L = 0.45$ ($L = 60$mm) and $k_N = 3.66$ ($N_s = 60$). However, it's worth mentioning that the axial length could be reduced while maintaining peak performance; this option is indicated as Mot3 in Fig. 5.19. Mot3 has a smaller volume compared to Mot2 (and Prius). The stall torque is above 60 Nm for Mot2 and below 40 Nm for Mot3, as expected from a shorter motor with the same peak performance.

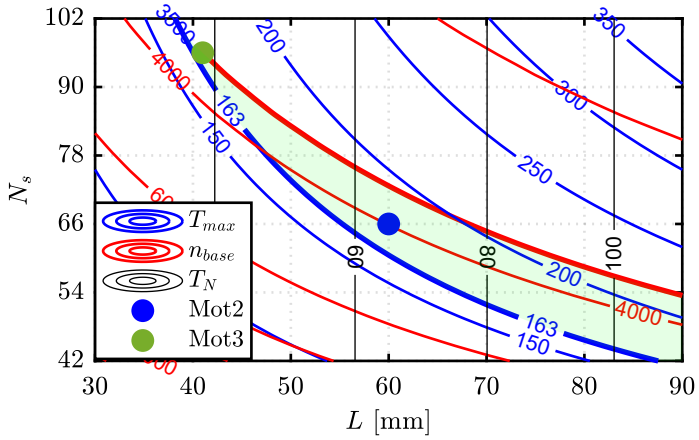

Fig. 5.19 Scaling plane for design case 2. The target torque and speed contours are represented by thicker lines. The domain of feasible machines is shaded in green, with the selected motors, Mot2 and Mot3, marked with blue and green dots, respectively.

The efficiency map of Mot2 is presented in Fig. 5.20: in this case, too, the torque versus speed requirements are met. The thermal analysis confirms the predicted stall torque value. The stress analysis of Mot2 in Fig. 5.17-b confirms that the maximum stress condition is reached at 12800 rpm.

5.8.3 Machines comparison

The reference machines and scaled motors are summarized in terms of magnetic and thermal performance in Tab. 5.3 and Tab. 5.4, respectively. However, thermal information about the PRIUS machine is missing. The scaled versions of the BMW i3, referred to as Mot1 and Mot2, meet the peak torque and power requirements. If the PRIUS has continuous performance similar to the scaled motors, scaling the BMW i3 for the PRIUS application could be advantageous in terms of volume and power density. Additionally, maintaining a higher speed for the motor is beneficial to reduce both volume and mass (Mot1 wins on Mot2).

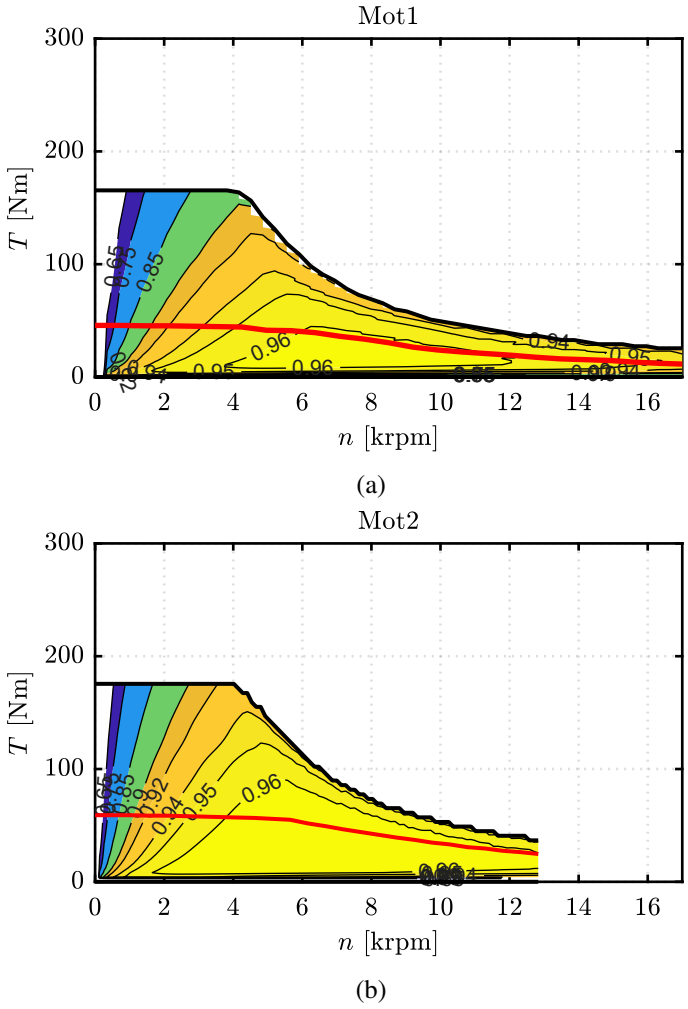

Fig. 5.20 (a) Mot1 and (b) Mot2 efficiency maps. Continuous performance are reported in red.

Table 5.3 Peak performance and dimensions of the machines

		BMW i3	PRIUS MG2	Mot1	Mot2	
Peak torque	T_{max}	270	163	163	176	[Nm]
Peak power	P_{max}	125	53	62	79	[kW]
Maximum speed	n_{max}	11400	17000	17000	12800	[rpm]
Nominal speed	n_{base}	4500	3500	3580	3888	[rpm]
Outer diameter	D	242	215	162	215	[mm]
Stack length	L	132	60	71	60	[mm]
Turns	N_s	18		72	66	
Active mass	m_{act}	31.3		10	15.8	[kg]
Volume	V	6.1	2.2	1.5	2.2	[L]

Table 5.4 Thermal data of the reference and scaled machines

		BMW i3	Mot1	Mot2	
Nominal torque	T_N	201	49	59	[Nm]
Sustainable loss	P_{cu}	1951	994	1850	[W]
Max Cu temperature	Θ_{Cu}	180	180	180	[°C]
Inlet temperature	Θ_{WJ}	95	95	95	[°C]
Fluid flow rate	Q	6	6	6	[L/min]
Pump power	P_{pump}	1.61	1.73	1.19	[W]
Channel height	h_c	4	2.68	3.55	[mm]
Channel width	w_c	23	24.32	23.45	[mm]
Axial spacer	w_s	8	8.46	8.16	[mm]
Radial spacer	h_s	2	1.34	1.78	[mm]
Pressure drop	Δp	0.16	0.17	0.12	[bar]
Fluid velocity	v	1.09	1.53	1.20	[m/s]
Conductivity	h	4391	6197	4848	$[\frac{\mathrm{W}}{^\circ\mathrm{Cm}^2}]$
Surface conductivity	$h \cdot A$	548	313	548	[W/°C]

Chapter 6

Turn-off safe state mode

This chapter focuses on analyzing safe turn-off strategies recommended for permanent magnet synchronous machines, particularly considering two common safe state modes: active short circuit (ASC) and active open circuit (OC). Active short circuit mode is useful for preventing dangerous levels of uncontrolled generator voltages, while active open circuit mode is preferred to avoid abrupt torque transients and the risk of irreversible demagnetization. The two types of PMSM traction motors with NdFeB magnets (IPM) and the with ferrite magnets (PM-SyR), reported in Chapter 4 are studied highlighting their respective advantages and disadvantages regarding the safe state modes. The analysis involves evaluating steady-state and transient operation under active short circuit and open circuit conditions for the existing designs using offline flux maps manipulation. Additionally, the influence of magnet temperature on safe turn-off is investigated. Furthermore, novel indexes on the (x, b) design and scaling plane are introduced, facilitating the generalization of results and enabling early evaluation of safe state modes during the early design phase of the machine.

In automotive applications, when there's a loss of control of the inverter, two turn-off safe modes may be activated: the active short-circuit (ASC) [113] or the opening of inverter switches, known as the open circuit (OC) strategy [114]. These two modes offer contrasting advantages and disadvantages, potentially leading to damage to the PMs [115] or the inverter. In the ASC state, there's assurance that no harmful voltage is present outside the motor, enhancing safety by preventing overvoltage on the inverter DC link and Uncontrolled Generator Operation (UGO)

[116]. However, ASC can generate high transient currents, exposing the motor to the risk of irreversible demagnetization of PMs and unsustainable shaft torques. On the contrary, the OC condition ensures the motor's safety against demagnetization since no current circulates within it. Nevertheless, it poses the risk of dangerous voltages outside the motor, potentially exceeding the DC link limit and risking UGO as well as inverter and battery damage. OC operation can only be utilized if the machine's back electromotive force is smaller than the DC link voltage; otherwise, UGO occurs. For more comprehensive insights into turn-off safe strategies, refer to [117].

6.1 Demagnetizing current and UGO limits

To determine whether the active short-circuit (ASC) state is safe, it's crucial to investigate the irreversible demagnetization of the permanent magnets at the peak ASC current. Note that the inverter must be designed for the short circuit current. Moreover, in case of hardware fault on an inverter leg, the ASC should not be feasible. To expedite the computation process and circumvent the need for FEA simulation at each operating point [88], the demagnetization curve is computed. This curve delineates the maximum demagnetizing current that does not irreversibly demagnetize the PMs (with a tolerance of 1% of the PM volume), contingent upon the PM temperature [87]. The demagnetization limit is derived via an iterative process and FEA simulations. In each iteration, a test current is applied aligned against the PMs, and the flux density in each mesh element of the PMs is compared with the knee point of the BH curve: if the FEA flux density is lower than the knee point, the mesh element is considered irreversibly demagnetized.

The results for the two case studies are depicted in Fig. 6.1; here, the demagnetizing currents are plotted with the maximum inverter current. As anticipated, from the demagnetization point, the worst-case scenario for ferrite occurs at the lowest temperature, while the opposite is true for NdFeB. Conversely, defining the Uncontrolled Generator Operation (UGO) speed is more straightforward, as it can be analytically determined once the magnet flux is known.

$$n_{UGO} = \frac{V_{DC}}{\sqrt{3} \cdot p \cdot \lambda_m} \cdot \frac{30}{\pi} \tag{6.1}$$

where p represents the number of pole pairs and V_{DC} signifies the DC voltage. So if the UGO speed is greater

Hence, Fig. 6.2 illustrates n_{UGO} as a function of the PM temperature for the two benchmark motors. By plotting n_{UGO} with the maximum motor speed n_{max}, it becomes easy to note that the IPM machine exhibits an OC unsafe area within its torque-speed domain for every PM temperature. In contrast, the PM-SyR machine showcases the opposite behavior owing to its smaller PM remanence.

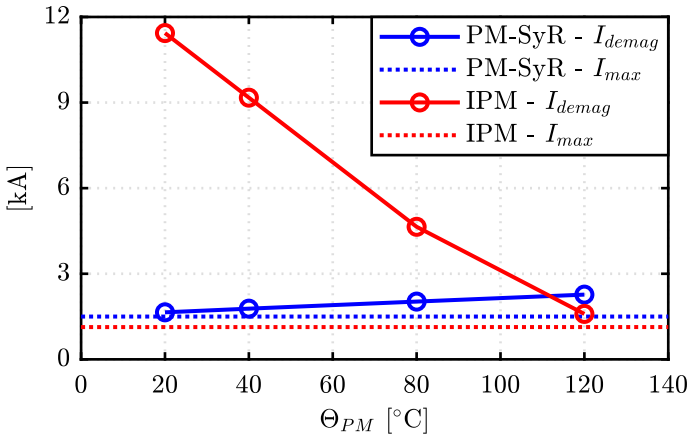

Fig. 6.1 Demagnetizing current limit at different PM temperatures for the IPM and PM-SyR machines. Note that the displayed currents demagnetize 1% of the total PM volume.

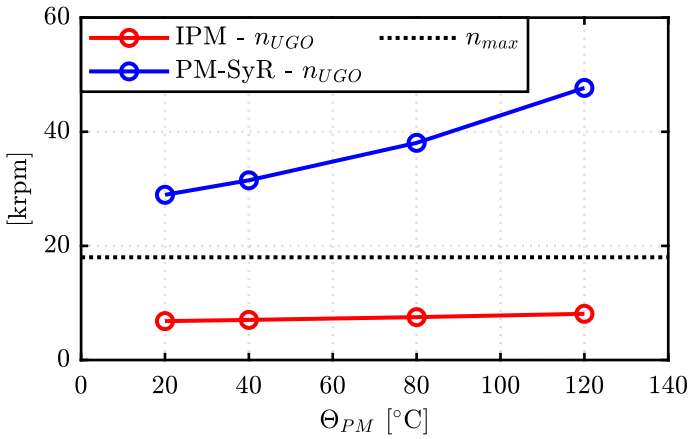

Fig. 6.2 UGO speed as function the PM temperature for the IPM and PM-SyR machines. The maximum speed is reported with a dotted black line.

6.2 Torque-speed domain

In this section, the achievable safe modes are identified in the torque-speed domain to ensure a secure turn-off under various working conditions. Additionally, guidelines on managing the influence of PM temperature are presented.

6.2.1 ASC and OC modes evaluation

In the ASC mode, the motor terminals are short-circuited, ensuring zero voltage outside the motor and mitigating the risk of inverter and battery damage while averting harmful voltages. However, the peak transient short-circuit current poses a significant challenge as it can lead to irreversible demagnetization of the motor PMs, resulting in performance degradation. Therefore, the ASC state can be considered safe if the motor can withstand the peak transient short-circuit current without experiencing irreversible demagnetization. Typically, the steady-state short-circuit current is not critical as the system is stopped after the fault occurs.

To assess the safety of the ASC mode, the HWC short-circuit currents are computed in the (T,n) domain for every working point. Instead of computing the full transient solution, the HWC current is determined due to computational efficiency. This approach avoids additional FEA simulations, with the HWC current identified by interpolating the pre-fault flux density contour with the negative d axis, ensuring instantaneous computation. Subsequently, the HWC current is compared with the demagnetization current limit at all (T,n) points. If the HWC current exceeds the demagnetization limit, the point is labeled as ASC unsafe and marked in red. This process distinguishes ASC safe points as those below a certain flux linkage, while points in the low-speed/high-torque region are deemed unsafe for ASC. However, in the flux-weakening region, ASC is less critical. Notably, the demagnetized volume of the PMs under peak short circuit current depends on the PM design criteria, which in this case is based solely on geometric considerations.

Conversely, the OC mode involves leaving the motor terminals open, resulting in zero phase current. While this ensures motor safety, potential issues may arise due to the motor's no-load voltage. For each (T,n) point, the OC state is considered safe if the motor's no-load voltage is below the rated motor voltage, accordingly to (6.2). This evaluation process is repeated similarly to the ASC state case.

$$E_0 = \lambda_m \cdot n \cdot \frac{\pi}{30} \cdot p \leq \frac{V_{DC}}{\sqrt{3}} \tag{6.2}$$

where E_0 is the no-load voltage.

6.2.2 PM-SyR machine

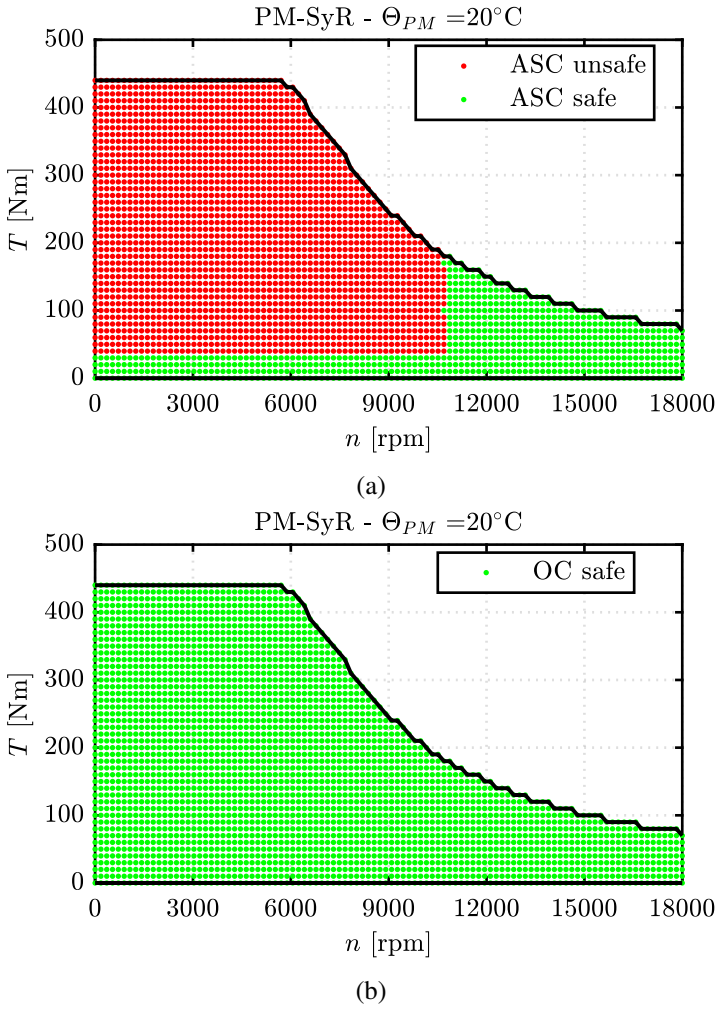

Fig. 6.3 PM-SyR machine safe operating area in cold condition (PM at 20°C). (a) ASC and (b) OC.

Considering the ASC operation, Fig. 6.1 illustrates that the worst-case PM temperature occurs at the minimum considered temperature (20 °C). Similarly, in the OC mode, as shown in Fig. 6.2, lower PM temperatures result in greater magnet

flux (6.1). Hence, once a safe area is identified in the torque-speed domain for a PM temperature of 20 °C, it remains valid even for higher temperatures. Fig. 6.3 investigates the safe areas for the ASC and OC modes with PMs at 20 °C. The ASC operation is deemed unsafe for nearly every working point below approximately 10500 rpm, while the OC mode is consistently safe. This is attributed to the very low demagnetizing current limit at 20 °C (Fig. 6.1), causing most of the i_{HWC} values in the torque-speed domain to exceed this limit. Conversely, the n_{UGO} at 20 °C extends beyond the maximum speed. Therefore, for the PM-SyR machine, the OC mode is identified as the optimal turn-off safe state mode under all operating conditions. Lastly, for clarity, the ASC safe area at the maximum PM temperature of 120 °C is depicted in Fig. 6.4 to reinforce the notion that the ASC safe area expands with increasing PM temperature for ferrite machines.

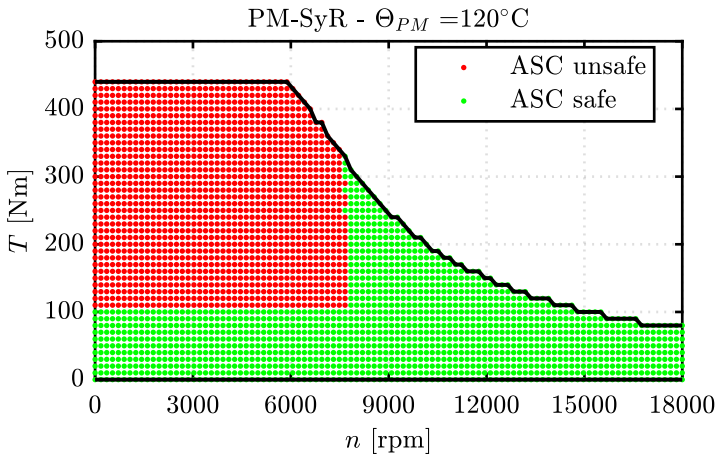

Fig. 6.4 PM-SyR machine ASC safe area in hot condition (PM at 120°C).

As a remark, the ASC plane is evaluated considering the HWC current, which makes it a conservative assumption. There may be points over the plane that are not critical from an ASC perspective, especially at low speeds. For example, in cold conditions, the 10-period current waveforms for 500 rpm and 1000 rpm are shown in Fig. 6.5. The prefault condition is set to 100 Nm in MTPA. The figure also displays the demagnetization current limit. It can be observed that, contrary to the ASC plane, the short circuit at 500 rpm is not critical. The results align for the 1000 rpm case.

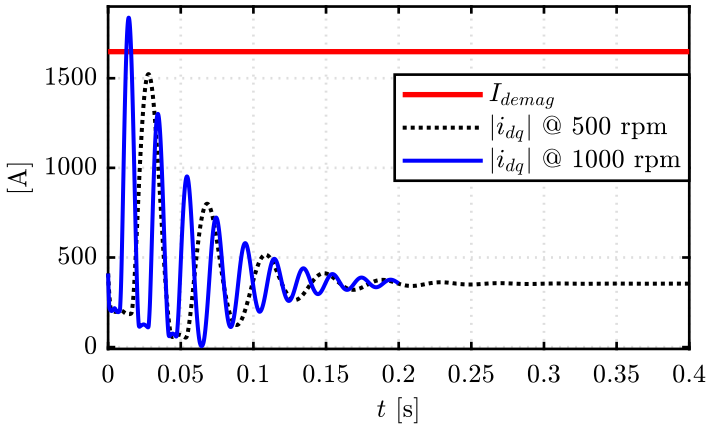

Fig. 6.5 Transient current waveform during a short circuit at 500 rpm and 1000 rpm in cold condition (PM at 20°C).

6.2.3 IPM machine

The NdFeB-based machine exhibits an opposite trend in the ASC mode concerning the PM temperature, as evident in Fig. 6.1. Therefore, there isn't a single worst-case PM temperature since the demagnetizing current limit decreases at higher temperatures (resulting in smaller ASC safe areas). Conversely, according to Fig. 6.2, n_{UGO} decreases at lower temperatures (leading to smaller OC safe areas). Hence, a precautionary approach is warranted: each turn-off safe state is evaluated at its respective worst-case PM temperature. Fig. 6.6 illustrates the ASC safe area at 120°C and the OC safe area at 20°C. As depicted, defining a single safe mode applicable to every working point in the torque-speed domain is not feasible. Nonetheless, each point has at least one viable safe mode. Hence, a hybrid strategy can be employed: OC mode for speeds below 6500 rpm and ASC mode for higher speeds.

Lastly, similar to the PM-SyR machine, the ASC safe area at the opposite PM temperature is depicted to underscore the temperature effect. As indicated, the ASC safe area for NdFeB machines widens at lower PM temperatures. At 20°C, the demagnetizing current limit significantly increases to a value approximately 11 times the maximum inverter current (Fig. 6.7). Consequently, in every working point, the i_{HWC} does not reach such an high value, rendering the ASC mode consistently safe.

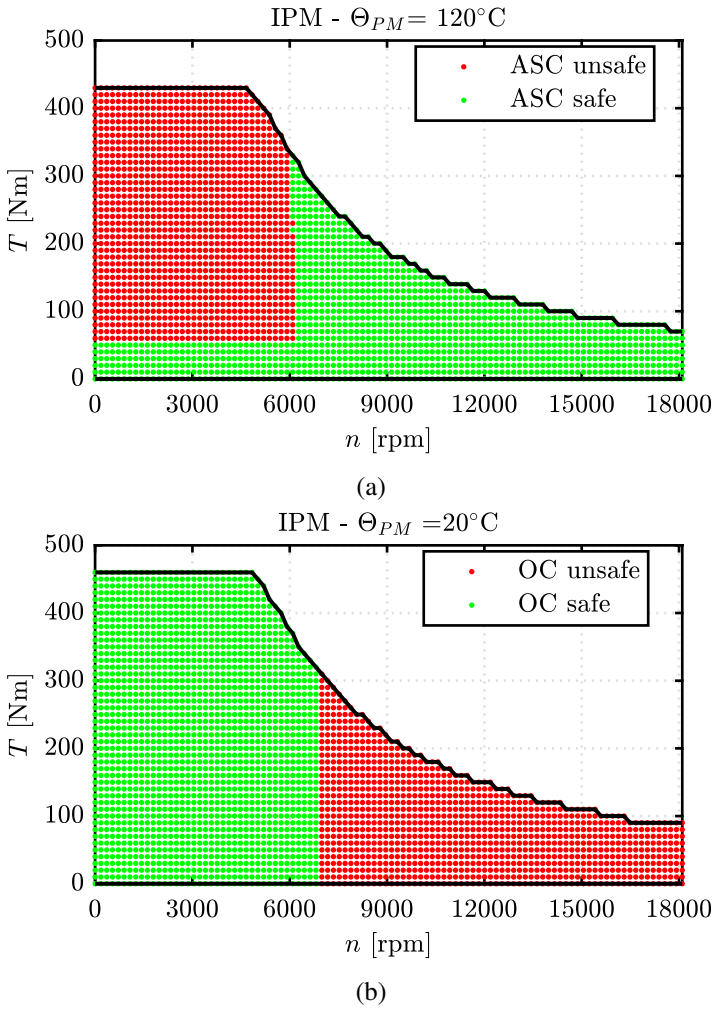

Fig. 6.6 IPM machine afe area. (a) ASC mode in hot condition (PM at 120°C) and (b) OC mode in cold condition (PM at 20°C).

6.3 ASC and OC indexes in the design procedures

6.3.1 Safe state modes on the (x,b) design plane

The Chapter 4 has already addressed the determination of the number of turns to satisfy the inverter ratings and fundamental design prerequisites, such as torque and power factor. This study shifts its attention towards evaluating safe operating conditions. Novel indexes have been introduced into the initial design phase to assess the ASC and OC states. These indexes are formulated to be unaffected by the number

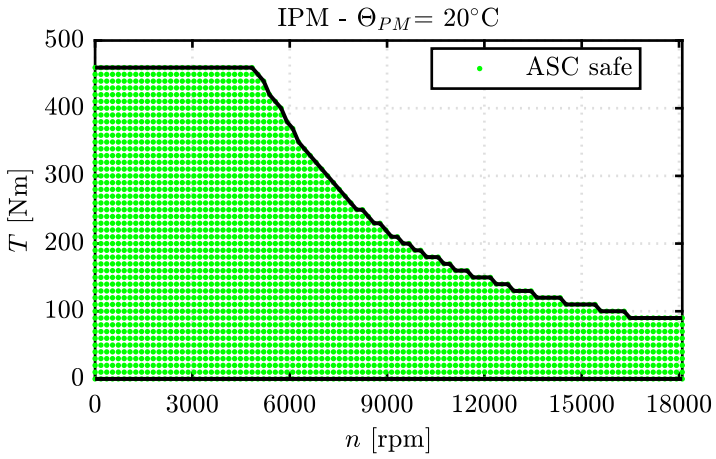

Fig. 6.7 IPM machine ASC safe area in cold condition (PM at 20°C).

of turns, as elaborated below. It's important to mention that the planes mentioned herein pertain to a permanent magnet temperature of 80°C.

Given the current I, function of the (x,b) coordinated and fixed by the constant current density along the plane, the peak current during an ASC transient is assessed with the ratio i_{HWC}/I. In every FEAfix point, iterative FEA simulations are run to retrieve the i_{HWC}, thus, the percentage of demagnetized PM volume at i_{HWC} is computed and the percentage of demagnetized PM saved. As done before, the ASC operation is deemed feasible if less than 1% of PM is demagnetized. From Fig. 6.8, it can be noted that the peak currents during an ASC are slightly higher for the IPM machine than the PM-SyR, because of the higher PM content (higher steady-state short circuit). However, the IPM plane results in having almost zero demagnetized motors at its i_{HWC}/I, while for the PM-SyR plane 100% of the motors suffer from demagnetization. Please note that here the demagnetized volume contours are computed using the HWC current, instead in Chapter 4 refer to the nominal current. This communicates that even if the two planes have similar i_{HWC}, for the IPM machine the ASC can be triggered in MTPA and peak current condition for every (x,b) design, while for the PM-SyR machine is valid the opposite. These findings match the analysis reported in Fig. 6.3a, where the PM-SyR, at corner speed and peak current, is unsafe with respect to the ASC. Moreover, the ferrite design plane demonstrates that even changing the machine geometry, it is unfeasible to achieve a safe ASC at peak current/corner speed; whilst, all the opposite happens for the IPM motor.

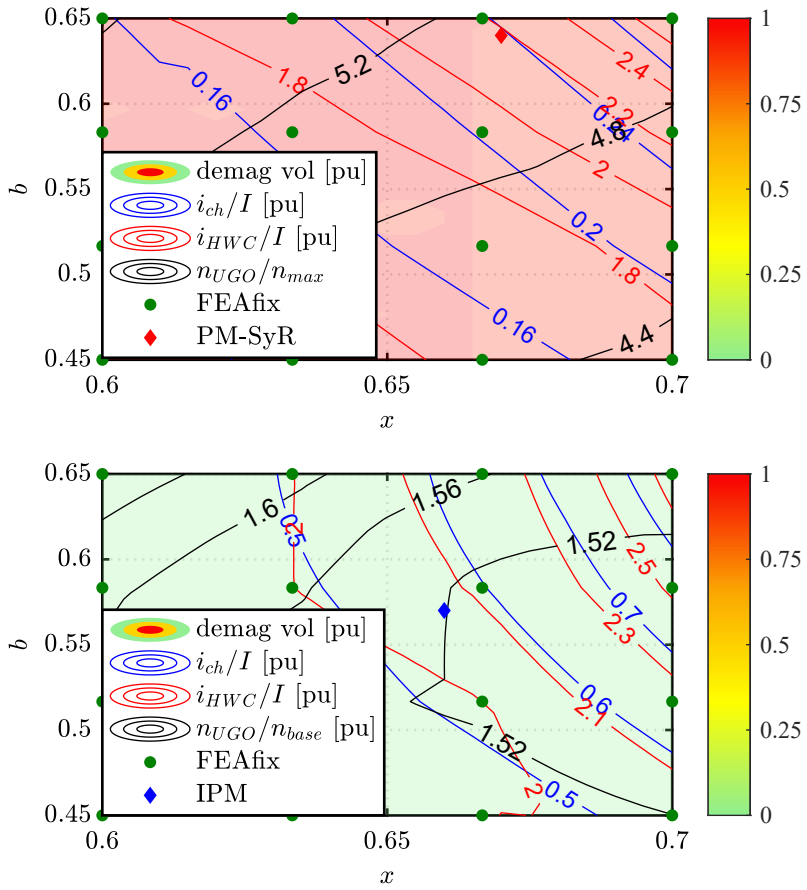

Fig. 6.8 Design planes of the PM-SyR and IPM machines with indexes on ASC and OC states.

Dealing with the UGO limit, it is evaluated as the ratio between the UGO and base speeds, respectively n_{UGO} and n_{base}. The latter depends on the machine flux at the MTPA maximum inverter current λ_{max}, which is the working point evaluated along the design plane.

$$n_{base} = \frac{V_{DC}}{\sqrt{3} \cdot p \cdot \lambda_{max}} \cdot \frac{30}{\pi} \tag{6.3}$$

Therefore, from (6.1) and (6.3), it can be found the ratio between the UGO and base speed (6.4), which does not depend on the number of turns.

$$\frac{n_{UGO}}{n_{base}} = \frac{\lambda_{max}}{\lambda_m} \tag{6.4}$$

Note that the defined ratio (6.4) strongly depends on the magnet flux; therefore, as expected, the Fig. 6.8 shows that the NdFeB plane has a significantly lower UGO speed than the ferrite plane. According to the ratings, the maximum speed and base speed ratio is equal to 3.8. In Fig. 6.8, it can be noted that the UGO limit in the PM-SyR plane always exceeds the 3.8 target, whilst the opposite results for the IPM machine. Thus, as for the ASC mode, also the OC mode feasibility can be directly assessed from the design plane during the preliminary design since it is able to forecast some of the results shown in Section 6.2, namely the OC safety limit and the ASC safety at maximum MTPA current.

6.3.2 Safe state modes on the (L,Ns) scaling plane

Referring to the process outlined in Chapter 5, if λ_{max} were scaled based on the constant flux-density principle (5.5), I_{HWC} would accordingly scale as shown in (5.6). However, in a general context, when scaling the machine, it's necessary to recalculate the HWC value after scaling all quantities involved in its computation, as the scaled machine might exhibit a more or less saturated maximum torque condition. For instance, I_{HWC} is determined across the (L, N_s) plane of the not radial scaled BMW i3 and the results are depicted in Fig. 6.9. The same principle applies to UGO speed: if the constant flux-density condition (5.5) were upheld for both flux linkages in the numerator and denominator of (6.4), the n_{UGO}/n_{base} ratio would be unaffected by dimensional and turns scaling.

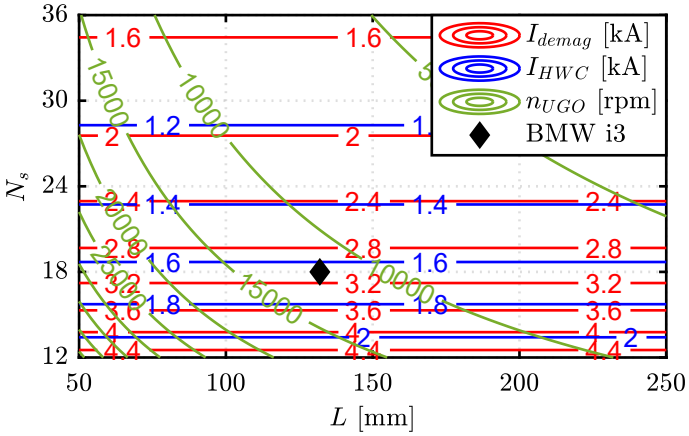

Fig. 6.9 (L, N_s) plane of the BMW i3 motor before radial scaling. Demagnetization current limit and HWC short circuit current, and UGO speed limit.

However, similar to HWC current, the λ_{max} condition doesn't necessarily follow to the strict scaling law followed by λ_m, thus necessitating a case-by-case scaling of n_{UGO}. For instance, it's computed for each (L, N_s) combination of the plane, as shown in Fig. 6.9.

The new indices on the scaling plane are also depicted for the presented case studies in Fig. 6.10a for case 1 and in Fig. 6.10b for case 2.

The analysis reveals that Mot1 will not experience PM demagnetization, indicated by the ratio $\frac{I_{HWC}}{I_{demag}} = 0.72 < 1$. This suggests that this machine can withstand an ASC even under pre-fault conditions of maximum torque, where the short-circuit current would reach 72% of the demagnetization limit. UGO would pose a risk above 11600 rpm, which is more than three times greater than the corner speed of this motor. In practice, the ASC will be initiated well above the corner speed, ensuring it never commences from maximum torque conditions, further reducing the short-circuit peak current and hence the risk of demagnetization.

Concerning Mot2, neither demagnetization nor UGO are critical: the short circuit safety index is $\frac{I_{HWC}}{I_{demag}} = 0.64$, and the UGO speed limit is 11700 rpm, once again significantly above the corner speed, contributing to the ASC's harmlessness.

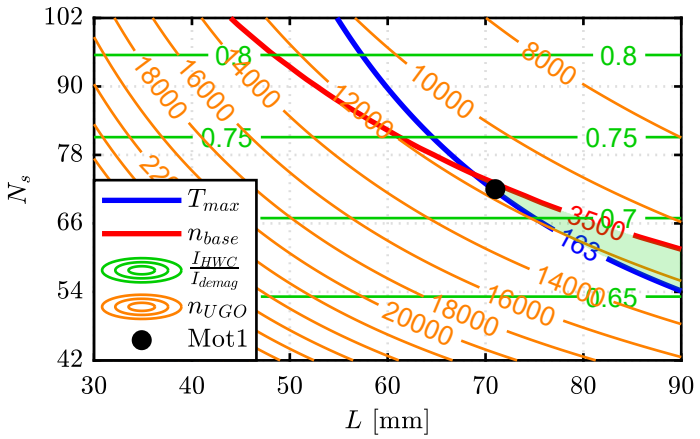

(a)

Fig. 6.10 Scaling planes of (a) the case study 1 and (b) the case study 2 with indexes on ASC and OC states.

Lastly, Mot3 is also safe against demagnetization under ASC ($\frac{I_{HWC}}{I_{demag}} = 0.72$), with a UGO speed limit of 11700 rpm. It's worth noting that both indices are identical to

those of Mot1. Additionally, Mot1 and Mot3 have practically the same stack volume, as well as maximum torque and speed figures, as evident from their respective planes.

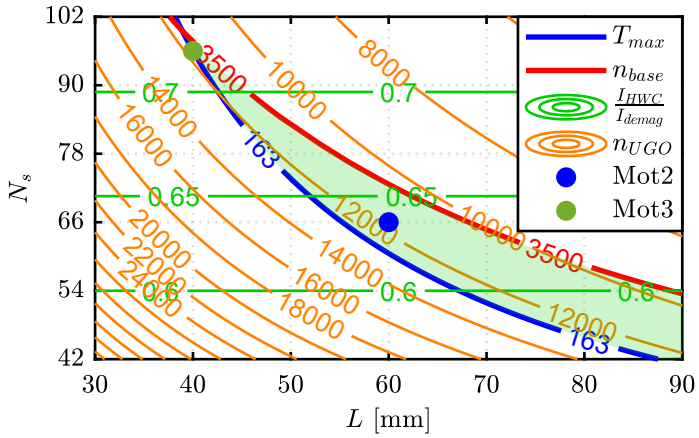

(b)

Fig. 6.10 Scaling planes of (a) the case study 1 and (b) the case study 2 with indexes on ASC and OC states.

Chapter 7

Thermal characterization and winding hotspot observer

The contemporary market continually demands higher torque and power density in high-performance drives, particularly for traction applications [118–121]. Achieving a cost-effective, lightweight, and compact design for high-performance electric machines necessitates a multi-physics approach [122], wherein magnetic design is integrated with considerations from the mechanical and thermal domains [123–125]. This approach is particularly crucial today due to the automotive industry's stringent requirements for cost and performance in traction electric motors [126, 127, 57]. The escalating demand for power density underscores the importance of enhanced thermal management, leading to the adoption of liquid-cooled motors in traction applications, which offer reduced thermal impedance and shorter thermal time constants. Consequently, the evaluation of electric motors extends beyond their magnetic characteristics [128, 129], with the development of reliable procedures for experimentally assessing the machine's thermal properties becoming indispensable [130].

Accurate thermal models are indispensable both during the design phase and in controlling electric machines for advanced thermal management [131, 132]. These models typically rely on either FEA or Lumped Parameters Thermal Networks (LPTNs) [133], or sometimes a combination of both. FEA thermal models [134] offer a highly accurate representation of temperature distribution within the machine. However, their computational burden are typically too high for real-time

implementation on commercial microcontrollers. Additionally, accurately capturing thermal transients requires precise calibration of material properties, which can be challenging to obtain experimentally. In contrast, the LPTN approach provides a simplified representation of the machine's thermal behavior. It discretizes the machine into a reduced number of components, modeling each part with thermal capacitances and resistances [135]. While this approach offers lower computational demands compared to FEA, making it suitable for real-time execution, it lacks the fine accuracy of FEA. One common limitation of many LPTN models found in the literature [19],[136] is that the thermal parameters defining the network are often derived from machine geometry and material properties, rather than being directly measured through experimental tests. This reliance on derived parameters can introduce uncertainties into the thermal modeling process.

To construct an accurate LPTN model, essential motor components such as rotor and stator iron, windings, and Permanent Magnets (PM) must be included. Among these components, the winding is particularly vulnerable due to its strict isolation class temperature limit, especially in scenarios involving liquid cooling where hotspot thermal transients occur rapidly. The thermal interaction between the winding conductors and the surrounding insulation material and stator iron is challenging to calculate analytically or numerically [137, 138, 135]. Consequently, the Short Time Thermal Transient (STTT) test procedure was introduced [23, 139] to directly evaluate the winding's thermal capacitance and resistance through experimental means, employing a 1st order model and general-purpose induction motors with accessible winding terminals. However, this chapter highlights the inadequacy of the STTT method in describing the transient behavior of high-performance machines featuring liquid cooling and low thermal inertia [140, 141]. Specifically, the original STTT procedure assumes that the winding-to-iron thermal time constant is significantly faster than the iron-to-ambient heat exchange temperature effect, which is not valid for the liquid-cooled motors under investigation. Consequently, the winding thermal capacitance and resistance derived from STTT are highly contingent on the test duration and the selected STTT temperature rise.

Moreover, the interplay of high power losses and an efficient cooling system often leads to uneven temperature distribution within the motor [19]. Typically, the stator winding is among the most critical components, and its temperature must be controlled to prevent faults or premature aging of the insulation [125, 142–144]. While most traction motors incorporate one or more winding thermistors,

the hottest point is often inaccessible in highly compact machines [145], making direct measurement during operation challenging. Consequently, the measured temperature may not accurately reflect the most critical point. For instance, as illustrated in Fig. 7.1, the motor under test typically contains a single thermistor in the only accessible winding point, usually near the phase connections with the inverter, which tends to be considerably cooler than the winding hotspot situated internally. Moreover, the hotspot's overtemperature relative to the measurement dynamically changes during drive operation, depending on the driving cycle. Given this variability and the general lack of knowledge about the hotspot temperature, a significant safety margin is often necessary when determining motor current and torque ratings to mitigate thermal failures probabiliy.

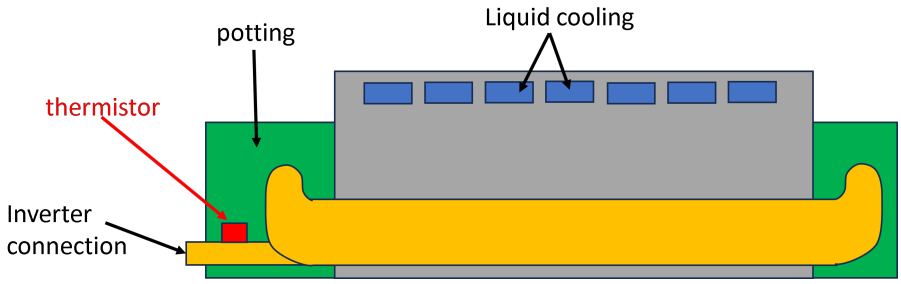

Fig. 7.1 Axial section of electric motor.

Given the criticality of accurate temperature monitoring and the challenges of direct measurement, various real-time temperature observers have been proposed, designed to be integrated into the motor control routine [146, 147, 131, 132]. These observers may focus on monitoring different components such as the inverter, PMs, or winding temperatures. Stator winding temperature observers often rely on estimating stator resistance variation [148] or dynamic inductance [132]. However, techniques like those in [131, 132] are typically based on an average model of the machine, limiting their ability to estimate the winding temperature gradient accurately.

In this chapter, builds upon the STTT (Short Time Thermal Test) model and data processing methodology introduced in a prior work [23]. The improvements are experimentally validated using a star-connected traction motor with three-phase input terminals, including a weak connection to the star point. The enhanced model overcomes the limitations of the previous work by incorporating the temperature variation of the back iron during the STTT test. This refinement significantly reduces the dependency of estimated thermal parameters on the test duration. Additionally,

an innovative real-time observer leveraging an enhanced LPTN is illustrated. This observer dynamically predicts the hotspot temperature of the stator winding while the drive is operational, allowing for the full utilization of the drive's transient overload capacity. This proactive approach enhances reliability and minimizes the risk of thermal failures. The chapter presents an analytical solution for the LPTN, facilitating its straightforward and rapid implementation on industrial microcontrollers.

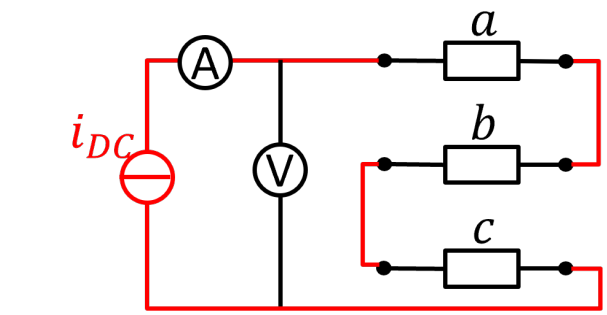

(a)

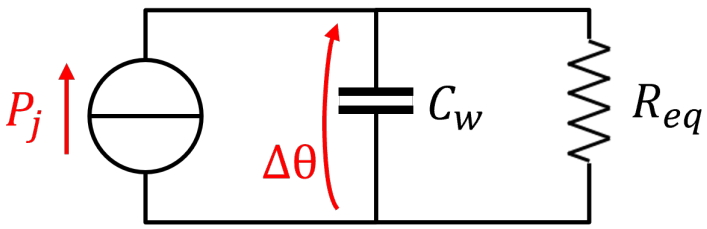

(b)

Fig. 7.2 Existing STTT procedure [23]. (a) DC identification test. (b) Equivalent LPTN.

7.1 Motor under test

The machine chosen for validating the proposed method is a Permanent Magnet Synchronous Motor (PMSM) designed for high-performance traction applications with a tipycal spiral water jacket for cooling. Typical for traction motors, the phase resistance is in the range of a few milliohms. In the portable version, only the input terminals of the three phases are accessible, rendering the existing STTT procedure [23] impractical. However, in the prototype being tested, an additional wire of reduced cross-section allows access to the winding star point with limited current capability and a resistance comparable to the phase resistance.

The motor is equipped with seven thermistors for mapping the thermal gradient within the machine. It's important to note that the design of this machine is proprietary, so all physical quantities mentioned in the paper are normalized. The nominal thermal capacitance of the winding and thermal resistance are determined based on the finite element model of the machine, while the rated temperature rise is defined as the difference between the maximum allowable winding temperature and the nominal ambient temperature during operation.

Initially, the assessment of the winding hotspot location necessitates an examination of both longitudinal and radial thermal gradients. A thermal analysis of the motor was executed [149], utilizing a model developed by the carmaker. Given that the hottest stator point may vary depending on operating conditions, simulations were conducted under various speeds and loads, encompassing standard and custom driving cycles. This enabled the identification of the most critical winding hotspot, which can reach temperatures up to 50°C higher than the measurable point.

Specifically, the motor under evaluation underwent simulation using both a 3D LPTN and dedicated thermal FEAs. The FEA analysis was conducted in 2D, focusing on the motor section. While the 3D LPTN offers a precise representation of the motor and the cooling system due to its high number of nodes, it effectively describes the radial and longitudinal thermal gradients. The thermal resistances and capacitances of the network are defined by the motor geometry and materials.

An example of a simulated thermal transient is depicted in Fig. 7.3. In this simulation, a load step was applied, commencing with the motor at room temperature. The figure illustrates the average winding temperature $\bar{\theta}$, as well as the temperatures of the hotspot θ_h and the measurable θ_m points. It's evident that the hotspot temperature experiences a rapid increase, whereas the measurable point follows with a noticeable delay and a slower dynamic. This underscores the importance of a real-time estimator capable of monitoring the winding hotspot temperature during transient conditions.

7.2 1st order original STTT procedure

The Short Time Thermal Transient (STTT) is a testing procedure designed to estimate the slot thermal parameters of three-phase motors [23] or multi-phase electric motors

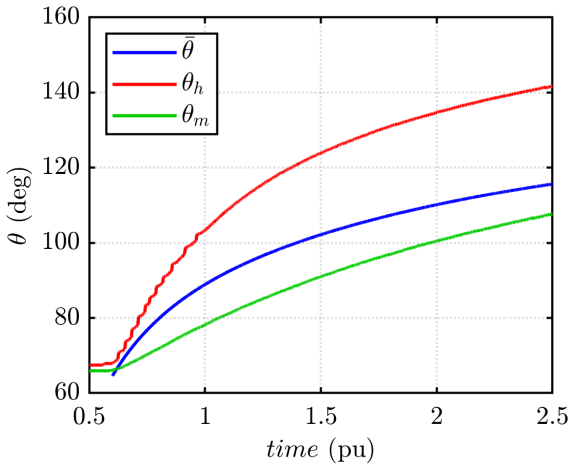

Fig. 7.3 Simulation of thermal transient. Average winding temperature (blue), hotspot temperature (red) and measurable temperature (green).

[139]. Through experiments, the winding thermal capacitance C_w and the equivalent thermal resistance R_{eq} between the winding and the stator iron, which includes isolation and potting, are determined.

In the testing procedure [23], the three phases are connected in series, as depicted in Fig. 7.2a. Beginning with the motor at a uniform initial temperature θ_o, the series of the three phases is excited with a DC current value compatible with the RMS nominal current, resulting in a measurable temperature rise. The series connection ensures that all three phases are heated uniformly. The imposed current i_{dc} and the voltage v_{dc} across the series of the three phases are measured, allowing for the computation of the winding resistance R_{dc}, Joule loss P_j, and average winding temperature θ:

$$R_{dc} = \frac{v_{dc}}{3i_{dc}} \tag{7.1}$$

$$P_j = v_{dc} \cdot i_{dc} \tag{7.2}$$

$$\theta = \frac{R_{dc}}{R_o}(234.5 + \theta_o) - 234.5 \tag{7.3}$$

Here, R_o represents the winding resistance measured at θ_o. During DC excitation, the input power aligns with the Joule loss in the windings. Hence, the copper energy loss W can be calculated as the time integral of P_j:

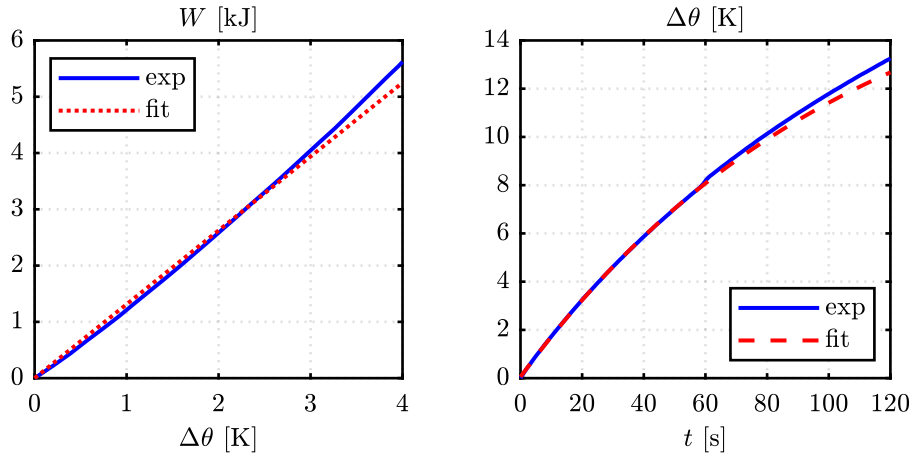

Fig. 7.4 example of STTT test results for an industrial motor drive, as outlined in [23]. On the left the dissipated energy plotted against the overtemperature; on the right, the overtemperature is plotted against time. The blue lines represent the measured data, while the red lines represent interpolations using (7.6) and (7.8) respectively.

$$W = \int_{t_0}^{t} P_j \, dt \tag{7.4}$$

t_0 denotes the time at which the current step is applied, and the associated energy is $W(t_0) = 0$.

The central assumption of the STTT procedure [23] is that during the initial short time period of the thermal transient, the system behaves adiabatically. This implies that heat exchange from the winding to the rest of the machine is negligible. This assumption is justifiable since heat is initially generated within the copper winding and is later dissipated primarily to the stator iron. The validity of the adiabatic hypothesis holds for minor initial temperature increases of the winding, denoted as $\Delta\theta_{st}$.

$$\Delta\theta = \theta - \theta_o < \Delta\theta_{st} \tag{7.5}$$

where $\Delta\theta$ denotes the increase in temperature compared to the initial state. To clarify further, the initial heating of copper is regarded as adiabatic until the temperature rise reaches approximately $\Delta\theta_{st}$, typically ranging between 3 to 5 degrees Celsius.

Given this assumption, the dissipated energy increases linearly with the winding temperature during the initial moments of the transient phase. Consequently, the

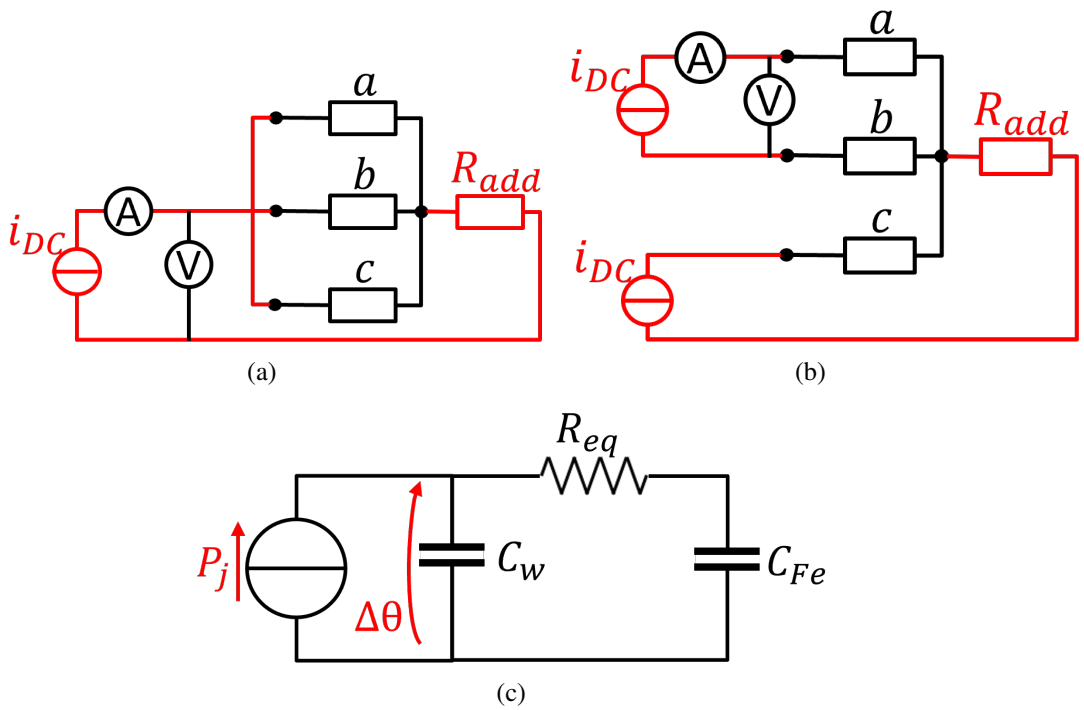

Fig. 7.5 Proposed STTT procedure. (a) Parallel DC identification. (b) Proposed DC identification. (c) Proposed LPTN.

energy evolution, denoted as $W(\Delta\theta)$, can be effectively approximated by a linear function $\hat{W}(\Delta\theta)$ that correlates with the temperature rise. By observing the rate of change of this interpolating linear function, is derived an estimation of the thermal capacitance of the winding, denoted as C_w:

$$\hat{W}(\Delta\theta) = a \cdot \Delta\theta \tag{7.6}$$

$$C_w = a \tag{7.7}$$

During the adiabatic STTT period, the first-order LPTN illustrated in Fig. 7.2b models the behavior of the stator winding. Here, the recently determined C_w undergoes "charging" due to Joule loss, while the thermal resistance R_{eq} facilitates heat dissipation to the surrounding iron. Given the assumption of constant θ_o for the stator iron in the initial phase of the thermal transient, its thermal capacitance is omitted from the LPTN.

The parameter R_{eq} symbolizes the combined thermal resistance between the stator copper and iron. Its determination involves fitting the temporal evolution of the winding temperature rise using the analytical solution of the LPTN. This fitting process is conducted within the time interval $[0 \quad \Delta t_{st}]$, where Δt_{st} represents the duration of the STTT time horizon:

$$\hat{\Delta\theta}(t) = P_j R_{eq} \left(1 - e^{-t/\tau_{eq}}\right) \tag{7.8}$$

$$R_{eq} = \frac{\tau_{eq}}{C_w} \tag{7.9}$$

An STTT test conducted on an industrial motor drive is depicted in Fig. 7.4, following the methodology outlined in [23]. In the figure, the dissipated energy and overtemperature characteristics are represented in blue, while their respective interpolations using equations (7.6) and (7.8) are plotted in red. It's evident that for this motor type, the methodology in [23] yields accurate results, as the fitting functions closely align with the measured data, enabling the extraction of reliable values for C_w and R_{eq}. However, it's worth noting that this testing approach tends to encounter difficulties with high-performance motors, as elaborated in the following section.

7.3 New identification method

The motor being tested exhibits several unique characteristics that render the conventional STTT procedure impractical (due to inaccessible phase terminals) and unreliable (owing to the failure of the first-order model). In the following these challenges have been addressed and resolved.

7.3.1 Parallel phase connection

As discussed in Section 7.2, the series connection illustrated in Fig. 7.2a is not viable for onboard traction motors, where typically only the input terminals of the three phases are accessible. In the prototype under examination, the star point is made accessible through an additional connection, introducing a resistance R_{add} compatible with the phase resistance, due to the small section of the additional wire.

An initial alternative to the all-series connection is the parallel configuration depicted in Fig. 7.5a. While this setup still ensures uniform heating across the three phases, it comes with two drawbacks:

1. managing a high direct current through a small resistance.
2. Introducing the resistance R_{add} in series with the motor resistances.

Regarding point 1, the DC current generator must supply three times the rated RMS phase current of the machine, which is typically already in the order of hundreds of amperes, to a load of a few milliohms or less, given the paralleled phases. For instance, it may need to provide 300 to 700 amperes at 1 to 5 volts. Achieving stable and accurate control of such a high direct current poses a significant challenge for most DC sources, necessitating specialized equipment.

Concerning point 2, the term R_{add} is unrelated to the winding temperature and consequently invalidates the estimation of winding temperature through (7.3). Taking these challenges into account, the parallel connection depicted in Fig. 7.5a has been disregarded.

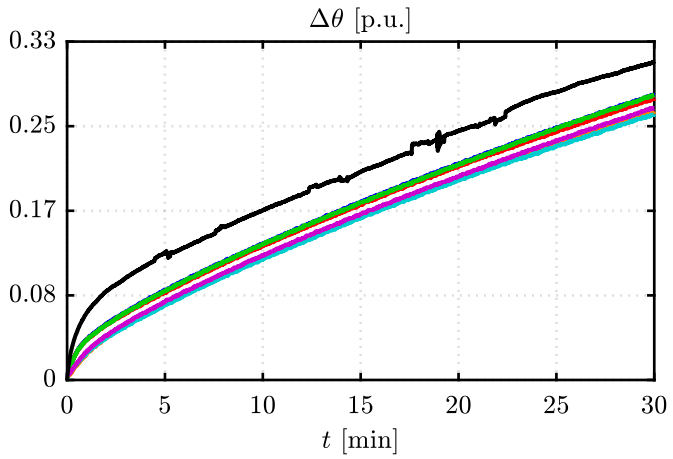

Fig. 7.6 Impact of R_{add} on the average winding temperature estimate (black line) under parallel phase connection with DC excitation. The colored lines represent local winding temperatures measured using dedicated thermistors.

The impact of R_{add} on the average temperature estimate is shown in Fig. 7.6, where the three phases were parallel connected and DC excited. The figure displays, in black, the average winding temperature estimated using (7.3), alongside measurements from all the thermistors embedded in the prototype's winding. These

thermistors are intended to map its thermal gradient, including temperature hotspots. As observed, the temperature estimate computed with (7.3) exceeds any measured temperature, which is not realistic. This discrepancy can be attributed to the additional wire used to access the star point, which, due to its reduced section, was considerably hotter than the stator winding. Consequently, it distorts the average temperature estimate.

7.3.2 Dual supply connection

As an alternative to the parallel phase connection, two DC current sources were employed, as illustrated in Fig. 7.5b. The first DC source excites phases a and b and is utilized for measuring phase resistance, losses, and temperature variation. The second DC source excites the third phase through the star point with the exact same current, ensuring thermal symmetry among the phases. This configuration necessitates two DC sources with a current rating one-third that of the setup in Fig. 7.5a. Additionally, the measurement branch from a to b does not include R_{add}, allowing for an independent estimation of the average winding temperature using (7.3). Consequently, the computations for resistance and dissipated power are adjusted as follows:

$$R_{dc} = \frac{v_{dc}}{2i_{dc}} \tag{7.10}$$

$$P_j = \frac{3}{2} v_{dc} \cdot i_{dc} \tag{7.11}$$

The phase connection illustrated in Fig. 7.5b has demonstrated accuracy and reliability, thus it was selected for the proposed STTT test.

7.3.3 New model and parameters evaluation

A crucial aspect of the original STTT in [23] is that the duration of the initial thermal transient, i.e. the adiabatic temperature rise range $\Delta\theta_{st}$ and the corresponding time interval Δt_{st} where the system follows a first order transient, was easy to be chosen arbitrarily. In practice, the temperature domain of interpolation of the dissipated

energy with (7.6) and the time domain of interpolation of the temperature rise with (7.8) were easily determined by trial and error.

In this regard, the technique has demonstrated its robustness for industrial motors, accommodating significant variations in temperature and time intervals. However, compact and highly-loaded traction machines are engineered for extremely rapid heat extraction. Consequently, the fundamental assumption of STTT, namely that the initial phase of the thermal transient is adiabatic, tends to be invalid. Specifically, the function $W(\Delta\theta)$ begins to exhibit nonlinear growth immediately, precluding its approximation with a straight line to determine the thermal capacitance C_w using (7.6).

To address this challenge, a nonlinear $W(\Delta\theta)$ function was considered and approximated using its third-order Taylor series expansion.

$$\hat{W}(\Delta\theta) = a_3 \cdot \Delta\theta^3 + a_2 \cdot \Delta\theta^2 + a_1 \cdot \Delta\theta \tag{7.12}$$

The initial derivative of $W(\Delta\theta)$ remains indicative of the winding thermal capacitance C_w and can be determined analytically as:

$$\left.\frac{d\hat{W}}{d\Delta\theta}\right|_{\Delta\theta=0} = a_1 \tag{7.13}$$

$$C_w = a_1 \tag{7.14}$$

Furthermore, the significant thermal coupling between the stator winding and iron undermines the reliability of the original LPTN depicted in Fig. 7.2b, as the heat transfer to the iron cannot be ignored. Additionally, in this scenario, estimating R_{eq} using (7.8) would heavily depend on the selected interpolation time Δt_{st}. This limitation was addressed by incorporating the iron thermal capacitance C_{Fe} into the equivalent LPTN, as illustrated in Fig. 7.5c. The dissipation of heat from the stator iron to the coolant or ambient environment is disregarded, as it is negligible during the initial thermal transient. Consequently, the adiabatic assumption is extended from the winding alone to encompass the entire stator. The temperature rise is once again interpolated using the analytical solution of the LPTN, facilitating the estimation of the parameter R_{eq} from the time constant τ_{eq}:

$$\hat{\Delta\theta}(t) = \frac{P_j}{C_w + C_{Fe}} t + P_j R_{eq} \frac{C_{Fe}^2}{(C_w + C_{Fe})^2} \left(1 - e^{-t/\tau'_{eq}}\right) \tag{7.15}$$

$$\tau'_{eq} = \frac{C_w C_{Fe}}{C_w + C_{Fe}} \cdot R_{eq} \approx C_w \cdot R_{eq} \tag{7.16}$$

7.4 DC steady state test

The DC Steady State (SS) test utilizes the same excitation and measurement setup as the STTT, allowing for the combination of both tests into a single procedure. While the STTT focuses on the initial thermal transient, typically within the first few minutes of DC excitation, the SS test aims to measure the winding temperature once the thermal equilibrium is reached. Similarly, the excitation voltage and current are monitored during the SS test. This DC excitation enables an accurate evaluation of the regime power loss without any influence from AC or iron losses.

The steady-state overtemperatures of the measurable and hotspot points are denoted as $\Delta\theta_m^{ss}$ and $\Delta\theta_h^{ss}$ respectively, and are used to compute the equivalent steady-state thermal resistances:

$$\begin{cases} R_m^{ss} = \dfrac{\Delta\theta_m^{ss}}{P_j} \\ R_h^{ss} = \dfrac{\Delta\theta_h^{ss}}{P_j} \end{cases} \tag{7.17}$$

7.5 Hotspot winding temperature observer

7.5.1 Decoupling of stator and rotor

The primary focus of this section is to monitor the winding temperature hotspot. The temperature of the motor is influenced by both stator and rotor losses, with heat dissipation primarily occurring through liquid cooling and partially through the rotor,

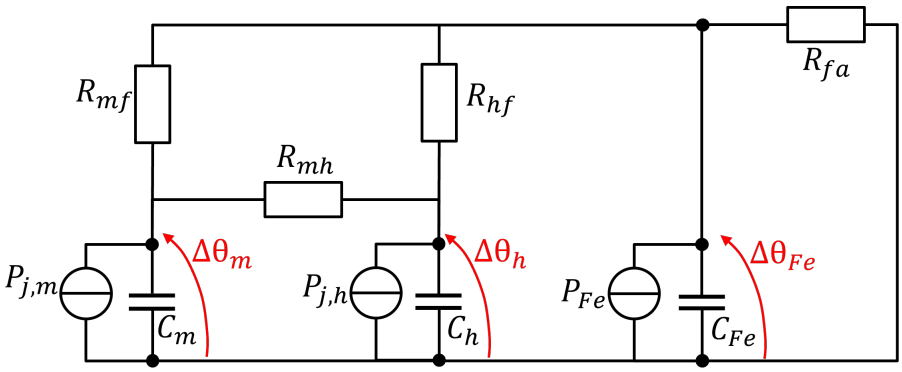

(a)

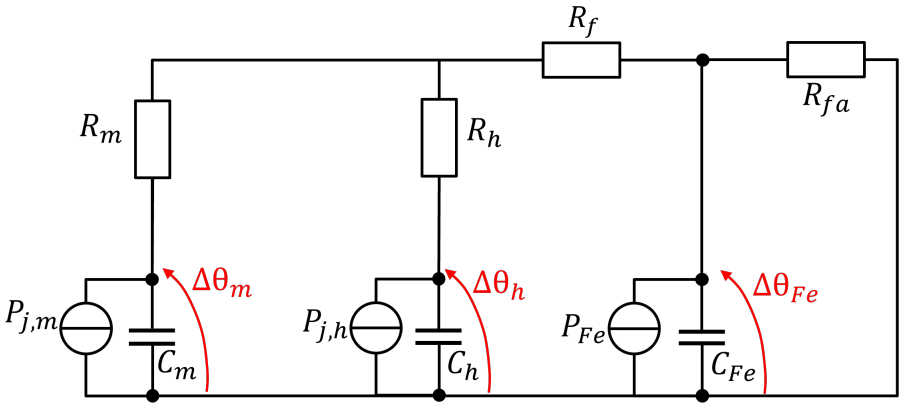

(b)

Fig. 7.7 Proposed LPTN for the hotspot temperature observer. (a) Physical model, delta connected. (b) Equivalent star connection, for calibration purposes.

shaft, end winding, and other components. In essence, there exists thermal coupling between the stator and rotor.

However, it's observed that the thermal time constant for heat transfer from the stator to the rotor is significantly slower compared to the thermal coupling between the measurable and hotspot winding points. This observation is supported by both FEA and experimental evidence. Consequently, when designing a stator hotspot observer, the rotor losses and thermal dynamics can be disregarded, provided that a thermistor is present at the accessible winding point. Hence, the proposed hotspot observer only models the behavior of the stator while neglecting the rotor temperature and losses.

Nevertheless, if a rotor thermal model is available, it can be incorporated into the proposed stator LPTN described in the following paragraph, thereby enhancing the accuracy of hotspot temperature estimation.

7.5.2 Stator thermal network

In the proposed LPTN, the stator winding is divided into two sections, each considered to be at a uniform temperature. The first section, denoted with the subscript m, corresponds to the measurable temperature θ_m, and it includes the inverter connection where the thermistor is located (refer to Fig. 7.1). The second section, indicated with the subscript h, corresponds to the unknown hotspot temperature θ_h, which needs to be estimated. This simplified discretization of the winding enables differentiation between measurable and hotspot temperatures, with limited complexity of the thermal network, facilitating real-time execution of the observer.

A thermal capacitance is assigned to each section (C_m and C_h respectively), along with the corresponding Joule losses P_{jm} and P_{jh}. Both the capacitance and the losses are assumed to be proportional to the volume of the corresponding winding section. The sum of C_m and C_h represents the total winding thermal capacitance C_w:

$$\begin{cases} C_h &= x \cdot C_w \\ C_m &= (1-x) \cdot C_w \end{cases} \tag{7.18}$$

$$0 < x < 1 \tag{7.19}$$

where x represents the fraction of the winding associated with the hotspot. Similarly, for copper losses:

$$\begin{cases} P_{jh} &= x \cdot P_j \\ P_{jm} &= (1-x) \cdot P_j \end{cases} \tag{7.20}$$

where P_j represents the aggregate stator AC and DC copper losses.

Additionally, the stator iron thermal capacitance C_{Fe} and temperature θ_{Fe} are introduced, and the associated iron losses P_{Fe}.

Regarding heat transfer, the thermal resistances R_{mf} and R_{hf} model the thermal coupling between each winding section and the stator iron, while R_{mh} represents the interaction between the two winding sections, and R_{fa} represents the iron-to-ambient

thermal resistance. To maintain a manageable complexity of the LPTN, the direct heat dissipation from the winding to the ambient (e.g., through end-windings) is neglected.

The system is described in terms of overtemperature with respect to the ambient temperature θ_a:

$$\begin{cases} \Delta\theta_h &= \theta_h - \theta_a \\ \Delta\theta_m &= \theta_m - \theta_a \\ \Delta\theta_{Fe} &= \theta_{Fe} - \theta_a \end{cases} \tag{7.21}$$

In practice , for PMSM with liquid cooling, θ_a can be considered equal to the inlet liquid temperature, which is typically measured in traction drives.

The resulting LPTN, as shown in Fig. 7.7a, effectively captures the physical thermal behavior of the stator winding. However, for calibration and real-time implementation purposes, it is convenient to apply a $\Delta - Y$ transformation to the three resistances R_{mf}, R_{hf}, and R_{mh}, resulting in the LPTN presented in Fig. 7.7b:

$$\begin{cases} R_m = \dfrac{R_{mf} \cdot R_{mh}}{R_{mf} + R_{mh} + R_{hf}} \\ R_h = \dfrac{R_{hf} \cdot R_{mh}}{R_{mf} + R_{mh} + R_{hf}} \\ R_f = \dfrac{R_{mf} \cdot R_{hf}}{R_{mf} + R_{mh} + R_{hf}} \end{cases} \tag{7.22}$$

It is worth mentioning that the two LPTNs in Figs. 7.7a and 7.7b are analytically equivalent. However, while the first one represents a realistic thermal network, the second one allows for a simpler solution, calibration, and real-time implementation. Therefore, the latter LPTN will be utilized in the following sections.

7.6 Design and calibration of the observer

The proposed temperature observer, depicted in Fig. 7.8, constitutes a Multiple Input Single Output (MISO) system with three inputs: the measured overtemperature $\Delta\theta_m$, the estimated Joule and iron losses P_j, P_{Fe}, and a single output, that is the observed hotspot overtemperature $\Delta\theta_h$.

Within the feasible operational range of the drive, such as between 0°C and 200°C, the thermal properties of all stator materials (iron, copper, potting, insulation, etc.) remain relatively constant. Hence, the system is considered linear, and the principle of superposition holds.

7.6.1 Solution of the LPTN and hotspot observer implementation

The solution of the network shown in Fig. 7.7b is retrieved in the Laplace domain:

$$\hat{\theta}_h = \left.\frac{\hat{\theta}_h}{\theta_m}\right|_{\theta_m} \cdot \theta_m + \left.\frac{\hat{\theta}_h}{P_j}\right|_{P_j} \cdot P_j + \left.\frac{\hat{\theta}_h}{P_{Fe}}\right|_{P_{Fe}} \cdot P_{Fe} \tag{7.23}$$

$$\hat{\Delta\theta}_h = H_\theta \cdot \Delta\theta_m + H_j \cdot P_j + H_{Fe} \cdot P_{Fe} \tag{7.24}$$

The 3 transfer functions H_θ, H_j, and H_{Fe} can be combined and expressed as:

$$\hat{\Delta\theta}_h = \frac{(a_\theta s + b_\theta)\,\Delta\theta_m + (a_j s + b_j)\,P_j + b_f P_{Fe}}{p_1 s^2 + p_2 s + p_3} \tag{7.25}$$

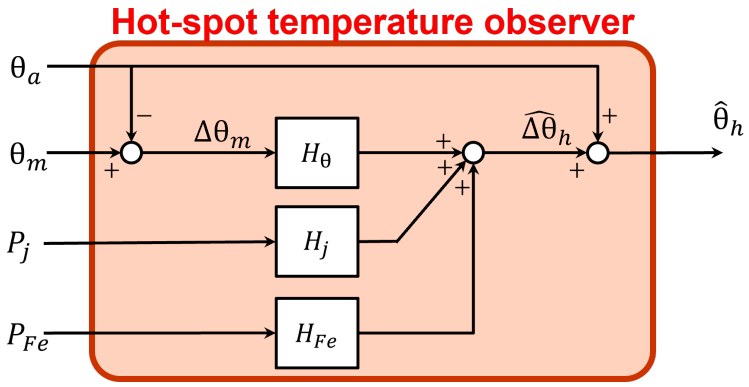

Fig. 7.8 MISO hotspot windings observer block diagram.

In other words, the two transfer functions H_θ and H_j each have one zero. The numerator of H_{Fe} is real, and the three transfer functions share the same two poles, representing the poles of the physical system. Altogether, the solution of the LPTN (7.25) involves seven parameters, which are analytically determined based on the four thermal resistances and three capacitances:

$$\begin{cases} a_\theta = R_{fa} R_f C_{Fe} \\ b_\theta = R_{fa} + R_f \\ a_j = R_{fa}\left(R_f R_m + R_f R_h + R_m R_h\right) C_{Fe} \\ b_j = R_f R_m + R_f R_h + R_m R_h + R_m R_{fa} + R_h R_{fa} \\ b_f = R_m R_f a \\ p_1 = C_{Fe} C_h R_{fa}\left(R_h R_f + R_m R_f + R_h R_m\right) \\ p_2 = C_{Fe} R_{fa}\left(R_f + R_m\right) + \\ \quad + C_h\left(R_h R_f + R_m R_f + R_h R_m + R_h R_{fa} + R_m R_{fa}\right) \\ p_3 = R_f + R_m + R_{fa} \end{cases} \tag{7.26}$$

The analytical derivation of (7.26) is not provided here for brevity, but it can be easily obtained by solving the LPTN depicted in Fig. 7.7b.

The hotspot observer can be implemented as shown in Fig. 7.8 and embedded in real-time control systems. To achieve this, each transfer function H_θ, H_j, and H_{Fe} needs to be discretized. For instance, H_θ can be discretized as H_θ^d:

$$H_\theta^d = \frac{-\frac{a_\theta}{T_s} z^{-1} + \left(\frac{a_\theta}{T_s} + b_\theta\right)}{\frac{p_1}{T_s^2} z^{-2} - \left(\frac{2p_1}{T_s^2} z^{-2} + \frac{p_2}{T_s}\right) z^{-1} + \left(\frac{p_1}{T_s^2} z^{-2} + \frac{p_2}{T_s} + p_3\right)} \tag{7.27}$$

where T_s is the sampling time. The discretization of the two transfer functions H_j and H_{Fe} follows a similar form as (7.27) but is not detailed here.

7.6.2 Calibration of the hotspot observer

One of the primary challenges with most temperature observers lies in determining the LPTN parameters, such as the thermal resistances and capacitances. These parameters could be theoretically determined based on motor geometry and materi-

als, but this information is often uncertain due to complex design geometries and manufacturing tolerances. Therefore, an experimental-based calibration procedure is strongly preferred, involving direct measurement of LPTN parameters on the motor under test.

In this study, the proposed calibration procedure relies on two simple characterization tests: the STTT and the SS tests, as previously described in Section 7.1. The STTT estimates C_w, C_{Fe}, and R_{eq}, while the SS test provides R_m^{ss} and R_h^{ss}. A dedicated post-processing method is proposed to extract the LPTN parameters from the results of these tests.

Specifically, the winding capacitance measured during the STTT allows computation of the capacitances C_h and C_m according to (7.18), where the coefficient x is arbitrarily determined. Moreover, during the STTT, i.e., in the initial phase of the thermal transient, the following assumptions can be made:

- the iron losses are negligible due to DC excitation, and the stator iron remains at room temperature ($\Delta\theta_{Fe} = 0$, $P_{Fe} = 0$);
- the temperature of the two parts of the winding increases simultaneously, meaning the winding temperature can be considered uniform ($\Delta\theta_h = \Delta\theta_m$, $R_{mh} = 0$).

The second hypothesis corresponds to shorting the resistance R_{mh}. Therefore, the two winding sections can be aggregated, leading to the equivalent LPTN in Fig. 7.9. By comparing this network with the one in Fig. 8.20, and still neglecting R_{mh}, the equivalent thermal resistance estimated by the STTT can be interpreted as:

$$R_{eq} = R_{mf} \parallel R_{hf} = R_f \tag{7.28}$$

In other words, the equivalent thermal resistance R_{eq} measured in the STTT test can be interpreted as the thermal resistance R_f.

Regarding the SS test, during the DC thermal regime, the LPTN in Fig. 7.7b simplifies to the configuration shown in Fig. 7.10, where all the capacitances and the iron loss term are removed. The series combination of thermal resistances R_f and R_{fa} is denoted as R_{ff}. Additionally, the parameter y is introduced:

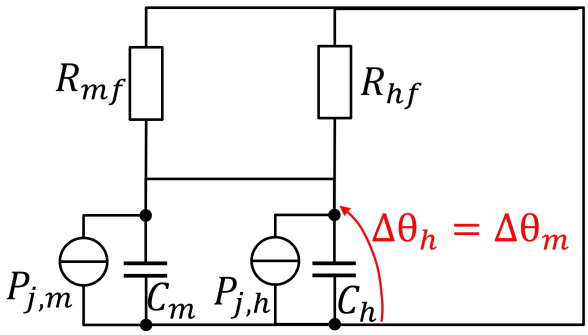

Fig. 7.9 Equivalent LPTN for the STTT test.

$$y = \frac{R_f}{R_{ff}} \tag{7.29}$$

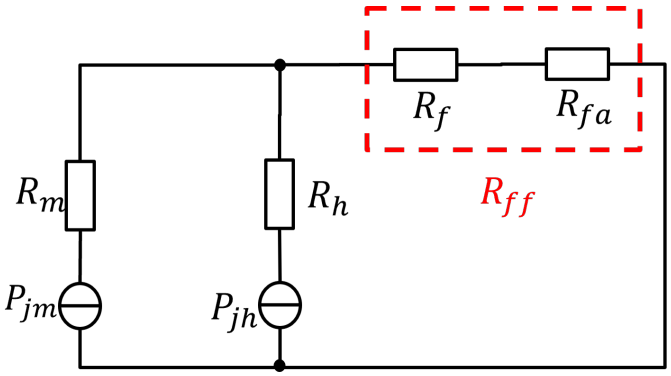

Fig. 7.10 Equivalent LPTN for the DC steady state test.

The steady-state solution of this DC network, expressed in terms of overtemperatures, is given by:

$$\begin{cases} \Delta\theta_m^{ss} = P_j R_{ff} + (1-x) P_j R_m \\ \Delta\theta_h^{ss} = P_j R_{ff} + x P_j R_h \end{cases} \tag{7.30}$$

The same solution can be expressed in terms of the steady-state equivalent thermal resistances as follows:

$$\begin{cases} R_m^{ss} = R_{ff} + (1-x) R_m \\ R_h^{ss} = R_{ff} + x R_h \end{cases} \tag{7.31}$$

Finally, by manipulating (7.31), all the resistances of the LPTN can be determined and expressed as a function of the measurements obtained during commissioning and the parameters x and y:

$$\begin{cases} R_m = \dfrac{R_m^{ss} - \dfrac{R_{eq}}{y}}{(1-x)} \\ R_h = \dfrac{R_h^{ss} - \dfrac{R_{eq}}{y}}{x} \\ R_f = R_{eq} \\ R_{fa} = R_{eq} \cdot \dfrac{1-y}{y} \end{cases} \tag{7.32}$$

To ensure that the LPTN parameters have physical significance, meaning all thermal capacitances and resistances are greater than zero, and considering $R_h^{ss} > R_m^{ss}$, the parameter y is bounded as follows:

$$\frac{R_{eq}}{R_m^{ss}} < y < 1 \tag{7.33}$$

Overall, the LPTN parameters are fully calibrated based on the STTT and SS tests along with the two arbitrary parameters x and y, which are determined based on the user's experience. However, according to (7.19) and (7.33), these parameters are bounded within a narrow range, simplifying the tuning procedure. Once the coefficients are determined, the hotspot temperature observer is implemented following the block diagram in Fig. 7.8. This observer can be easily discretized according to (7.27), (7.26), and embedded in the motor control algorithm for real-time hotspot temperature monitoring during drive operation.

7.6.3 Final considerations

To thermally characterize the machine, the STTT procedure is employed. This method requires an accessible star point for parameter evaluation. Notably, temperature measurements are not necessary. To bypass the need for a star point, an alternative solution worth investigating is supplying the machine with low-frequency

sinusoidal currents. This approach aims to minimize the impact of AC losses in both copper and iron. However, using an inverter for this purpose might not be feasible due to the non-negligible effects of PWM.

For hotspot calibration in conjunction with the STTT, a DC steady-state test and the hotspot temperature measurement is essential. Therefore, for a series production, the prototyped must have an accessible star point and dedicated thermistors for mapping the thermal gradient and identifying the hotspot. Although FEA and CAD models can be utilized, achieving an accurate thermal model is challenging. Consequently, experimental testing is often the most reliable method.

Chapter 8

Experimental results on traction motors

In this chapter, the aspects discussed in this work are validated with experimental results. All tested machines are used in traction applications. The following is a brief overview of each subsection:

- In Section 8.1, the experimental procedure to magnetically characterize machines by retrieving the flux maps is described using two different approaches.
- In Section 8.2, a ferrite motor for a battery electric vehicle, designed in collaboration with an automotive company, is tested, and the efficiency map is evaluated under both hot and cold conditions.
- In Section 8.3, an IPM motor is tested and characterized at McMaster University, using a power analyzer-based identification to retrieve the flux map. Moreover, the experimental procedure is adopted to test the full e-Axle, including the gearbox and differential. Finally, the efficiency map of the e-Axle is evaluated.
- In Section 8.4, the proposed methodology for short circuit current computation is validated using a commercial automotive motor, both in steady-state and transient conditions.

- In the last two sections, the thermal parameters of an e-motor are retrieved using the improved STTT, and the results are used for winding hotspot calibration.

8.1 Flux maps identification procedure

In this section, the procedure to retrieve the flux maps are briefly reported. As [24], direct measurement of flux linkages is not feasible; however, they can be retrieved using voltage equations (2.26), with respect the model illustrated in Section 2.5.1. By specifying an operating point, characterized by current and speed, the flux linkages can be determined via (8.1).

$$\begin{cases} \lambda_d = \dfrac{v_q - R_s i_q}{\omega} \\ \lambda_q = -\dfrac{v_d - R_s i_d}{\omega} \end{cases} \tag{8.1}$$

The key principle in identifying experimental flux maps is to conduct tests with the Motor Under Test (MUT) operating at low speed. At low speeds, iron losses can be reasonably disregarded. Referring to Fig. 2.17, it can be observed that $\boldsymbol{i}_{dq}^{Fe}$ equals zero, thereby making the total current equivalent to the magnetizing current as per (8.2).

$$\boldsymbol{i}_{dq} = \boldsymbol{i}_{dq}^{m} \tag{8.2}$$

Essentially, the objective is to maintain a low speed while ensuring it's high enough for accurate voltage measurements. A general guideline is to operate the Machine Under Test (MUT) at one-third of its nominal (or corner) speed. The main challenge is to achieve flux maps that are unaffected by variations in stator resistance. In the study referenced as [24], two separate measurements are conducted for each operating point to compensate for the series voltage drop, both in motor and generator (or braking) conditions. Averaging the dq flux for both motor and generator using equation (8.3) renders these quantities independent of stator electrical resistance. For an IPM machine, motoring condition implies operating with $(i_d < 0, i_q > 0)$, while in braking it's $(i_d < 0, i_q < 0)$. Basically, the q current is reversed while maintaining

the same amplitude, or alternatively, supplying the motor with $\boldsymbol{i}_{dq}$ and then with $\boldsymbol{i}^{*}_{dq}$. To visualize this, Fig. 8.1 illustrates a vector diagram, where the quantities labeled with subscripts 1 and 2 correspond to motor and generator conditions, respectively.

$$\begin{cases} \lambda_d = \dfrac{1}{\omega} \cdot \left(\dfrac{v_{q1} + v_{q2}}{2} \right) \\ \lambda_q = \dfrac{1}{\omega} \cdot \left(\dfrac{v_{d1} - v_{d2}}{2} \right) \end{cases} \tag{8.3}$$

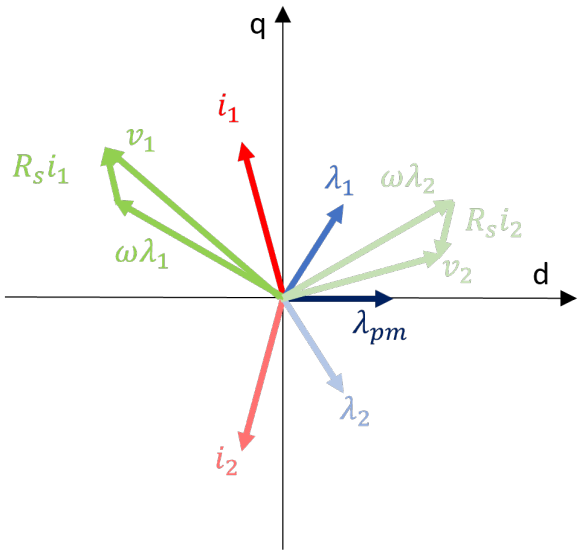

Fig. 8.1 Vector diagram depicts motoring conditions (subscript 1) and braking conditions (subscript 2) in the dq frame. Throughout the flux map identification process, i_1 and i_2 represent complex conjugates.

Additionally, the control reference signals can used for measurements, following a similar principle as discussed in [150]. If the reference signals from the inverter are utilized instead of actual measurements, it's essential to compensate for inverter errors. These errors can be represented by equation (8.4), where x^{ref} denotes a reference quantity, R_d represents the equivalent resistance of the converter, and k is a constant parameter.

$$\boldsymbol{v}_{dq} = \boldsymbol{v}^{ref}_{dq} + \Delta\boldsymbol{v}_{dq} = \boldsymbol{v}^{ref}_{dq} + k \cdot sign(\boldsymbol{i}_{abc}) + R_d \cdot \boldsymbol{i}_{dq} \tag{8.4}$$

Similarly, the combination of motor and brake operations also compensates for the effects of the inverter. Consequently, equations (8.3) can be reformulated as shown in (8.5).

$$\begin{cases} \lambda_d = \dfrac{1}{\omega} \cdot \left(\dfrac{v_{q1}^{ref} + v_{q2}^{ref}}{2} \right) \\ \lambda_q = \dfrac{1}{\omega} \cdot \left(\dfrac{v_{d1}^{ref} - v_{d2}^{ref}}{2} \right) \end{cases} \tag{8.5}$$

To account for the temperature effect on resistance, an additional motoring condition is necessary. It's observed that the average copper temperature during the two motor operations is reasonably close to the average temperature during braking operations. Consequently, the final expressions for retrieving the flux linkage are represented by equation (8.6). It's worth noting that the last measurement becomes less crucial if both copper temperature and PM flux linkages are monitored and can be treated as constant.

$$\begin{cases} \lambda_d = \dfrac{1}{2 \cdot \omega} \left(\dfrac{v_{q1} + v_{q3}}{2} + v_{q2} \right) \\ \lambda_q = \dfrac{1}{2 \cdot \omega} \left(\dfrac{v_{d1} + v_{d3}}{2} - v_{d2} \right) \end{cases} \tag{8.6}$$

In an ideal scenario, the identification of flux maps necessitates the direct measurement of voltages and currents in 3-phase coordinates, converted to the dq frame using the measured rotor position. Additionally, a torque sensor is essential. The preferred approach involves capturing waveforms of all quantities for at least one mechanical period to expedite the test process and prevent excessive heating of the machine. However, achieving this requirement is not always feasible. It is possible to relate the procedure solely on the dq reference current, average measurements of 3-phase currents, voltages, power, and torque. While a position sensor is part of the setup, its signal accuracy can be compromised due to low communication rates. Therefore, an alternative method for retrieving flux linkages is proposed in [151]: in dq coordinates, electrical power can be computed as outlined in equation (8.7), and by reversing this calculation, the voltages can be obtained.

$$\begin{cases} P = \dfrac{3}{2}(v_d \cdot i_d^{ref} + v_q \cdot i_q^{ref}) \\ Q = \dfrac{3}{2}(v_q \cdot i_d^{ref} + v_d \cdot i_q^{ref}) \end{cases} \tag{8.7}$$

$$\begin{cases} v_d = \dfrac{2 \cdot (P \cdot i_d^{ref} - Q \cdot i_q^{ref})}{3 \cdot |\boldsymbol{i}_{dq}^{ref}|^2} \\ v_q = \dfrac{2 \cdot (P \cdot i_q^{ref} - Q \cdot i_d^{ref})}{3 \cdot |\boldsymbol{i}_{dq}^{ref}|^2} \end{cases} \tag{8.8}$$

In the flux map identification process, the tested operating points can span various areas on the i_d, i_q plane. Typically, the current domain is discretized regularly in a rectangular area, covering all relevant working points. However, for high-power density motors, such as those used in traction applications, it might be advantageous to explore a polar domain on the current plane. This entails fixing the current amplitude at the maximum motor current and varying the current angle γ. Consider conducting the identification test with Cartesian coordinates ranging from 0 to the maximum current for both i_d and i_q. Some working points may necessitate a current exceeding the maximum, reaching the point $(i_d = i_{max}, i_q = i_{max})$, i.e., an amplitude of $\sqrt{2} i_{max}$. For such machines, even a few seconds under these conditions could lead to motor failure due to thermal overload. It's important to note that for synchronous reluctance motors, the current domain can be selected on the one quadrant of the plane, as symmetries can be applied for the others. Conversely, for PM motors, a region of the second quadrant is required if the entire machine is to be characterized.

In the following two motors for traction application are characterized. In Section 8.2 a ferrite motor is tested using the direct measurement of the dq voltages, while in Section 8.3 the machine is be tested using the power analyzer method.

8.2 Ferrite PMSM for BEV

The prototype discussed and evaluated in this section is one of three prototypes resulting from a collaboration between Politecnico di Torino and an automotive company. The objective of the research project was to design, manufacture, and test

three motors, all sharing the distinctive feature of lacking rare earth magnets. As of now, the first prototype has been manufactured and tested, the second is ready for testing, and the design for the final prototype is finalized. Since the machine's design is proprietary, all quantities are expressed in p.u..

8.2.1 Test rig setup

The test rig in question is the TEST-eDRIVE infrastructure located at the Power Electronics Innovation Center (PEIC) at Politecnico di Torino. The overall schematic is depicted in Fig. 8.2, and key specifications are provided in Table 8.1. The components of the test rig include:

- MUT: prototype to be tested;
- MUT inverter: OnSemi inverter with dSpace interface;
- Driving Machine (DM): induction motor from Velicon, set the speed of the prototype;
- DM inverter: supply the DM and it is controlled by the control system. It is equipped with an Active Front End (AFE), to regenerate the power;
- DC source: battery emulator from ITECH, 1500 V, 400A, 180 kW peak, with AFE;
- HBK data logger: Gen7t data logger from HBK + acquisition module at 2 MS/s
  - direct measure of line voltages and, phase currents through LEM IT-600s current sensors;
  - temperature measurement utilizing thermocouple interfaces for accurate temperature readings;
  - shaft torque and speed measured by an HBK T12HP torque meter for accurate measurements of shaft torque and speed;
  - acquisition of the electric angle from the control and measure trigger from dSpace board;

- cooling system: integrated within the test rig system, allowing for control of inlet temperature and flow rate.

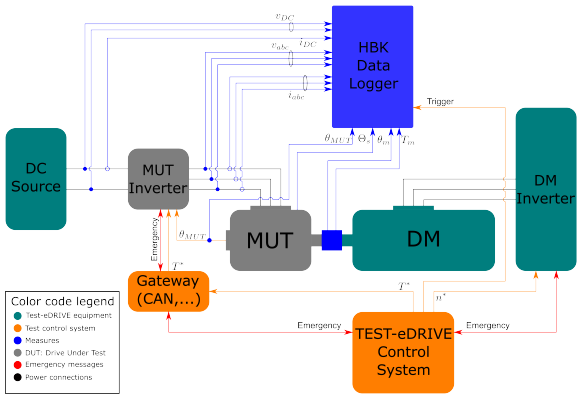

Fig. 8.2 Scheme of the TEST-eDRIVE infrastructure.

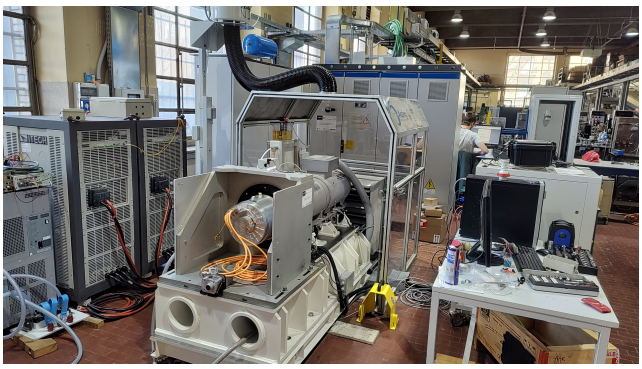

Fig. 8.3 Experimental setup at TEST-eDRIVE.

Table 8.1 Main data of the TEST-eDRIVE infrastructure.

Max torque	[Nm]	200
Max power	[kW]	150
Base speed	[rpm]	6000
Max speed	[rpm]	20000
Coolant temperature	[°C]	0-80
Flow rate	[l/min]	0-20
Max inlet pressure	[bar]	2
Max loss for cooling system	[kW]	10

8.2.2 Experimental flux maps

The flux maps of the motor are measured according to the procedure described at the beginning of this Chapter. The test is conducted in cold conditions, and it is performed according to the expected demagnetization limits of the motor. The contours of the measured λ_d, λ_q and T are reported in Fig. 8.4 together with the curves of the flux maps, i.e. the flux linkages function of the currents, showing good accuracy compared with the simulated results. Note that the currents are normalized to the maximum tested current per axis.

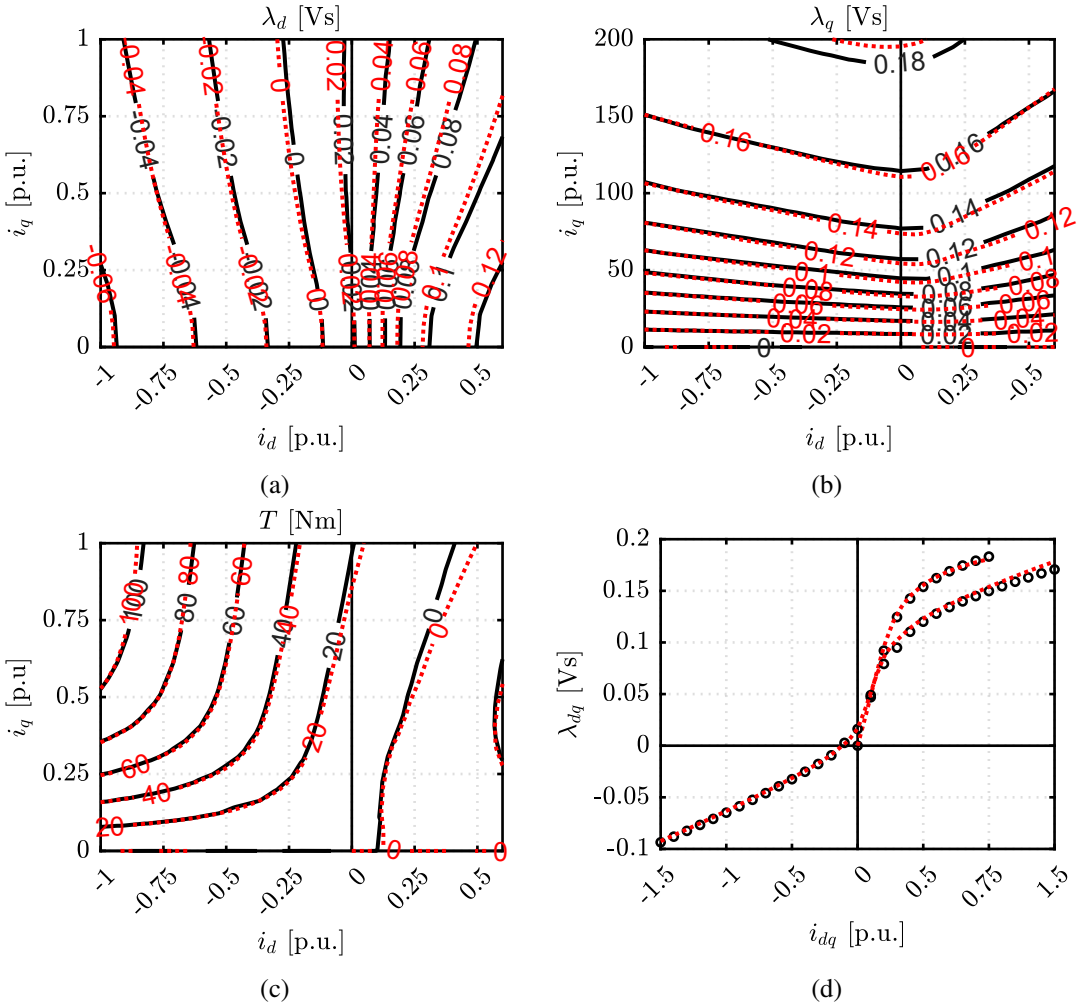

Fig. 8.4 Comparison between measured (black) and simulated (red) flux maps: (a) d-axis flux linkage function of (i_d, i_q) (b) q-axis flux linkage function of (i_d, i_q), (c) measured torque function of (i_d, i_q) and (d) flux curves.

8.2.3 Experimental efficiency maps

The efficiency map is measured by setting the speed of the drive motor (DM) and controlling the torque of the motor under test (MUT). Throughout the test, winding temperatures are sampled along with other measurements. Additionally, waiting times are inserted between speed changes to prevent winding overheating and an increase in permanent magnet temperature. The test is conducted twice:

1. The first test is performed with permanent magnets at ambient temperature (25°C).
2. The second test is conducted after 2 hours, with the coolant at 60°C.

Before both tests, control calibration and some preliminary runs are carried out. These preliminary runs aim to check and calibrate the Direct Flux Vector Control (DFVC) [82] at the operating limits and identify mechanical limits, particularly with reference to vibrations.

Efficiency map in cold conditions

The test is initiated at ambient temperature, with the MUT controlled using DFVC. The DM sets the speed across the test grid. Winding temperature is continuously measured and monitored during the test, with waiting periods introduced when the temperature exceeds predefined thresholds. Additionally, the temperature data is utilized to adjust the DC loss in post-processing.

The efficiency map and the loss map under cold conditions are depicted in Fig. 8.5. The contours represent simulated values, while the colored dots represent measured points. The color scale remains consistent for both experimental and simulated data. The comparison between experimental and simulated results shows good agreement, with a slight tendency for the model to overestimate losses, thereby marginally impacting efficiency.

During the cold test, the current is limited to prevent irreversible demagnetization of the ferrite PMs. Consequently, this results in a reduced peak torque of 140 Nm.

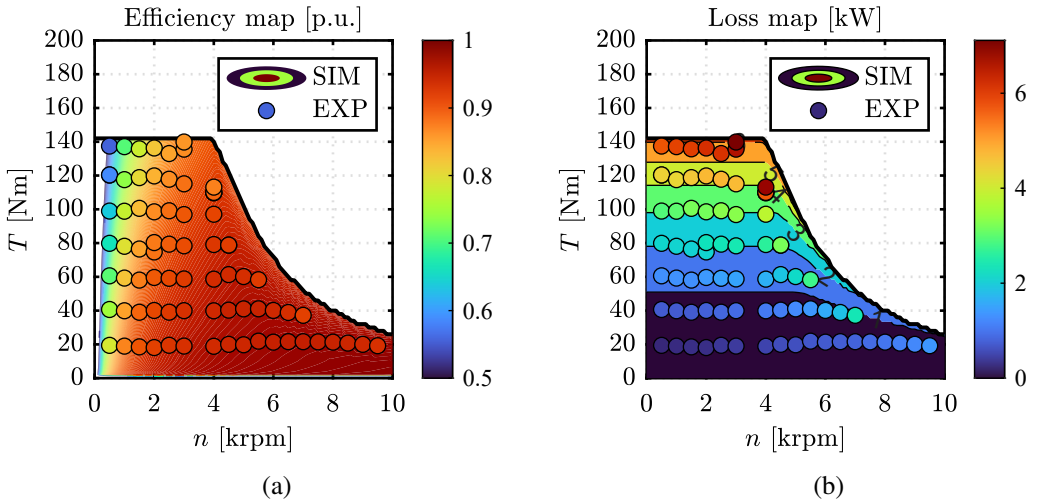

Fig. 8.5 Comparison between measured data and simulated values of (a) efficiency map and b) loss map for the cold condition test.

Efficiency map in hot conditions

The efficiency map is repeated after 2 hours of heating at 60°C to elevate the temperature of the PMs and increase the demagnetization limit. Under these conditions, the maximum current is set accordingly, enabling higher torque. The comparison between measurements and simulations reveals good agreement, as shown in Fig. 8.6, albeit with a general tendency to overestimate efficiency. This overestimation is partly due to the neglect of iron and mechanical losses in the model.

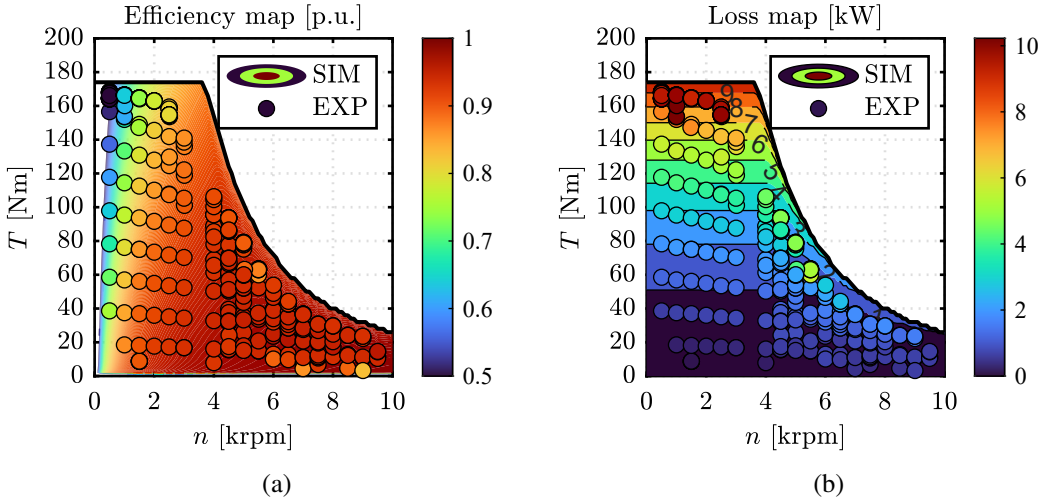

Fig. 8.6 Comparison between measured data and simulated values of (a) efficiency map and (b) loss map for the hot condition test.

8.3 Power analyzer based identification of traction PMSM

In this section, an IPM motor for a subcompact production EV is tested. While supplier data for the motor was not available, the torque rating, maximum DC bus voltage, and speed limitations of the motor were determined based on the specifications of the vehicle the motor is used in [152]. An automotive-grade inverter controls the motor under examination, while a power analyzer is employed to measure electrical quantities. Notably, the flux map identification process does not depend on position sensor data; instead, it solely relies on the dq current control supplied by the inverter. This methodology is not limited to electric motors but can be extended to the entire e-Axle system. To validate its efficacy, the methodology is tested on an IPM 2-in-1 e-Axle, encompassing the electric machine, gearbox, and differential. The tests are conducted at the McMaster Automotive Research Centre (MARC) of the McMaster University, Hamilton ON, Canada.

8.3.1 Test rig setup

The experimental test setup, depicted in Fig. 8.8, and schematized in Fig. 8.7, comprises an automotive Drive Unit (DU) assembled into two Output Dynamometers. The electric motor is controlled by a power inverter and a central computer processing torque sensors and resolver signals. Additionally, a power analyzer acquires current and voltage probe signals. The drive unit houses a three-phase IPM motor which was determined to require around 450 Arms to achieve the 220 Nm rated torque and to have a top speed a bit over 13000 rpm, where both rated torque and top speed are derived from the specifications of the vehicle the motor is from. With the 9.56:1 gearbox, the DU reaches up to 2103 Nm at the output shafts. While the motor can be supplied with voltage somewhat higher than 400 Vdc (based on the battery pack specifications for the vehicle it is from), with a DC bus of just 225 Vdc and 450 Arms the motor was observed to produce 110 kW of peak power, and a peak power of 190 kW was calculated for a bus voltage of 400 Vdc. The drive unit is liquid-cooled using a 20kW -5 to 85 ^{o}C rated Thermofisher liquid chiller

Each of the two dynamometers used in the setup is rated at 157 kW and 3500 Nm of torque, operating at up to 4300 rpm. The MUT control is facilitated through the

Cascadia Motion PM250DZR inverter, capable of being supplied with up to 820 Vdc and supplying up to 700 Arms phase current and 300 kW output power. The inverter's EEPROM is programmed using RMS GUI, computational software by Cascadia. Torque command, expressed in terms of i_d and i_q, and safety thresholds management are controlled through iTest, computation software by A&D Technology, utilizing the CAN communication protocol. Motor control tables are generated by analyzing the flux map. The Yokogawa WT1800 Power Analyzer is employed to measure, filter, and analyze phase signals during the tests. Voltage and current probes are connected to this instrument to monitor the inverter's commands and overall motor response.

During the experimental test, signals from and signals captured by the power analyzer, as well as signals from sensors including temperature, torque, speed, and vibration, are sent to iTest, serving as a data hub to manage and control the test. These signals are then processed and stored in a data file for further analysis. Details regarding the devices and their accuracy are provided in Table 8.2.

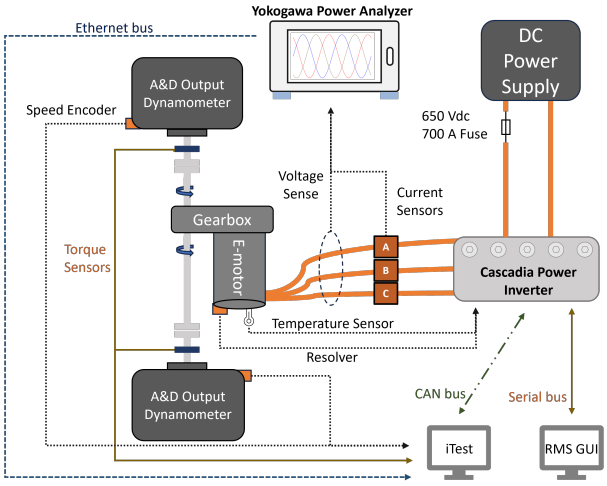

Fig. 8.7 Experimental setup connections and layout.

8.3.2 Experimental flux maps

Following the flux maps of the IPM traction motor are retrieved according to the procedure described in Section 8.1 that relies on a power analyzer. As mentioned before, the procedure is applied to the e-axle, so the combination of electric machine

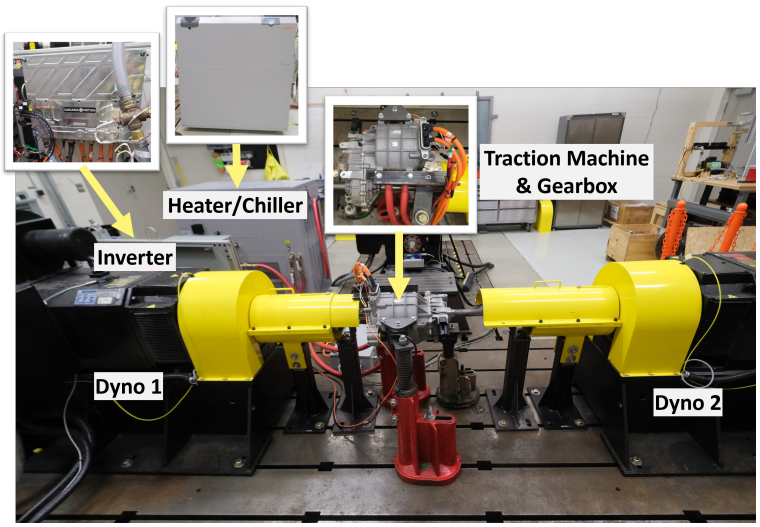

Fig. 8.8 Experimental setup.

Table 8.2 Measurements accuracy and devices.

Signal	Accuracy	Device
Resistance	0.02%	Hioki RM3548
Current	0.05 ppm	Danfysik Ultrastab 867-700I-S2
Voltage	0.15%	Yokogawa WT1800 Power Analyzer
Torque	0.05%	HBM T40B
Speed	N/A	Encoder

and gearbox. The results are shown in Fig. 8.9. Here the 3D flux maps are reported showing d-flux, q-flux and torque function of the dq current. Please note that the maps are obtained in polar coordinates, and the tested points are marked with red dots. The other half of the maps are obtained by applying symmetries. To validate the results, in Fig.,8.9d, the torque measured by the torquemeter is plotted as a function of the current angle for different current amplitudes and compared with the calculated torque, obtained as the cross-product between current and flux. It's important to note that on the x-axis, γ' is reported, which represents the current angle defined starting from the q-axis, essentially $\gamma' = \gamma - 90^o$. The results demonstrate good agreement between the calculated and directly measured data.

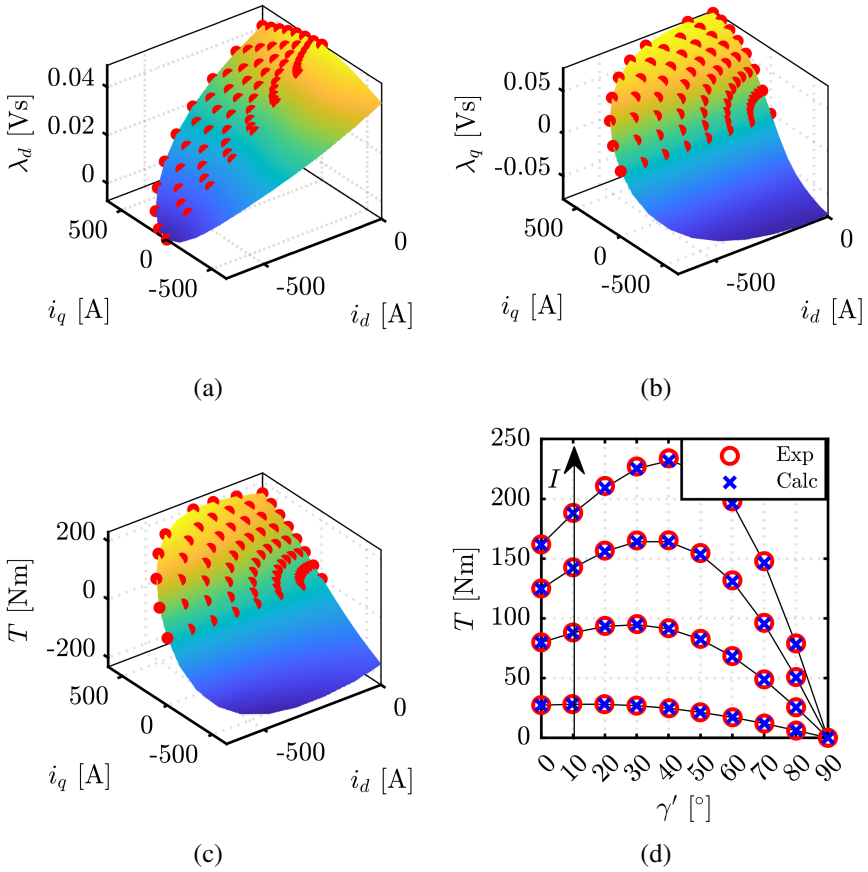

Fig. 8.9 Magnetic model of the tested machine: (a) d flux linkage, (b) q flux linkage and (c) torque function of (i_d,i_q). The tested points are marked in red, the other quadrat on the current plane is obtained by applying symmetries.

8.3.3 Experimetal efficiency maps

The MTPA and MTPV loci are derived from the flux maps, and by imposing maximum current and DC-link voltage constraints, reference currents on the Torque-Speed plane are determined. These values are subsequently utilized to conduct efficiency map tests using a current Field-Oriented Control (FOC). It's crucial to test the torque points as swiftly as possible to maintain stable copper and magnet temperatures, which significantly impact efficiency computations. The procedure tests all reference operating points by creating an equispaced mesh in the torque-speed plane. For each point, the speed is initially set, and once steady-state conditions are achieved, the torque value is changed. After a transient period, measurements are acquired using a

digital trigger. The mandatory sampled quantities include current, voltage, electric power, torque, and mechanical speed. It's important to note the power measurement: since the motor operates under PWM supply, a filter must be employed to capture only the fundamental component, which should be inserted on the power analyzer. Additionally, the frequency of the filter must be lower than the switching inverter frequency but sufficiently higher than the fundamental electrical frequency at maximum speed $f_{1,max}$ (8.9).

$$f_{1,max} < f_{filter} < f_{PWM} \tag{8.9}$$

The resulting efficiency of each test point is computed as in (8.10).

$$\eta = \frac{P_{shaft}}{P_{elt}} \cdot 100 \tag{8.10}$$

The efficiency map test results are based on operating conditions with a current of 450 Arms, achieving a maximum speed of 11 krpm. Here are some important setup details: the electric motor's maximum speed is somewhat greater than 13 krpm but is capped to 11 krpm due to mechanical vibrations of the dyno setup beyond this speed; additionally, there's a power restriction of about 110 kW imposed by the dynos' DC power supply current limitation of 250 A. Since the DC-link is shared with the MUT, the DC-link voltage is set at 450 V to attain the maximum allowed power. However, it's important to note that the motor is controlled as if there were different voltages available by calculating the negative I_d current in the flux weakening range such that the AC voltage does not exceed the intended DC bus voltage (e.g. 225 Vdc, 300 Vdc, 400 Vdc).

The initial data is collected with i_d and i_q calculated for a maximum DC-link voltage of 225 V. In Fig. 8.10a, current curves for different speeds as a function of the produced torque are depicted. It's observed that up to 4000 rpm, these curves are nearly superimposed. This indicates that up to 4 krpm, the motor operates in MTPA condition and up to the maximum torque without reaching the maximum voltage. The corner speed lies somewhere between 4 and 6 krpm, where the motor is already in flux weakening.

Similar observations can be made regarding the line voltage plot in Fig. 8.10b: up to 4 krpm, the voltage limit is not reached, indicating that these speeds are below the base speed. From 6 krpm up to the maximum speed, this limit is reached for progressively lower torques. Additionally, this plot highlights the accuracy of the

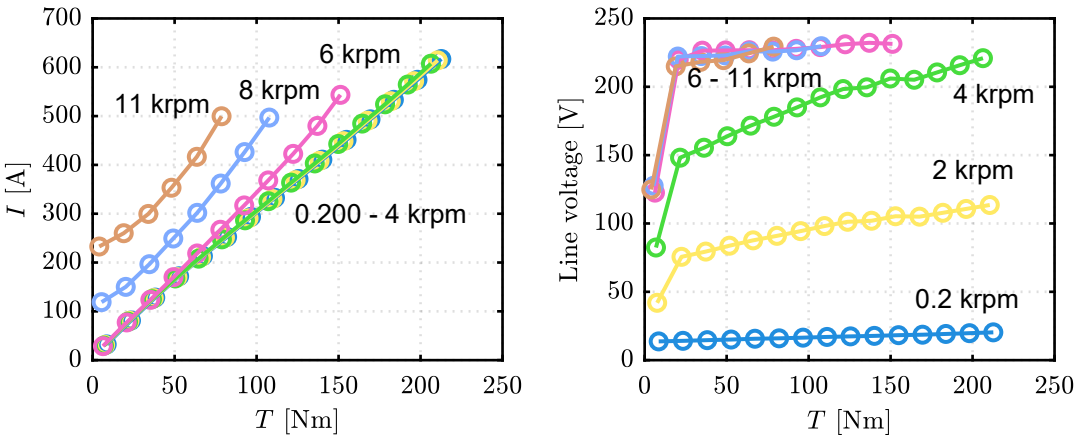

Fig. 8.10 (a) Currents and (b) line voltage function of torque for different speeds at 225 V of DC-link and 450 Arms.

model used for evaluating the reference current: the error on the voltages is less than 5%. The trend of the total electric power recorded during the test is depicted in Fig. 8.11a. It's evident that the power increases with the torque for each speed, as well as with the speed for a given torque value.

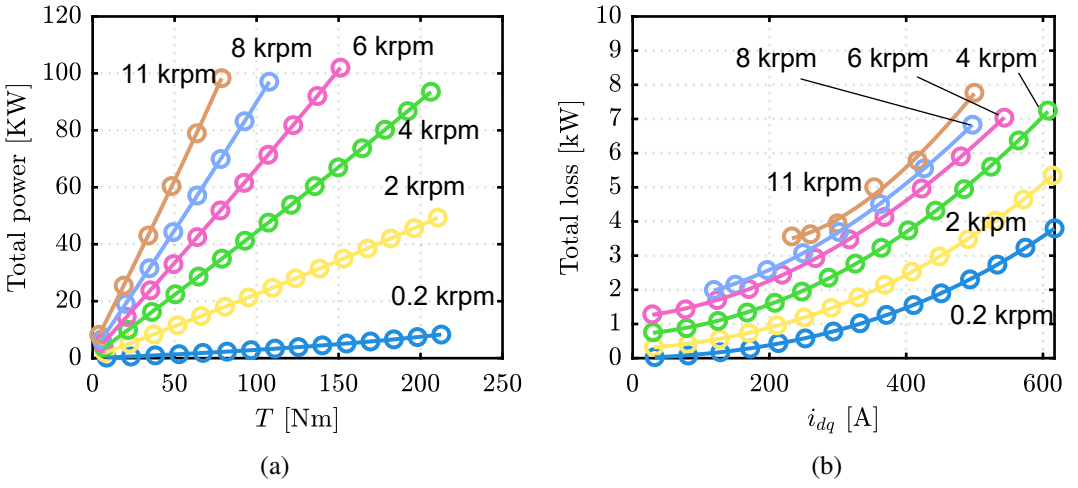

Fig. 8.11 Total loss function of (a) torque and (b) total power function of torque for different speeds at 225 V of DC-link and 450 Arms.

The total losses are calculated as the difference between the total electric power and the power at the shaft. They are illustrated in Fig. 8.12a and Fig. 8.11b, as functions of torque and current, respectively. In both cases, the losses increase with

increasing current, torque, or speed. It's worth noting that the losses can be fitted by a polynomial function.

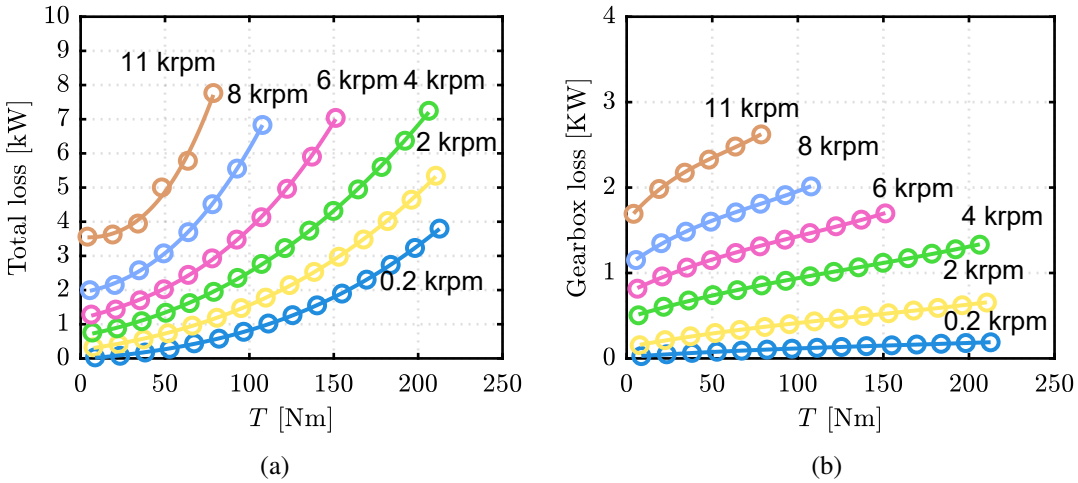

(a) (b)

Fig. 8.12 (a) Total loss and (b) gearbox loss function of torque for different speeds at 225 V of DC-link and 450 Arms.

The efficiency map of the total system, representing the combination of electric motor and gearbox, is depicted in Fig. 8.13a. The gearbox loss in Fig. 8.12b are analytically calculated according [153]. The operational limits, evaluated using the presented approach, are delineated by a solid black line. The white area within the map results from insufficient data for the power limitation. The contour lines' shape and the efficiency eye of 0.94 are realistic for the considered e-axle.

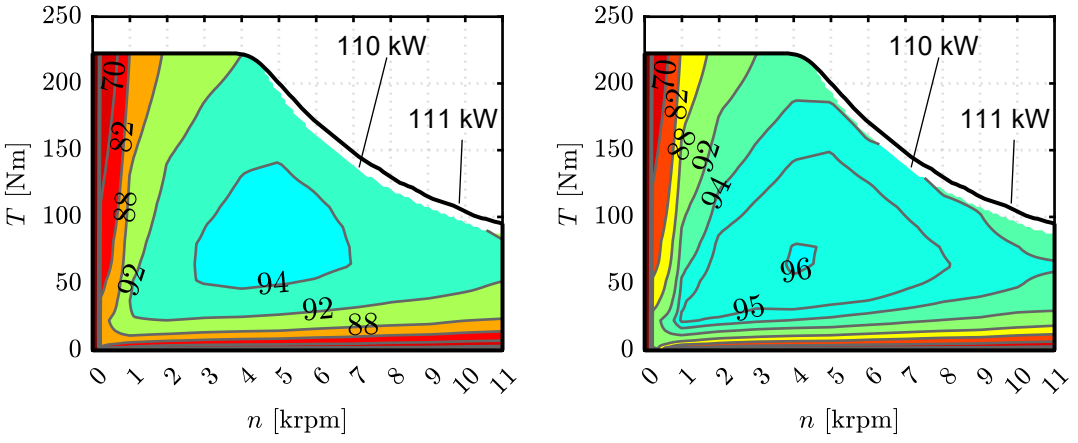

(a) (b)

Fig. 8.13 (a) e-Axle and (b) electrical machine efficiency maps at 225V and 450Arms.

Furthermore, the efficiency of the electric motor alone is estimated by adding gearbox losses, obtained through the analytical model, to the shaft torque in the efficiency equation (8.11). The results are presented in Fig. 8.13b. The efficiency eye of the electric machine reaches 96%, and its position shifts downward in the torque-speed plane. Details on the gearbox analytical model can be found in [154].

$$\eta_{EM} = \frac{P_{shaft} + P_{gear}}{P_{elt}} \cdot 100 \tag{8.11}$$

The total efficiency map is also evaluated considering maximum DC-link voltages of 300 V and 400 V, as displayed in Fig. 8.14a and Fig. 8.14b, respectively. Several considerations are outlined below:

- Increasing the voltage extends the operating limits of the motor. The corner speed shifts to the right, while the limit power curve moves towards higher torque, as expected.
- Up to the corner speed of the 225V map, approximately 4500 rpm, the contour lines of the three efficiency maps coincide. This suggests that in this region, the motor operates in the same MTPA condition, utilizing exactly the same control current. It's important to note that in our setup, the actual DC-link voltage remains constant, and the maximum voltage is imposed by the control strategy. However, in real-world scenarios, different DC-link voltages may lead to slightly different contours due to varying PWM losses. Specifically, the PWM ripple on the current depends on the DC-link voltage for the same operating point, resulting in different PWM losses in both copper and iron.
- At 400 V, an efficiency of 0.95 is achieved at high speed. This indicates that increasing the voltage allows exploration of high-efficiency areas, suggesting optimal conditions for the system.
- It's worth noting that at 400 V, the contour line for 94% efficiency does not have a smooth shape. This may be attributed to measurement issues in the 4-6 krpm range.

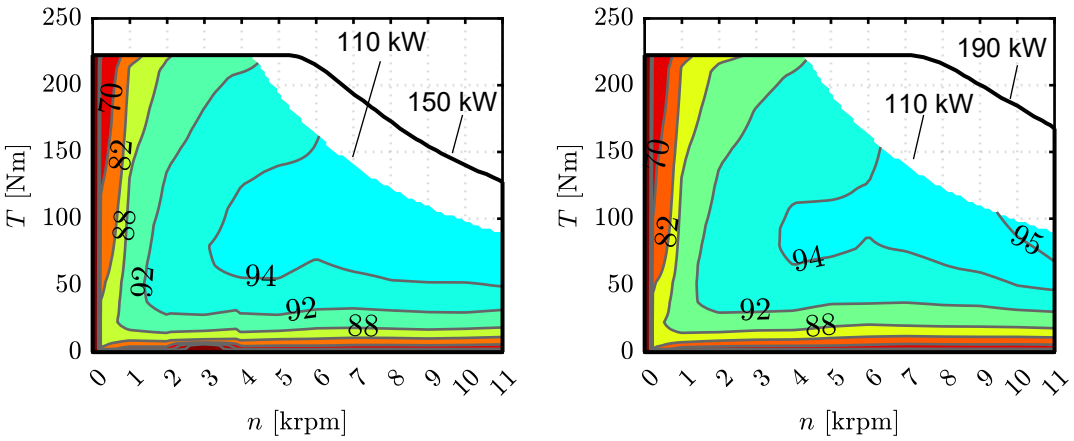

Fig. 8.14 e-Axle efficiency maps at (a) 300V and (b) 400V and 450Arms.

8.4 Short-circuit tests

The proposed methodology in Chapter 3 is validated experimentally using the Brusa HSM1-6.17.12 commercial automotive motor [86], with its specifications detailed in Table 8.3. As there is no FEA model available for this machine, the flux maps of the Motor Under Test (MUT) are initially experimentally measured, following the approach outlined in [24]. Subsequently, both steady-state and transient short-circuit currents and torque are measured on the test rig under safe conditions. These experimental values are then compared to the corresponding estimates derived through manipulation of the experimental flux maps.

Table 8.3 Specifications of commercial automotive motor Brusa HSM1-6.17.12

Nominal torque	T_{nom}	130	[Nm]
Nominal power	P_{nom}	70	[kW]
Base speed	n_{base}	4200	[rpm]
Max torque	T_{max}	220	[Nm]
Max power	P_{max}	96	[kW]
Max speed	n_{max}	12000	[rpm]
Max current	I_{max}	292	[Apk]
DC link voltage	V_{dc}	400	[V]
Pole pairs	p	3	

8.4.1 Test rig setup

The experimental setup is delineated in Fig. 8.15. The MUT is directly linked to a speed-controlled Driving Machine (DM), and it can operate either in current-controlled mode or be connected for short-circuit testing. Control of the MUT is facilitated by a custom inverter through a dSPACE 1202 MicroLabBox fast prototyping board, and the short circuit can be applied directly via the power converter.

The data acquisition system incorporates an HBK Gen7t data recorder with direct line voltage pickup and Ultrastab LEM current transducers. Additionally, an HBM T40B torque meter is integrated, imposing a torque limit of 200 Nm. The upper limit for current is set at 1800 A peak, utilizing the inverter switches for imposing the short-circuit condition. To monitor the temperature, two sensors are strategically positioned at the ends of the stator windings.

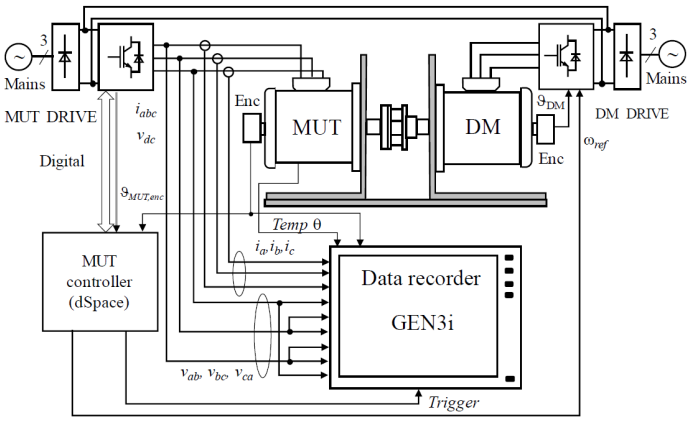

(a)

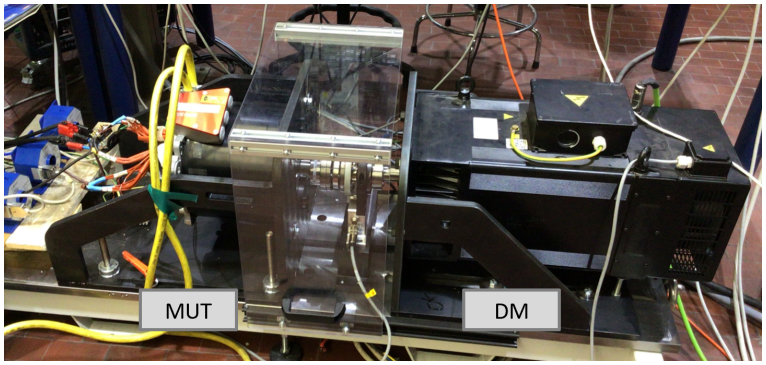

(b)

Fig. 8.15 (a) The test-rig schematic [24] and (b) MUT picture on the test rig.

8.4.2 Steady-State short-circuit test

The initial validation test focuses on the steady-state characteristics of the motor, where the MUT is directly short-circuited, and the inverter is disconnected. This test involves measuring torque and phase currents at various speeds under steady-state conditions. Apart from the rig limits, a crucial consideration is the winding temperature, monitored for safety reasons and due to its impact on phase resistance, influencing the steady-state short-circuit response.

Fig. 8.16 illustrates the dq currents, torque, and temperature as functions of speed during the test. The measured data points are represented by blue dots, while the results derived from the flux maps elaboration outlined in Section,3.1 are depicted with red lines. The phase resistance of the model is updated based on the measured temperature. The test is conducted in two steps, with a pause at 200 rpm for some checks on the experimental setup, as evident in the temperature plot with a step at 200 rpm.

In terms of results, there is notable agreement between the measured data and the estimates obtained with the proposed model, particularly for currents and torque. The d axis current component, being the dominant component against the PM flux linkage, demonstrates the best estimation. The error on peak braking torque is approximately 2 Nm (2.5%), and the speed of the peak braking torque is well estimated, with only a 20 rpm discrepancy.

8.4.3 Transient short-circuit test

The transient short-circuit is imposed by the inverter, with two pre-fault conditions considered, chosen at safe points for testing (with peak torque below 200 Nm and peak current below 1800 A). Due to torque limitations, the pre-fault current is set to zero, and two different speeds are examined: 500 rpm and 1500 rpm.

Currents and torque during the tests are presented in Fig. 8.17 for the 1500 rpm test and Fig. 8.18 for the 500 rpm test. Measured values are depicted in blue, while results from the proposed model are shown in red. The analysis reveals that the measured current waveform (blue curves) closely aligns with the model results (red curves) with minimal discrepancy.

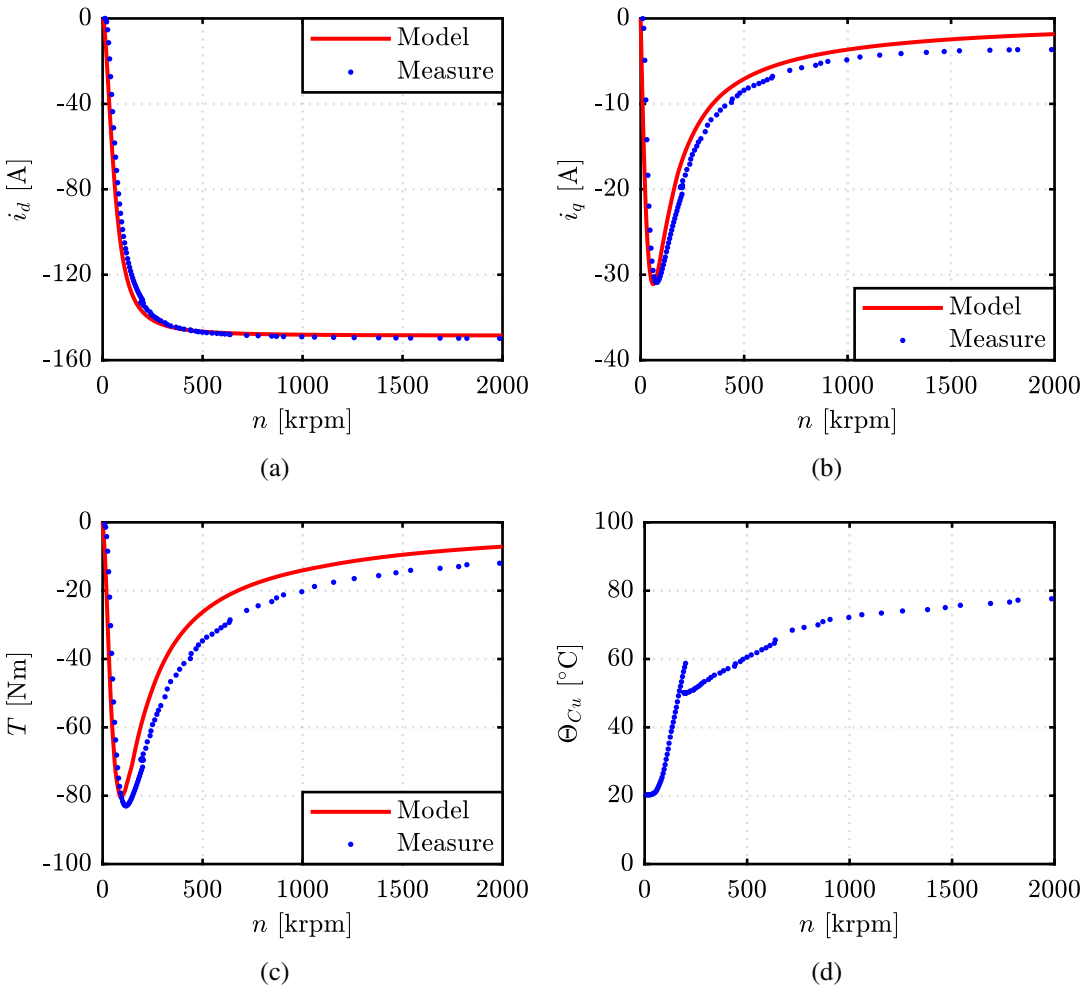

Fig. 8.16 Experimental validation of the steady-state short circuit: comparison between simulated and measured data as a function of speed. The copper temperature is measured and utilized to adjust the simulated results.

Regarding torque, the validation is more intricate due to its transient behavior during a short circuit. The torque transducer measures the transmitted torque between the MUT and the DM, given by:

$$T_m = T_e + \frac{P_{f\&w}}{\omega_r} + J \cdot \frac{d\omega_r}{dt} \tag{8.12}$$

where T_m is the measured torque, T_e is the electromagnetic torque, retrieved bym the cross-product between flux linkages and current, $P_{f\&w}$ is the mechanical loss (friction and windage) component, $\omega_r = n \cdot \frac{\pi}{30}$ is the rotor speed, expressed in rad/s

and J is the sensor inertia. The electromagnetic torque can be derived from the dq current component and the measured flux maps.

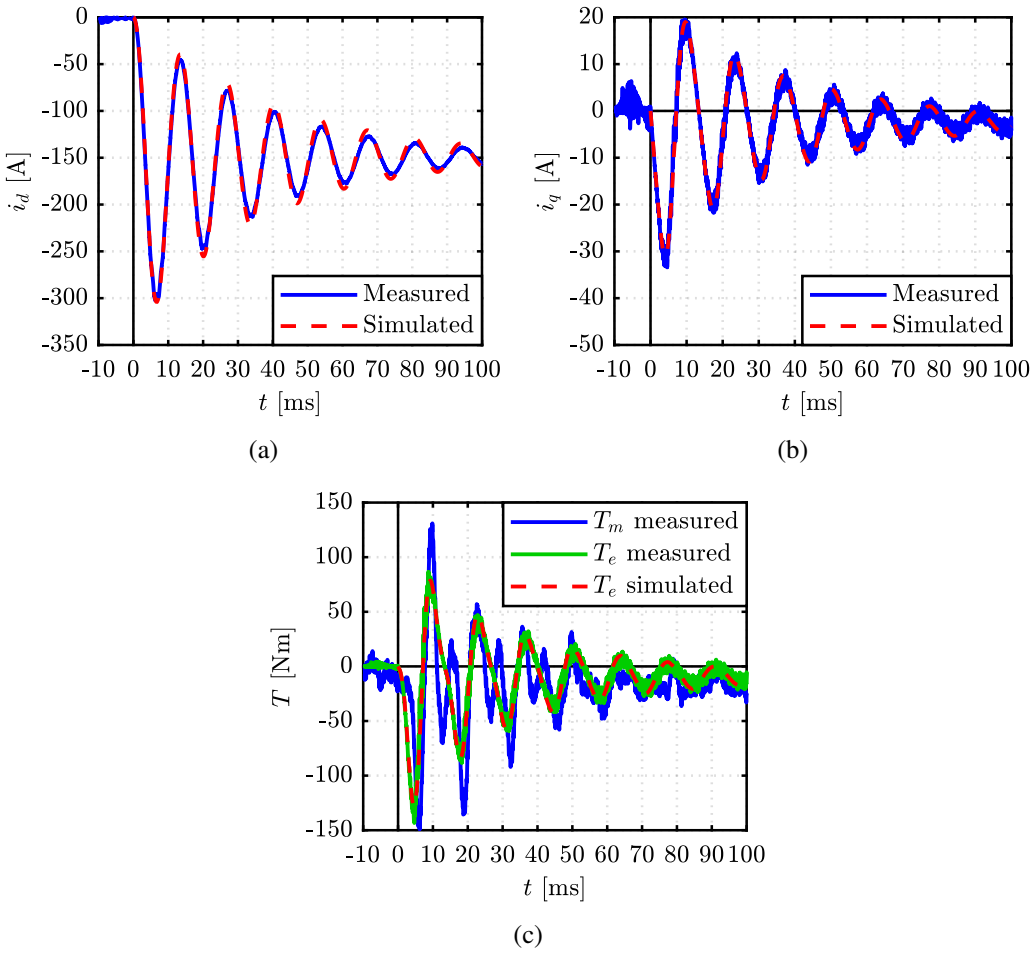

Fig. 8.17 Experimental measurements of transient short circuits (red dots) compared to simulated data (blue lines) at 1500 rpm. The short-circuit was initiated at $t = 0$.

As the method suggested in this study calculates the electromagnetic torque while excluding harmonic effects and overlooking system inertia, both T_m and T_e are displayed in the comparison plots, represented by blue and green lines, respectively. As anticipated, there is a notable alignment between the electromagnetic and computed torque. When dealing with the measured torque, the waveform distinctly reveals the torque ripple contribution, and the impact of inertia becomes more noticeable in the low-speed plot.

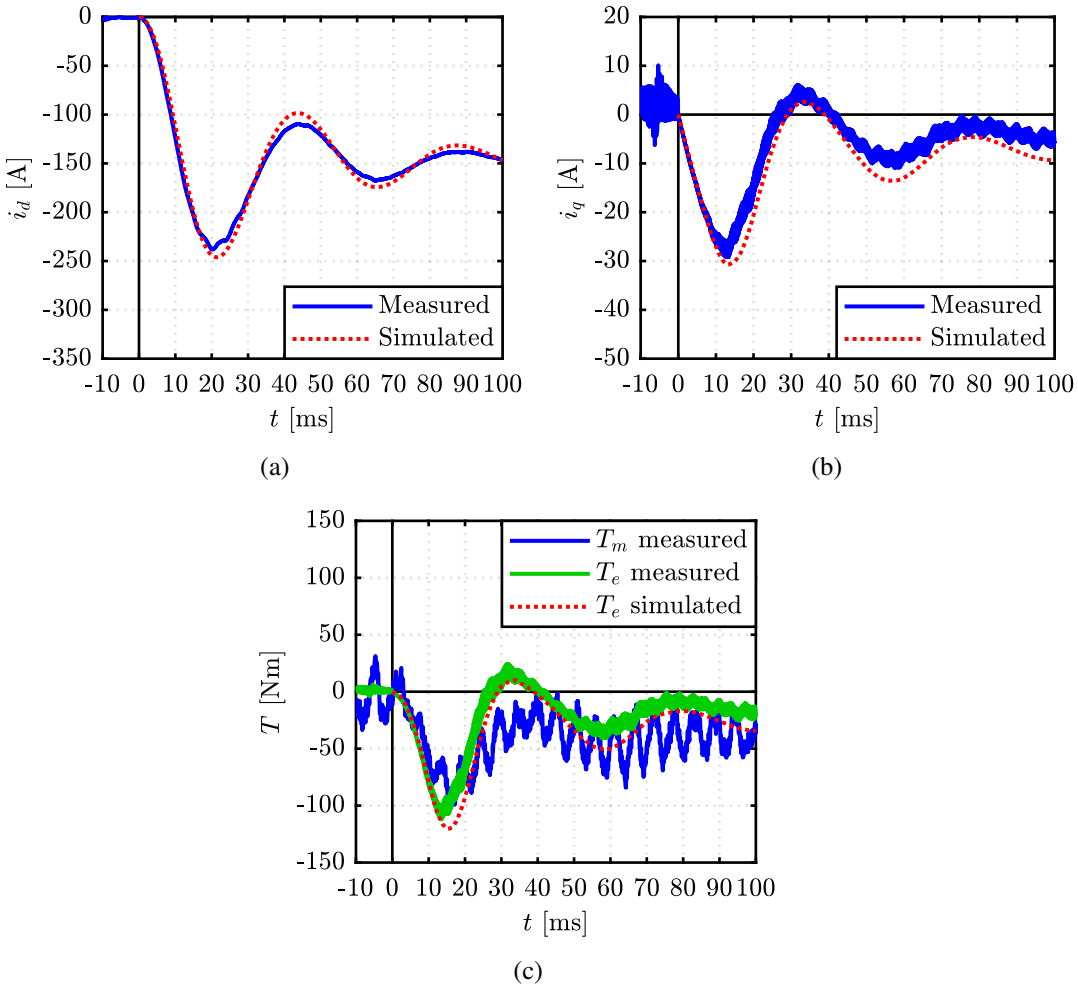

Fig. 8.18 Experimental measurements of transient short circuits (red dots) compared to simulated data (blue lines) at 500 rpm. The short-circuit was initiated at $t = 0$.

8.5 Short Time Thermal tests

The suggested method, concerned the novel STTT procedure, was experimentally validated. Fig. 8.19 illustrates the test experimental setup. Beginning at a consistent room temperature, the motor received excitation as shown in Fig. 7.5b with a current of 0.5 per unit. While the primary focus of interest lies in the initial thermal transient for the STTT procedure, the DC excitation was sustained for an extended duration to assess the impact of calibrating $\Delta\theta_{st}$ and Δt_{st}.

Fig. 8.19 Experimental setup.

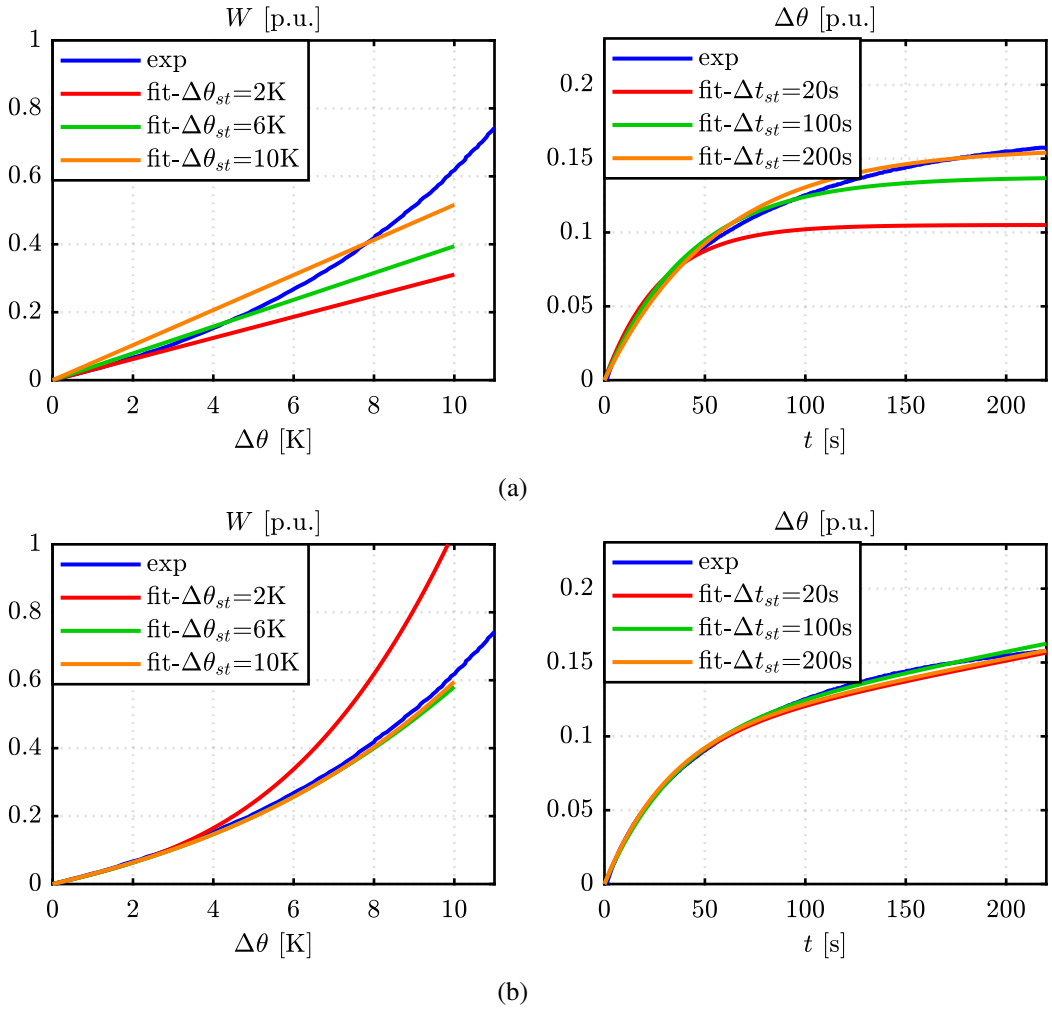

Fig. 8.20 STTT test results. (a) implementation outlined in [23]: $W(\Delta\theta)$ interpolated using (7.6) and $\Delta\theta(t)$ interpolated with (7.8); (b) Proposed approach: $W(\Delta\theta)$ interpolated using (7.13) and $\Delta\theta(t)$ interpolated with (7.3.3). The recorded energy and temperature rise are interpolated while varying $\Delta\theta_{st}$ and Δt_{st}, respectively.

8.5.1 Parameters identification

In Fig. 8.20, the experimentally measured energy variation versus temperature rise and temperature rise versus time curves are depicted in blue. Fig.8.20a shows data interpolation following the method outlined in [23], utilizing (7.6) and (7.8) across different fitting domains, with $\Delta\theta_{st}$ ranging from 2 to 10 K and Δt_{st} from 10 to 200 seconds. The estimation of C_w as the slope of the interpolating straight line (7.6) is heavily reliant on the chosen $\Delta\theta_{st}$. Additionally, according to (7.8), the

estimation of R_{eq} is derived from the time constant of the first-order temperature rise fit, which again exhibits significant variation based on the selected time interval. This highlights the inadequacy of the existing STTT procedure, resulting in unreliable estimation of the STTT parameters.

The identical set of measurements underwent analysis using the proposed procedure, specifically employing (7.13) and (7.3.3), within the same ranges of fitting domains. The outcomes are illustrated in Fig. 8.20b. In this instance, C_w represents the initial slope of the fitting function $\hat{W}(\Delta\theta)$. Notably, the thermal capacitance is consistently evaluated independently of the interpolation domain. Furthermore, almost identical thermal constants are estimated for the evolution of $\Delta\theta$, irrespective of the calibration of $\Delta\theta_{st}$.

The thermal parameters obtained with the approach from [23] and the proposed procedure are presented in Fig. 8.21, represented by blue and red dots, respectively. Table 8.4 provides their average values and dispersion. It is evident that the sensitivity of parameters in the original procedure is significantly higher compared to the proposed one, resulting in a reduction in the standard deviation by approximately one order of magnitude in comparison to [23].

Table 8.4 Mean value (μ) and standard deviation (σ) of the estimated parameters for both the original and proposed procedures.

	$\boldsymbol{\mu}$		$\boldsymbol{\sigma}$	
	[23]	Proposed	[23]	Proposed
C_w [p.u.]	1.220	0.859	0.222	0.021
τ_{eq} [p.u.]	1.389	1.091	0.299	0.051
R_{eq} [p.u.]	1.177	1.272	0.331	0.067

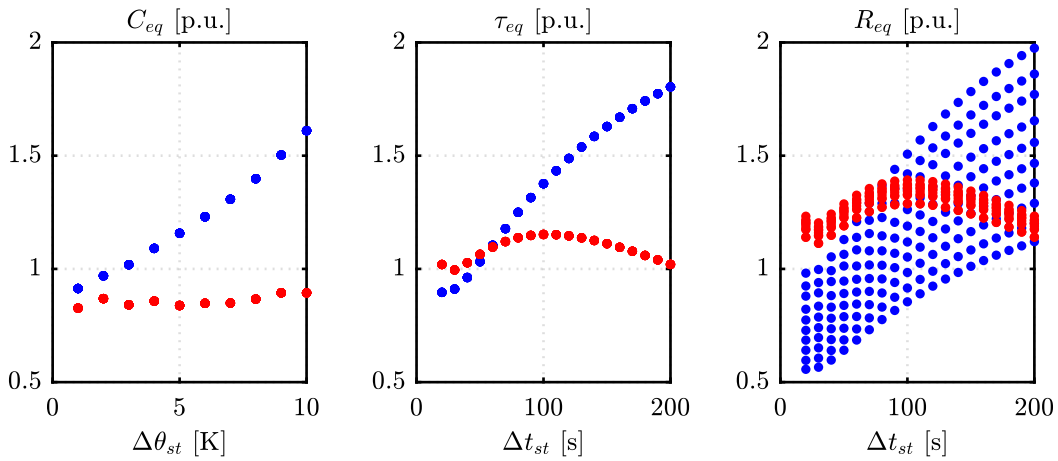

Fig. 8.21 Dispersion of the estimated parameters under varying $\Delta\theta_{st}$ and Δt_{st}: method in [23] (blue) and proposed analysis (red).

8.6 Hotspot observer

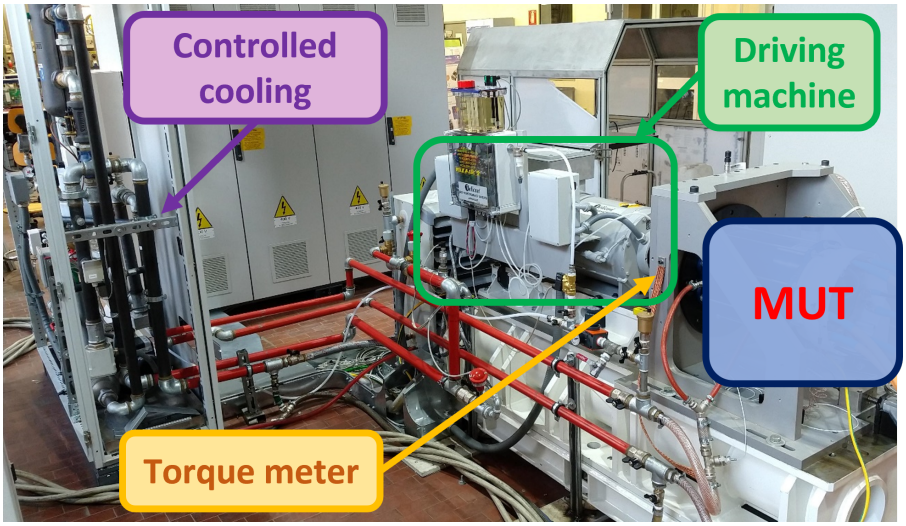

Fig. 8.22 Test bench adopted for experimental validation.

The validation of the winding hotspot observer was conducted concurrently using both the motor simulation model and experimental data. While the MUT remained the same with that used for the STTT thermal test, the test bench employed (shown in Fig. 8.22) differed. Specifically, this test bench enabled precise regulation of the machine's coolant temperature.

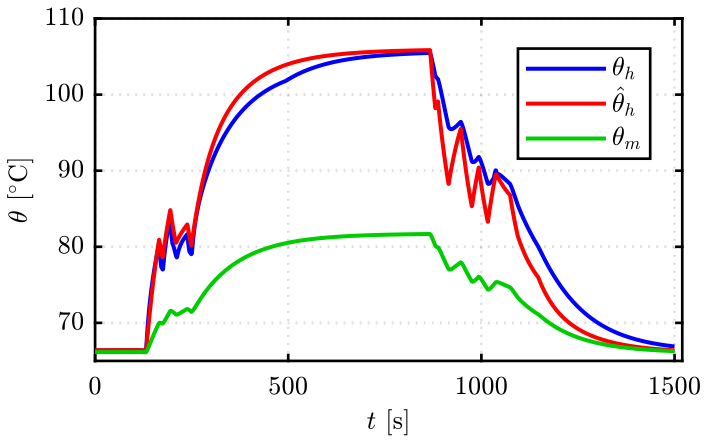

Fig. 8.23 Temperature prediction based on FEA simulation. Blue and red: measured and estimated hotspot temperature; green: accessible measurement point.

In both FEA simulations and experimental tests, the proposed temperature observer was calibrated as outlined in Section 7.6.2 for each case. It's important to note that the simulations and experiments resulted in two distinct parameter sets for observer calibration due to variations between the FEA model and the real machine.

Following calibration of the hotspot temperature observer, a typical load cycle was applied. Figs 8.23 and 8.24 illustrate this cycle for the FEA and experimental tests, respectively, including a sequence of different idle periods and load torques corresponding to various motor losses. Due to hardware constraints, only a partial load could be applied in experiments, preventing the motor from reaching its maximum temperature. Nonetheless, the differences between the measurable and hotspot temperatures was clearly evident, both in simulation and experimentation.

The simulation and experimental results are reported in Fig. 8.23 and 8.24, respectively. As said, the prototype embeds a number of thermistors, which permit monitoring the hotspot temperature, while only one thermistor is available in the final application. In both simulation and experimental tests, the hotspot temperature dynamic is considerably faster than the measurable point, with a significant thermal gradient. Nevertheless, the proposed observer is capable of accurately tracking the hotspot temperature both under transient and steady state conditions, with a transient estimation error in the order of 5°C.

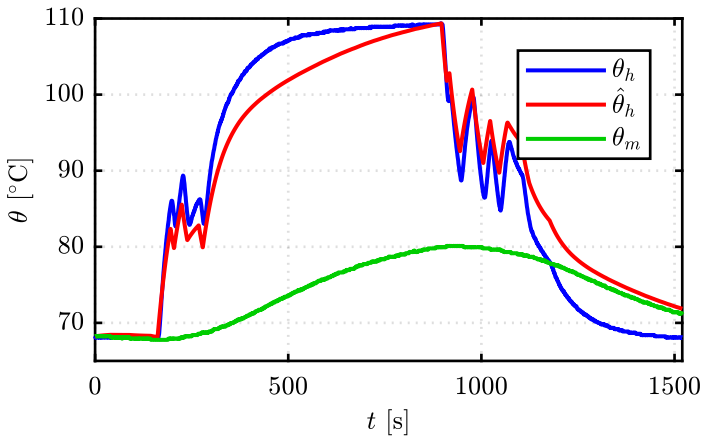

Fig. 8.24 Temperature prediction based on the experimental test. Blue and red: measured and estimated hotspot temperature; green: accessible measurement point.

8.6.1 Sensitivity Analysis

Moreover, a sensitivity analysis was performed using the experimental results and assuming a $\pm 20\%$ error in the estimation of Joule losses, based on the same load cycle. Fig. 8.25 illustrates the corresponding errors in the estimation of θ_h. Despite the significant inaccuracies in the input losses, exceeding realistic scenarios in the automotive field, the estimation error remains within acceptable ranges.

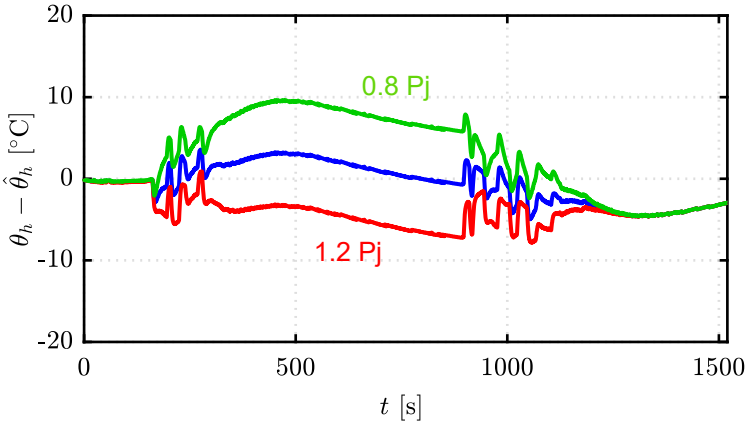

Fig. 8.25 Sensitivity analysis: temperature estimation error considering misestimation of P_j.

Another sensitivity analysis is conducted on the variation of the x parameter of the observer and the results are depicted in Fig. 8.26 considering $x = 0.1$ and $x = 0.9$.

The y parameter is not considered because it is restricted to a very small range, and its influence is negligible for this prototype.

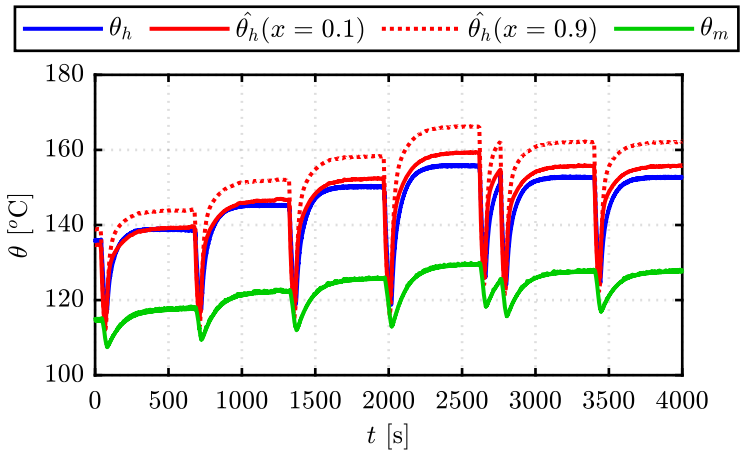

Fig. 8.26 Sensitivity analysis on x parameter of the hotspot observer.

Chapter 9

Conclusion

The thesis focuses on the design methodologies and testing of electric machines for traction application. In the following, the major contributions of the research activities are outlined. All the procedures are integrated into the open-source environment SyR-e, facilitating broader utilization within both academic and industrial communities.

9.1 Short circuit current determination

Main new contributions:

- Fast evaluation of transient and steady-state short circuit current via flux maps manipulation
- Fast Hyper-Worst-Case peak current computation

A fast method for assessing the transient short-circuit current and torque of PM synchronous machines is presented. This method, based on FEA or experimental flux maps, provides excellent accuracy within a reasonable computational time. Validation against a circuit-coupled dedicated transient FEA in Simcenter MAGNET confirms its effectiveness. Additionally, a method for directly evaluating the hyper-worst-case peak current value using dedicated FEA simulations, without the need for pre-calculated flux maps, is proposed. Regarding pre-fault conditions, as demonstrated, that higher pre-fault flux amplitude leads to higher short-circuit peak

current. It also reveals that the braking mode poses a more severe initial condition than motoring, and any type of loss helps mitigate the peak current. The study compares four motors with different per unit PM flux linkage and saliency, including a SyR motor.

9.2 Design methodologies

Main new contributions:

- Fast preliminary design procedure of PMSM machines from scratch via the (x,b) design plane
  - the existing procedure is extended to PMSM machines and impproved
  - new figure of merits are introduced into the design plane
- Design procedure based on scaling method starting from an existing design
  - the new length-turns design plane is introduced
  - guidelines for scaling the thermal water jacket are provided

9.2.1 Design via the (x,b) design plane

A rapid and efficient procedure for the preliminary design of PMSM machines, specifically focused for traction applications, is introduced. The method is demonstrated with reference to the front-axle IPM motor of the Tesla Model 3. The (x,b) design plane is utilized to quickly determine the motor cross-section, considering dimensional, electrical, magnetic, thermal, and maximum speed constraints. The design plane incorporates two variables, x and b, representing the ratio between rotor and stator diameter and between airgap and iron flux density, respectively. With the aid of design equations, each (x,b) point corresponds to a distinct cross-section, enabling visualization of a plethora of performance figures directly on the design plane for a continuum of candidate machines. The design plane is constructed and computed using an analytical model and design equations. Furthermore, a few FEA simulations are employed to refine the analytical model through a process called FEAfix. Two PMSM motors for traction application are designed and compared,

one utilizing NdFeB PMs and the other with ferrite PMs. The study demonstrates how the procedure can assist designers in identifying feasible and optimal solutions. The paper's findings aim to highlight the potential and prospects of the new design method, which serves as a robust starting point for more detailed and time-consuming thermal and mechanical optimization processes.

9.2.2 Design via scaling laws

A comprehensive scaling method is proposed for the preliminary design and system-level studies of traction Permanent Magnet Synchronous Motors with a liquid cooling jacket. The approach starts from a reference design, suggesting that the stack diameter be scaled to meet the structural requirements dictated by the maximum operating speed of the final application. A new design plane, termed the length-turns design plane, is presented. This plane represents the contours of peak torque and base speed of the scaled machine under Maximum Torque Per Ampere conditions, as a function of the stack length and number of turns. Additional figures of merit are depicted in the scaling plane, illustrating the demagnetization limit and its distance from the peak short-circuit current, as well as the threshold for uncontrolled generator operation speed. Derived from the flux maps of the reference machine, the design plane visually demonstrates how the stack length can be minimized, provided that the corresponding number of turns is feasible. Guidelines for scaling the water-glycol cooling jacket are provided and validated through simulation, along with loss scaling to evaluate the efficiency map of the scaled machine. Various design choices can be explored thanks to the length-turn plane and the structural and thermal scaling rules presented.

9.3 Thermal characterization and winding hotspot observer

Main new contributions:

- Improved STTT procedure for traction machines
- Hotspot winding temperature observer

The STTT model provides a means to determine the thermal capacitance of the stator winding and the equivalent thermal resistance between the winding and the stator iron, crucial elements for constructing an accurate thermal model of an AC machine. This thermal model facilitates the safe operation at peak and continuous performance levels, thereby enhancing the overall reliability of electric drives. An enhanced STTT testing procedure tailored for high-performance, liquid-cooled motor drives is introduced and validated. A novel experimental setup ensures the thermal symmetry of the motor without necessitating access to the winding output terminals. Furthermore, an effective observer for real-time monitoring of hotspot winding temperature in a heavily loaded electric motor for traction applications is presented. The temperature observer utilizes an advanced thermal network, calibrated through dedicated experimental commissioning tests. This observer enables full utilization of the machine even during transient overload conditions. The calibration process of the observer is thoroughly described, and the discrete-time solution of the observer is provided, allowing for rapid implementation into motor control systems with minimal computational overhead.

9.4 Experimental tests

Here a recap of the testing activities is reported.

- Short circuit current: the computation for the short-circuit peak current is validated on a commercial traction motor through experimental tests, demonstrating good accuracy in both transient and steady-state conditions.
- Machine characterization: both the FEA simulated flux maps and efficiency maps are validated against experimental results on an industrial application motor. The procedure is then applied to characterize two traction motors. The first prototype is a ferrite motor for automotive purposes, designed using the presented (x,b) design plane. It was tested at Politecnico di Torino. The second motor is part of an e-axle, so the tests were conducted on the combination of the motor and gearbox. The procedure, extended to the entire e-axle, confirms its validity, showing favorable results. Furthermore, for testing, a commercial inverter and a power analyzer-based method were employed. The tests were conducted at McMaster University when the author was a visiting PhD student.

- Thermal characterization and winding hotspot observer: the improved Short Time Transient Thermal procedure is validated with experimental results, utilizing a high-density motor for traction. Additionally, the winding hotspot observer is calibrated based on experimental data, and its temperature estimation is compared with the measurement from thermocouples.

9.5 Future works

The work illustrated in this thesis opens up new research paths and suggests potential future activities. Here are some possible topics:

- determining the peak short circuit current may involve accounting for loss factors, such as iron loss;
- the design process can include additional performance criteria and can be expanded and adjusted to accommodate various machine topologies, such as induction and wound field machines.
- the scaling procedure can account for AC copper losses. Furthermore, enhancing thermal scaling can be achieved through advanced modeling techniques and incorporating diverse cooling systems.
- the thermal machine model can be enhanced by incorporating the rotor network and developing a temperature observer for the magnets.
- segregate the losses of the electrical machine and gearbox during characterization tests, without relying on analytical gearbox models.

References

[1] IEA. Energy Technology Perspectives 2023. Technical report, International Energy Agency (IEA), IEA, Paris, 2023.

[2] European Commission. Joint Research Centre. *GHG emissions of all world countries: 2023.* Publications Office, LU, 2023.

[3] Redazione Autoappassionati.it. Ford Kuga Hybrid: focus tecnico sull'ibrido "di mezzo" dell'Ovale. https://www.autoappassionati.it/ford-kuga-hybrid-focus-tecnico-sullibrido-di-mezzo-dellovale/, April 2021.

[4] Mauro Vallotti. Nuova Ford Kuga - Ridefinisci l'avventura - SUV - AUTHOS Torino. https://www.authos.it/nuova-ford-kuga/.

[5] Ireneusz Pielecha, Wojciech Cieslik, and Filip Szwajca. Energy Flow and Electric Drive Mode Efficiency Evaluation of Different Generations of Hybrid Vehicles under Diversified Urban Traffic Conditions. *Energies*, 16(2):794, January 2023.

[6] Berker Bilgin, Pierre Magne, Pawel Malysz, Yinye Yang, Vera Pantelic, Matthias Preindl, Alexandre Korobkine, Weisheng Jiang, Mark Lawford, and Ali Emadi. Making the Case for Electrified Transportation. *IEEE Transactions on Transportation Electrification*, 1(1):4–17, June 2015.

[7] Toyota Prius Gen 4 XW50 - Groovy Shades. https://groovy.com.my/product/toyota-prius-gen-4-xw50/.

[8] Auto ibride: che tipologia di cambio hanno? https://www.automobilismo.it/auto-ibride-che-tipologia-di-cambio-hannot-32449.

[9] Jeep Renegade e Compass 4xe: cosa c'è sotto la "pelle". https://www.alvolante.it/news/jeep-renegade-compass-4xe-tecnica-sistema-ibrido-369539, 2020.

[10] Mahir Alani, Yasemin Oner, and Ahmed Tameemi. Electrical machines in automotive: evaluation of current technologies and future requirements. *Electrical Engineering*, 105(1):477–491, February 2023.

[11] MotorXP. *Performance Analysis of the Tesla Model 3 Electric Motor using MotorXP-PM*. VEPCO, June 2020.

[12] What's inside the Tesla Hairpin Motor. https://www.youtube.com/watch?v=DSpTh5B4nYk.

[13] Robin Thomas, Hugo Husson, Lauric Garbuio, and Laurent Gerbaud. Comparative study of the tesla model s and audi e-tron induction motors. In *2021 17th Conference on Electrical Machines, Drives and Power Systems (ELMA)*, pages 1–6, 2021.

[14] Hannah Koke. Comparative study of stranded and bar windings in an induction motor for automotive propulsion applications. https://macsphere.mcmaster.ca/handle/11375/29564.

[15] Tesla Model S Plaid Motor EXTRAVAGANZA!! https://www.youtube.com/watch?v=4lGVimLK58g.

[16] Josef Binder, Mario Silvagni, Simone Ferrari, Björn Deusinger, Andrea Tonoli, and Gianmario Pellegrino. High-speed IPM Motors with Rotor Sleeve: Structural Design and Performance Evaluation. In *2023 IEEE Workshop on Electrical Machines Design, Control and Diagnosis (WEMDCD)*, pages 1–6, April 2023. ISSN: 2380-856X.

[17] Eric Hendrich. TRADIUM Price Charts for November Published - rawmaterials.net. https://rawmaterials.net/tradium-price-charts-for-november-published/, November 2023.

[18] Mish Talk. Critical Materials Risk Assessment by the US Department of Energy – MishTalk. https://mishtalk.com/economics/critical-materials-risk-assessment-by-the-us-department-of-energy/, 2023.

[19] Zi-Qiang Zhu and Dawei Liang. Perspective of Thermal Analysis and Management for Permanent Magnet Machines, with Particular Reference to Hotspot Temperatures. *Energies*, 15(21):8189, January 2022.

[20] Eclipse Magnetic. Alnico Magnets | Eclipse Magnetics. https://www.eclipsemagnetics.com/products/magnetic-materials-and-assemblies/magnet-materials/alnico-magnet-material/.

[21] M. J. Kramer, R. W. McCallum, I. A. Anderson, and S. Constantinides. Prospects for Non-Rare Earth Permanent Magnets for Traction Motors and Generators. *JOM*, 64(7):752–763, July 2012.

[22] BOMATEC. BOMATEC – Führender Anbieter in der Magnettechnik. https://www.bomatec.com/.

[23] Aldo Boglietti, Enrico Carpaneto, Marco Cossale, and Silvio Vaschetto. Stator-Winding Thermal Models for Short-Time Thermal Transients: Definition and Validation. *IEEE Transactions on Industrial Electronics*, 63(5):2713–2721, 2016.

[24] Eric Armando, Paolo Guglielmi, Gianmario Pellegrino, and Radu Bojoi. Flux linkage maps identification of synchronous AC motors under controlled thermal conditions. In *2017 IEEE International Electric Machines and Drives Conference (IEMDC)*, pages 1–8, Miami, FL, USA, May 2017. IEEE.

[25] Daniel G. Barroso, Yinye Yang, Fabricio A. Machado, and Ali Emadi. Electrified Automotive Propulsion Systems: State-of-the-Art Review. *IEEE Transactions on Transportation Electrification*, 8(2):2898–2914, June 2022.

[26] Wuqiang Wang, Yong Li, Dajun Huan, Xiaodong Chen, Hongquan Liu, Yanrui Li, and Lisha Li. Research on Stress Design and Manufacture of the Fiber-Reinforced Composite Sleeve for the Rotor of High-Speed Permanent Magnet Motor. *Energies*, 15(7):2467, January 2022.

[27] HGT Advanced Magnets. Sintered SmCo Magnets. https://www.advancedmagnets.com/sintered-smco-magnets/.

[28] IMI. International Magnaproducts, Inc. https://magnetsim.com/.

[29] Shajjad Chowdhury, Emre Gurpinar, Gui-Jia Su, Tsarafidy Raminosoa, Timothy A. Burress, and Burak Ozpineci. Enabling Technologies for Compact Integrated Electric Drives for Automotive Traction Applications. In *2019 IEEE Transportation Electrification Conference and Expo (ITEC)*, pages 1–8, June 2019.

[30] Samantha Gross. The challenge of decarbonizing heavy transport. Technical report, Brookings, 2020.

[31] REPowerEU: A plan to rapidly reduce dependence on Russian fossil fuels and fast forward the green transition. https://ec.europa.eu/commission/presscorner/detail/en/IP_22_3131.

[32] IEA. CO2 Emissions in 2022. Technical report, International Energy Agency (IEA), IEA, Paris, 2023.

[33] Global Electric Vehicles Sales, 2010-2022 | The Geography of Transport Systems. https://transportgeography.org/contents/chapter4/transportation-sustainability-decarbonization/global-electric-vehicles-sales/, June 2022.

[34] Ali Emadi. *Advanced Electric Drive Vehicles*. CRC Press, October 2014.

[35] What Is a Powertrain? https://www.kia.com/id/discover-kia/ask/what-is-a-powertrain.html.

[36] S. M. Nayeem Hasan, Mohammad N. Anwar, Mehrdad Teimorzadeh, and David P Tasky. Features and challenges for Auxiliary Power Module (APM) design for hybrid/electric vehicle applications. In *2011 IEEE Vehicle Power and Propulsion Conference*, 2011.

[37] Alireza Khaligh and Michael D'Antonio. Global Trends in High-Power On-Board Chargers for Electric Vehicles. *IEEE Transactions on Vehicular Technology*, 68(4):3306–3324, April 2019.

[38] Antti Lajunen, Yinye Yang, and Ali Emadi. Recent Developments in Thermal Management of Electrified Powertrains. *IEEE Transactions on Vehicular Technology*, 67(12):11486–11499, December 2018.

[39] Antti Lajunen, Yinye Yang, and Ali Emadi. Review of Cabin Thermal Management for Electrified Passenger Vehicles. *IEEE Transactions on Vehicular Technology*, 69(6):6025–6040, June 2020.

[40] Behrooz Mashadi and David Crolla. *Vehicle Powertrain Systems*. Wiley, 1 edition, January 2012.

[41] Sanjaka G. Wirasingha and Ali Emadi. Pihef: Plug-In Hybrid Electric Factor. *IEEE Transactions on Vehicular Technology*, 60(3):1279–1284, March 2011.

[42] x-engineer.org. What is the difference between micro, mild, full and plug-in hybrid electric vehicles – x-engineer.org. https://x-engineer.org/micro-mild-full-hybrid-electric-vehicle/.

[43] Rafael Garbelini Lorena and Eduardo Kazumi Yamakawa. Overview of the main powertrain architectures for hybrid and electric vehicles. *Semina: Ciências Exatas e Tecnológicas*, 42(2):201–208, December 2021.

[44] Technical data and specifications Peugeot 208 5-Door | Small City Car. https://www.peugeotliban.com/showroom/208/5-doors/informations-techniques-1.html.

[45] Fiat Panda | Hybrid City Car. https://www.fiat.com/fiat-panda/panda.

[46] 2023 Toyota Prius | Toyota.com. https://www.toyota.com/prius/.

[47] X5 xDrive50e Plug-In Hybrid SUV | BMW USA. https://www.bmwusa.com/vehicles/x-models/x5/sports-activity-vehicle/plug-in-hybrid.html.

[48] Fully electric e-tron collection > Electric & Hybrid > Audi UK. https://www.audi.co.uk/uk/web/en/electric/e-tron.html.

[49] Michele De Santis, Sandro Agnelli, Fabrizio Patanè, Oliviero Giannini, and Gino Bella. Experimental Study for the Assessment of the Measurement Uncertainty Associated with Electric Powertrain Efficiency Using the Back-to-Back Direct Method. *Energies*, 11(12):3536, December 2018.

[50] Yinye Yang, Kamran Arshad Ali, Joel Roeleveld, and Ali Emadi. State-of-the-art electrified powertrains - hybrid, plug-in, and electric vehicles. *International Journal of Powertrains*, 5(1):1, 2016.

[51] Yinye Yang and Ali Emadi. Integrated electro-mechanical transmission systems in hybrid electric vehicles. In *2011 IEEE Vehicle Power and Propulsion Conference*, 2011.

[52] Toyota. Prius Gen4 launch pack. https://media.toyota.co.uk/wp-content/uploads/sites/5/pdf/Prius-Gen4-launch-pack.pdf.

[53] Jeep® Renegade 4xe | Plug-in Hybrid SUV | Jeep® UK. https://www.jeep.co.uk/jeep-renegade/plug-in.

[54] CarInfo. Jeep Renegade 4XE BU Facelift 240ps. https://www.car.info/en-se/jeep/renegade/renegade-phev-18354460/specs.

[55] GruppoZago. Jeep Renegade e-Hybrid. Come funziona e quanto consuma. https://www.gruppozago.it/it/jeep-renegade-e-hybrid-come-funziona-e-quanto-consuma/default.asp.

[56] Ali M. Bazzi, Yiqi Liu, and Daniel S. Fay. Electric Machines and Energy Storage: Over a Century of Technologies in Electric and Hybrid Electric Vehicles. *IEEE Electrification Magazine*, 6(3):49–53, September 2018.

[57] Andreas Krings and Christian Monissen. Review and Trends in Electric Traction Motors for Battery Electric and Hybrid Vehicles. In *2020 International Conference on Electrical Machines (ICEM)*, volume 1, pages 1807–1813, August 2020. ISSN: 2381-4802.

[58] Federica Graffeo, Silvio Vaschetto, Alberto Tenconi, and Andrea Cavagnino. Fast Sizing Procedure for Salient-Pole Wound Field Synchronous Motors for Transportation Electrification. In *2023 IEEE International Electric Machines & Drives Conference (IEMDC)*, pages 1–7, May 2023.

[59] Giuseppe Volpe, Mircea Popescu, Lino di Leonardo, and Shaoshen Xue. Efficient Calculation of PWM AC Losses in Hairpin Windings for Synchronous BPM Machines. In *2021 IEEE International Electric Machines Drives Conference (IEMDC)*, pages 1–5, May 2021.

[60] Grazia Berardi and Nicola Bianchi. Design Guideline of an AC Hairpin Winding. In *2018 XIII International Conference on Electrical Machines (ICEM)*, pages 2444–2450, September 2018. ISSN: 2381-4802.

[61] Shaoshen Xue, Melanie Michon, Mircea Popescu, and Giuseppe Volpe. Optimisation of Hairpin Winding in Electric Traction Motor Applications. In *2021 IEEE International Electric Machines Drives Conference (IEMDC)*, pages 1–7, May 2021.

[62] Bikrant Poudel, Ebrahim Amiri, Parviz Rastgoufard, and Behrooz Mirafzal. Toward Less Rare-Earth Permanent Magnet in Electric Machines: A Review. *IEEE Transactions on Magnetics*, 57(9):1–19, September 2021.

[63] Maria Alejandra León. The rare earth problem: Sustainable sourcing and supply chain challenges. https://www.circularise.com/blogs/the-rare-earth-problem-sustainable-sourcing-and-supply-chain-challenges, 2023.

[64] Miotti Electric Evolution. Magneti Permanenti. Catalogue Rev4, Miotti srl, November 2021.

[65] Z.W. Liu, R.V. Ramanujan, and H.A. Davies. Improved thermal stability of hard magnetic properties in rapidly solidified RE–TM–B alloys. *Journal of Materials Research*, 23(10):2733–2742, October 2008.

[66] A Brief Introduction to Neodymium Magnets (NdFeB). https://www.stanfordmagnets.com/introduction-to-neodymium-magnets-ndfeb.html, September 2020.

[67] Powder Metallurgy Process Overview | Refractory Metals & Alloys. https://www.refractorymetal.org/basic-info-powder-metallurgy-process-video/, October 2019.

[68] OBD Magneti. bonded / plastic. https://www.odbmagneti.com/en/bonded-plastic-magnets, 2023.

[69] Samarium Cobalt Magnets (SmCO Magnets) Supplier. https://www.stanfordmagnets.com/smco-magnets.html.

[70] A Brief Introduction to Ferrite Magnets. https://www.stanfordmagnets.com/introduction-to-ferrite-magnets.html, September 2020.

[71] Integrated Magnetics. Standard & Custom Alnico Magnets | Alnico Magnet Materials. https://www.intemag.com/alnico-magnet-material.

[72] Master Magnetics. Types and Applications Alnico Magnets. https://www.magnetsource.com/pages/alnico-magnets.

[73] Jian-Ping Wang. Environment-friendly bulk Fe16N2 permanent magnet: Review and prospective. *Journal of Magnetism and Magnetic Materials*, 497:165962, March 2020.

[74] K.H. The occurrence and the crystal structure of *α"* -iron nitride; a new type of interstitial alloy formed during the tempering of nitrogen-martensite. *Proceedings of the Royal Society of London. Series A. Mathematical and Physical Sciences*, 208(1093):216–224, August 1951.

[75] T. K. Kim and M. Takahashi. New Magnetic Material Having Ultrahigh Magnetic Moment. *Applied Physics Letters*, 20(12):492–494, June 1972.

[76] Yutaka Sugita, Hiromasa Takahashi, Matahiro Komuro, Katsuya Mitsuoka, and Akimasa Sakuma. Magnetic and Mössbauer studies of single-crystal Fe16N2 and Fe-N martensite films epitaxially grown by molecular beam epitaxy (invited). *Journal of Applied Physics*, 76(10):6637–6641, November 1994.

[77] Jorge O. Estima and Antonio J. Marques Cardoso. Efficiency Analysis of Drive Train Topologies Applied to Electric/Hybrid Vehicles. *IEEE Transactions on Vehicular Technology*, 61(3), March 2012.

[78] K. Venkatachalam, C.R. Sullivan, T. Abdallah, and H. Tacca. Accurate prediction of ferrite core loss with nonsinusoidal waveforms using only Steinmetz parameters. In *2002 IEEE Workshop on Computers in Power Electronics, 2002. Proceedings.*, pages 36–41, Mayaguez, Puerto Rico, 2002. IEEE.

[79] C. Simao, N. Sadowski, N. J. Batistela, and J. P. A. Bastos. Evaluation of Hysteresis Losses in Iron Sheets Under DC-biased Inductions. *IEEE Transactions on Magnetics*, 45(3):1158–1161, March 2009.

[80] Katsumi Yamazaki and Hidetada Takeuchi. Impact of Mechanical Stress on Characteristics of Interior Permanent Magnet Synchronous Motors. *IEEE Transactions on Industry Applications*, 53(2):963–970, March 2017.

[81] M. Hullmann and B. Ponick. General Analytical Description of the Effects of Segmentation on Eddy Current Losses in Rectangular Magnets. In *2022 International Conference on Electrical Machines (ICEM)*, pages 1757–1762, September 2022. ISSN: 2381-4802.

[82] Gianmario Pellegrino, Radu Iustin Bojoi, and Paolo Guglielmi. Unified Direct-Flux Vector Control for AC Motor Drives. *IEEE Transactions on Industry Applications*, 47(5):2093–2102, September 2011.

[83] Plexim. PLECS. https://www.plexim.com/products/plecs.

[84] S.D. Pekarek, O. Wasynczuk, and H.J. Hegner. An efficient and accurate model for the simulation and analysis of synchronous machine/converter systems. *IEEE Transactions on Energy Conversion*, 13(1):42–48, March 1998.

[85] Anantaram Varatharajan, Dario Brunelli, Simone Ferrari, Paolo Pescetto, and Gianmario Pellegrino. syreDrive: Automated Sensorless Control Code Generation for Synchronous Reluctance Motor Drives. In *2021 IEEE Workshop on Electrical Machines Design, Control and Diagnosis (WEMDCD)*, pages 192–197, April 2021.

[86] HSM1-6.17.12 – BRUSA. https://www.brusa.biz/portfolio/hsm1-6-17-12/?lang=en.

[87] Sami Ruoho, Jere Kolehmainen, Jouni Ikaheimo, and Antero Arkkio. Interdependence of Demagnetization, Loading, and Temperature Rise in a Permanent-Magnet Synchronous Motor. *IEEE Transactions on Magnetics*, 46(3):949–953, March 2010.

[88] K.-C. Kim, S.-B. Lim, D.-H. Koo, and J. Lee. The Shape Design of Permanent Magnet for Permanent Magnet Synchronous Motor Considering Partial Demagnetization. *IEEE Transactions on Magnetics*, 42(10):3485–3487, October 2006.

[89] Jongman Hong, Sanguk Park, Doosoo Hyun, Tae-june Kang, Sang Bin Lee, Christian Kral, and Anton Haumer. Detection and Classification of Rotor Demagnetization and Eccentricity Faults for PM Synchronous Motors. *IEEE Transactions on Industry Applications*, 48(3):923–932, May 2012.

[90] M. Meyer and J. Bocker. Transient peak currents in permanent magnet synchronous motors for symmetrical short circuits. In *International Symposium on Power Electronics, Electrical Drives, Automation and Motion. SPEEDAM.*, pages 404–409, Taormina, Italy, 2006. IEEE.

[91] B. A. Welchko, T. M. Jahns, W. L. Soong, and J. M. Nagashima. IPM synchronous machine drive response to symmetrical and asymmetrical short circuit faults. *IEEE Transactions on Energy Conversion*, 18(2):291–298, June 2003.

[92] W. Q. Chu and Z. Q. Zhu. Analytical modeling and investigation of transient response of PM machines with 3-phase short-circuit fault. In *2011 IEEE International Electric Machines Drives Conference (IEMDC)*, pages 125–130, May 2011.

[93] James D. McFarland and Thomas M. Jahns. Investigation of the Rotor Demagnetization Characteristics of Interior PM Synchronous Machines During Fault Conditions. *IEEE Transactions on Industry Applications*, 50(4):2768–2775, July 2014.

[94] Jawad Faiz and Ehsan Mazaheri-Tehrani. Demagnetization Modeling and Fault Diagnosing Techniques in Permanent Magnet Machines Under Stationary and Nonstationary Conditions: An Overview. *IEEE Transactions on Industry Applications*, 53(3):2772–2785, May 2017.

[95] Zhigang Sun, Jiabin Wang, David Howe, and Geraint Jewell. Analytical Prediction of the Short-Circuit Current in Fault-Tolerant Permanent-Magnet Machines. *IEEE Transactions on Industrial Electronics*, 55(12):4210–4217, December 2008.

[96] Min Dai, A. Keyhani, and T. Sebastian. Fault analysis of a PM brushless DC Motor using finite element method. *IEEE Transactions on Energy Conversion*, 20(1):1–6, March 2005.

[97] Simone Ferrari, Eric Armando, and Gianmario Pellegrino. Torque Ripple Minimization of PM-assisted Synchronous Reluctance Machines via Asymmetric Rotor Poles. In *2019 IEEE Energy Conversion Congress and Exposition (ECCE)*, pages 4895–4902, September 2019.

[98] Simone Ferrari, Gaetano Dilevrano, Paolo Ragazzo, and Gianmario Pellegrino. The dq-theta Flux Map Model of Synchronous Machines. In *2021 IEEE Energy Conversion Congress and Exposition (ECCE)*, October 2021.

[99] Siemens. Simcenter MagNet. plm.automation.siemens.com/global/en/products/simcenter/magnet.html.

[100] Burak Ozpineci. Oak Ridge National Laboratory Annual Progress Report for the Electric Drive Technologies Program. Technical Report ORNL/SPR-2015/626, Oak Ridge National Lab. (ORNL), Oak Ridge, TN (United States). Power Electronics and Electric Machinery Research Facility, October 2015.

[101] Simone Ferrari and Gianmario Pellegrino. FEAfix: FEA Refinement of Design Equations for Synchronous Reluctance Machines. *IEEE Transactions on Industry Applications*, 56(1):256–266, January 2020.

[102] Chao Lu, Simone Ferrari, Gianmario Pellegrino, Claudio Bianchini, and Matteo Davoli. Parametric design method for SPM machines including rounded PM shape. In *2017 IEEE Energy Conversion Congress and Exposition (ECCE)*, pages 4309–4315, 2017.

[103] Paolo Ragazzo, Gaetano Dilevrano, Simone Ferrari, and Gianmario Pellegrino. Design of IPM Synchronous Machines Using Fast-FEA Corrected Design Equations. In *2022 International Conference on Electrical Machines (ICEM)*, pages 1–7, September 2022. ISSN: 2381-4802.

[104] Thomas A. Lipo. *Introduction to AC Machine Design*. John Wiley, Hoboken, NJ, USA: Wiley, 2017.

[105] Francesco Cupertino, Marco Palmieri, and Gianmario Pellegrino. Design of high-speed synchronous reluctance machines. In *2015 IEEE Energy Conversion Congress and Exposition (ECCE)*, pages 4828–4834, September 2015. ISSN: 2329-3748.

[106] Simone Ferrari, Paolo Ragazzo, Gaetano Dilevrano, and Gianmario Pellegrino. Determination of the Symmetric Short-Circuit Currents of Synchronous Permanent Magnet Machines Using Magnetostatic Flux Maps. In *2021 IEEE Energy Conversion Congress and Exposition (ECCE)*, pages 3697–3704, 2021.

[107] Tesla. Model 3 Owner's Manual. https://www.tesla.com/ownersmanual/model3/en_cn/GUID-E414862C-CFA1-4A0B-9548-BE21C32CAA58.html.

[108] Stjepan Stipetic, Damir Zarko, and Mircea Popescu. Ultra-fast axial and radial scaling of synchronous permanent magnet machines. *IET Electric Power Applications*, 10(7):658–666, August 2016.

[109] Stjepan Stipetic, James Goss, Damir Zarko, and Mircea Popescu. Calculation of Efficiency Maps Using a Scalable Saturated Model of Synchronous Permanent Magnet Machines. *IEEE Transactions on Industry Applications*, 54(5):4257–4267, September 2018.

[110] F. Pauli, A. Ruf, and K. Hameyer. Thermal Overload Capability of Permanent Magnet Synchronous Motors Employing Scaling Laws. In *2018 XIII International Conference on Electrical Machines (ICEM)*, pages 433–439, September 2018. ISSN: 2381-4802.

[111] Frank P. Incropera, editor. *Fundamentals of heat and mass transfer*. John Wiley, Hoboken, NJ, 6th ed edition, 2007. OCLC: ocm62532755.

[112] P. Ragazzo, S. Ferrari, N. Riviere, M. Popescu, and G. Pellegrino. Efficient Multiphysics Design Workflow of Synchronous Reluctance Motors. In *2020 International Conference on Electrical Machines (ICEM)*, pages 2507–2513, Gothenburg, Sweden, August 2020. IEEE.

[113] Antoni Ruiz, Athanasios Meseamanolis, Lluis Santolaria, Milad Maleki, and Andreas Baschnagel. Active Short Circuit Capability of HalfBridge Power Modules Towards EMobility Applications. In *PCIM Europe digital days 2021; International Exhibition and Conference for Power Electronics, Intelligent Motion, Renewable Energy and Energy Management*, pages 1–7, May 2021.

[114] Ali Akay, Paul Lefley, and Mohan Kansara. Open-Circuit Fault-Tolerant Control for a Five-Phase Permanent Magnet Synchronous Machine Drive. In *2020 7th International Conference on Electrical and Electronics Engineering (ICEEE)*, pages 150–154, April 2020.

[115] Wang Peng, Wang Kun, and Fan Meng. Demagnetization Study of Permanent Magnet Machine Under Three Phase Short Circuit. In *2023 IEEE 6th International Electrical and Energy Conference (CIEEC)*, pages 2705–2710, May 2023.

[116] T.M. Jahns and V. Caliskan. Uncontrolled generator operation of interior PM synchronous machines following high-speed inverter shutdown. *IEEE Transactions on Industry Applications*, 35(6):1347–1357, November 1999.

[117] Aravind Ramesh Chandran, Martin D. Hennen, Antero Arkkio, and Anouar Belahcen. Safe Turn-Off Strategy for Electric Drives in Automotive Applications. *IEEE Transactions on Transportation Electrification*, 8(1):9–22, March 2022.

[118] Srivatsan Ramarathnam, Abdul Kalam Mohammed, Berker Bilgin, Anand Sathyan, Hossein Dadkhah, and Ali Emadi. A Review of Structural and Thermal Analysis of Traction Motors. *IEEE Transactions on Transportation Electrification*, 1(3):255–265, 2015.

[119] Cody Rhebergen, Berker Bilgin, Ali Emadi, Elizabeth Rowan, and Jason Lo. Enhancement of electric motor thermal management through axial cooling methods: A materials approach. In *2015 IEEE Energy Conversion Congress and Exposition (ECCE)*, pages 5682–5688, 2015.

[120] Amitav Tikadar, David Johnston, Nitish Kumar, Yogendra Joshi, and Satish Kumar. Comparison of electro-thermal performance of advanced cooling techniques for electric vehicle motors. *Applied Thermal Engineering*, 183:116182, 2021. Publisher: Elsevier.

[121] Peer-Ole Gronwald and Thorsten A. Kern. Traction Motor Cooling Systems: A Literature Review and Comparative Study. *IEEE Transactions on Transportation Electrification*, 7(4):2892–2913, 2021.

[122] Nicolas Rivière, Markus Stokmaier, and James Goss. An Innovative Multi-Objective optimization Approach for the Multiphysics Design of Electrical Machines. In *2020 IEEE Transportation Electrification Conference & Expo (ITEC)*, pages 691–696, June 2020. ISSN: 2377-5483.

[123] Silong Li, Yingjie Li, Wooyoung Choi, and Bulent Sarlioglu. High-Speed Electric Machines: Challenges and Design Considerations. *IEEE Transactions on Transportation Electrification*, 2(1):2–13, March 2016.

[124] Aldo Boglietti, Ayman M. El-Refaie, Oliver Drubel, Avoki M. Omekanda, Nicola Bianchi, Emmanuel B. Agamloh, Mircea Popescu, Antonino Di Gerlando, and James Borg Bartolo. Electrical Machine Topologies: Hottest Topics in the Electrical Machine Research Community. *IEEE Industrial Electronics Magazine*, 8(2):18–30, June 2014.

[125] Riccardo Leuzzi, Paolo Cagnetta, Simone Ferrari, Paolo Pescetto, Gianmario Pellegrino, and Francesco Cupertino. Transient Overload Characteristics of PM-Assisted Synchronous Reluctance Machines, Including Sensorless Control Feasibility. *IEEE Transactions on Industry Applications*, 55(3):2637–2648, 2019.

[126] Faizul Momen, Khwaja Rahman, and Yochan Son. Electrical Propulsion System Design of Chevrolet Bolt Battery Electric Vehicle. *IEEE Transactions on Industry Applications*, 55(1):376–384, January 2019.

[127] Wenying Jiang and Thomas M. Jahns. Coupled Electromagnetic–Thermal Analysis of Electric Machines Including Transient Operation Based on Finite-Element Techniques. *IEEE Transactions on Industry Applications*, 51(2):1880–1889, March 2015.

[128] Anantaram Varatharajan, Paolo Pescetto, and Gianmario Pellegrino. Sensorless Self-Commissioning of Synchronous Reluctance Machine with Rotor Self-Locking Mechanism. In *2019 IEEE Energy Conversion Congress and Exposition (ECCE)*, pages 812–817, September 2019. ISSN: 2329-3748.

[129] Paolo Pescetto and Gianmario Pellegrino. Determination of PM Flux Linkage Based on Minimum Saliency Tracking for PM-SyR Machines Without Rotor Movement. *IEEE Transactions on Industry Applications*, 56(5):4924–4933, September 2020.

[130] Yaohui Gai, Mohammad Kimiabeigi, Yew Chuan Chong, James D. Widmer, Xu Deng, Mircea Popescu, James Goss, Dave A. Staton, and Andrew Steven. Cooling of Automotive Traction Motors: Schemes, Examples, and Computation Methods. *IEEE Transactions on Industrial Electronics*, 66(3):1681–1692, March 2019.

[131] Oliver Wallscheid. Thermal Monitoring of Electric Motors: State-of-the-Art Review and Future Challenges. *IEEE Open Journal of Industry Applications*, 2:204–223, 2021.

[132] Nikola Z. Popov, Slobodan N. Vukosavic, and Emil Levi. Motor Temperature Monitoring Based on Impedance Estimation at PWM Frequencies. *IEEE Transactions on Energy Conversion*, 2014.

[133] Christian Kral, Anton Haumer, Matthias Haigis, Hermann Lang, and HansjÖrg Kapeller. Comparison of a CFD Analysis and a Thermal Equivalent Circuit Model of a TEFC Induction Machine With Measurements. *IEEE Transactions on Energy Conversion*, 24(4):809–818, 2009.

[134] Sunghyun Moon and Sungho Lee. High-Reliable Temperature Prediction Considering Stray Load Loss for Large Induction Machine. *IEEE Transactions on Magnetics*, 55(6):1–5, 2019.

[135] Claudio Sciascera, Paolo Giangrande, Luca Papini, Chris Gerada, and Michael Galea. Analytical Thermal Model for Fast Stator Winding Temperature Prediction. *IEEE Transactions on Industrial Electronics*, 64(8):6116–6126, 2017.

[136] Longfei Cao, Xinggang Fan, Dawei Li, Wubin Kong, Ronghai Qu, and Zirui Liu. Improved LPTN-Based Online Temperature Prediction of Permanent Magnet Machines by Global Parameter Identification. *IEEE Transactions on Industrial Electronics*, 70(9):8830–8841, 2023.

[137] Kevin Bersch, Stefano Nuzzo, Peter H. Connor, Carol N. Eastwick, Robert Rolston, and Michael Galea. Thermal and Electromagnetic Stator Vent Design Optimisation for Synchronous Generators. *IEEE Transactions on Energy Conversion*, 36(1):207–217, March 2021.

[138] Mehmet Caglar Kulan and Nick J. Baker. Development of a Thermal Equivalent Circuit to Quantify the Effect of Thermal Paste on Heat Flow Through a Permanent Magnet Alternator. *IEEE Transactions on Industry Applications*, 55(2):1261–1271, March 2019.

[139] Paolo Pescetto, Simone Ferrari, Gianmario Pellegrino, Enrico Carpaneto, and Aldo Boglietti. Winding Thermal Modeling and Parameters Identification for Multithree Phase Machines Based on Short-Time Transient Tests. *IEEE Transactions on Industry Applications*, 56(3):2472–2480, 2020.

[140] J. Goss, P. H. Mellor, R. Wrobel, D. A. Staton, and M. Popescu. The design of AC permanent magnet motors for electric vehicles: A computationally efficient model of the operational envelope. In *6th IET International Conference on Power Electronics, Machines and Drives (PEMD 2012)*, pages 1–6, March 2012.

[141] Pratik Roy, Alexandre J. Bourgault, Muhammad Towhidi, Pengzhao Song, Ze Li, Shruthi Mukundan, Gary Rankin, and Narayan C. Kar. An Algorithm for Effective Design and Performance Investigation of Active Cooling System for Required Temperature and Torque of PM Traction Motor. *IEEE Transactions on Magnetics*, 57(2):1–7, February 2021.

[142] Vincenzo Madonna, Adam Walker, Paolo Giangrande, Giovanni Serra, Chris Gerada, and Michael Galea. Improved Thermal Management and Analysis for Stator End-Windings of Electrical Machines. *IEEE Transactions on Industrial Electronics*, 66(7):5057–5069, 2019.

[143] Yatai Ji, Paolo Giangrande, Weiduo Zhao, Vincenzo Madonna, He Zhang, and Michael Galea. Determination of Hotspot Temperature Margin for Rectangular Wire Windings Considering Insulation Thermal Degradation and Partial Discharge. *IEEE Transactions on Transportation Electrification*, pages 1–1, 2023.

[144] Kan Liu, Z. Q. Zhu, and David A. Stone. Parameter Estimation for Condition Monitoring of PMSM Stator Winding and Rotor Permanent Magnets. *IEEE Transactions on Industrial Electronics*, 60(12):5902–5913, 2013.

[145] Tenghui Dong, Xi Zhang, Chong Zhu, Yansong Lu, and Mayan Li. Improved hotspot monitoring method for thermal management system of automotive traction motor. *IET Electric Power Applications*, 14(11):2255–2262, 2020. Publisher: Wiley Online Library.

[146] Fausto Stella, Gianmario Pellegrino, and Eric Armando. Coordinated Online Junction Temperature Estimation and Prognostic of SiC Power Modules. In *2018 IEEE Energy Conversion Congress and Exposition (ECCE)*, pages 1907–1913, 2018.

[147] David Reigosa, Daniel Fernández, María Martínez, Juan Manuel Guerrero, Alberto B. Diez, and Fernando Briz. Magnet Temperature Estimation in Permanent Magnet Synchronous Machines Using the High Frequency Inductance. *IEEE Transactions on Industry Applications*, 55(3):2750–2757, 2019.

[148] Shuaichen Ye and Xiaoxian Yao. A Modified Flux Sliding-Mode Observer for the Sensorless Control of PMSMs With Online Stator Resistance and Inductance Estimation. *IEEE Transactions on Power Electronics*, 35(8):8652–8662, 2020.

[149] Motor Design Ltd. Motor-CAD Software. https://www.motor-design.com.

[150] Gianmario Pellegrino. Identification of PM Synchronous Machines Parameters for Design and Control Purposes. In Gianmario Pellegrino, Thomas M. Jahns, Nicola Bianchi, Wen Soong, and Francesco Cupertino, editors, *The Rediscovery of Synchronous Reluctance and Ferrite Permanent Magnet Motors: Tutorial Course Notes*, SpringerBriefs in Electrical and Computer Engineering, pages 77–107. Springer International Publishing, Cham, 2016.

[151] Sandro Rubino, Luisa Tolosano, Fabio Mandrile, Simone Ferrari, Eric Armando, and Radu Bojoi. Magnetic Model Identification of Multi-Three-Phase Synchronous Motors. In *2023 IEEE Energy Conversion Congress and Exposition (ECCE)*, pages 4775–4782, October 2023. ISSN: 2329-3748.

[152] Ian Osborne. ElectricDrives | GKN Automotive supplies innovative two-in-one eDrive system for Fiat 500 electric cars. https://electricdrives.tv/gkn-automotive-supplies-innovative-two-in-one-edrive-system-for-fiat-500-electric-cars/, June 2021.

[153] Fabricio Machado, Phillip J. Kollmeyer, and Ali Emadi. Analytical loss model for single- and two-speed electric vehicle gearboxes. In *2023 IEEE Transportation Electrification Conference and Expo, Asia-Pacific (ITEC Asia-Pacific)*, pages 1–8, Chiang Mai, Thailand, November 2023. IEEE.

[154] Fabricio Machado, Phillip J. Kollmeyer, and Ali Emadi. Analytical loss model for single- and two-speed electric vehicle gearboxes. In *2023 IEEE Transportation Electrification Conference and Expo, Asia-Pacific (ITEC Asia-Pacific)*, pages 1–8, 2023.